Insertion of fluorescent manganese compounds - models of catalase - into mesoporous nanoparticles of silica, resol-silica and carbon-silica

François-Xavier Turquet

Tesi doctoral

Insertion of fluorescent manganese compounds - models of catalase - into mesoporous nanoparticles of silica, resol-silica and carbon-silica

François-Xavier Turquet

UNIVERSITAT DE BARCELONA

ENS DE LYON

Insertion of fluorescent manganese compounds - models of catalase - into mesoporous nanoparticles of silica, resol-silica and carbon-silica

Programa de doctorat en Nanociènces

Autor: François-Xavier Turquet

Directores: Dra. Montserrat Corbella, Dra. Belén Albela

UNIVERSITAT DE BARCELONA

ENS DE LYON

Numéro National de Thèse : 2018LYSEN086

THESE de DOCTORAT DE L'UNIVERSITE DE LYON

opérée par
l'Ecole Normale Supérieure de Lyon
en cotutelle avec
l'Universitat de Barcelona

Ecole Doctorale N° 206
École Doctorale de Chimie (CHIMIE, PROCÉDÉS, ENVIRONNEMENT)

Discipline : **Chimie**

Soutenue publiquement le 17/12/2018, par :

François-Xavier TURQUET

Insertion of fluorescence manganese compounds – models of catalase – into mesoporous nanoparticles of silica, resol-silica and carbon-silica

Insertion de composés fluorescents du manganèse
- modèles de la catalase – à l'intérieur de nanoparticules mésoporeuses de silice, résol-silice et carbone-silice

---

Devant le jury composé de :

Mme Carole DUBOC, Directrice de Recherche du CNRS, Grenoble	Rapporteure
Mme Christelle HUREAU, Directrice de recherche du CNRS, Toulouse	Rapporteure
M. Dominique LUNEAU, Professeur des Universités, UCBL Lyon 1	Examinateur
M. Albert FIGUEROLA SILVESTRE, Professeur Associé, Universitat de Barcelona	Examinateur
Mme Montserrat RODRIGUEZ PIZARRO, Professeure Associée, Universitat de Girona	Examinatrice
Mme Belén ALBELA CASTRILLO, Maître de Conférence, ENS de Lyon	Directrice de thèse
Mme Montserrat CORBELLA CORDOMI, Professeure des Universités, Universitat de Barcelona	Co-directrice de thèse

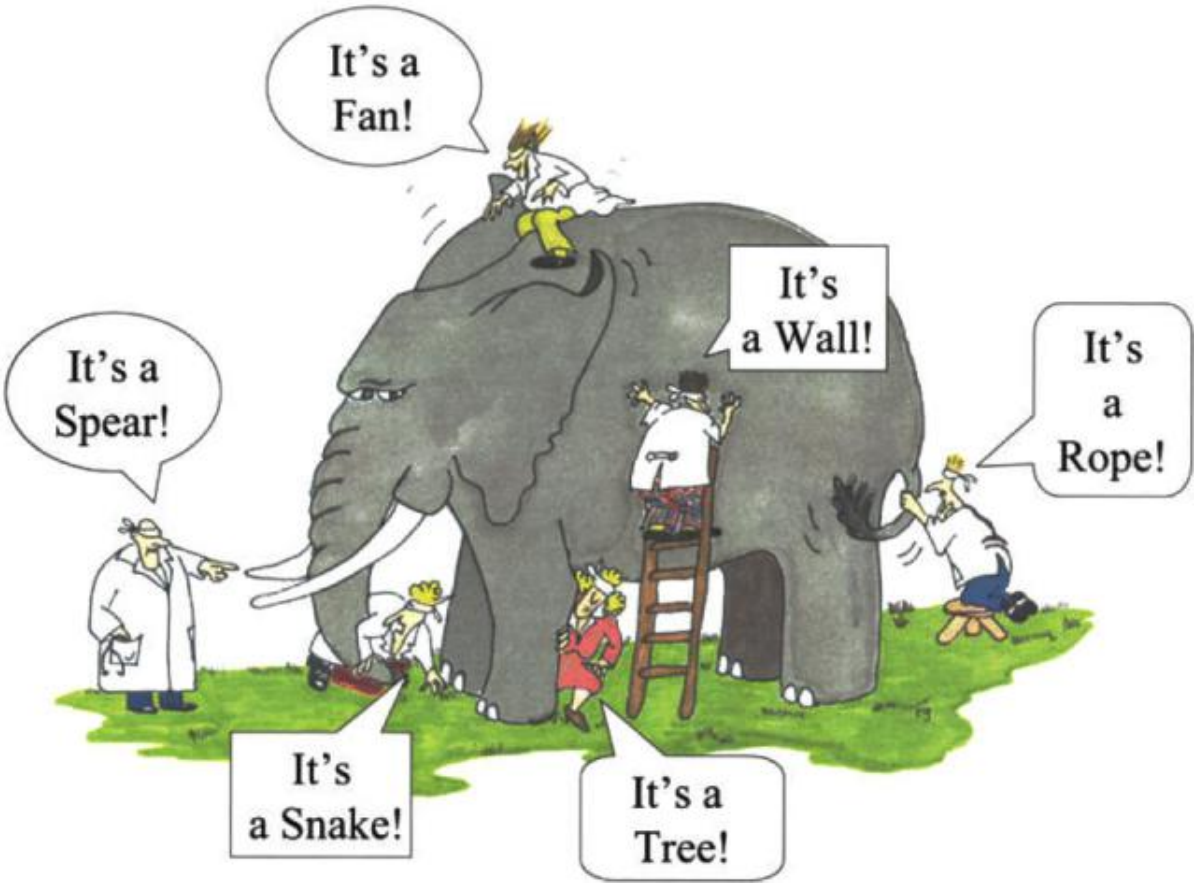
It's a Fan!
It's a Spear!
It's a Wall!
It's a Rope!
It's a Snake!
It's a Tree!

Summary

Manganese compounds display many properties of interest. Manganese is known for its variety of oxidation states (-III to +VII) and can form mono to multinuclear compounds. The richness of its chemistry is strengthen with the ability of this metal to bond easily with a wide array of ligands and exhibits multiple coordination modes.
From this vast family of manganese compounds, many exhibit strong magnetic properties, ferromagnetism as well as antiferromagnetism. In the last decades, this drove the interest of manganese compounds for fields relative to magnetic properties such as single molecular magnets.
Nontheless, manganese is also known for its redox properties and can be used as a strong oxidant or for its catalytic properties. This latter feature is actually found in many life forms, in particular those provided with manganese metalloproteins. These proteins often have to do with the processing of dioxygen or species derived from dioxygen, in the organism. The main illustration of this being the role of manganese in the Photosystem II, responsible for dioxygen production from photosynthesis or Mn-based enzymes that catalyse the degradation of Reactive Oxygen Species (ROS) such as Mn-catalase or superoxyde dismutase.

ROS are well known for their role in some metabolism disorders and many serious diseases. As a consequence the use of metallo-enzyme mimics like Mn-catalase is seen as a potential tool in the field of antioxydative therapies. Unfortunately, many synthetic Mn-catalase mimics are not stable nor active in physiological conditions. But this issue can be overcomed thanks to nanomedicine and the use of nano-sized vectors for the manganese compounds. Progress has recently been made towards this goal with Mn-catalase mimics loaded inside mesoporous silica exhibiting activity in water. Nevertheless, these advances are still far from the application in living organisms.

In order to build on these foundations several issues remain to be overcome and this work proposes to contribute to it. It focuses on two points: the improvement of the biocompatibility of the manganese support and the introduction of multifunctionality in the system with the addition of luminescence to the Mn-catalase mimics. This study is divided into three parts: **Part I** focuses on molecular chemistry of Mn compounds, **Part II** deals with materials science of the nanovectors and **Part III** reports the chemical and physical properties of the hybrid system.

Part I

The synthesis and characterisation of three new luminescent manganese compounds of oxidation states II and III is presented. They are all designed with the same base ligands, 2,2'-bipyridine (bpy) and the fluorescent 9-anthracenecarboxylate ($AntCO_2^-$).
Mn^{II} compounds, a chain and a dinuclear complex of respective formulas $[Mn(bpy)(AntCO_2)_2]_n$ and $[\{Mn(bpy)(AntCO_2)\}_2(\mu\text{-}AntCO_2)_2(\mu\text{-}OH_2)]$, are neutral and have very similar compositions. An equilibrium is found to exist between the two compounds in the conditions of the synthesis. However, they can be separated and the chain compound can be crystallised to form the dinuclear one. Crystals of the dinuclear compound can also be obtained directly through microwave-assisted synthesis and enabled us to perform the resolution of its structure.
The Mn^{III} compound is tetranuclear and the formula $[Mn_4O_2(AntCO_2)_6(bipy)_2(ClO_4)_2]$ is proposed based on elemental analysis and magnetic measurements. No crystal structure was obtained for this compound despite many attempts and the use of different salts. Moreover, during the synthesis of this compound and due to several crystallisations attempts, an organic compound derived from the anthracenecarboxylate ligand, the 10-oxo-9,10-dihydroanthracene-9-yl anthracene-9-carboxylate was obtained and crystallised for the first time.

In addition to standard characterisation techniques such as IR spectroscopy and elemental analysis the magnetic properties of these compounds were studied. For all of them, magnetic susceptibility measurements versus temperature were performed and fits and simulations were run to determine the magnetic coupling constant (J) and propose, when possible, zero-field splitting (ZFS) parameters (D and E). Mn^{II} compounds were studied using electron paramagnetic resonance (EPR) spectroscopy and simulations were performed to confirm ZFS parameters. For the Mn^{III} compound, magnetisation measurements versus temperature were recorded at different fields and simulations used to establish the three magnetic coupling constants of the system as well as the axial anisotropy .

All compounds synthesised show antiferromagnetic coupling, with the strongest values found for the Mn^{III} compound, which also exhibits the strongest ZFS due to Jahn-Teller effect. Thanks to the combination of techniques used for its characterisation, despite no X-ray diffraction resolution this compound is strongly suspected to present a butterfly geometry.

Part II

The synthesis of the nanoparticles (NPs) used as the Mn-support and the preparation of the hybrid [Mn]@NP materials are presented. The particles were synthesised by reproducing a very recent technique, the syntaxy, which enables the formation of entangled "sisters" nanospheres of silica and a polyphenol resin, the resol. The result are bi-phasic mesoporous nanoparticles with two phases that are the negative of each other, one organic, one inorganic. Further thermal treatment was applied to this base material (resol-silica) to obtain pure mesoporous silica nanoparticles and hybrid amorphous carbon-silica nanoparticles.

These three nanoparticles types were then loaded with three different amounts of two of

the complex prepared in the **Part I**, the Mn^{II} chain and the tetranuclear Mn^{III} compounds. The porosity of these eighteen hybrid materials was studied using nitrogen-sorption isotherms, suggesting the insertion of the compounds inside the nanoparticles. Further studies were performed using thermogravimetric analysis (TGA) and elemental analysis and completed with electronic microscopy (both in scanning and transmission modes) and energy dispersive X-ray spectroscopy (EDS). They confirmed the presence of manganese compounds inside the material in quantities in relation to the aimed Mn-compound loading, highlighting, however, the possibility that some of them, especially for the more bulky Mn^{III} compound might not be intact inside the nanoparticles.

Part III

The physical and chemical properties of the materials prepared are described in this chapter. Magnetic properties of hybrid [Mn]@NPs materials is discussed. The optical properties of the nanoparticles and the coordination compounds are examined separately before studying the fluorescence of the hybrid materials. Finally, some tests were run to measure the disproportion of hydrogen peroxide catalysed by the manganese compounds in acetonitrile solutions and of the Mn^{II} compounds inserted inside resol-silica nanoparticles in aqueous suspensions.

The magnetic properties of the hybrid materials were evaluated by studying the magnetic susceptibility as a function of temperature and using EPR spectroscopy for nanoparticles loaded with Mn^{II} compounds. They reveal the presence of electronic radicals inside carbon-silica NPs, which is consistent with the properties of C_{sp^2} materials. EPR signals of [Mn^{II}]@NPs also show a weak magnetic interaction between neighbouring manganese, suggesting the presence of dinuclear entities inside the nanoparticles.

Both Mn^{II} chain and tetranuclear Mn^{III} compounds have a strong luminescence in ethanol solution in the 380-480 nm region.As it is believed that the chain compound is fragmented in solution, its spectra is assimilated to the one of the dinuclear compound. Their emission spectra is very similar to the one of their anthracenic ligand. The intensity of emission of the tetranuclear Mn^{III} is higher than that of the Mn^{II} compound for the same concentration, likely because it carries six anthracene groups per molecule versus four for the dinuclear. However, for concentrations above 10^{-5} mol/L a large band at 470 nm becomes prevalent for the Mn^{III} compound. It is explained by its low solubility in ethanol and the formation of aggregates, which contribute to the modification of the emission through electronic interactions between the ligands.
The particles themselves do show some luminescence. Hybrid resol-silica nanoparticles have a small fluorescence around 470 nm that is due to the polymer. This emission band disappears on the carbon-silica particles as the resol is turned into amorphous carbon. Interestingly, all nanoparticle types have an emission peak at 410 nm and pure silica particles emit on a broader range, between 380 and 540 nm. This is the fluorescence of the silica, which is more often observed for organised silica phases like quartz, or silica prepared in acidic conditions followed by thermal treatment. This emission is rare for silica phases prepared in basic conditions (like the Stöber-like process used) and is likely due to carbon defects introduced inside the silica

network during the preparation of the material.
The luminescence of all hybrid [Mn]@NPs is very low, with a quenching of both the signal of the complexes and of the particles. Once again it can be explained by the defects of the silica that are known dye luminescence quenchers. However, this property enables us to evaluate qualitatively the efficiency of the prepared materials to retain their cargo when dispersed in ethanol. It appears that Mn^{II} compounds are less released than Mn^{III} compounds, but that both pure silica and carbon-silica NPs do leak significantly. This is not very surprising considering the absence of surface modification that is normally employed to bond manganese complex to silica nanoparticles. Nevertheless, the Mn^{II} compounds inserted inside resol-silica nanoparticles seem to be efficiently retained for long periods of time. This can be attributed to the affinity of the complex for the polymer that presents both aromatic rings and oxygen atoms, like its ligands.

To conclude, preliminary catalytic tests to measure hydrogen peroxide disproportion in the presence of Mn^{II} and Mn^{III} compounds have been run. All the compounds show a moderate activity in acetonitrile (between 130 and 150 turnover number (TON) per hour). The Mn^{II} compounds loaded inside resol-silica NPs were tested in aqueous solution. They show a low TON but it is due to the important Mn^{II} compound load compared to the amount of hydrogen peroxide rather than a lack of activity. They show sensibility towards the pH of the solution, with a significantly higher disproportionation rate of hydrogen peroxide at pH $= 9$ than at pH $= 7.5$. This difference is due to the kinetics of the reaction. Indeed, a competition is evidenced between the catalytic disproportion of hydrogen peroxide into dioxygen and the oxidation of the resol support by the same molecule. This paves the way for optimising the process in ideal conditions, both in terms of Mn compound load and pH, to maximise the dismutation of hydrogen peroxide and reduce the oxydation of the organic part of support.

Résumé

Les composés du manganèse font preuve de nombreuses propriétés intéressantes. Le manganèse est connu pour avoir une grande variété d'états d'oxydation (de -III à +VII) et peut former des composés mono- ou poly-nucléaires. La richesse de sa chimie est renforcée par la capacité de ce métal à se lier facilement avec un grand nombres de ligands et il possède de nombreux modes de coordination.
Dans la grande famille des composés du manganèse, beaucoup sont dotés de propriétés magnétiques, aussi bien ferromagnétiques qu'antiferromagnétiques. Ces dernières décennies, l'intérêt porté aux composés du manganèse est venu des domaines s'intéressant à ses propriétés magnétiques, comme la possibilité de créer les aimants monomoléculaires.
Cependant, le manganèse est aussi connu pour ses propriétés redox et peut-être utilisé comme un puissant oxydant ou pour ses propriétés en catalyse. Ce dernier aspect se retrouve d'ailleurs dans de nombreuses organismes vivants, en particulier ceux muni de métalloprotéines à manganèse. Ces protéines ont souvent à voir, dans l'organisme, avec le traitement de l'oxygène ou des espèces dérivées du dioxygène. Les illustrations la plus connues de ce rôle sont la place du manganèse dans le Photosystème II qui est responsable de la production du dioxygène par photosynthèse ou les enzymes à base de manganèse qui catalysent la dégradation des dérivés réactifs de l'oxygène (DRO) comme la catalase à manganèse ou la superoxyde dismutase.

Les DRO sont bien connus pour leur rôle dans certains déséquilibres métaboliques et de nombreuses maladies graves. Par conséquent, l'utilisation de mimes de metalloenzymes comme la catalase à manganèse est considéré comme un outil potentiel dans le domaine des des thérapies antioxydantes. Malheureusement, de nombreux mimes synthétiques de la catalase à manganèse ne sont ni stables ni actifs en conditions physiologiques. Cette difficulté peut-être contournée grâce à la nano-médecine et l'utilisation de nano-vecteurs pour transporter les composés de manganèse. Des progrès récents ont été faits dans cette direction grâce à des mimes de la catalase à manganèse insérés à l'intérieur de silice mésoporeuse et qui se révèlent actifs dans l'eau. Néanmoins ces avancées sont encore assez éloignées d'une application à des organismes vivants.

Pour construire sur ces fondations, plusieurs étapes doivent être franchies et ce travail se propose d'y contribuer. Il se concentre sur deux points : l'amélioration de la biocompatibilité du support du manganèse, et l'introduction de la multifonctionnalité dans ce système avec l'ajout de la luminescence aux mimes de la catalase. Cette étude est divisée en trois parties : la **Partie I** se concentre sur la chimie des composés du manganèse, la **Partie II** concerne la chimie des matériaux, appliquée aux nano-vecteurs et la **Partie III** examine les propriétés physiques et chimiques du système hybride.

Partie I

La synthèse et la caractérisation de trois nouveaux composés luminescents du manganèse de nombre d'oxydation II et III est présentée. Ils sont tous conçus à partir des mêmes ligands, la 2,2'-bipyridine (bpy) et l'anthracène-9-carboxylate ($AntCO_2^-$). Les composés du Mn^{II}, une chaîne et un composé dinucléaire de formules respectives $[Mn(bpy)(AntCO_2)_2]_n$ et $[\{Mn(bpy)(AntCO_2)\}_2(\mu\text{-}AntCO_2)_2(\mu\text{-}OH_2)]$ sont neutres et ont une composition très similaire. Dans les conditions de la synthèse, il existe un équilibre entre ces deux composés. Ils peuvent cependant être séparés et la chaîne peut être cristallisée pour former le complexe dinucléaire. Des cristaux du composé dinucléaire peuvent également être obtenus directement grâce à une synthèse assistée par micro-ondes et ont permis d'effectuer sa résolution structurale.
Le composé du Mn^{III} est tétranucléaire et sa formule, proposée grâce aux analyses élémentaires et à ses propriétés magnétiques, est $[Mn_4O_2(AntCO_2)_6(bipy)_2(ClO_4)_2]$. Aucune structure cristalline n'a pu être obtenue pour ce composé, malgré de nombreux essais et l'utilisation de différents sels et solvants. De plus, durant la synthèse de ce composé, au cours des essais de cristallisation, un composé dérivé du ligand anthracène-9-carboxylate, le 10-oxo-9,10-dihydroanthracène-9-yl anthracène-9-carboxylate à été obtenu et cristallisé pour la première fois.

En plus des techniques de caractérisation standard, comme la spectroscopie IR et les analyses élémentaires, les propriétés magnétiques de ces composés ont été étudiées. Des mesures de susceptibilité magnétique ont été effectuées pour tous les composés et des fits et des simulations ont été calculés afin de déterminer les constantes de couplages magnétiques (J) et de proposer, quand c'est possible, les paramètres (D et E) de la fragmentation à champ nul (zero-field splitting, ZFS, en anglais). Les composés du Mn^{II} ont été étudiés grâce à la spectroscopie de résonance paramagnétique de l'électron (RPE) et des simulations ont été effectuées pour confirmer les paramètres du ZFS. Pour les composés du Mn^{III}, des mesures de magnétisation ont été enregistrées pour différents champs et des simulations utilisées pour déterminer les trois constantes de couplage magnétique du système ainsi que le paramètre d'anisotropie axiale.

Tous les composés synthétisés présentent un couplage antiferromagnétique, les valeurs les plus élevées ont été trouvées pour le composé du Mn^{III} qui présente également, à cause de l'effet Jahn-Teller, le ZFS le plus important. Grâce à la combinaison des techniques de caractérisation, malgré l'absence de résolution par diffraction des rayons X, ce composé est fortement suspecté de présenter une géométrie de type papillon.

Partie II

La synthèse des nanoparticules servant de support aux complexes de manganèse et la préparation des matériaux hybrides [Mn]@NP sont présentés dans cette partie. Les particules ont été synthétisées en reproduisant une technique très récente, la syntaxie, qui permet la formation de deux phases enchevêtrées « soeurs » de silice et d'une résine de polyphénol, le résol. Il en

résulte des nanoparticules bi-phasiques mésoporeuses possédant deux phases, une organique, l'autre inorganique, formant le négatif l'une de l'autre. Ce matériau de base a été soumis à un traîtement thermique supplémentaire visant à obtenir de pures nanoparticules de silice et des nanoparticules hybrides carbone amorphe-silice.

Ces trois types de nanoparticule ont été impregnés de trois différentes quantitées des deux complexes préparés dans la **Partie I**, la chaîne de Mn^{II} et le composé tétranucléaire de Mn^{III}. La porosité de ces dix-huit matériaux hybrides à été étudiée grâce à des isothermes d'adsorption d'azote, suggérant la présence des composés à l'intérieur des nanoparticules. Des études plus approfondies ont été effectuées par analyse thermogravimétrique (ATG) et analyses élémentaires et ont été complétées par des études en microscopie électronique (à la fois en balayage et en transmission) et par spectroscopie de dispersion d'énergie des rayons X (SDE). Elles ont confirmé la présence des composés du manganèse à l'intérieur des matériaux en quantités relatives à la masse de composés prévue, mettant cependant en lumière la possibilité que certains complexes, en particulier le composé de Mn^{III}, plus encombrant, ne soient pas intactes à l'intérieur des particules.

Partie III

Les propriétés physiques et chimiques de ces matériaux sont décrites dans ce chapitre. Tout d'abord, les propriétés magnétiques des matériaux hybrides [Mn]@NPs sont discutées. Les propriétés optiques des nanoparticules et des supports sont ensuite examinées séparément avant d'étudier la fluorescence des matériaux hybrides. Enfin, des test ont été menés pour évaluer la capacité des composés du manganèse et des composés insérés dans les nanoparticules résol-silice, à dismuter le peroxyde d'hydrogène dans des solutions d'acétonitrile et des suspensions aqueuses, respectivement.

Les propriétés magnétiques des matériaux hybrides ont été évaluées par l'étude de leur susceptibilité magnétique et grâce à la spectroscopie RPE pour les nanoparticules chargées en composés du Mn^{II}. Elles révèlent la présence de radicaux à l'intérieur des nanoparticules carbone-silice ce qui est en accord avec les propriétés des matériaux C_{sp^2}. Les signaux RPE des matériaux [Mn^{II}]@NPs montrent également de faibles interactions magnétiques entre les manganèses voisins et suggèrent la présence d'entités dinucléaires à l'intérieur des nanoparticules.

La chaîne de Mn^{II} et le composé tétranucléaire de Mn^{III} présentent tous deux une luminescence importante en solution d'éthanol dans la région 380-480 nm. Comme on pense que la chaîne se retrouve fragmentée en solution, son spectre est assimilé à celui du composé dinucléaire. Leurs spectres d'émission sont très similaires à celui de leur ligand anthracènique. L'intensité d'émission du composé tétranucléaire de Mn^{III} est plus élevé que celui du composé de Mn^{II} aux mêmes concentrations, probablement car il porte six groupement anthracène contre quatre pour le composé dinucléaire. Cependant, pour des concentrations supérieures à 10^{-5} mol/L, une bande large à 470 nm devient prépondérante dans le spectre du composé du Mn^{III}. Ce phénomène est expliqué par sa faible solubilité dans l'éthanol et la formation

d'agrégats qui contribuent à la modification de son spectre d'émission par le biais d'interactions électroniques entre les ligands.
Les particules elles-mêmes présentent de la luminescence. Les nanoparticules hybrides résol-silice sont faiblement fluorescente autour de 470 nm à cause du polymère. Cette bande d'émission disparaît pour les particules carbone-silice, alors que le résole est transformé en carbone amorphe. De façon intéressante, tous les types de particules émettent dans un domaine plus large, de 380 à 540 nm. Il s'agit de la fluorescence de la silice qui est observée plus souvent pour des phases organisées comme le quartz ou pour des silices préparées en milieux acide et soumises à un traitement thermique. Ce type d'émission est rare pour les phases de silices préparées en conditions basiques (comme le simili procédé Stöber utilisé) et est probablement due à l'introduction de défauts carbonés dans la matrice de silice durant la préparation du matériau.
La luminescence de tous les hybrides [Mn]@NPs est très faible et présente une extinction à la fois du signal du complexe et de celui des particules. Une fois encore, cela peut-être expliqué par la présence de défauts dans la silice qui sont des quenchers de luminescence connus pour les molécules organiques. Malgré tout, cette propriété nous permet d'évaluer qualitativement l'efficacité avec laquelle les matériaux préparés conservent leur chargement quand ils sont dispersés dans l'éthanol. Il apparaît que les composés du Mn^{II} sont moins libérés dans le milieu que les composés du Mn^{III} mais que les particules de silice pure et de carbone-silice fuient de façon importante. Ce n'est pas très surprenant si l'on considère que la surface des particules n'a pas été modifiée, ce qui est normalement le cas, afin d'attacher les complexes de manganèse à la silice. Cependant, les composés du Mn^{II} insérés dans les particules résol-silice apparaissent retenus dans le matériaux pour de longues durées. Cela peut-être attribué à l'affinité du complexe pour le polymère qui présente, comme ses ligands, des cycles aromatiques et des atomes d'oxygène.

Pour conclure, des tests catalytiques préliminaires ont été menés afin de mesurer la dismutation du peroxyde d'hydrogène en présence des composés de Mn^{II} et Mn^{III}. Tous les composés font preuve d'une activité modérée dans l'acétonitrile (entre 130 et 150 cycles par heure ; turnover number per hour, TON/h, en anglais). Les composés du Mn^{II} chargés à l'intérieur des NPs résol-silice ont été testés en milieux aqueux. Elles présentent un faible TON mais cela est dû au quantités importantes de composé du Mn^{II} à l'intérieur des NPs comparé aux quantités de peroxyde d'hydrogène employé plutôt qu'à un manque d'activité. L'activité du matériau est sensible au pH de la solution, avec une un taux de dismutation du peroxyde d'hydrogène significativement plus haut à pH = 9 qu'à pH = 7,5. Cette différence est due à la cinétique de la réaction. En effet, un compétition entre la dismutation catalytique du peroxyde d'hydrogène et l'oxydation du résol du support par la même molécule à été mis en évidence. Ces conclusions préparent le terrain pour l'optimisation du procédé dans des conditions idéales, en termesde quantité de composé chargé dans les NPs ainsi que pour le pH, afin de maximiser la dismutation du peroxyde d'hydrogène et réduire l'oxydation de la partie organique du support.

Resumen

Los compuestos de manganeso presentan diversas propiedades de interés. Al manganeso se le conoce por sus varios números de oxidación (desde –III hasta +VII) y puede formar compuestos que abarcan desde mono- a multinucleares. La riqueza de su química se fortalece por la habilidad de este metal a enlazarse fácilmente a una gran variedad de ligandos y a que exhibe múltiples modos de coordinación.

De esta vasta familia de compuestos de manganeso, muchos poseen fuertes propiedades magnéticas, tanto ferromagnéticas como antiferromagnéticas. En las últimas décadas, esto condujo el interés de los compuestos de manganeso a campos relacionados con las propiedades magnéticas tales como imanes uni-moleculares.

No obstante, el manganeso también se conoce por sus propiedades redox y se puede utilizar como un oxidante fuerte y por sus propiedades catalíticas. De hecho, esta última propiedad se encuentra en varias formas de vida, en particular en las que poseen metaloproteinas de manganeso. A menudo estas proteínas están relacionadas en procesar oxígeno o especies derivadas de este en el fotosistema II, responsable de la producción de oxígeno a través de la fotosíntesis o relacionadas con encimas derivadas de manganeso que catalizan la degradación de especies reactivas de oxígeno (ROS, por sus siglas en inglés Reactive Oxygen Species) tales como las catalasas de manganeso o las superóxido dismutasas. Las ROS son conocidas por su función en algunas enfermedades metabólicas y en otras enfermedades graves. Como consecuencia el uso de modelos metalo-encimáticos como las catalasas de manganeso son una potencial herramienta en el campo de la terapia antioxidativa. Desafortunadamente, muchos modelos sintéticos de catalasas de manganeso no son estables ni activas en condiciones fisiológicas. Pero este problema puede superarse gracias a la nanobiomedicina y el uso de nanovectores para los compuestos de manganeso. Recientemente ha habido un gran progreso hacia este objetivo con modelos de catalasas de manganeso cargadas dentro de sílica mesoporosa exhibiendo actividad en agua. Sin embargo, estos avances están todavía lejos de poder ser aplicados en organismos vivos.

Con el fin de construir sobre estas bases se deben sobrepasar varios obstáculos que todavía permanecen y el trabajo presentado aquí propone contribuir en este propósito. Éste está centrado en dos puntos: la mejora de la biocompatibilidad de los soportes de manganeso y la introducción de multifuncionalidad en el sistema añadiendo propiedades luminescentes a los modelos de catalasas de manganeso. Este estudio se divide en tres partes: la **Parte I** se centra en la química molecular de compuestos de manganeso, la **Parte II** se centra en la ciencia de materiales de los nanovectores y la **Parte III** en las propiedades químicas y físicas de los sistemas híbridos.

Parte I

Se presenta la síntesis y caracterización de tres nuevos compuestos luminescentes de manganeso con estados de oxidación II y III. Todos están diseñados con los mismos ligandos, la 2,2'-bipiridina (bpy) y el ligando fluorescente 9-antracenocarboxilato ($AntCO_2^-$).

Los compuestos de Mn^{II}, una cadena de fórmula $[Mn(bpy)(AntCO_2)_2]_n$ y un compuesto dinuclear de fórmula $[\{Mn(bpy)(AntCO_2)\}_2(\mu\text{-}AntCO_2)_2(\mu\text{-}OH_2)]$, son neutros y tienen una composición muy parecida. Parece que existe un equilibrio entre los dos compuestos en las condiciones de síntesis seguidas. Sin embargo, se pueden separar y el compuesto cadena se puede cristalizar para formar el compuesto dinuclear. También se pueden obtener cristales del compuesto dinuclear directamente utilizando síntesis asistida por microondas y esto nos permitió resolver su estructura cristalina.

Para el compuesto de Mn^{III}, basándonos en análisis elementales y medidas magnéticas, proponemos que se trata de un compuesto tetranuclear de fórmula $[Mn_4O_2(AntCO_2)_6(bipy)_2(ClO_4)_2]$. A pesar de diversos intentos de cristalización y cambios en la síntesis no se pudo obtener cristales aptos para su caracterización estructural. Es más, durante la síntesis de este compuesto y debido a los diferentes intentos de cristalización, se cristalizó por primera vez el ligando 10-oxo-9,10-dihidroantraceno-9-il antraceno-9-carboxilato derivado del ligando 9-antracenocarboxilato.

Además de las técnicas de caracterización estándar como la espectroscopia infrarroja y análisis elemental se estudiaron las propiedades magnéticas de estos compuestos. Para todos ellos, se midió la susceptibilidad magnética frente a la temperatura y se realizaron simulaciones y ajustes para determinar las constantes de acoplamiento magnético (J) y proponer, en la medida de lo posible, los parámetros de desdoblamiento de campo nulo (ZFS, por sus siglas en inglés) D y E. Los compuestos de Mn^{II} se estudiaron utilizando espectroscopia de resonancia paramagnética electrónica (EPR, por sus siglas en inglés) y se realizaron simulaciones para confirmar los parámetros de ZFS. Para el compuesto de Mn^{III}, se registraron medidas magnéticas frente a la temperatura a diferentes campos magnéticos y se usaron simulaciones para establecer las tres constantes de acoplamiento magnético del sistema además de su anisotropía axial.

Todos los compuestos sintetizados presentan acoplamiento antiferromangético, presentando valores más elevados el compuesto de Mn^{III}, que también posee mayor valor de ZFS debido al efecto Jahn-Teller de este ion. Gracias a la combinación de las diferentes técnicas de caracterización utilizadas, y a pesar de no disponer de la resolución estructural por difracción de rayos-X, se sugiere una geometría de mariposa para este compuesto.

Parte II

En esta parte se presenta la síntesis de las nanopartículas (NPs) usadas como soportes de manganeso y la preparación de los materiales híbridos [Mn]@NP. Las partículas se sintetizaron reproduciendo una técnica muy reciente, la sintaxis, que permite la formación de nanoesferas "hermanas enredadas" de sílica y una resina polifenólica, el resol. El resultado son nanopartículas bifásicas mesoporosas con dos fases que son el negativo la una de la otra, una orgánica y una inorgánica. Se aplicaron tratamientos térmicos adicionales a este material base (resol-sílica) para obtener nanopartículas de sílica mesoporosas puras y nanopartículas híbridas amorfas carbón-silica.

Estos tres tipos de nanopartículas se cargaron después con tres cantidades diferentes de dos de los compuestos preparados en la Parte I, la cadena de MnII y el compuesto tetranuclear de MnIII. La porosidad de estos dieciocho materiales híbridos se estudió utiliznado isotermas nitrógeno-sorción, sugiriendo la inserción de los compuestos dentro de las nanopartículas. Se realizaron estudios adicionales como análisis termogravimétrico (ATG), análisis elemental, microscopia electrónica (tanto el modo de barrido como de transmisión) y fluorescencia de rayos-X por energía dispersiva (EDS, por sus siglas en inglés). Todas estas técnicas confirman la presencia de los compuestos de manganeso dentro del material en cantidades relacionadas con la carga esperada de compuesto de manganeso, destacando la posibilidad de que algunos de ellos, especialmente el compuesto más voluminoso de Mn^{III} puede no estar intacto dentro de las nanopartículas.

Parte III

Se describen en esta parte las propiedades físicas y químicas de los materiales preparados. También se discuten las propiedades magnéticas de los materiales híbridos [Mn]@NP. Se estudian las propiedades ópticas de las nanopartículas y de los compuestos de coordinación por separado antes de estudiar la fluorescencia de los materiales híbridos. Finalmente, se realizan algunos ensayos para medir la desproporción de peróxido de hidrógeno catalizada por los compuestos de manganeso en una suspensión de acetonitrilo y catalizada por los compuestos de Mn^{II} insertados dentro de nanopartículas resol-silica en solución acuosa.

Las propiedades magnéticas de los materiales híbridos se evaluaron estudiando la susceptibilidad magnética en función de la temperatura y por espectroscopia EPR para las nanopartículas cargadas con compuestos de Mn^{II}. Estas medidas revelan la presencia de radicales electrónicos en las NPs carbón-silica, que es consecuente con las propiedades de materiales C_{sp^2}. Las señales EPR de las [Mn^{II}]@NPs también presentan interacciones magnéticas débiles entre manganesos vecinos, sugiriendo la presencia de entidades dinucleares dentro de las nanopartículas.

Tanto el compuesto dinuclear de Mn^{II} como el compuesto tetranuclear de Mn^{III} presentan una fuerte luminescencia en solución etanólica en la región comprendida entre 380-480 nm. Sus espectros de emisión son similares a los del ligando antracénico. La intensidad de emisión

del compuesto tetranuclear de Mn^{III} es mayor que la del compuesto dinuclear de Mn^{II} para la misma concentración. Sin embargo, para concentraciones superiores a 10^{-5} mol/L predomina una banda ancha a 470 nm para el compuesto Mnm. Esto se explica por su baja solubilidad en etanol y la formación de agregados, que contribuyen a la modificación de la emisión a través de interacciones electrónicas entre los ligandos.

Las partículas en sí ya presentan luminiscencia. Las nanopartículas híbridas resol-sílice presentan una leve fluorescencia alrededor de 470 nm que se debe al polímero. Esta banda de emisión desaparece en las partículas de carbono-sílice ya que el resol se convierte en carbono amorfo. Curiosamente, todos los tipos de nanopartículas tienen un pico de emisión a 410 nm y las partículas de sílice pura emiten en un rango más amplio, entre 380 y 540 nm. Ésta es la fluorescencia de la sílice, que se observa más a menudo en fases de sílice organizadas como el cuarzo o la sílice preparada en condiciones ácidas seguidas por un tratamiento térmico. Esta emisión es rara para las fases de sílice preparadas en condiciones básicas (como el proceso tipo Stöber utilizado) y es probable que se deba a defectos de carbono introducidos en la red de sílice durante la preparación del material.

La luminiscencia de todos los híbridos [Mn]@NPs es muy baja, con quenching tanto de la señal de los complejos como de las partículas. Una vez más puede explicarse por los defectos de la sílice que son conocidos tintes inhibidores de luminiscencia. Sin embargo, esta propiedad nos permite evaluar cualitativamente la eficiencia de los materiales preparados para retener su carga cuando se dispersan en soluciones etanólicas. Parece que los compuestos de Mn^{II} se liberan menos que los compuestos Mn^{III}, pero que tanto la sílcia pura como las NPs carbon-sílica presentan pérdidas significativas. Esto no es muy sorprendente considerando la ausencia de modificación de la superficie que normalmente se utiliza para enlazar los compuestos de manganeso a las nanopartículas de sílice. Sin embargo, los compuestos de Mn^{II} insertados en las nanopartículas resol-sílice parecen retenerse eficientemente durante largos períodos de tiempo. Esto se puede atribuir a la afinidad del complejo por el polímero que presenta tanto anillos aromáticos como átomos de oxígeno, al igual que los ligandos que presenta el compuesto.

Para concluir, se han realizado pruebas catalíticas preliminares para medir la desproporción de peróxido de hidrógeno en presencia de compuestos de Mn^{II} y MnII. Todos los compuestos muestran una actividad moderada en acetonitrilo (entre 130 y 150 número de rotación (TON) por hora). Los compuestos de Mn^{II} cargados en NPs resol-sílice se probaron en solución acuosa. Muestran un bajo TON pero esto se debe más bien a la alta carga de compuesto Mn^{II} en comparación con la cantidad de peróxido de hidrógeno que a una falta de eficiencia. Los compuestos muestran sensibilidad hacia el pH de la solución, con una velocidad de desproporción significativamente mayor de peróxido de hidrógeno a pH $= 9$ que a pH $= 7.5$. Esta diferencia se debe a la cinética de la reacción. De hecho, se evidencia una competición entre la desproporción catalítica del peróxido de hidrógeno a dioxígeno y la oxidación del soporte de resol por la misma molécula. Esto allana el camino para optimizar el proceso en condiciones ideales, tanto en términos de carga de compuesto de Mn como de pH, para maximizar la dismutación del peróxido de hidrógeno y reducción de la oxidación del soporte orgánico.

Contents

Abbreviations

AcO_2^-	acetate
AE	Auger electron
AF	antiferromagnetic
$AntCO_2^-$	9-anthracenecarboxylate
APTES	(3-aminopropyl)triethoxysilane
ATR	attenuated total reflectance
BdB	Broekhoff and De Boer
BET	Brunauer-Emmett-Teller
BJH	Barret-Joyner-Halenda
bpy	2,2'-bipyridine
BS	back-scattered electron
Bu	butyl
butca	1,2,3,4-butenetetracarboxylate
CAT	catalase
CL	light cathodoluminescence
CPS	counts per second
CTA^+	cethyltrimethylammonium
CTAB	cethyltrimethylammonium bromide
DLS	dynamic light scattering
DMT	Derjaguin-Muller-Toporov
DNA	deoxyribonucleic acid
dpm	dipivaloymethane
EPR	electron paramagnetic resonance
ESR	electron spin resonance
Et	ethyl
F	ferromagnetic
FT	Fourier transform
Glu	glutamate
His	histidine
HK	Horvàth-Kawazoe
im	imidazole
IR	infrared
IUPAC	Internal Union of Pure and Applied Chemistry
L	monodentate ligand sharing two electrons
LP	*Lactobacillus plantarum*
LPC	*Lactobacillus plantarum* Mn-catalase
MCM	Mobil Composition Matter
MNP	mesoporous nanoparticle
MO	molecular orbital
NMR	nuclear magnetic resonance
NN	bidentate nitrogen-based ligand
NP	nanoparticle
Ph	phosphate
phen	1,10-phenantroline

pic	picolinate
piv	pivalate
Pr	propyl
PSII	photosystem II
py	pyridine
QD	quantum dot
R	organic substitute
RB	raspberry
RF	resorcinol-formaldehyde or radio-frequency
RNA	ribonucleic acid
ROS	reactive oxygen species
SBA	Santa Barbara Amorphous
SBS	3-dimethyl(3-trimethoxysilyl)propyl)ammonio)propane-1-sulfonate
SE	secondary electron
SEM	scanning electron microscopy
SHE	standard hydrogen electrode
SOA	small organic amine
SOD	superoxide dismutase
ST	stellate
TA	*Thermophilum album*
TAC	*Thermophilum album* Mn-catalase
TEA	triethanolamine
TEM	transmission electron microscopy
TEOS	tetraethyl orthosilicate
TGA	thermogravimetric analysis
Th	thiophene
tmeda	N,N,N',N'-tetramethylenediamine
tolf	tolfenamic acid
TON	turnover number
Tos^-	tosylate
TT	*Thermus thermophilus*
TTC	*Thermus thermophilus* Mn-catalase
UV	ultraviolet
UVRRS	UV Resonant Raman Spectroscopy
WO	worm-like
WOC	water oxidizing center
X	anionic monodentate ligand sharing one electron
XPS	X-ray photoelectron spectroscopy
XRD	X-ray diffraction
ZFS	zero-field splitting
Φ	phenyl function

Compounds and materials

Mn compounds

$[Mn_2^{II}]$	$[Mn(bpy)(AntCO_2)_2(\mu\text{-}AntCO_2)_2(\mu\text{-}OH_2)]$
$[Mn^{II}]_n$	$[Mn(bpy)(AntCO_2)_2]_n$
$[Mn_4^{III}]$	$[Mn_4O_2(anthCO_2)_6(bipy)_2(ClO_4)_2]$

Materials

Supports

RSMNP	resol-silica mesoporous nanoparticle
SMNP	silica mesoporous nanoparticle
CSMNP	resol-silica mesoporous nanoparticle

Materials loaded with Mn compounds

$[Mn^{II}]$@RSMNP	$[Mn^{II}]_n$ inserted inside RSMNP
$[Mn^{II}]$@SMNP	$[Mn^{II}]_n$ inserted inside SMNP
$[Mn^{II}]$@CSMNP	$[Mn^{II}]_n$ inserted inside CSMNP
$[Mn^{III}]$@RSMNP	$[Mn_4^{III}]$ inserted inside RSMNP
$[Mn^{III}]$@SMNP	$[Mn_4^{III}]$ inserted inside SMNP
$[Mn^{III}]$@CSMNP	$[Mn_4^{III}]$ inserted inside CSMNP

In chapter III, the $[Mn]^w$@NPs notation is used with w the weight percentage of the compound, [Mn], loaded in the particle, NP. We assume that the Mn quantity measured with elemental analysis can be directly related to the load of each sample in Mn compound (even if it is debatable).

Introduction

1 Generalities about manganese

Manganese is found naturally under the form of oxides, hydroxides, carbonates and silicates often mixed with iron oxides.[1] It can exist under a wide range of oxidation states, from -III to +VII; II, III, IV and VII being the most common and II, III and IV the ones found in living organisms.
Manganese is primarily used in industry in iron alloys to prevent rust and it is also a component of dry-batteries. In chemistry, its oxidation states superior to III are used as oxidant for both organic and inorganic synthesis. However, due to the number of available oxidation states, it is also a versatile element used as the catalyst of many reactions.[2–8]

It is worth noting that manganese compounds can be prepared in monomers as well as much higher order systems, up to the Mn_{84} cluster, the size of some metallic nanoparticles ($\simeq$ 4.2 nm).[9]
In biology, it is often found bonded to oxygen, nitrogen and sulphur in an octahedral configuration.[10] This ability to coordinate easily with amino-acids makes it a good candidate for metalloproteins center.[11] In these systems it is bonded to amino-acids and manganese versatility combines with the richness of carboxylates coordination modes from monodentate and chelating to a variety of bridging modes.[12–14] In addition, polynuclear manganese compound are often found with oxo, hydroxo and aquo bridges which contribute to create complex magnetic systems. The small size of this ligands enabling elecronic interactions between the metal ions.

2 Bioinorganic chemistry of manganese

The mimicry of biological compounds through synthetic chemistry helps to understand the chemical processes in which they are involved. The preparation of biomimetic compounds, outside the complex environment that surrounds and interact with their natural counterpart, is the key to the investigation of catalytic mechanisms. It introduces both control and versatility. Further exploration on the substitution or conformation of the metallic sites can also give valuable information on the behaviour of a catalytic site than cannot be observed in biological organisms.

In nature, Mn is notably present in a wide range of enzymes and can play different roles. Manganese-based enzymes present typically, mono, di or tetranuclear centres. The manganese is usually found coordinated to amino-acids (histidine notably) and carboxylates (aspartate or glutamate).[13]
Manganese can have a non-oxidative role in enzymes, acting as a conformation agent to maintain the protein, structure like in pyruvate carboxylase or lectins such as concanavalin A. Alternatively, it also often has a Lewis acid role for hydration like in arginase, or hydrolysis in hydrolases of retroviral reverse transcriptases.[15]
Though our main interest for manganese in this work lies in its redox role, usually relative to dioxygen-centred mechanisms. It ranges from the oxidation of catechol to the still ill-understood mechanism of water oxidation by the photosystem II. But our concern lies in its

role in the dismutation of hydrogen peroxide with the manganese-catalase. **Table 5** lists some of the most studied manganese metalloproteins and the reactions where they are involved.[11,15]

Table 5: Metalloenzymes containing manganese and reactions in which they are involved.[11,13,16]

Type	Enzyme	Mn form	reaction	class	distribution
Non-RedOx	Arginase	Mn_2^{II}	arginine $\rightarrow$ ornithine + urea	hydration	yeast, bacteria, mammals
	Ribonucleotide reductase	Mn_2^{III}	RNA $\rightarrow$ DNA	dehydroxylation	bacteria
	Ribonuclease H	Mn_2^{II}	RNA + H_2O $\rightarrow$ cleaved RNA	hydrolysis	retrovirus, bacteria
	Xylose isomerase	Mn_2^{II}	glucose $\rightarrow$ fructose	isomerisation	bacteria
RedOx	Photosystem II[i]	$Mn_3^{III}Mn^{IV} \leftrightarrow Mn_4^{III}$	$2H_2O \rightarrow O_2 + 4H^+ + 4e^-$	oxidation	algae, plants
	Superoxide dismutase	$Mn^{II} \leftrightarrow Mn^{III}$	$2O_2^{-\bullet} + 2H^+ \rightarrow H_2O_2 + O_2$	dismutation	bacteria, mammals
	Catechol dioxygenase	$Mn^{II} \leftrightarrow Mn^{III}$	catechol + O_2 $\rightarrow$ *cis,cis*-muconic acid	oxydation	bacteria
	Mn-catalase	$Mn_2^{II} \leftrightarrow Mn_2^{III}$	$2H_2O_2 \rightarrow 2H_2O + O_2$	dismutation	bacteria

ROS unbalance

The reactive oxygen species (ROS) are a category of metabolism products. They usually designate hydrogen peroxyde (H_2O_2), superoxyde ($O_2^{-\bullet}$) and the hydroxyl radical ($HO^\bullet$). They are regulation agents in cellular life. Depending on the context, they can encourage or inhibit cell development. Under normal conditions, H_2O_2 and $O_2^{-\bullet}$ are produced by enzymes as part of cell metabolism.[13,18,19] $HO^\bullet$ is a subsequent product of the reaction between H_2O_2 and Fe^{II} ions present in biological media described as the Fenton reaction.[20]
Another category of enzymes, present in all living organisms, balances the ROS production by decomposing it. They are known as ROS scavengers and count catalases, hydrogen peroxydases and superoxyde dismutases. These ROS scavengers are necessary because ROS are potentially harmful species. Indeed, as a neutral species, H_2O_2 is able, contrary to $O_2^{-\bullet}$, to pass through cell membranes and reach iron-rich areas where they can lead to $HO^\bullet$ production. $HO^\bullet$ itself is a very reactive species and can cause serious damage to DNA, inducing cell-death or harmful mutations.[18]
The phenomenon of ROS overproduction and its negative consequences is encompassed in the broader spectrum of oxidative stress, which is found in many serious diseases like Alzheimer's or Parkinson's, or some cancer and sclerosis types.[21–24] However, the role of ROS is complex and their means of action multiple. For instance, ROS are known to promote tumor production (as $O_2^{-\bullet}$ can damage DNA and lead to cancerous cells), but they can also be exploited as anti-carcinogenic agents (as ROS can induce cancerous cell apoptosis).[19,25]

The ambivalence of ROS, a potential cause of disorders in the metablism or the remedy to pathologies, does not cancel the fact that they are potentially harmful to the whole system. Consequently, anti-oxidative species could be use to counter or limit their effect to the designated area. Indeed, the use of a mix of catalase and superoxyde dismutase mimics has been reported successful to reduce the oxydative stress of yeasts. They protect from the effect of ROS on their membrane, and increase the lifespan of these organisms.[26] Unfortunately most of medical trials of anti-oxidative therapies show poor results, they are however still considered to be a potential solution for specific cases.[27–30]

[i] Photosystem II exact structure and catalytic cycle is not fully described yet[17]

The use of antioxidants is still seen as a viable strategy in the case of the early stages of pathologies that can have severe consequences if they grow uncontrolled. Notably the α-antitrypsin deficiency, an inhibitor protein that counters the development of inflammatory inducing enzymes, could be treated for children by an anti-oxidative therapy.[31]
Antioxidant therapy could also be considered as a complementary treatment in disease causing ROS unbalance but with more specific targets. For instance, they could play a role to counter neurodegenerative diseases (sclerosis, Alzheimer, Parkinson), but would require a suitable vectorisation in order to be able to get through the blood-brain barrier, which is impassable for many dugs.[32–35] Being able to take specific targets, in order to regulate local disorder like would also be a path for anti-oxidative therapies. For instance, the oxydative stress generated in asthma is caused by a mitochondrial ROS unbalance.[36] All these vectorisation issues are the core of nanomedicine research and could provide new solutions for anti-oxidative treatments.

2.1 The manganese catalase

Catalase enzymes are divided into two categories, the heme-catalases (with Fe^{III}), found in a wide range of organisms, and the manganese-ones, found in microbial life. The are both able to catalyse the disproportionation of H_2O_2 into O_2 and H_2O. Under normal physiological conditions (pH = 7.35) this reaction is spontaneous but very slow and needs therefore to be catalysed in order to achieve reasonable H_2O_2 regulation. The oxydation involves O_2/H_2O_2 (+0.28 V; pH=7 SHE) and H_2O_2/H_2O (+1.35 V; pH=7 SHE) half-reactions.[37]

Mn-catalases seem to be wide spread among living organisms, but have only been characterised in *lactobacillus plantarum* (LP),[38–40] *thermoleophilum album* (TA),[41] *thermus thermophilus* (TT)[42] and in a bacteria of *anabaena* genus.[43] There are differences between the structure of the active site for the three first species cited and the last one, the only one able to perform photosynthesis. It seems that these differences are due to independent evolution paths and that *anabaena* catalase could have to do with the evolution of the photosytems.[43] Thus rising the hopes of geneticists to understand them better.

For *lactobacillus plantarum* catalase (LPC) and *thermus thermophilus* catalase (TTC), the active site of the enzyme consists in two Mn ions bound by a carboxylate function and two $O(H)_x$ bridges. These Mn are coordinated to glutamate and histidine amino-acids (**Figure 1**). When the catalytic activity takes place, the two Mn ions alternate between Mn_2^{II} and Mn_2^{III} oxidation states.[40,44]

Anabaena catalase presents an active site organisation different from LPC and TTC (**Figure 2**). The two Mn ions are coordinated to the same number of glutamates and histidines but the active site is symetrical and does not display $O(H)_x$ bridges. The Mn are instead linked through two $\mu_{1,3}$-carboxylates.[43] Contrary to LPC and TTC where an external glutamate is believed to assist H_2O_2 movement towards the active site, the symetrical environment may favor a direct $\mu_{1,2}$-bridging mode for H_2O_2, replacing both solvent molecules.

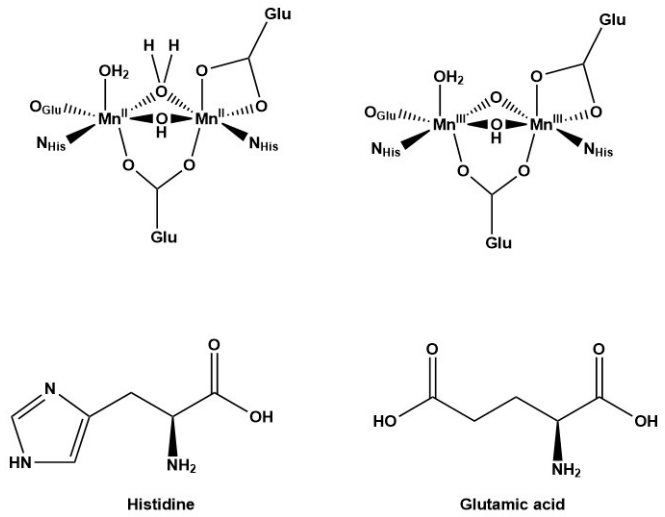

Figure 1: Active site of Mn-catalase from *lactobacillus plantarum* catalase in reduced form (left) and oxidised form (right). His stands for histidine and Glu for glutamate. Both amino acids are also displayed.

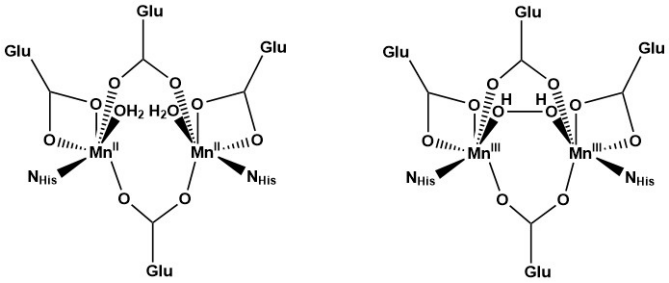

Figure 2: Active site of Mn-catalase from *anabaena* in reduced form (left) and presumed oxidised form (right). His stands for histidine and Glu for glutamate.

The main issue of Mn-catalase mimics is their stability in water. For the natural compound, this stability is ensured by the protein folds. These folds are also organised to let the H_2O_2 access the active site and they reduce $Mn^{III}_{(aq)}/Mn^{II}_{(aq)}$ redox potential enabling the catalytic cycle to run smoothly. **Figure 3** and **Figure 4** display the protein fold structure and H_2O_2 access to the reactive site for both LPC and *anabaena* catalase types.

A mechanism of the disproportionation of H_2O_2 was proposed for LPC by Whittaker and coworkers[40,44] (**Figure 5**). It involves a first step where the H_2O_2 molecule replaces a coordinated water molecule. The carboxylate of a glutamate group from the substrate helps the proton transfer between H_2O_2 and a bridging oxygen atom. The oxygen molecule is then liberated, exchanged with a water molecule. Another H_2O_2 coordinates, forming a $\mu_{1,1}$-bridge thus replacing a water molecule, again with the assistance of the external glutamate. In the final step, the peroxo bridge is reduced, liberating a water molecule. During this cycle the two Mn ions are always simultaneously in the same oxydation state (alternating between (II,II) and (III,III)). This is due to the NO_5 environment of both Mn ions, as well as the contribution of the $\mu_{1,3}$-glutamate bridge, which is a common feature of metallo-enzymes performing multielectronic redox reactions.[16,45]

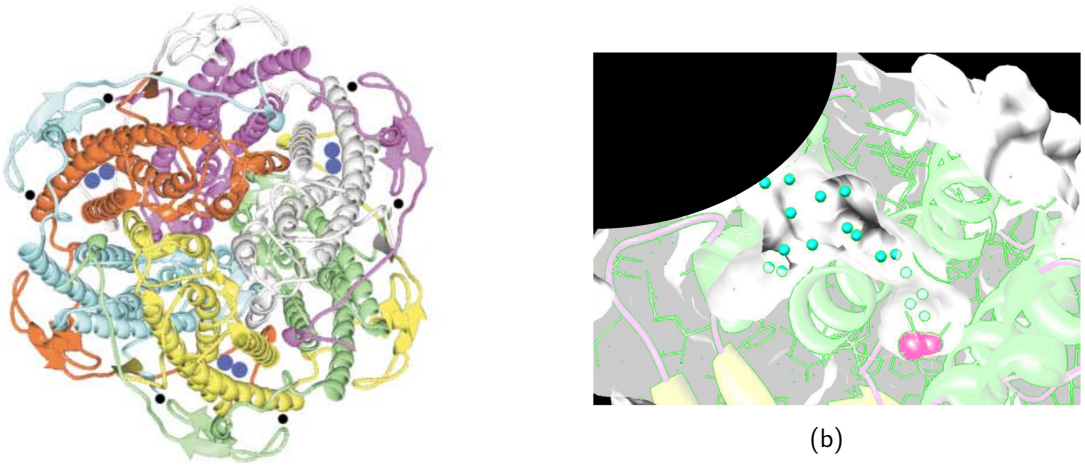

(a) (b)

Figure 3: (a) Structure of *lactobacillus plantarum* catalase. Blue spheres represent Mn ions. Image taken from *Structures* 2001 by Barynin *et al.*[40] (b) Access channel to the Mn active site of the enzyme (22 Å long). Cyan spheres represent solvent molecules and pink ones Mn ions. Image taken from *Archives of Biochemistry and Biophysics* 2012 by Whittaker.

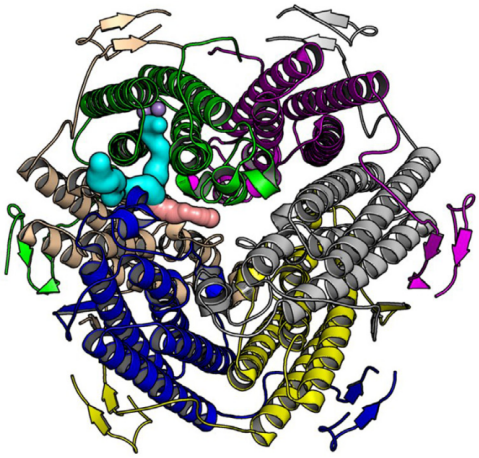

Figure 4: Structure and access channels of *anabaena* catalase. Access channel to the Mn active site of the enzyme is represented in cyan along with the channel closed by a Ca ion in pink. Magenta spheres represent Mn ions. Image taken from *Radical Biology and Medicine* 2016 by Bihani *et al.*[43]

As depicted **Figure 5**, the mechanism is largely based on assisted proton transfer which implies that pH conditions are important for the efficiency of the reaction. The activity of natural Mn-catalase is optimum between pH 7 and 10, and it becomes inactive for too acid ($pH < 5$) or too basic ($pH > 12$) environments. In acidic conditions, the efficiency drop is associated to the protonation of the oxo-bridges, thus opening the active center and increasing the distance between the two Mn ions.[46]

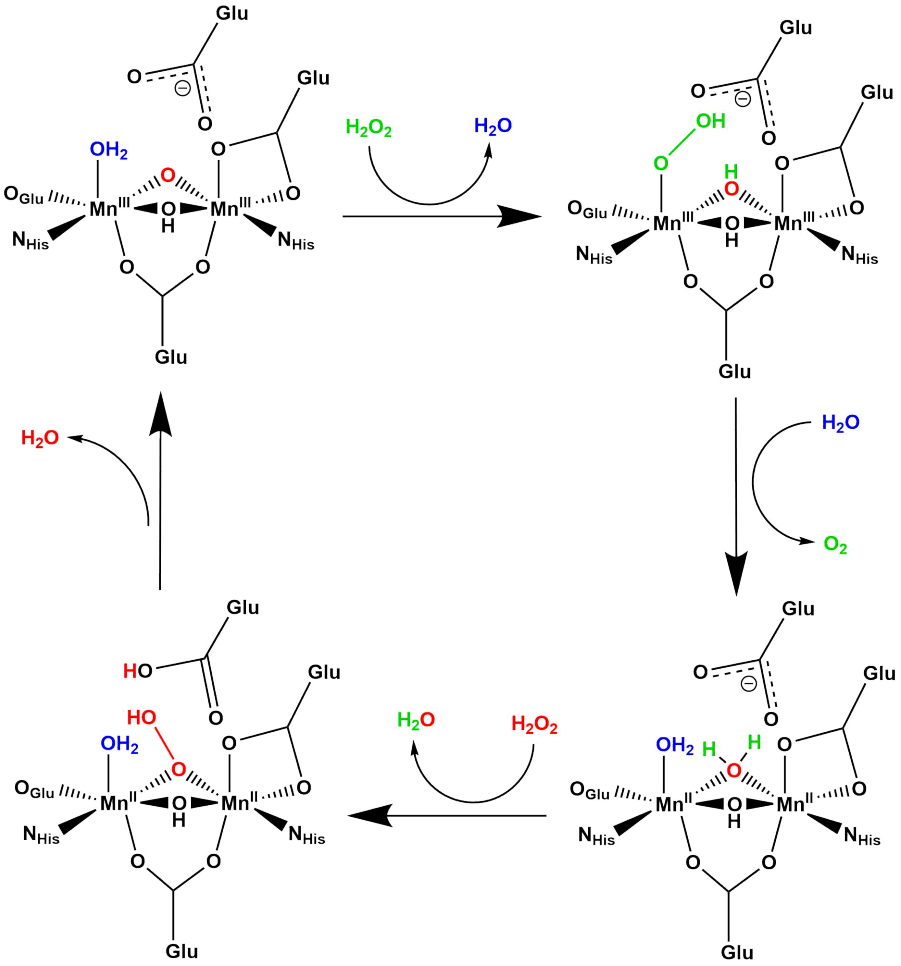

Figure 5: Disproportion of H_2O_2 catalytic cycle proposed for LPC Mn-catalase.[44] His stands for histidine and Glu for glutamate.

The reaction kinetics for TAC, LPC and TTC catalase follow a Michaleis-Menten mechanism, with a saturation plateau, which is a classical model for enzymes:

$$r_i = \frac{k_{\text{cat}}[\text{MnCAT}][\text{H}_2\text{O}_2]_i}{\text{K}_\text{M} + [\text{H}_2\text{O}_2]_i} \quad \text{K}_\text{M} = \frac{k_d k_{\text{cat}}}{k_b} \tag{1}$$

where r_i is the initial reaction rate, k_{cat} is the catalytic rate constant, k_b and k_d the reaction rates of the binding and detaching reaction between the enzyme and H_2O_2. Thereby K_M is a measure of the affinity between the enzyme and H_2O_2.[45] **Table 6** sums up these kinetics constants for TAC, LPC and TTC:

Table 6: Reaction rates of TAC, LPC and TTC.[11,47]

Enzyme origin	k_{cat} (s^{-1})	K_M (mM)
Thermophilum album	2.6×10^4	15
Lactobacillus plantarum	2.0×10^5	350
Thermus thermophilus	2.6×10^5	83

Considering the efficiency of the enzyme, a large number of Mn-catalase mimics have been prepared and are documented in *Coordination Chemistry Reviews* 2012 by Signorella

and Hureau,[45] and more recently in *Coordination Chemistry Reviews* 2018 by Signorella *et al.* with a focus on mononuclear complexes.[48] The most recent attempts have been focused on mononuclear Mn^{III} systems complexed with Schiff bases or porphyrins, as some have been reported to be active in aqueous media.[49–54] As consequence, the amount of new Mn_2^{III} mimics has been less important in the past years.[55–58]As far as we know, no dinuclear compound has been reported to be stable and active in physiological conditions without encapsulation methods.

3 Mesoporous silica

3.1 Silica synthesis in soft conditions

In order to enable Mn-catalase mimics to be active in physiological conditions, a strategy is, again, to inspire from its natural model. In natural catalase, the metallic core is inserted in the protein fold. For our nanocarrier the aim is to build a protective shell.

In fact, there is also a model in nature for this protection strategy: the single-cell algae of diatom group. Diatoms are micro-organisms found in the phytoplankton and phytobenthon all around the world (**Figure 6**). These 2 to 200 μm life-form have a distinctive feature, the frustule, a 3D-structured silica shell organised to the ten nanometer scale (**Figure 7**) and endowed of multiple functionalities.[59] The frustule is a mechanical defence against environment or predators but also has optical properties, contributing to harvest light for the alga and it has its own luminescence.[60] The frustule is also reinforced by a strong adhesive exopolymer preventing the dissolution of the silica in water and showing an affinity for this material superior to its artificial counterparts.[61]
Thereby, even if the size of this organism is superior to nanomaterials (considered below 500 nm), it is a source of inspiration for design and processes in nanotechnology and especially in nanomedicine, given the conditions where diatoms reproduce and live.

Silica is a widely used material to design biocompatible nanoparticles or to protect the body from harmful species by encapsulating them in a silica layer. In addition to its biocompatibility, silica structures are also easy to form in soft conditions, as first described by Stöber *et al.* in 1968.[62] Moreover it is easily functionalisable with the use of organosilane molecules.

The formation of silica materials in soft conditions follows the hydrolysis-condensation mechanism of organoalcoxysilanes ($Si(OR)_nR'_{n-4}$ species, where R and R' are organic groups). This process can take place in neutral media, but is catalysed under acidic or basic conditions.[63–65] For organoalcoxysilanes, the pH directly dictates the organisation of the network. In acidic conditions the protonation of alcoxo and hydroxo groups is easier on weakly substituted species, thus promoting the formation of linear chains. On the other hand, in basic conditions the partial charge on the Si increases as the the molecule gets substituted, promoting the nucleophilic addition to take place on those monomers and leading to more branched and dense networks (**Figure 8**).[66–69]

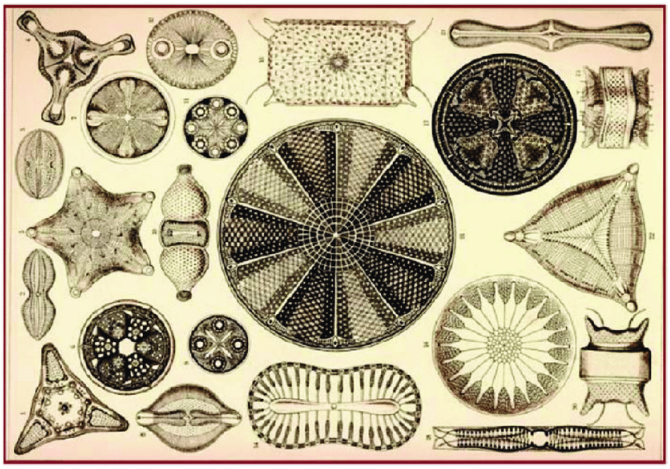

Figure 6: The diversity of diatom frustules represented by Haeckel in *Kunstformen der Natur* in 1904.[70]

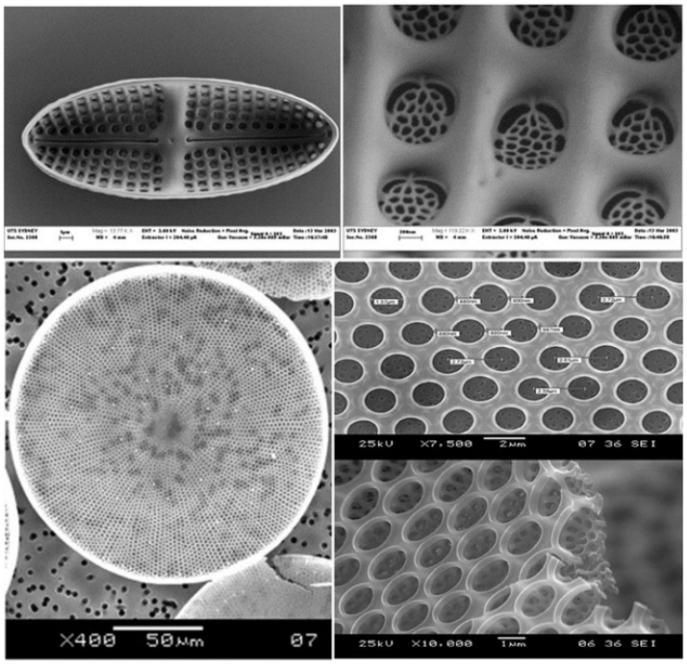

Figure 7: Illustration of diatoms hierachical porosity. Top: *Achnanthes subsessilis*, bottom: *Coscinodiscus walesii*. Image adapted from *Chemical Society Reviews* 2011 by Nassif and Livage,[71] based on the work of Butcher *et al.*[60] and De Stefano *et al.*[72]

The kinetics of the hydrolysis reaction is also driven by the type of substituant chosen for the organosilane precursor. For exemple, under basic conditions the nucleophilic reaction is inhibited by non-hydrolisable groups like methyl or vinyl, reducing the rate of hydrolysis.[73–75] Introducing a steric hindrance with a phenyl group, for instance, can also slow down the reaction rate.[75] Other factors like the proticity of the solvent play a role as well in the reaction kinetics.[73,75–77] For these reasons, mastering the thermodynamic and kinetic parameters of the hydrolysis-condensation of organosilanes leads to a great diversity of silica structures.

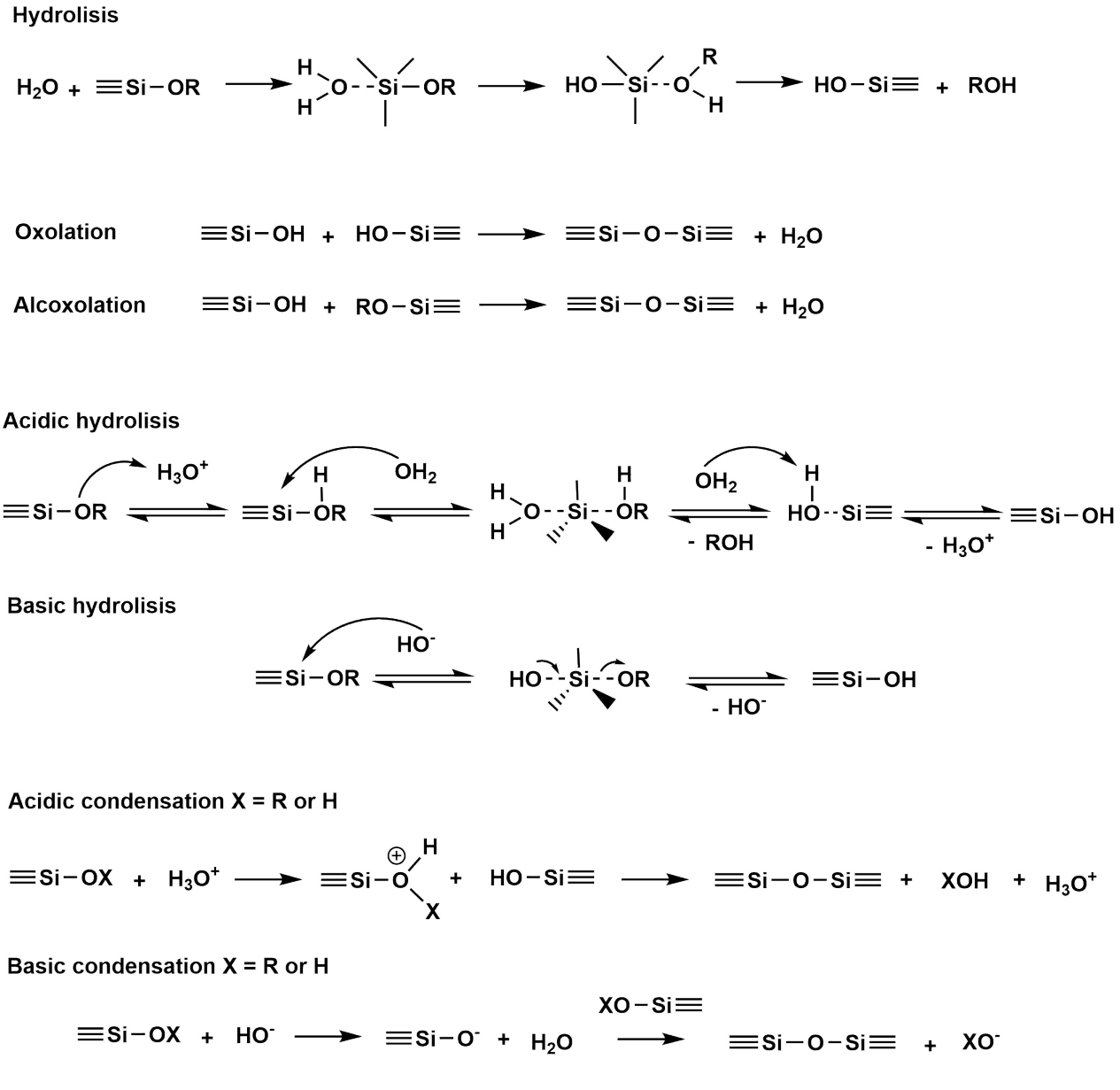

Figure 8: Hydrolysis and condensation of organosilanes.[66–69]

3.2 Porogenesis

In order for the molecular mimic to be protected, as well as being accessible by the reactive species, porous material design is an efficient approach. IUPAC classifies pore size in three categories: macroporous (above 50 nm), mesoporous (between 50 and 2 nm) and microporous (below 2 nm).[78] For silica, the most well known examples of mesoporous materials are the MCM (Mobil Composition Matter) 41 and 48, where the pore network is organised on a long range, respectively in hexagonal planes and cubic 3D-network, and SBA (Santa Barbara Amorphous) 15 also with hexagonal planes (**Figure 9**).[79–81]

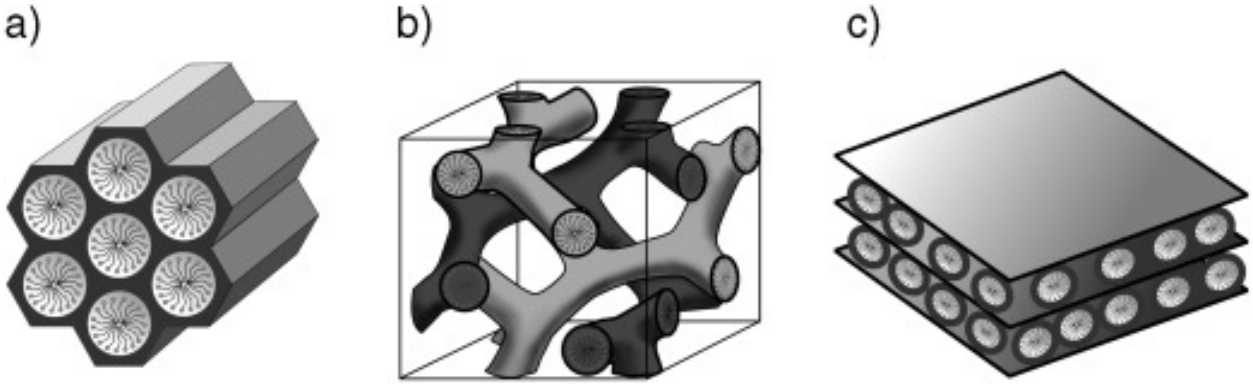

Figure 9: Structure of MCM materials a) MCM-41 b) MCM-48 and c) MCM-50. Image taken from *Angew. Chem. Int. Ed.* 2006 by Fröba *et al.*[82]

In order to control the porosity of the material, the usual method is to perform the solid condensation around a template, which is often a surfactant. In 1994, Huo and coworkers proposed a classification of the interaction between the surfactant (S), the inorganic material (I) and an optional mediating species (X or M depending if it is metallic or not).[83] The interaction between this components is, most of the time, electrostatic, but it sometimes relies on hydrogen bonds. For instance, MCM-41 is prepared in basic conditions, so $I^- = SiO^-$, and requires a cationic surfactant for the template (cetyltrimethylammonium bromide CTAB), so $S^+ = CTA^+$.[79] On the other hand, SBA-15 is synthesised in acidic conditions and the interactions are mainly hydrogen bonds between the template triblockcopolymer (poly(alkyleneoxide)) and the silica phase, so its type is (S^0; I^0).[81] The **Figure 10** sums up the different interfaces inventoried.[82]

Surfactant molecule naturally organize in micelles in aqueous media, and the silica condensates around it, forming a mesoporous network (**Figure 11**). This way, with a proper choice of alkyl chain length, and concentration, which dictates micellar organisation, it is possible to tune the size of the pores and their long range network template.[78] It is also possible to combine techniques to tune more precisely the structure of the material. On one side, to mix cationic surfactants with a short chain, in order to perform the synthesis in basic conditions and ensure a good density of the silica. With, on the other side, a long chain neutral multiblock copolymer that stacks with the amphiphilic part of the surfactant to enlarge the micelle diameter. This way, the material prepared has the solidity of silica materials prepared in basic conditions along with a larger pore-size.[78,84,85]

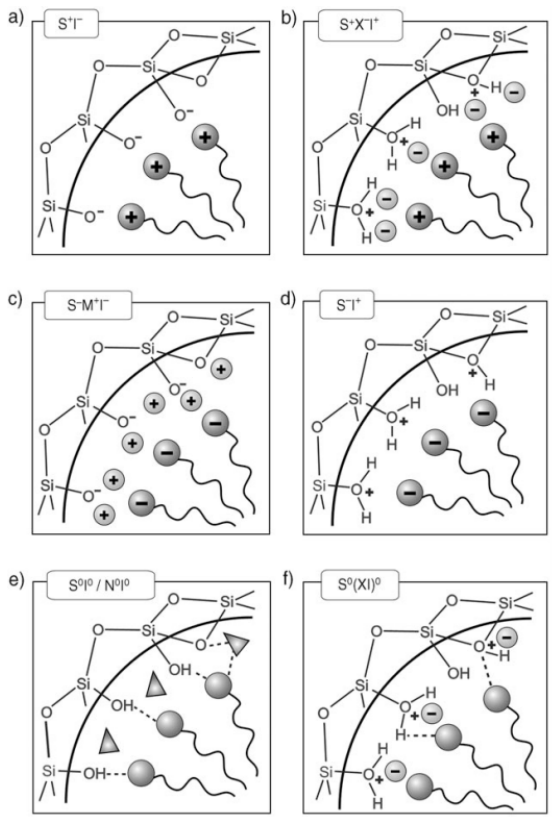

Figure 10: Possible interface types between inorganic species (I) and surfactant heads (S). Electronic interactions: a), b), c) and d) ; hydrogen bonds: e) and f). Image taken from *Angew. Chem. Int. Ed.* 2006 by Fröba *et al.*[82]

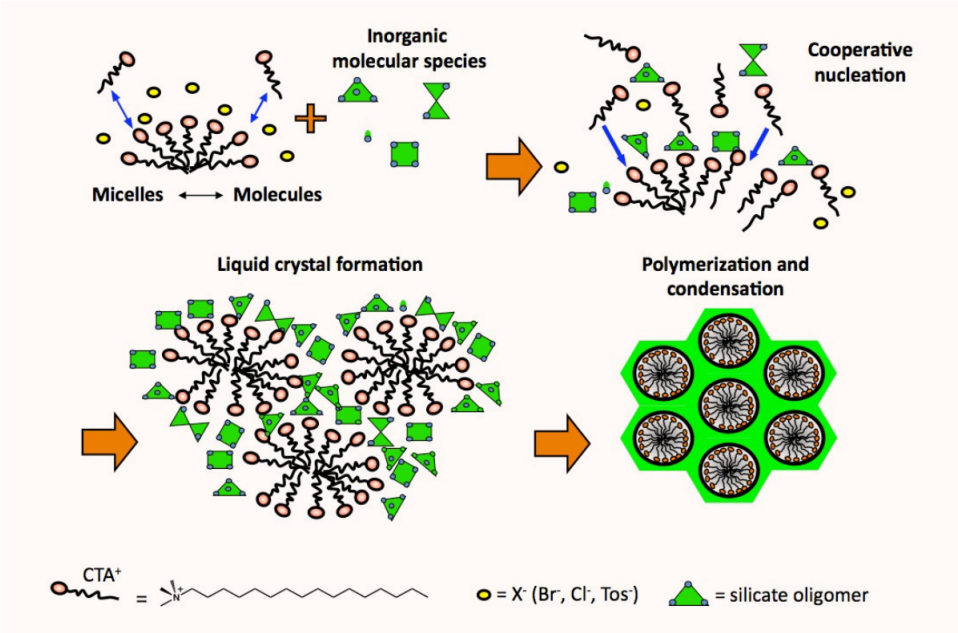

Figure 11: Formation mechanism of 2D hexagonal mesostructured porous silica using a cationic template of the type CTA^+X^- in basic conditions. CTA^+: cethyltrimethylammonium, Tos^-: tosylate. Figure taken from *New J. Chem.* 2016 by Albela and Bonneviot.[86]

3.3 Silica-based biomimetics

It is possible to go further in biomimetism by reproducing properties like hydrophobicity and confinement effects and thus not only stabilise the compound but actually increase its efficiency.[87–91] For instance, the protein folds of metalloenzymes can be reproduced with a set diameter for pores. Their design must be sufficient for the active molecule to flow through and have an homogeneous dispersion inside the material, that is 0.5 to 1 nm. However, the pore diameter should be small enough to observe an efficiency increase due to confinement. The optimal pore diameter is, so, set between 3 and 5 nm.[86]
In nanomedicine specific requirements are a challenge for the development of suitable therapies:

(i) The treatment should be non-cytotoxic.

(ii) The treatment should be specific to the target.

(iii) The administration route of the treatment should be compatible with human physiology (*i. e.* it should not be metabolised too fast or accumulate in non-desired tissues).

(iv) The treatment should release or put the target in contact of a set amount of drug.

(v) The drug should be released only when the target is reached.[91]

With these requirements in mind, silica nanosystems already proved they were suited for several tasks.

(i) Silica, despite not being naturally present in human body, is not toxic from a chemical point of vue.[92] But the material itself requires careful shaping. It is the reason why nanospheres are preferred to fibers for instance.

(ii) and (iii) Silica nanocarrier external surface can be functionalised with suitable groups. Despite being a costly technique, modified antibodies can be grafted to the nanoparticle surface making it specific towards the antibody's target.[93,94] The particle can also be decorated with zwitterionic molecules, which ensures both colloidal stability and furtivity towards the immune system (**Figure 12**).[95–97]

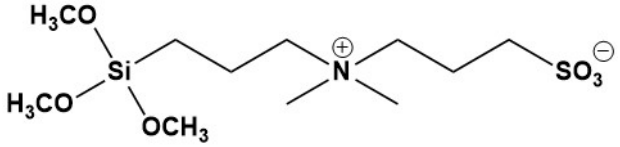

Figure 12: 3-(dimethyl(3-(trimethoxysilyl)propyl)ammonio)propane-1-sulfonate (SBS) a zwitterion used to provide stealth and stability to silica NPs.[95]

(iv) and (v) The growth of carefully designed particle layer can ensure both the solvent or small molecules like ROS to flow through the material while constituting a physical barrier avoiding drug release.[98,99] In addition, the pore's entrance can be specifically functionalised with gatekeepers molecules. The gatekeepers candidates are many, depending on the particle's cargo and the stimulus designed to open the gate. It can range from inorganic materials, most of the time in the shape of small nanoparticles

(Au, CdSe, Fe_3O_4)[98] that can be functionnalised themselves to response to the environment, to organic macromolecules (poly(amidoamine), insulin)[98] for increased biocompatibility. More interestigly, some molecules can be grafted to answer directly to a change in the environment: spiropyrans and gold (light), poly(N-isopropylacrylamide) and DNA (temperature), rotaxanes and disulfides (redox), polyamides, metal complexes and macrocycles (pH) and many more.[100]

Indeed, some hybrid materials containing bio-mimetic Mn complexes have been reported in the past few years, based on catalase[56,57,101,102] , superoxyde dismutase[103–105] and the water oxidizing center.[106] These multiple examples include silica gel[102,104] , SBA-15,[106] amorphous silica nanoparticles,[105] mesoporous silica,[56,57] core-shell nanoparticles[101] and hollow mesoporous microspheres[103] as silica support. Among these examples, only few work has been performed on nanoparticles that could fit biological conditions.[101,103,105] Among them, only one[101] deals with Mn-catalase mimics. In this work, the complex is prepared in-situ with the ligand grafted to the silica NP before metallation and the Rhodamine dye entrapped during the formation of the NPs. The material, however, shows a very slow kinetics of H_2O_2 disproportionation, likely because the nanoparticle does not provide any protection to the Mn-complex. On the other hand, very good results in terms of kinetics and overall activity have been obtained for dinuclear Mn^{III} catalase mimics entrapped into functionalised mesoporous silica.[56,57] They evidence that the control of the environment of the entrapped complex, in terms of pH and polarity can contribute to yield better result than the lone compound, even in aqueous media. However, these systems are based on bulk silica, which is not adapted to living biological systems. Hence, as far as we know, no system is able to fulfil all the requirements of nanomedicine and combine these complex multifonctional properties at the same time in physiological conditions.

Concerning mesoporous silica nanoparticles, that are one of the most common supports for drug delivery, their synthesis is now fully mastered with a wide range of size, pore type and distribution.[81,108–112] Their formation mechanism and morphologies are also understood better and better. Zhang and coworkers proposed in 2013[107] a detailed three steps formation process of nanoparticles with different templating conditions for (S^+, I^-) silica systems, depending on the counteranion chosen for the surfactant ammonium head, the pH of the suspension and the base type chosen to alter it. The viscosity of the solution, controlled with the mixture of ethanol, water and in that particular case, a viscous small organic amine (SOA), also plays a role for the surface tension of the micelles and contributes to the final size of the nanoaprticle. The control of these factors enable to drive the formation of different types of mesoporous networks and thus to start the implementation of a classification of amorphous phases. The authors inventory three controllable phases types with their technique: stellar, raspberry and worm-like (**Figure 13**). This work complements the research made on more atypical morphologies like hollow[113] or yolk-shell[114] silica nanoparticles.

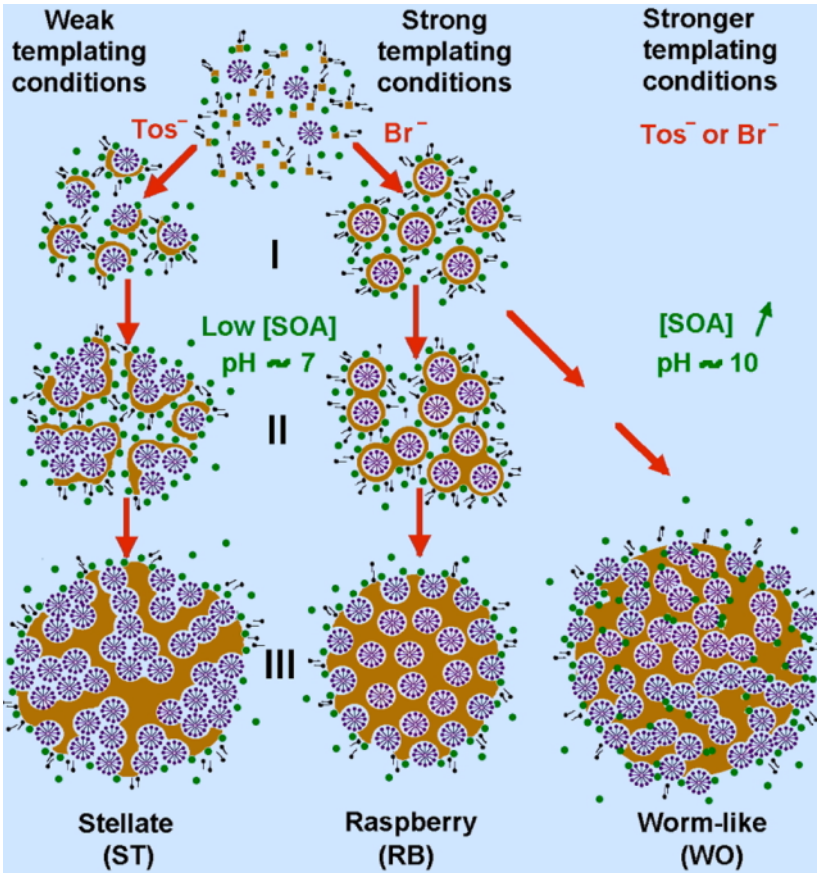

Figure 13: Syntheis mechanism in different conditions. SOA: small organic amines, Tos^-: tosylate. Figure taken from *J. Amer. Chem. Soc.* 2013, by Zhang *et al.*[107]

4 Silica and optically active materials

In our approach we want to combine two properties inside the material. The complexes are designed to be close to the Mn-catalase metallic center and be able to decompose hydrogen peroxyde. But the aim is also to introduce some luminescent ligands in order to spot the particles with fluorescence microscopy. Or, at least, to make observations about their insertion inside the nanoparticles through modification of the luminescence between free compounds in solution and the inserted ones.
To this end, silica support is also largely used. Many optical materials use silica, it is indeed a translucent material with a low refractive index. This feature is also necessary for the diatoms mentioned in section **3.1** in order to be protected by the frustule, but also to harvest light.[59] The main role of silica found in nanomaterials is to separate the luminescent species from the external environment while not interfering with the emission. This separation can be necessary for a number of reasons.

A first reason can be the toxicity of the luminescent species. This is particularly true for quantum dots (QD). QD are a very popular type of semi-conductor nanoparticles with tunable luminescent and magnetic properties. This versatility comes from quantum confinement properties, due to the size of these particle (they are usually smaller than 10 nm).[115,116] This way,

the emission of nanoparticles of a set composition can be adjusted to the intended application by controlling its size during the synthetic process. These particles are usually made of two metals or semi-conductors like arsenic, cadmium, indium, lead, selenium, sulfur or zinc which, for some of them, are highly toxic. This way, the use of a silica shell around the QD protects the body from potential harm caused by these materials. Moreover, the shell can also serve as a base to functionalise the particle with the versatile chemistry of organosilanes.[115,116] Protective silica shells can also be found around gold or silver nanoparticles, that are of interest for their plasmonic resonance in optics but which have a known antibiotic effect.[115]

Another use of silica is, on the contrary, to protect the fluorophore from the environment. Indeed, the action of singlet oxygen is known to quench the luminescence of many species, especially organic dyes (like rhodamine or pyrene).[117,118] As mentioned in section **2**, the biological environment favours the formation of many ROS and singlet oxygen can be counted among them. It is, for example, generated in organism using photosynthesis and neutralised with carotenoids. This way, a dense silica shell or a host silica particle can isolate the luminescent species from the physiological environment and strongly reduce the generation of singlet oxygen in the direct vicinity of the fluorophore.[117,119] This ability improves the emission of the luminescent species but, especially in the case of organic dyes, also enhances their stability.[118,120,121]

In addition, like our Mn-catalase mimics, most of organic dyes are not soluble in high concentration in water. Using a nanovector enables to load a higher amount of molecules than what could be dissolved and locally increase their concentration.[117,118,122,123] This increase itself can lead to potentially interesting modifications of the emission, most notably a red-shift, that can be used to reach the transparency window of human body (650-1350 nm).[118,123] The dyes themselves can be covalently bonded to ensure the absence of leaking and sometimes improve their photostability.[119,123] This method has also been used for the preparation of luminescent lanthanide complexes supported on silica particles (**Figure 15**), with a first graft of the ligand on the particle surface or inside its network before performing the metallation step.[124] But non-covalent entrapment is also used, especially in the case of one pot synthesis where the dye is mixed with silica precursor and mechanically entrapped inside the particle during their formation.[117,118,120,122,123] This principle is illustrated **Figure 14** for pyrene dyes.

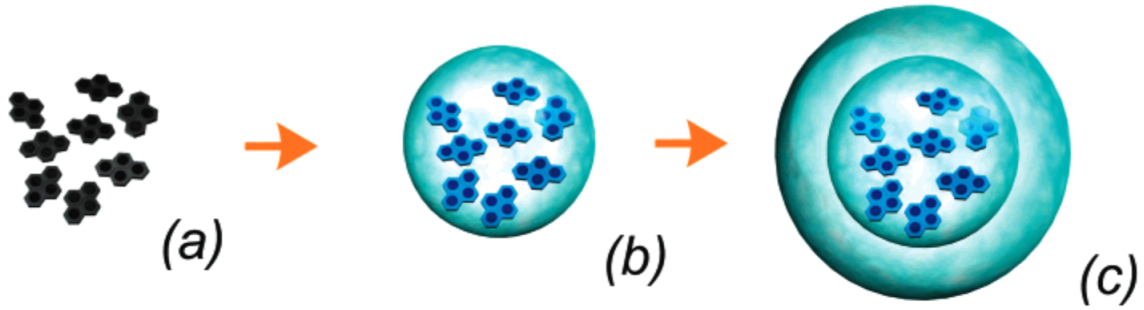

Figure 14: Entrapment of pyrene dyes into a double layer silica NP. The authors mention the apparition of an excimeric band at 470 nm depending of the dye concentration inside their material. This picture is adapted from *J. Am. Chem. Soc.* 2007 by Rampazzo *et al.*[117]

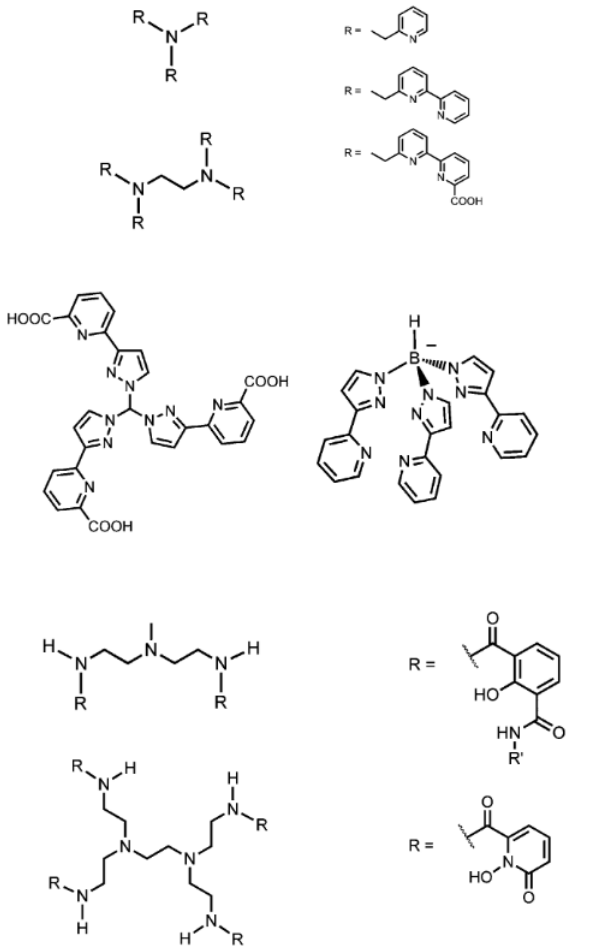

(a)

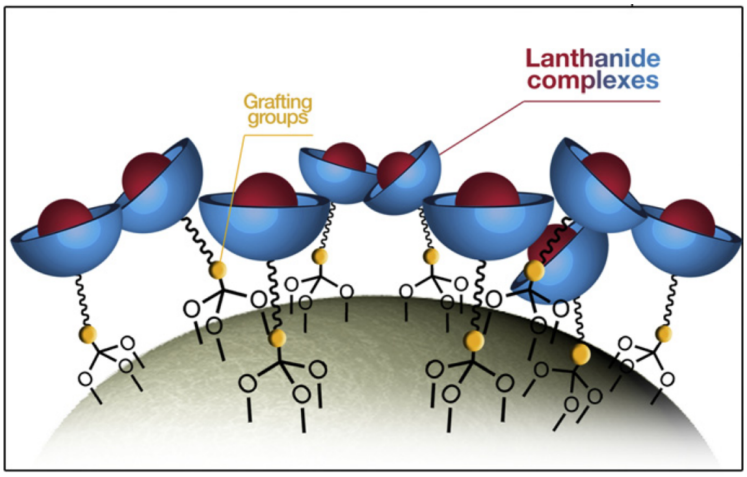

(b)

Figure 15: (a) Examples of ligands used for the preparation of luminescent Ln^{3+} complexes. (b) Grafting of luminescent lanthanide complex at the surface of silica nanoparticles. Images are taken from *Coordination Chemistry Reviews* 2010 by Armelao *et al.*[124]

5 Resorcinol-formaldehyde nanoparticles

Silica shows strong advantages towards adaptability both in shape and functions, but what if it is possible to transfer these properties to an actual biomaterial ?
Polyphenols, formerly referred to as plant tannins, are, as their previous name suggests, widely present in plants, from berries to chocolate. Polyphenols exhibit antioxidative properties, which makes them potential therapeutic agents for the disorders mentioned in section **2**.[125,126] In particular, resorcinol-formaldehyde resin or resol was a popular glue used in construction and aeronautics before the epoxy resins and is still employed for specific materials that require UV protection.[127–131] It has already been used for heart surgical operations, showing no toxicity and good regeneration of the tissues.[132,133]
The ratio between formaldehyde (F) and resorcinol (R) dictates the polymer type. For instance with a F/R ratio inferior to one, linear novolac resin will form instead of the usual branched RF resin.[128] In the past few years resol was used for the design of new biocompatible nanomaterials such as aerogels and nanoparticles, as its condensation mechanism is close to the Stöber process employed for silica nanoobjects.[134–141] **Figure 16** depicts the first steps of the condensation process of the resin.

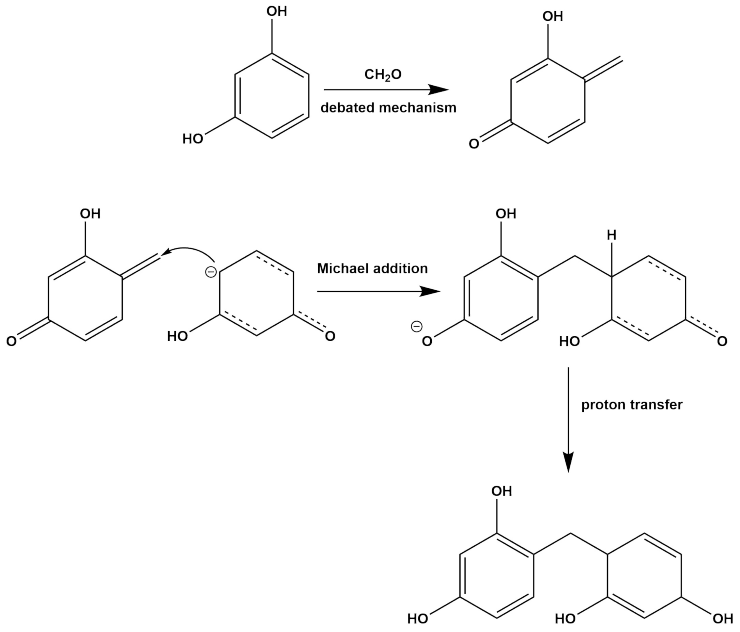

Figure 16: Formation of resol oligomers.[142]

However, until recently the preparation of mesoporous resol nanoparticles remained a challenge. Indeed, the polymer do not have the same affinity for surfactant micelles as silica and silanolates. The first success was communicated by D. Zhao team[134] with a soft templating technique in hydrothermal conditions, relying on (S^0, O^0 with O the organic phase) interface. However, given the flexibility of the polymer, carbonisation is required to maintain porosity in the material.
The triphasic approach introduced by the same group earlier[143] appears to be the answer to solve the issue of mesoporous resol. In their work of 2006, Liu and colleagues[143] present the triphasic coassembly method. The two hard phases are prepared ahead at different pH before being mixed together along with the surfactant. This leads to a (S^0, $(OI)^0$) hybrid material

with covalent bonds between each phase. As a result, the separation of each phase without modifying the porosity of the material is impossible.
The most recent technique, called syntaxy, is close to solve the problem. It was developed by Zhang and coworkers, and relies on a new process[144] to yield "sisters" nanospheres. This technique requires a careful adjustment of the pH in order for silica and resol condensation to take place at the same rate around the template. It can be classified as (O^-, S^+, I^-) interface. If the pH is not well adjusted, the two phases grow at different rates and phase partition occurs between silica and resol, forming various morphologies (resol@SiO_2 or resol@SiO_2@resol). But around pH $= 8$, both phases grow at the same speed and silica drives the condensation of resol resulting into two entangled mesostructured phases (**Figure 17**). Once this process is achieved it is possible to remove the surfactant and keep one or both phases or to turn resol into carbon by thermal treatment, leading to four possible types of nanoparticles with the same precursor material.

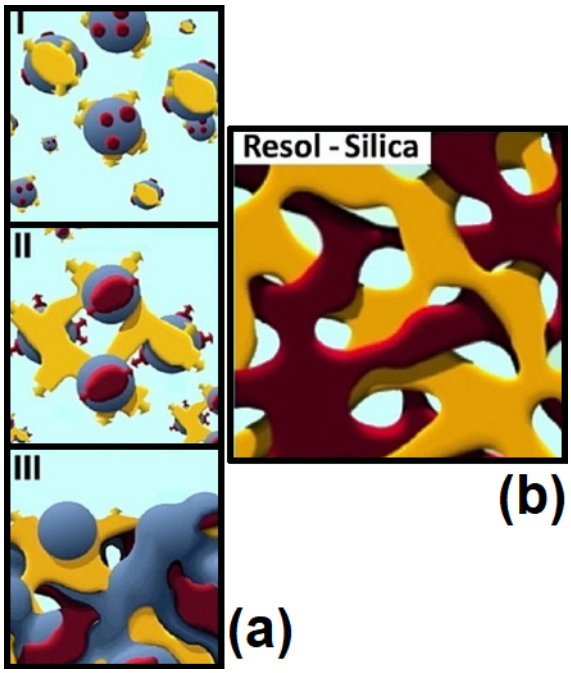

Figure 17: (a) Formation mechanism of sisters nanospheres. (b) Biphasic strucure of hybrid silica-resol nanoparticles. Pictures taken from *Chemistry A European Journal* 2018 by Zhang *et al.*[144] Dark red phase represents the resol, yellow the silica and light blue the micelles.

This process is of great interest for bio-compatible nanovectors as it paves the way for increased compatibility of the support with hybrid silica-resol or mesoporous resol nanoparticles. Moreover, given the antioxidant properties of polyphenol, it could combine with the properties of its guest molecule, such as Mn-catalase mimics, to strengthen the efficiency of the therapy as a whole. It is this idea that gave birth to this study.

6 Objectives

The aim of this work is the synthesis of polynuclear manganese complexes that can be relevant as Mn-catalase mimics and exhibit luminescent properties. These complexes are meant to be inserted inside different types of nanoparticles, silica, resol-silica and carbon-silica, to study the evolution of their physical properties, fluorescence and magnetism, and their chemical properties, the ability to catalyse H_2O_2 disproportion.

The manganese complexes are based on Mn^{II} and Mn^{III} ions as they correspond to the oxidation states of Mn inside natural catalase. The aim is to obtain polynuclear complexes, as the catalytic mechanism of Mn-catalase relies on the close distance separating the metallic ions. The 2,2'-bipyridine ligand has been chosen because it is present in several efficient Mn-catalase mimics synthesised in our group. The 9-anthracene carboxylate ligand is employed because it is a small fluorophore close to the organic carboxylate used for Mn-catalase mimics. Moreover, it has a high quantum yield and its fluorescence and the luminescence of many anthracene derivatives is well described, providing a solid base for interpretation of its behaviour. 9-anthracene carboxylate fluorescence is, as well, sensitive to some factors like pH, polarity and coordination, which can provide important information on the ligand and by extension, the complex environment.
A side goal of this project is also to evaluate the feasibility of the preparation of Mn^{III} Mn-catalase mimics by the oxidation of suitable Mn^{II} compounds, therefore multiplying the list of potential candidates for our application.

The choice of the nanoparticles supports, derived from the synthesis of the biphasic resol-silica nanoparticles was made for multiple reasons. With one base synthesis it is possible to prepare up to four different nanoparticle types (resol-silica, carbon-silica, pure silica and pure carbon) but with comparable properties (mainly pore size and organisation and particle size). It enables to study the compounds behaviour with different materials that are similar enough. The preparation of the particles in soft conditions is easily scalable. The method itself and the materials are compatible with physiological conditions, which is the long range target of the project. Finally, there is no equivalent example of this system design: fluorescent Mn-catalase mimics incorporated inside mesoporous nanoparticles. And furthermore, it is the first application of hybrid nanoparticles prepared by syntaxy. In particular, we wanted to observe the conjuction of resol and the Mn compounds on the luminescence and catalytic behaviour of the system.

Part I

Mn compounds

In this chapter we present the synthesis and characterisation of a series of polynuclear Mn^{II} and Mn^{III} compounds. They are designed as Mn-catalase mimics and are based on 2,2'-bipyridine and 9-anthracenecarboxylate ligands. The main techniques used to characterise the manganese compounds will be introduced first.

I.1 Introductory remarks

I.1.1 Infrared spectroscopy (IR)

Infrared spectroscopy is a common technique in chemistry: vibration energy of covalent bonds is in the IR range of the electromagnetic spectrum (1 to 1000 μm), and samples absorb more energy when they are subject to a beam whose wavelenght corresponds to the vibration of a specific type of chemical bond. It is, so, possible to scan the IR spectrum to detect which bonds are present in the sample.

Traditionally, the energy range of IR spectra are given in cm^{-1} as described by the Planck equation (**Equation 2**) :

$$E = h\nu = \frac{hc}{\lambda} \tag{2}$$

where E is the radiation energy, ν its frequency, λ its wavelenght, h the Plank constant and c the celerity of light in vacuum.
The wavenumber used in IR is defined by $\bar{\nu} = \frac{1}{\lambda}$. The number and type of vibration of molecules can be described and predicted with group theory.

Spectra of molecules and materials presented in this work have been recorded in Fourier transform analysis of reflected light (FTIR). The signal is recollected simultaneously for all frequencies and the use of an interferometer and Fourier transform processing allow the deconvolution of the signal to turn it back to transmittance versus frequency. This technique is quicker and has a better signal to noise ratio that a simple frequency scan. We had two apparatus at our disposition: a classical transmittance measuring device, working with solids shaped with potassium bromide (KBr) pellets, and one working in attenuated total reflectance (ATR), probing the surface of pure solid or liquid samples. The spectrum range studied for most compounds is 4000-300 cm^{-1}.

I.1.2 Thermogravimetric Analysis (TGA)

Thermogravimetric analysis is a simple technique which is useful to determine the composition of samples made of multiple species or materials; typically inorganic compounds like salts, complexes with several ligand types or hybrid materials. It consists of measuring the sample weight with micro-scales when it is submitted to gradual heating. Each chemical species comprised in the sample has a characteristic decomposition profile, reducing the total weight of the sample when it is degraded. From these mass losses, the amount of the decomposed species can be deduced relatively to the total mass of the sample. Species with the same chemical composition but with different environment such as coordinated or decoordinated ligands, ions bound to different counter ions often have different decomposition temperatures,

which may allow a more structural approach.
TGA performed for this work were made under artificial air atmosphere, with a temperature range from ambient to 1000 °C with a heating rate of 10 °C/min.

I.1.3 Single-crystal X-ray diffraction (XRD)

Principles

Single-crystal X-ray diffraction is a widely used technique in molecular chemistry as it allows to determine structural information of the crystal unit, namely cell dimensions, bond lengths and angles. These informations lead to the determination of the structure of the crystal building unit, which is often the studied molecule itself.

XRD is based on the diffraction phenomenon created by the interaction between the monochromatic X-ray radiation and the crystalline sample. Constructive interferences are observed when the wavelength of the X-ray source, λ and the characteristic distance of the sample (usually the distance between two atoms of the crystal or two crystalline molecular layers) d verify Bragg's law conditions (**Equation 3 ; Figure 18**):

$$n\lambda = 2d\sin\theta \tag{3}$$

where n is a whole number and θ the diffraction angle.

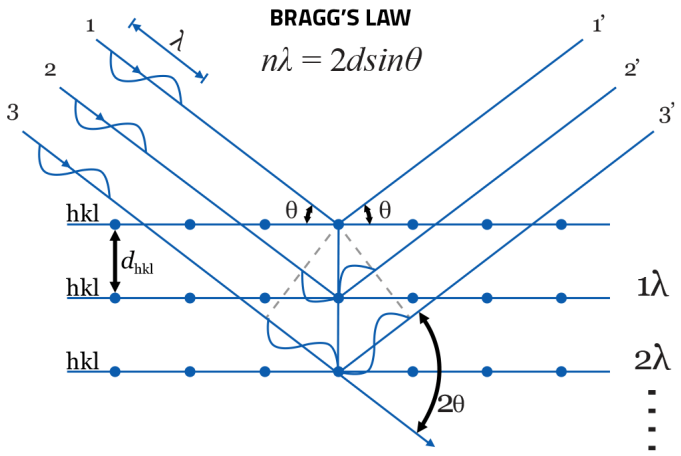

Figure 18: Illustration of Bragg's law.

So, each reflection angle θ can be labelled after the Miller's indices (hkl) of the characteristic distance d that it correspond to in the reciprocal lattice of the crystal.
In addition, the intensity of the diffracted beam is linked to the position of the nod and the energy dissipated when encountered. For an atom, the greater its electronic density is and the closest it is from the diffraction plane, the more intense the diffracted beam will be (as the more electrons an atom has, the more probability they have to interact with the ones of the beam).
The crystalline pattern obtained can thus be described in the reciprocal space with the hkl coordinates and intensities of each point. A Fourier transform can then draw from the points of the diffraction pattern the characteristics of the crystalline lattice and unit cell in the real space. This step is called the resolution of the crystal structure.

Each atom is attributed three sets of parameters: its site occupancy factor, its coordinates and its anisotropic displacement. They correspond to one occupancy parameter, three atomic coordinates and six displacement types. The obtained structure can be further refined by feeding the resolution algorithm with constraints and restraints. Constraints are equations relating several parameters to each other or setting their numerical values, effectively reducing the number of parameters. Restraints are external information about known chemical structures or functions, which increase the number of parameters to work with.[145]

Crystallisation

In order to have a structure resolution as precise and clear as possible, it is decisive to grow good quality crystals. In solution, the crystallization process occurs when the concentration of a compound is higher than its solubility in the media (in general locally) but also depends on many atomic, inter and intra-molecular interactions. It is a kinetically constraint process and thus occurs mainly in supersaturated solutions.
To prepare such solutions multiple techniques are available and divided into two main approaches: to reduce the compound solubility or to increase its concentration.[145] For the latter, the most common way to achieve the metastable state is to slowly evaporate the solvent. For the former, it is possible to gradually decrease the temperature of the solution or to mix the initial solution with a precipitant solvent. This can be achieved, either directly in liquid phase by layering the precipitant on or under (according to its density) the main solution, the slow diffusion of the liquid creating a gradient of solubility, or with the same mechanism with a precipitant gas phase progressively dissolving into the solution.

In our case, unfortunately, these classic techniques systematically produced urchin-like packs of crystalline needles, unsuitable for XRD. To overcome this a superior control of the crystallisation process is needed and can be achieved through micro-wave synthesis.
The micro-wave heating technique (a specific range of dielectric or radio frequency (RF) heating), allows to heat a sample homogeneously. Instead of relying on convective current and thermal conductivity of compounds or materials of classical heating techniques, micro-wave heating transfers the energy directly to the molecules thanks to dipolar polarisation and ionic conduction.[146]

LaMer and Dinegard proposed in the 1950's a mechanism for the formation of particles called nucleation-growth process.[147] This theory states that the nucleation of the particles seeds will only start when the supersaturated solution reaches a chemical potential where they can be stable. The particles will then grow until the concentration of the solution decreases under the supersaturation threshold **Figure 19**.
A third step might occur on a longer period of time called Ostwald ripening.[148,149] If the nucleation and growth condition are not well controlled the suspension can be constituted of particles of different sizes, the smaller just within the thermodynamical stability limits. With time and decrease of the solution concentration, they can then redisolve and their material is then used for the growth of the already larger, and more stable, particles. This usually leads to a bigger average particle size and size dispersion.

The advantage of the micro-wave assisted synthesis is the higher control of the temperature

parameter. With a short and homogeneous heating, the solution reaches the supersaturated state faster and for a shorter time. This treatment then quickly creates numerous seeds, which grow more homogeneously as they all appear and evolve in the same conditions, leading to an overall better crystal quality. It can also be used to achieve superheating in autoclaves, as the temperature homogeneity prevents the apparition of impurities generated by temperature difference, insuring temporary supersaturation of the liquid, thus homogeneously forming the first crystal seeds.

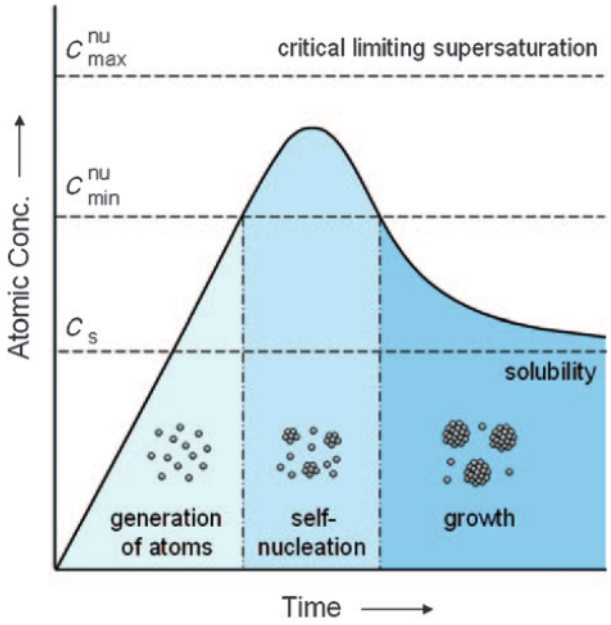

Figure 19: Representation of the LaMer and Dinegard nucleation and growth mechanism. The figure is adapted from *Angew. Chem. Int. Ed.* 2009 by Xia *et al.*[150]

I.1.4 Molecular Magnetism

Molecular magnetism measurement allows to study the behaviour of unpaired electrons when subject to an external magnetic field (H). The response of the sample can be expressed by a vector field representing the density of induced magnetic dipoles, the magnetisation (M).

Our present study focuses on polynuclear Mn compounds, where the metallic paramagnetic centres are linked through oxo/aqua and carboxylate bridges. These Mn atoms have an oxydation state of II or III, that is to say, respectively, d^5 or d^4 orbital configurations. The d orbitals of Mn ions, that contain unpaired electrons, can interact with the molecular orbitals (MO) of their neighbouring ligands. The linear combination of Mn d orbitals with the MO of their ligands create three new molecular orbitals (the ones of the complex): bonding, antibonding and non-bonding orbitals (**Figure 20**).

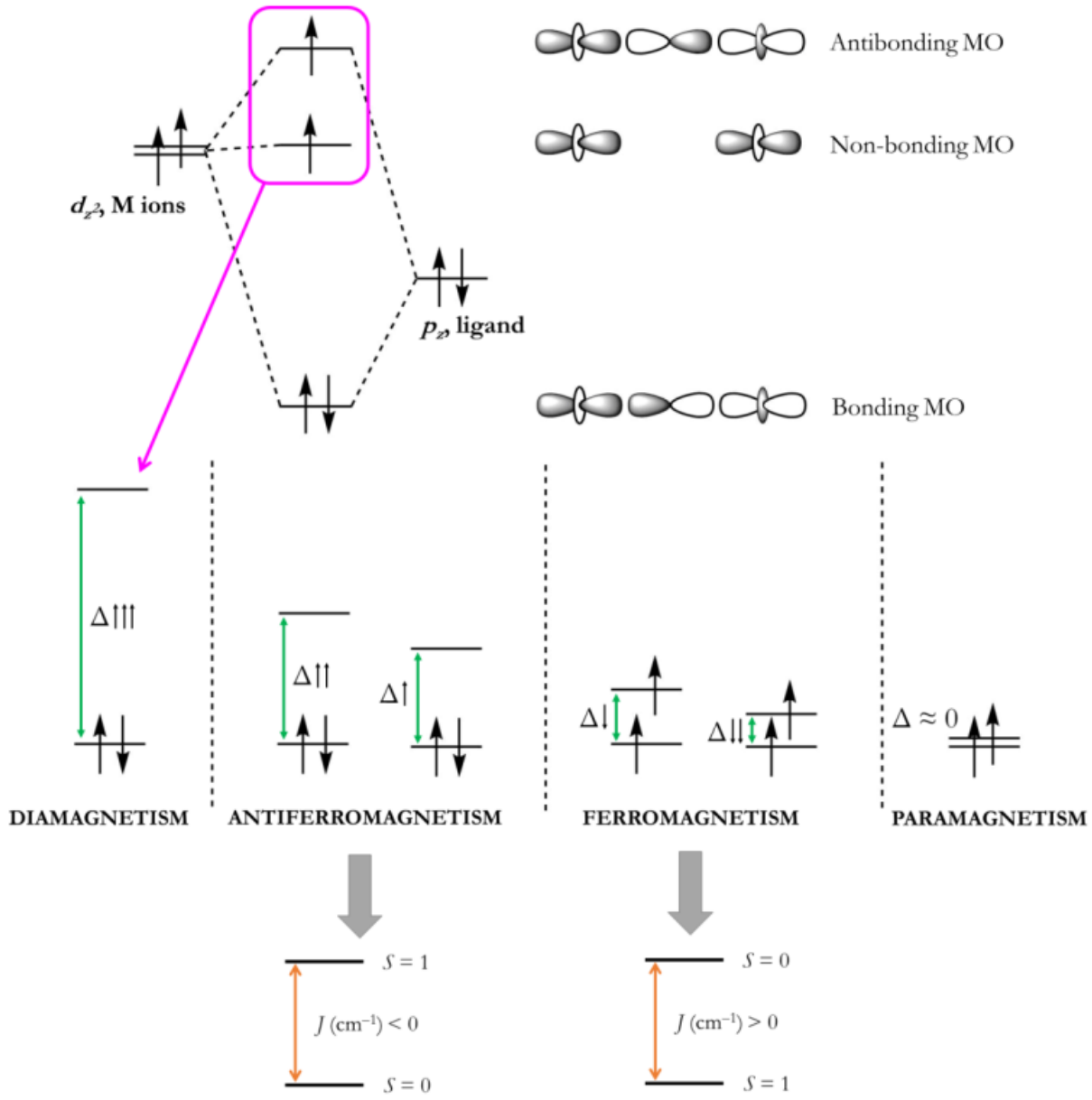

Figure 20: Diamagnetism, ferromagnetism and paramagnetism illustrated with the MOs of an M-X-M system. The figure is adapted from *Coordination chemistry* 2008 by Ribas.[151]

If the geometry of the d Mn orbitals with the MO of the ligands enables an important overlap, the resulting bonding orbital will be highly stabilised and the energy difference with non-bonding and antibonding orbitals will be strong. As a consequence, the two unpaired electrons can be found coupled in the same non-bonding MO. Alternatively, if the overlap is poor and the energy difference between non-bonding and antibonding is small, they will be associated to two different MO.

In typical molecular orbitals resulting from d^n ions, the energy gap between non-bonding and antibonding orbitals can range from 0 to 500 cm^{-1}. Therefore, the temperature has a strong impact on the thermodynamical repartition of the electrons between the orbitals. The

Boltzmann statistic is the general tool employed to described the population of these different energetic levels (**Equation 4**):

$$N_i = \frac{N e^{-E_i/k_B T}}{\sum_i e^{-E_i/k_B T}} \tag{4}$$

N is the total number of electrons in the system, N_i the number of electrons found in a non-degenerated state of energy E_i, T the temperature of the system and k_B the Boltzmann constant (0.695 $cm^{-1}K^{-1}$). And the probability, P_i, for the orbital E_i to be occupied can be deduced (**Equation 5**).

$$P_i = \frac{N_i}{N} \tag{5}$$

Depending on the repartition of the two electrons among non-bonding and antibonding levels, the interaction between their spin is different. When both electrons occupy the same MO, their ground state is a spin singlet ($S = 0$) and their interaction is antiferromagnetic. If the electrons are found in different MO, the ground state is a triplet ($S = 1$) and they interact in a ferromagnetic way.
If the energy gap between non-bonding and antibonding is large enough, the electrons will occupy the same orbital even at room temperature. In that case their interaction is diamagnetic. On the other hand, when the atomic and ligand orbital do not overlap, the electrons will remain on two different orbitals of similar energy and, therefore, do not interact. It is called paramagnetism.
The gap between triplet ferromagnetic and singlet antiferromagnetic states is caused by magnetic interactions and can be evaluated with the magnetic coupling constant J. J can be decomposed in two components, a ferromagnetic one, J_F and an antiferromagnetic one J_{AF}, which gives in the Hoffmann and Kahn models the **Equation 6**.[152,153]

$$J = J_F + J_{AF} \tag{6}$$

J_F favours the triplet state (S = 1) and is related to the coulombic repulsion of close electrons. J_{AF} on the other hand favours the singlet state (S = 0) and is proportional to the squared energy gap between the molecular orbitals ($J_{AF} \propto \Delta^2$).
As a result, the magnetic coupling between two Mn ions is the sum of these components for each of the electrons of the contributing orbitals (d) (**Equation 7**):

$$J = \sum_{m,n} J_{mn} \tag{7}$$

where m and n are the number of electrons of each Mn d orbital.

The magnetisation of the sample (M) is the sum of the contribution of all the magnetic dipolar moments of the individual states weighted with their Boltzmann distribution (**Equations 4 and 5**) and is given in the following equation (**Equation 8**):

$$M = N_A \sum_i \mu_i P_i \tag{8}$$

where N_A is the Avogadro number and μ_i the molecular magnetic moment.

For a fixed spin quantum number value, $S = \frac{n}{2}$ (where n is the number of unpaired electrons), the magnetisation can then be rewritten thanks to the Brillouin equation (**Equation 9**).

$$M = N_A g \mu_B S B_S(\eta) \tag{9}$$

Where g is the Lande constant or gyromagnetic factor ($g \simeq 2.0$ for a free electron), μ_B the Bohr magneton expresses the magnetic moment of an electron and B_S defined as (**Equation 10**):

$$B_S(\eta) = \frac{2S+1}{2S} \coth\left(\frac{2S+1}{2}\eta\right) - \frac{1}{2S} \coth\left(\frac{\eta}{2}\right) \text{with } \eta = \frac{g\mu_B H}{k_B T} \tag{10}$$

As a consequence at high temperature ($k_B T \gg g\mu_B H$), the magnetisation follows a linear trend with the magnetic field H and $M = H\frac{N_A g^2 \mu_B^2 S(S+1)}{3k_B T}$.

On the other hand, when the temperature is low enough ($k_B T \ll g\mu_B H$), the magnetisation tends to a constant value $M = H N_A g \mu_B S$ that only depends on the spin of the state. In this case, the magnetization is directly proportional to the number of unpaired electrons of the system.

The magnetic susceptibility, χ, measures the magnetic answer of a system to an applied magnetic field and is defined after the magnetisation : $\chi = M/H$. For molecular materials it is common to use its molar equivalent χ_M. As χ_M directly derivates from the equations of the magnetisation (**Equations 9 and 10**), and is proportional to the population of the states of the system, it feels natural to follow its evolution with the temperature. In general, graphics plot $\chi_M T$ versus T, which gives a good representation of the system behaviour.

For paramagnetic systems ($J = 0$), $\chi_M T$ is independent of T and they follow the Curie law (**Equation 11**):

$$\chi_M T = \frac{N_a g^2 \mu_B^2}{3k_B} S(S+1) = 0.125 g^2 \frac{n}{2}\left(\frac{n}{2}+1\right) = C \tag{11}$$

Where C is the Curie constant of the material.**Table 7** shows C values for sample n unpaired electrons.

Table 7: Curie constant values for n unpaired electrons and $g = 2.00$

n	C ($cm^3mol^{-1}K$)
1	0.37
2	1.00
3	1.87
4	3.00
5	4.38
6	6.00
7	7.87
8	10.00
9	12.37
10	15.00

However, for ferromagnetic materials ($J > 0$), $\chi_M T$ increases with T, and for antiferromagnetic materials ($J < 0$) it decreases (**Figure 21**). The evolution of the population of energetic levels described with Boltzmann statistics offers a good understanding of the phenomenon. For a Mn^{II}_2 complex which is the simplest system studied in this work, energy levels correspond to six states ($0 \leq S \leq 5$) with a ground state with ferromagnetic (F) interaction for $S = 5$ and a ground state with antiferromagnetic (AF) interaction for $S = 0$.
At low temperature, only the ground state is populated, hence from **Equation 11**, $\chi_M T = 15$ $cm^3mol^{-1}K$ (F) or $\chi_M T = 0$ $cm^3mol^{-1}K$. With the increase of temperature, more energetic states are occupied and the population of the ground states decreases. According to this, the electrons start to behave as if they were not coupled and $\chi_M T$ gets closer to 8.75 $cm^3mol^{-1}K$.

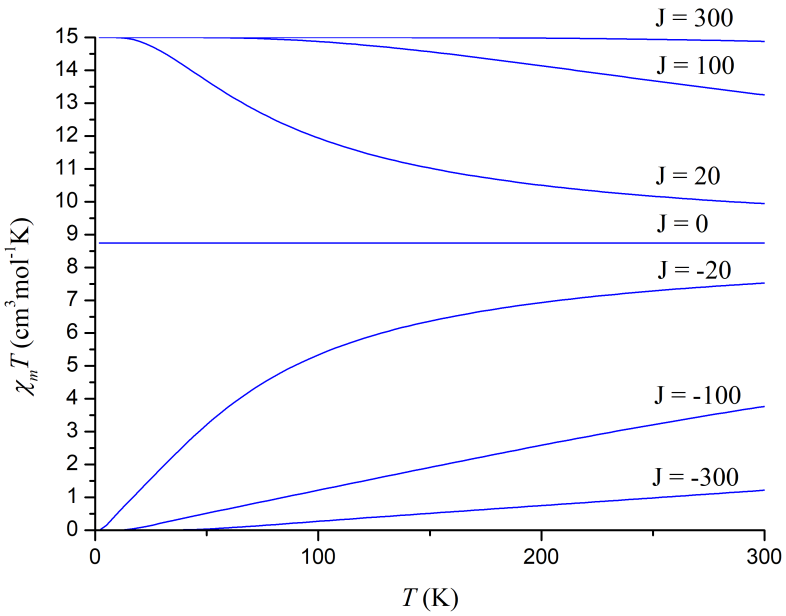

Figure 21: $\chi_M T(T)$ simulation for a Mn^{II}_2 system with different magnetic coupling constants.

In addition, the magnetic susceptibility depends of the strength of the interaction between the two metal atoms, quantified with the magnetic coupling constant J. The electrostatic

interactions between two atoms m and n can be quantified with the Heisenberg-Dirac-van Vleck Hamiltonian (**Equation 12**):

$$\hat{H}_J = -J_{mn}\hat{S}_m\hat{S}_n \tag{12}$$

where J_{mn} is the exchange constant between the spins S_m and S_n.

Compounds with more than one unpaired electron ($S > \frac{1}{2}$) may present distortions due to the Jahn-Teller effect: the system stabilises by losing degenerated states. These distortions can appear when spin-orbit coupling occurs with higher energy states. This leads to a splitting of the M_S states despite any external field. Hence, it is called zero-field splitting (ZFS). This spatial distortion is commonly separated in axial (D) and equatorial or rhombic (E) anisotropic contributions. The Hamiltonian of this interaction is stated in **Equation 13**:

$$\hat{H}_D = D\left({S_z}^2 - \frac{1}{3}S(S+1)\right) + E\left({S_x}^2 - {S_y}^2\right) \tag{13}$$

where S_x, S_y and S_z are the spin matrices along each axis. Contribution of the ZFS to energy levels is illustrated **Figure 22**.

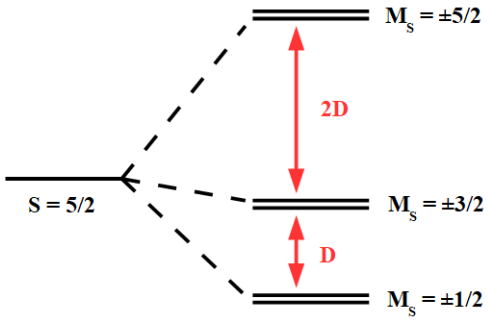

Figure 22: Representation of the axial (D) zero-field splitting of the enegy levels with $S = \frac{5}{2}$.

For Mn ions, ZFS contribution is well known and varies greatly between Mn^{II} and Mn^{III}. Mn^{III} ions with their d^4 configuration favour axial distortion of the octahedral environment through Jahn-Teller effect ($2 \leq |D| \leq 5$ cm^{-1}).[154–157] On the other hand, d^5 Mn^{II} tend to have a much regular octahedral environment with slight or no axial distortion ($|D| \leq 0.3$ cm^{-1}).[154,158–169] ZFS effect is only observable when population is mismatched through the energy levels, that is, at low temperature. A measurement a low T and variable external field enables to quantify ZFS impact for Mn^{III}.

Electron paramagnetic resonance (EPR)

Electron paramagnetic resonance (EPR), sometimes also referred as electron spin resonance (ESR) is a method to study the excitation of unpaired electron spin. The absorption frequency of the electron is measured as a function of the applied external magnetic field.
The EPR is based on the electronic Zeeman effect. It describes how the degeneration of M_S states is removed when subject to fluctuation of the magnetic field. Zeeman Hamiltonian is stated in **Equation 14**:

$$\hat{H}_Z = g\mu_B\hat{S} \tag{14}$$

As a consequence, this new energetic levels spawn new permitted transitions, in accordance to the spectroscopic selection rules ($\Delta M_S = \pm 1$; $\Delta S = 0$).[151] For EPR measurements, two main frequencies are used: X-band ($\nu = 9.5$ GHz) and Q-band ($\nu = 35$ GHz) with a magnetic field ranging from 0 to 6 T.
When evaluating the influence of Zeeman effect, the gyromagnetic constant of the electron g should first be adjusted, as the electron is not isolated but part of the electronic cloud of the molecule. **Equation 15** gives the value of the gyromagnetic constant of a bounded electron:

$$g = \frac{h\nu}{\mu_B H} \tag{15}$$

An EPR spectra usually represents the derivative of the signal along with the imposed external magnetic field, making it is easier to spot the transitions. **Figure 23** shows the evolution of the signal of an antiferromagnetic Mn_2^{II} unit, when it is submitted to more and more intense axial anisotropic field (z).
Under an isotropic field, all transitions appear for the sale field, and they occur for $g \simeq 2.0$. The corresponding plot of Zeeman energy levels is the same in all the direction of space (x, y and z).
When the axial anisotropy (D) is high enough, new transitions appear on the EPR signal, with different g values. The Zeeman plot becomes different along the the z axis and in the xy plane and the change in energy levels enables new transitions to appear, represented with arrows on **Figure 23**. It should be noted that these new transitions are normally forbidden, but that the anisotropy involves a mix of M_S states that makes them possible.
With a higher anisotropy, transitions become more visible on the EPR spectra as the high value of D further splits the M_S levels. When $D \gg h\nu$ transitions moves too far in energy for classical EPR measurement, and high-frequency EPR must be used.

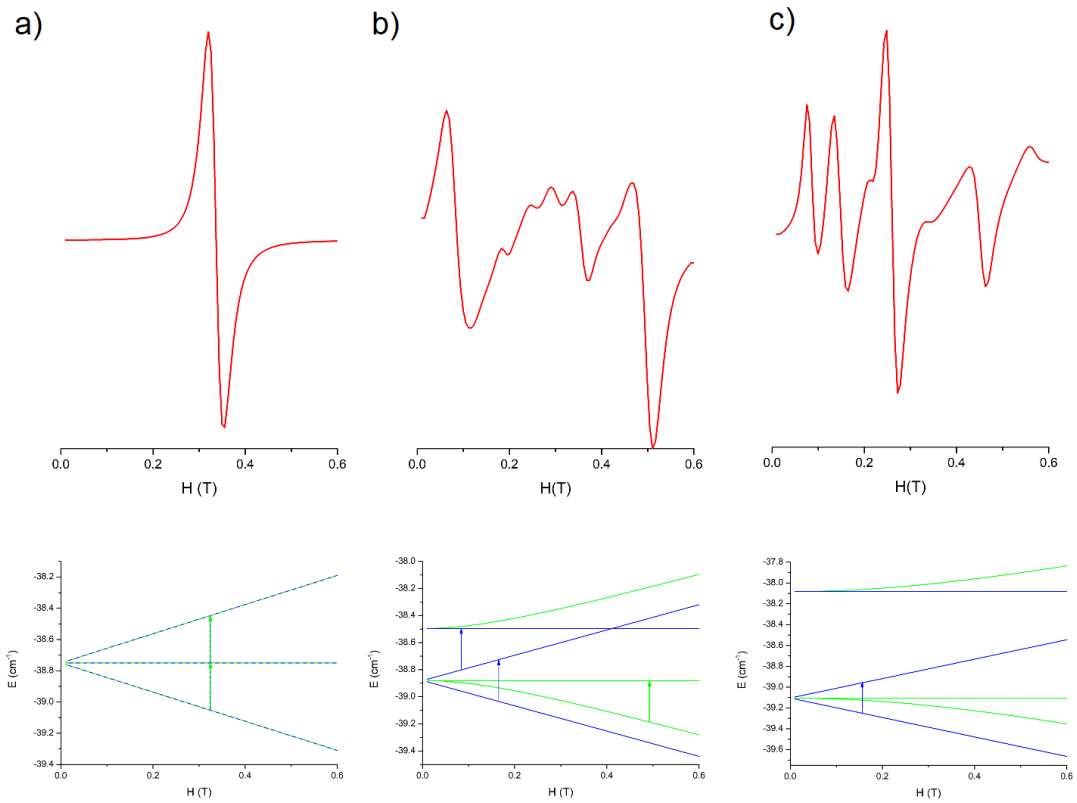

Figure 23: Effect of the axial anisotropy parameter (a) $D_{\mathrm{Mn}} = 0$ cm^{-1}, b) $D_{\mathrm{Mn}} = 0.03$ cm^{-1} and c) $D_{\mathrm{Mn}} = 0.08$ cm^{-1}) on the EPR spectrum and $S = 1$ energy levels of dinuclear Mn$^{\mathrm{II}}$ unit with magnetic coupling J = -5.0 cm^{-1} at 4 K and 9.4 GHz (X band). Green lines and arrows represent the contribution in the xy plan, blue lines and arrows, the contribution along the z axis.

I.2 Mn coordination compounds

The goal of this study is the synthesis of Mn$^{\mathrm{II}}$ and Mn$^{\mathrm{III}}$ complexes that mimic the active site of the Mn-catalase enzyme. This enzyme is able to decompose hydrogen peroxyde in water and O_2 by cycling between the oxydation state (II,II) and (III,III) of its dinuclear Mn active site.[44]
According to the configuration of the natural Mn-catalases, each Mn ion is surrounded by a NO_5 environment made of one histidine and two or three glutamates.[15,43,44] The Mn are bridged by one or two hydroxo, aqua or $\mu_{1,2}$-carboxylate groups, which is apparently fundamental for the catalytic disproportionation phenomenon, as they set the distance between the two metal atoms. In natural *Lactobacillus plantarum* catalase, they are spread from about 4 Å,[15] 3.6 Å for *Thermus thermophilus* catalase,[170] and 3.8 Å was measured for *anabaena* catalase.[43] Dinuclear mimics usually have a distance from 2.9 Å to 3.8 Å between the Mn atoms.[45]

The variety of ligands and coordination modes contribute to the wealth and complexity of coordination chemistry. Carboxylate and bidentate ligands, here respectively 9-anthracene carboxylate and 2,2'-bipyridine, can coordinate in variety of modes with Mn$^{\mathrm{II}}$. To describe

these different coordinations, the Harris nomenclature is most commonly used.[171]
In this nomenclature, coordination modes are noted [X. $Y_1Y_2...Y_n$]. X is the total number of metallic coordination centres whereas Y_i describes the number of metallic atoms bonded to each atom of the ligand. The order of the Y_i is defined after Cahn-Ingold-Prelog rules.[172]

As such, carboxylates, can coordinate in several ways : monodentate terminal, chelating, bidentate bridging or monodentate bridging modes. In particular, the $\mu_{1,1}$ notation is used when a carboxylate makes a coordination of one oxygen atom for two metal atoms or $\mu_{1,3}$ if each metal atom of the ligand is coordinated to a different metal.[173] In the case of $\mu_{1,3}$, the coordination mode can be further qualified as syn-syn or syn-$anti$ according to the conformation. The most common coodination modes are presented **Figure 24**.

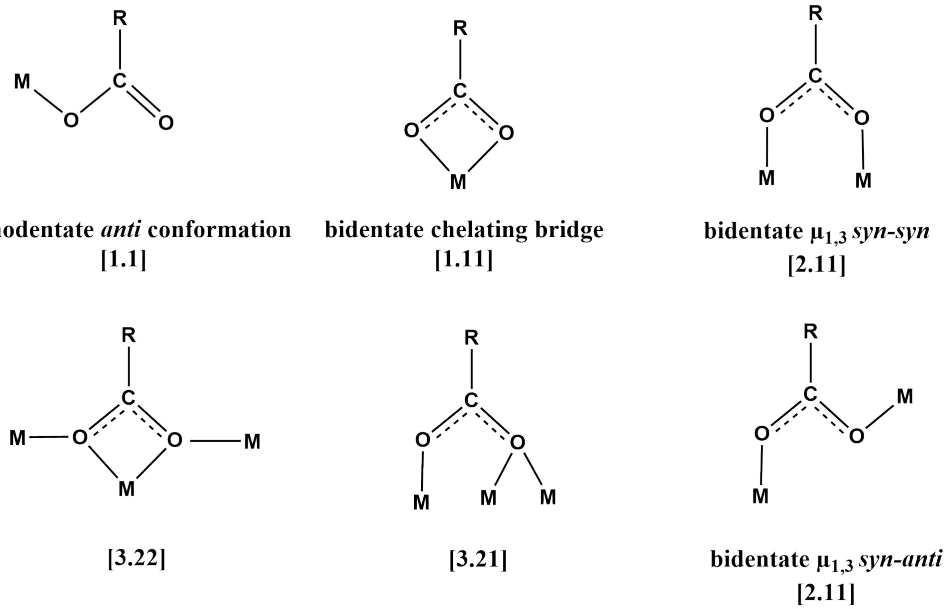

Figure 24: Some exemples of metal-carboxylate coordination modes.

In the case of Mn^{II}, this variety of coordination modes can drive the complex formation towards many nuclearities : mononuclear, dinuclear, trinuclear or 1D "chain" systems.

The recent polynuclear Mn-catalase mimics are dinuclear and based on Mn^{III} ions. Most of them link the two Mn ions with two $\mu_{1,3}$-carboxylate bridges and one oxo-bridge. These compounds rely on the use of multiple ligands in stoechimeric conditions, usually 2,2'-bipyridine and 1,10-phenantroline, and benzoate derivatives to build the Mn complex.[56,174,175] The alternative is the use of a bulky ligand, which provides a set environment for the Mn centres.[55,58] More diverse compounds were synthesised with Mn^{II} with a larger set of ligands types.[176–178] The environment found for the Mn ions is, most of the time, N_2O_4, but NO_5 can be found[55] as well as O_6.[176,178] With these previous works in mind, the 2,2'-bipyridine (bpy) was used as nitrogen chelating ligand and anthracenecarboxylate ($AntCO_2^-$) was chosen as second ligand to provide a fluorophore instead of more traditional carboxylates like benzoates derivatives. As polynuclear Mn-mimics can have Mn^{III} or Mn^{II} ions, like the natural catalases, we decided to explore both oxidation states.

I.2.1 Mn^{II} compounds

This section describes the synthesis and characterisation of polynuclear Mn^{II} compounds.

Chlorinated salts

In order to synthesize the Mn^{II} compounds, a series of approaches were designed. The aim was to prepare dinuclear or trinuclear complexes of Mn^{II} with labile positions (in order to allow the catalytic activity) and to yield suitable crystals for X-ray analysis.
The first attempt was to use Mn chlorinated salts, like $Mn(ClO_4)_2$ or $MnCl_2$, along with $AntCO_2H$ acid or $NaAntCO_2$ followed by bipyridine addition. It has been done with molarities corresponding to trinuclear or dinuclear complexes (3:1 and 2:1 $AntCO_2^-$:bpy ratios respectively) in ethanol or acetonitrile.

$MnCl_2$ gave really poor results. No compound precipitates and despite many crystallisation techniques, no complex was obtained, only $AntCO_2H$ crystals form.
Attempts with $Mn(ClO_4)_2$ are more interesting. In ethanol, the synthesis with $Mn(ClO_4)_2$ quickly generates some precipitate, but IR spectroscopy indicates a mix of an ionic compound (likely $[\{Mn(bpy)_2\}_2(\mu\text{-}AntCO_2)_2](ClO_4)_2$) along with carboxylic acid. In acetonitrile, crystals can be obtained but it is, again, a mix. The method to obtain the desired complex was found almost at the same time, therefore no further try was made to purify these compounds. In addition, the $[\{Mn(bpy)_2\}_2(\mu\text{-}AntCO_2)_2](ClO_4)_2$ species would not present any labile position and would be of little interest for our application.

In parallel, attempts to obtain Mn^{III} compounds were carried out, as more thoroughly in the next part. With this in mind, synthesis mentioned above were also performed with addition, of triethylamine or tetrapropylammonium hydroxyde. The goal here was to prepare Mn^{III} compounds from the oxidation of Mn^{II} complexes. These reactions never gave more than either MnO_2, or ammonium salts precipitation (see **Figure 25**).

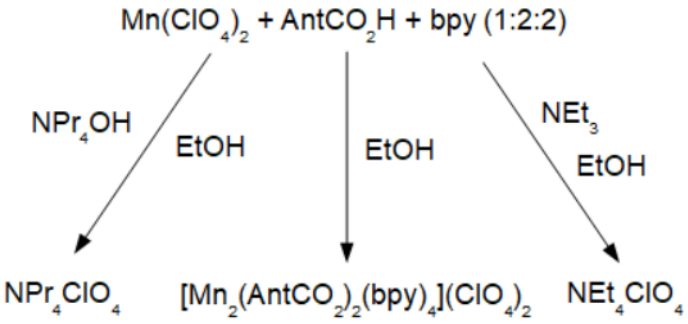

Figure 25: Products obtained from $Mn(ClO_4)_2$.

Mn^{II} acetate

The use of $Mn(AcO_2)_2$ instead of chlorinated precursors gave better results. $Mn(AcO_2)_2$ mixed with $AntCO_2H$ acid or $NaAntCO_2$ and bipyridine in acetonitrile, gives a yellowish white compound. In both cases, IR spectra are identical and indicate that the carboxylate groups

are coordinated to the manganese ions. On the other hand, a precipitate forms almost instantaneously when $Mn(AcO_2)_2$ is added to an ethanol solution of $AntCO_2H$, before bipyridne addition. This precipitate is manganese anthracene carboxylate.
In order to have more control on the reaction in acetonitrile, whose solid could be a mix of Mn carboxylate and other Mn compounds, it was decided to prepare the complex by using a two steps synthesis, as presented in the next paragraph. **Figure 26** summarise this approach.

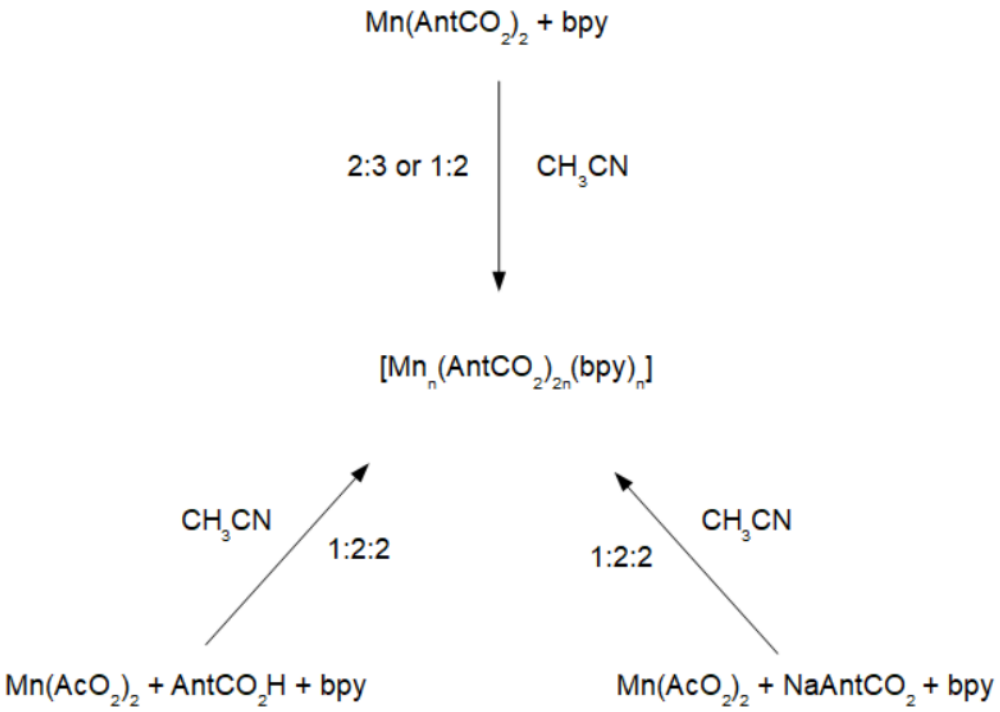

Figure 26: Synthesis with $Mn(AcO_2)_2$.

Table 8 sums up all the strategies that remained fruitless to give crystals suitable for X-ray diffraction.

Table 8: Unsuccessful attempts to obtain suitable crystals for X-ray diffraction. Syntheses labelled with a * were also attempted with extra salts added in excess at the end to facilitate later crystallisation, namely $NaB\Phi_4$ and NH_4PF_6. See page 18 for abbreviations.

label	Mn source	NN	carboxylate source	solvent	base
1	$MnCl_2$	bpy	$NaAntCO_2$	EtOH	-
2	$MnCl_2$	bpy	$NaAntCO_2$	EtOH	NPr_4OH
3	$Mn(ClO_4)_2$	bpy	$AntCO_2H$	EtOH	-
4	$Mn(ClO_4)_2$	bpy	$AntCO_2H$	EtOH	NPr_4OH
5	$Mn(ClO_4)_2$	bpy	$AntCO_2H$	EtOH	NEt_3
6*	$Mn(ClO_4)_2$	bpy	$NaAntCO_2$	EtOH	-
7	$Mn(AcO_2)_2$	bpy	$NaAntCO_2$	CH_3CN	-
8	$Mn(AcO_2)_2$	bpy	$AntCO_2H$	CH_3CN	-
9*	$Mn(AcO_2)_2$	bpy	$NaAntCO_2$	EtOH	-
10	$Mn(AcO_2)_2$	bpy	$AntCO_2H$	EtOH	-

For all the synthesis given in **Table 8** all the crystallisation techniques mentionned in I.1.3 at the exception of microwave assisted synthesis were attempted at different temperatures (usually T_{amb}, 4 °C and -20 °C) and various co-solvents (ether, water and n-hexane). Most of the synthesis led to non crystalline yellow-white powders or yellow needle-like crystals unsuitable for X-ray diffraction.

Mn^{II} carboxylates

A successful strategy found to obtain suitable compounds is to use a Mn-carboxylate intermediate to later react it with the second ligand type, 2,2'-bipyridine.
In fact, the use of $Mn(AntCO_2)_2$ was considered before working with $Mn(AcO_2)_2$. However, the reaction employed to prepare it at that point was not fitting our carboxylate and led to a bad quality MnII carboxylate. At first $Mn(AntCO_2)_2$ was generated through the reaction of $MnCO_3$ with 9-anthracene carboxylic acid in hot water (60 °C) for 48h. This reaction (**Equation 16**) was inspired from the work of B. Garcia-Cirera[179] with other carboxylic acids (benzoates derivatives).

$$\mathrm{MnCO_3} + 2\ \mathrm{RCO_2H} \longrightarrow \mathrm{Mn(RCO_2)_2} + 2\ \mathrm{CO_2} + \mathrm{H_2O} \tag{16}$$

The advantage of this technique is that it is driven by the liberation of CO_2 and thus produces generally good yields of MnII carboxylate. Unfortunately 9-anthracene carboxylic acid is poorly soluble in water, which doubles the reaction time to obtain a comparable yield (y $\simeq$ 90%) and gives a powder instead of good quality crystals.

As a consequence, the former reaction was replaced by the more simple one described in the previous paragraph: $Mn(AcO)_2$ is mixed with 9-anthracencarboxylic acid in technical ethanol at room temperature (**Equation 17**). The reaction is quick (10 min) and has a good yield (y $\simeq$ 84%). Again, crystals could not be obtained but IR spectra shows all the characteristics of the expected Mn^{II} carboxylate (**Figure 27**).

$$\mathrm{Mn(AcO)_2} + 2\ \mathrm{AntCO_2H} \longrightarrow \mathrm{Mn(AntCO_2)_2} + 2\ \mathrm{AcO_2H} \tag{17}$$

The main bands that are characteristic of $Mn(AntCO_2)_2$ are present in both synthesized compounds (**Figure 27**). The most striking evidence of the chelatation of the carboxylate is the reduction of the $\Delta(\nu(CO_2)_{asym} - \nu(CO_2)_{sym})$ of the carboxylate group from 423 cm^{-1} for the free acid to 178 cm^{-1} in the synthesised compound, which is characteristic of coordinated carboxylate ligands. The $\nu(CO_2)_{asym}$ and $\nu(CO_2)_{sym}$ values (respectively 1560 and 1252 cm^{-1}) match perfectly what is observed for common Mn carboxylate salts.[12] It is also possible to notice the apparition of bands on the $Mn(AntCO_2)_2$ compounds in the 760 cm^{-1} area, which can be attributed to the formation of Mn-O bonds.

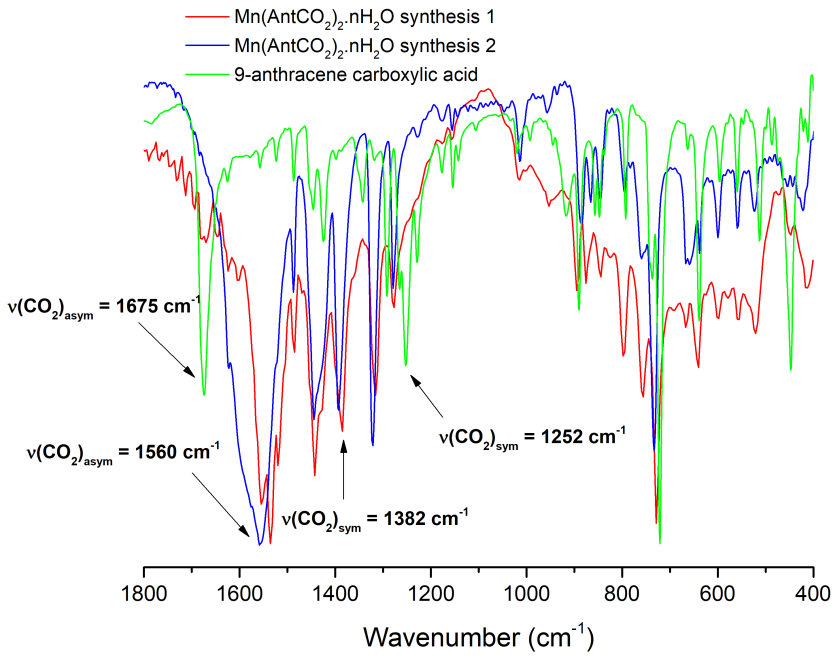

Figure 27: IR spectra of 9-anthracene carboxylic acid and Mn carboxylate obtained through synthesis 1 (Equation 16) and 2 (Equation 17). They are displayed in normalized transmittance.

$[\{Mn(bpy)(AntCO_2)\}_2(\mu\text{-}AntCO_2)_2(\mu\text{-}OH_2)]$ and $[Mn(bpy)(AntCO_2)_2]_n$

Once $Mn(AntCO_2)_2$ is obtained, it is reacted with 2,2'-bipyridine (1:1 molar ratio) in acetonirile to yield compounds with both anthracene carboxylate and bipyridine as ligands. Unfortunately, EPR spectra of several products shows that their composition vary between pure dinuclear $[\{Mn(bpy)(AntCO_2)\}_2(\mu\text{-}AntCO_2)_2(\mu\text{-}OH_2)]$ complex ($[Mn^{II}_2]$) and $[Mn(bpy)(\mu\text{-}AntCO_2)_2]_n$ chains ($[Mn^{II}]_n$) (see **Figure 35**). The chain appears most of the time and the dinuclear is formed more rarely. It is actually possible to explain the change of nuclearity in presence of a low amount of water: the chain can be broken in dinuclear units as depicted **Figure 28**. This factor would explain why the chain is formed more frequently than the dinuclear complex.

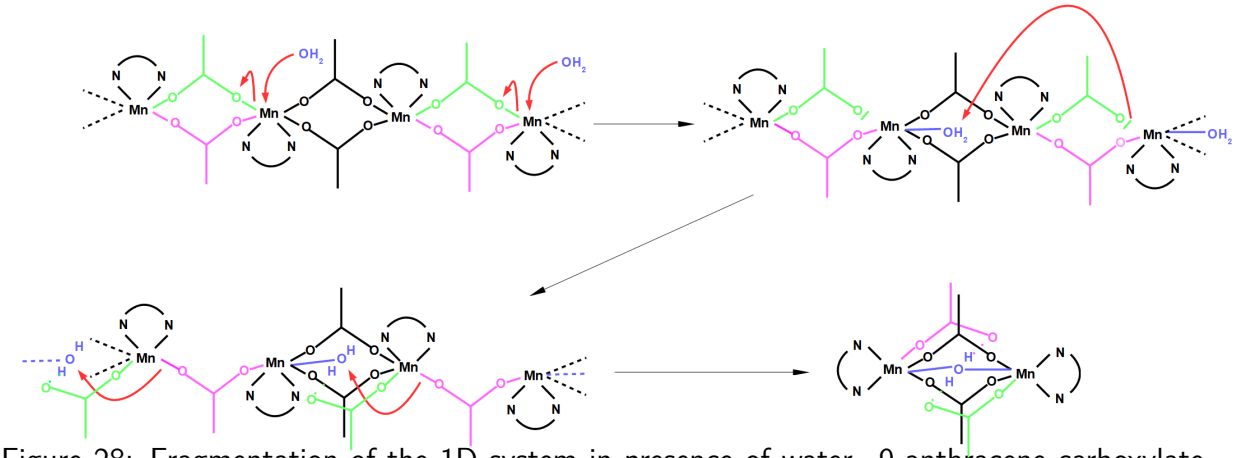

Figure 28: Fragmentation of the 1D system in presence of water. 9-anthracene carboxylate and 2,2'-bipyridine are represented in simplified versions.

Thermogravimetric analysis (TGA) was performed on $[Mn^{II}]_n$ (**Figure 29**) not so much for the sake of characterisation of the compounds but rather to identify it later inside the $[Mn^{II}]$@NPs materials.

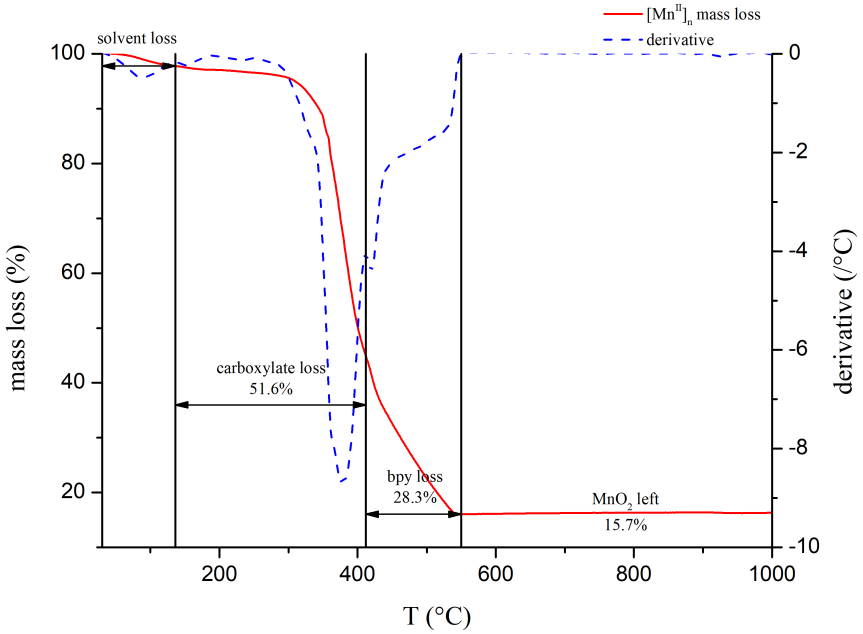

Figure 29: Thermogravimetric analysis of $[Mn(bpy)(AntCO_2)_2]_n$.

TGA of the chain shows a minor solvent loss below 136 °C, $AntCO_2^-$ ligands are decomposed between 136 °C and 412 °C (more precisely between 265 °C and 412 °C), bpy between 412 °C and 550 °C. Finally manganese oxyde is the only species left in the crucible at the end of the process. The values found for each component roughly match the expected ratio. For ligands, the imprecision comes very likely from the fact that bipyridine starts to decompose before $AntCO_2^-$ is completely consumed. As it is only possible to spot changes on the mass loss slope, bpy mass is overestimated while $AntCO_2^-$ mass is underestimated.

Table 9: Comparison between experimental and theoritical mass loss for each ligand group and final mass of Mn oxyde for $[Mn^{II}]_n$.

Group	Quantity	T (°C)	Experimental weight %	Theoretical weight %	Error %
$AntCO_2^-$	2	136-412	51.6	67.7	24
bpy	1	412-550	28.3	23.9	18
MnO_2	1	$>$ 1000	15.7	13.3	18

A possible route to form the dinuclear compound more reliably is to convert the chain in dinuclear compounds. Yellow crystalline polyhedra can be simply obtained by dissolving the Mn chain powder in acetonitrile in the presence of a small amount of water (100:1 v:v mix) and leaving it to crystallise for a few days. Unfortunately these crystals are of to poor quality to perform XRD measurements. However, IR spectra and EPR measurement identify this compound as the dinuclear complex (see the following section).

Another method to obtain crystals of the pure dinuclear complex suitable for the resolution of the structure by X-ray diffraction, is to perform a microwave assisted synthesis (see **I.1.3**). Reagents are mixed in the same proportion as for the reaction at room temperature but the solvent is ethanol and the solution is submitted to a microwave heating cycle (up to 85 °C with 5 °C/min, held at 85 °C for 2 min then cooled with compressed air). After a few days, yellow crystalline polyhedra form.

Figure 30 shows IR spectra of [Mn^{II}] compounds obtained with the different methods: chain powder from T_{amb} synthesis, dinuclear prepared from the chain and direct synthesis of the chain with microwaves. Their spectra are very similar and only two notable difference can be identified. First, pure dinuclear compounds have a sharp band at 1600 cm^{-1} that corresponds to $\nu(CO_2)_{asym}$ of coordinated carboxylate groups. Whereas the band of the chain compound is broader and has a second maximum at 1575 cm^{-1}. On the other hand, a change of the ratio of the three bands that appear respectively at 638, 652 and 665 cm^{-1} can be observed. For pure dinuclear compounds the ratio between the most intense band (638 cm^{-1}) and the two other is well defined (1, 0.96 and 0.92 respectively), whereas it fluctuates for the chain (respectively 1, 0.86 and 0.97 for the example displayed).

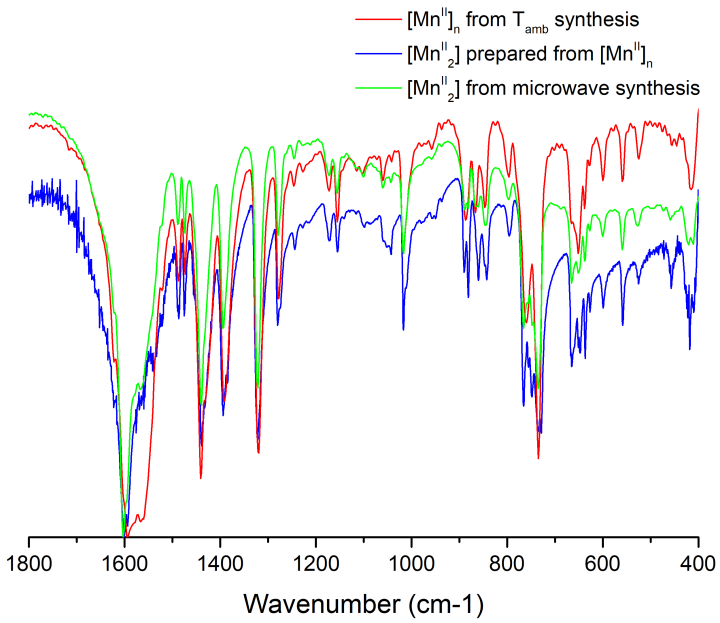

Figure 30: IR spectra of [Mn^{II}] dinuclear compounds and dinuclear/chain mix. They are displayed in normalized transmittance.

Elemental analysis of the [Mn^{II}_2] compound prepared from microwave synthesis was performed and results are given **Table 10**. The mass percentages are close to the expected composition, with an error inferior to 5% for each of the elements measured.

Crystals obtained with microwave synthesis (see **Equation 17**) are of suitable quality for the resolution of their structure through X-ray diffraction. The triclinic (P-1) crystalline unit is composed of two complexes, which are centrosymetric reflexion from each other (**Figure 31**). Two ethanol molecules are also part of the unit but are not displayed on the figure for the sake of clarity. π-stacking occurs between the bipyridine ligands of both entities.

Table 10: Comparison between experimental mass percentages of light atoms and theoretical ones for $[Mn_2^{II}]$.

	Experimental weight %	Theoretical weight %	Error %
N	4.1	4.2	2.4
C	71.1	72.6	2.1
H	4.2	4.0	5.0

The structure of the two complexes of the unit are similar, so the following comments are valid for both of them. And the values given in this paragraph are the averages of both units. Mn(II) ions have an octahedral geometry and are separated by 3.6 Å. The two Mn atoms are linked through one μ-aqua bridge and two $\mu_{1,3}$-carboxylates bridging in $syn-syn$ mode. The hexacoordination is further completed by a monodentate carboxylate in syn coordination mode and one bidentate chelating 2,2'-bipyridine per Mn ion. As for the Mn-catalase mimics cited at the begining of the part, the environment of the Mn ions is N_2O_4 and there is a triple bridge between the two metal ions, with two carboxylate and one water molecule.
Mn-O and Mn-N distances range are of 2.12-2.27 Å and 2.24-2.28 Å, respectively. The angle between the C and the two O of the carboxylates are almost the same regardless of their coordination mode (126 °). The Mn-O_w-Mn angle is found to be 107 °. **Table 11** sums up a selection of atom distances and angles of the subunit A.

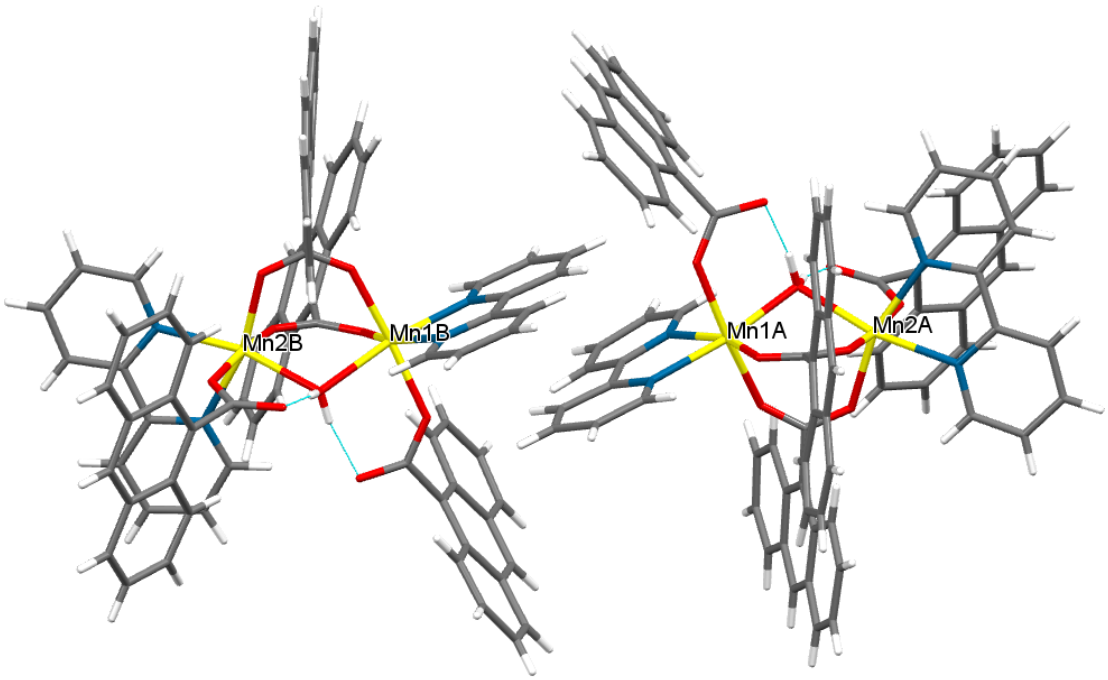

Figure 31: Crystal unit of $[\{Mn(bpy)(AntCO_2)\}_2(\mu\text{-}AntCO_2)_2(\mu\text{-}OH_2)]$.

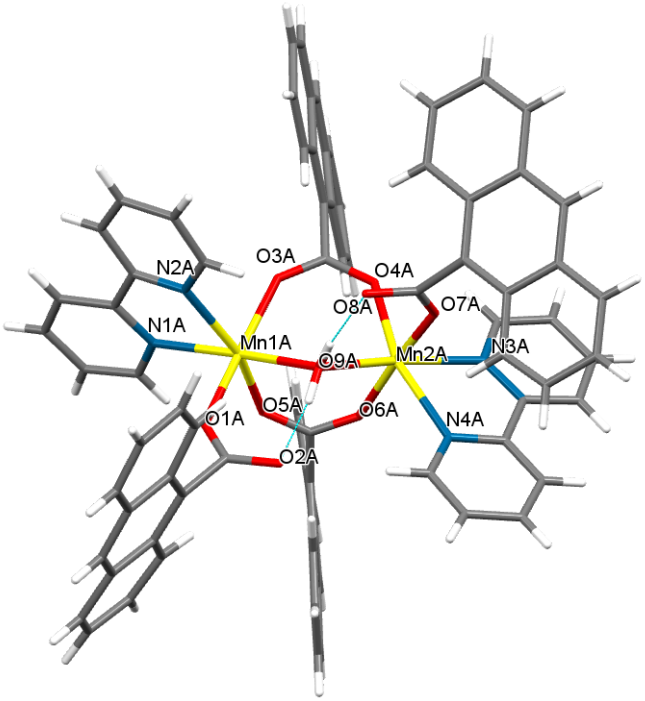

Figure 32: Crystal structure of subunit A.

Table 11: Distances and angles of $[Mn_2^{II}]$ complex subunit A. Values given inside the parenthesis are standard deviations.

atoms label	distance (Å)	atoms label	angle (°)
Mn(1A)···Mn(2A)	3.620	Mn(1A)-O(9A)-Mn(2A)	106.22(4)
Mn(1A)-N(1A)	2.2408(11)	N(1A)-Mn(1A)-O(9A)	172.59(4)
Mn(1A)-N(2A)	2.2821(12)		
Mn(1A)-O(1A)	2.1447(10)	O(1A)-Mn(1A)-N(1A)	90.78(4)
Mn(1A)-O(3A)	2.1151(10)	O(3A)-Mn(1A)-O(1A)	170.35(4)
Mn(1A)-O(5A)	2.1241(11)	O(5A)-Mn(1A)-O(1A)	90.91(5)
Mn(1A)-O(9A)	2.2706(10)	O(9A)-Mn(1A)-N(2A)	102.79(4)

From XRD, it is not possible to say if the μ-oxygen is really a water molecule or an oxo-bond with hydrogens belonging to the two monodentate anthracene ligands which would be carboxylic acids rather than carboxylates. Many dinuclear Mn complexes[176–178] present a similar configuration, with two μ-carboxylate bridges and one μ-aqua bridge stabilised by monodentates carboxylates, and it is always assumed that the hydrogens are bond to the oxygen-bridging atom. A different type of aqua bridge, not stabilised with carboxylates, has been reported for a 1D coordination polymer of Mn^{II} with O_6 environment.[180] This complex also presents monodentate water molecules stabilised by benzoates derivatives. The total environment of this complex is, therefore, two monotentate μ-H_2O as chain linkers, two monodentate H_2O and two monodentate carboxylates. However, the Mn centres are linked between each others through a single aqua bridge rather than a triple bridge. And in a more general scope, no polynuclear compound based only on Mn^{II} has ever been reported with Mn-oxo bridge.

The Mn-O bond strength (formula presented **Equation 18**) is normally close to 0 for H_2O molecules, around 1.4 for O-H and up to 2.0 for pure oxo bridges.[181,182]

$$\mathrm{BVS(O)} = \left(\frac{r}{r_0}\right)^{-N} \tag{18}$$

Where r is the experimental Mn-O bond length, r_0 the theoretical bond length, calculated with Bohr radius, and N an empirical factor. For Mn^{2+} ions, $r_0 = 2.186$ Å and $N = 5.5$.[181,182]

With the data available from the crystallographic resolution, the Mn-O bond strength of the bridge is found between 0.8 and 1.0 for our compound. Therefore, it suggests that even if these hydrogens seem to be linked to the oxygen bridging atom the effect of the neighbouring carboxylate disturbs the Mn-O_w-Mn group.

Magnetic measurements of the Mn^{II} compounds

Magnetic susceptibility measurements are carried out between room temperature and 2 K, they are displayed in **Figure 33** for $[Mn^{II}]_n$ and in **Figure 34** for $[Mn_2^{II}]$, along with fits plotted with parameters discussed later in this paragraph.

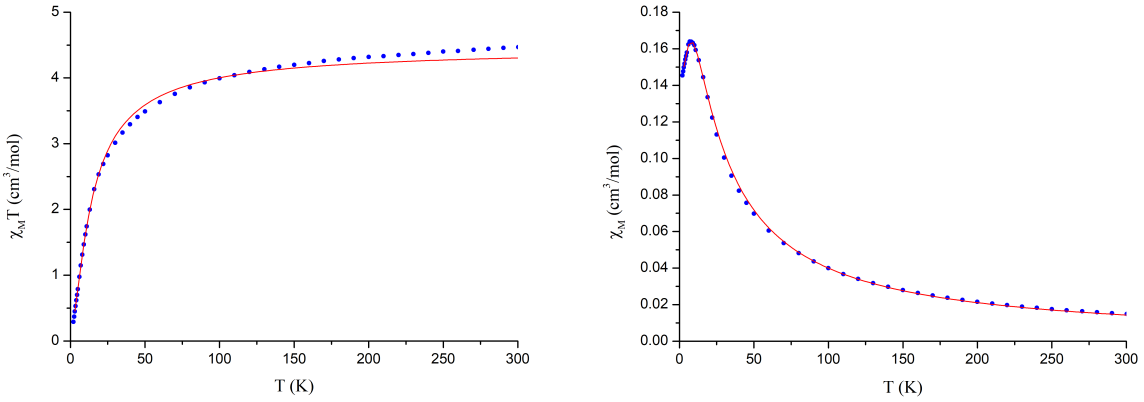

(a) (b)

Figure 33: (a) Molar magnetic susceptibility times temperature of $[Mn^{II}]_n$ plotted versus temperature. (b) Molar magnetic susceptibility of $[Mn^{II}]_n$ plotted versus temperature. Blue squares : experimental points ; red line : best fit.

For $[Mn^{II}]_n$, $\chi_M T$ rises up to 4.5 cm^3 K mol^{-1} at 300 K, which is approximately the value of a single uncoupled Mn^{II} ion and matches the mononuclear unit of the chain. At low temperature the $\chi_M T$ falls to 0, which corresponds to the behaviour of antiferromagnetic superexchange between the Mn^{II} ions. The χ_M curve of $[Mn^{II}]_n$ also displays the expected shape of antiferromagnetic compounds with a maximum at 0.16 $cm^3 mol^{-1}$ reached for 7 K. $\chi_M T$ is fitted with a Fischer function.[183] This function takes into account the following Hamiltonian for a chain of N atoms:

$$H = -\sum_{i=1}^{N}\sum_{j=1}^{N} J_{ij} S_i S_j \tag{19}$$

where i and j are two neighbouring atoms.
Fischer's function for magnetic susceptibility is:

$$\chi_M = \frac{N_A g^2 \beta^2}{k_B T} \frac{1+u(K)}{1-u(K)} \text{ with } u(K) = \coth K - \frac{1}{K} \text{ and } K = \frac{JS(S+1)}{k_B T} \qquad (20)$$

Parameters found to match the experimental data points are g = 2.0, J = -1.3 cm^{-1} with R values of 6.1 $\times$ 10^{-4} and 9.0 $\times$ 10^{-4} for χ_MT and χ_M fits, respectively.[ii]

For [Mn$_2^{\text{II}}$], $\chi_M T$ reaches 9.2 cm^3 K mol^{-1} at 300 K which is close to the expected value of 8.75 cm^3 K mol^{-1} for two uncoupled Mn$^{\text{II}}$ ions. At low temperature the behaviour of χ_MT drops to 0, which is a characteristic behaviour of antiferromagnetic superexchange between the Mn$^{\text{II}}$ ions. The shape of the χ_M plot of [Mn$_2^{\text{II}}$] is also distinctive of antiferromagnetic compounds with a maximum at 0.15 cm^{3}mol^{-1} reached, for 20 K.
χ_MT is fitted versus T thanks to the PHI program.[184] Parameters found to match the experimental data points are g = 2.1 and J = -4.8 cm^{-1} ($H = -JS_1S_2$) with R values of 6.5 $\times$ 10^{-5} and 2.1 $\times$ 10^{-5} for $\chi_M T$ and χ_M fits respectively[i].
If we compare the values of J for dinuclear and chain compounds, we find that the coupling is stronger for the dinuclear complex ($J = -4.8$ cm^{-1}) than in the chain ($J = -1.3$ cm^{-1}). It is not very surprising considering that the bridging modes are suspected to change between the two forms, and that μ-H$_2$O has often a significant effect on it. Indeed, the magnetic coupling of species with a triple bridge including a μ-water molecule, is often found stronger than compounds with only carboxylates bridges.[14]

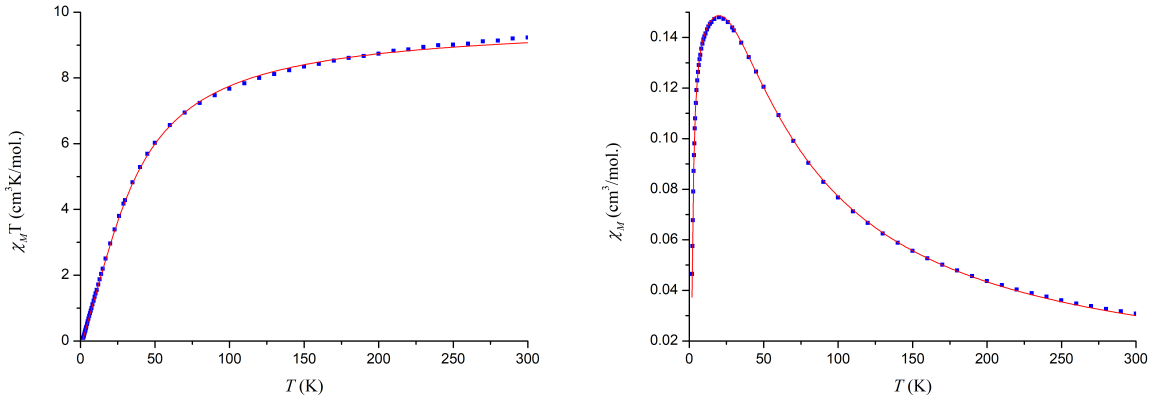

(a) (b)

Figure 34: (a) Molar magnetic susceptibility times temperature of [Mn$_2^{\text{II}}$] plotted versus temperature. (b) Molar magnetic susceptibility of [Mn$_2^{\text{II}}$] plotted versus temperature. Blue squares : experimental points ; red line : best fit.

As mentioned earlier in this paragraph, the most efficient way to make the distinction between dinuclear [{Mn(bpy)(AntCO$_2$)}$_2$(μ-AntCO$_2$)$_2$(μ-OH$_2$)] and [Mn(bpy)(μ-AntCO$_2$)$_2$]$_n$ chains is to observe their EPR spectra. The EPR spectrum of [Mn$_2^{\text{II}}$] presents multiple peaks whereas [Mn$^{\text{II}}$]$_{\text{n}}$ shows a more simple signal centred at $g \simeq 2.0$.

[ii] $R = \frac{\sum[(\chi_M T)_{exp} - (\chi_M T)_{calc}]^2}{\sum[\chi_M T]^2_{exp}}$

The EPR spectrum was recorded in powder for both compounds and at different temperatures. At room temperature, both compounds show a simple signal centered on $g \simeq 2$. However, especially for $[Mn_2^{II}]$, the signal becomes more complex at lower temperatures (**Figure 35**). Indeed, with a low temperatures, electrons become less energetic and are thus more likely to occupy their fundamental states rather than wandering around close energy excited levels, thus refining the signal and making it easier to interpret.

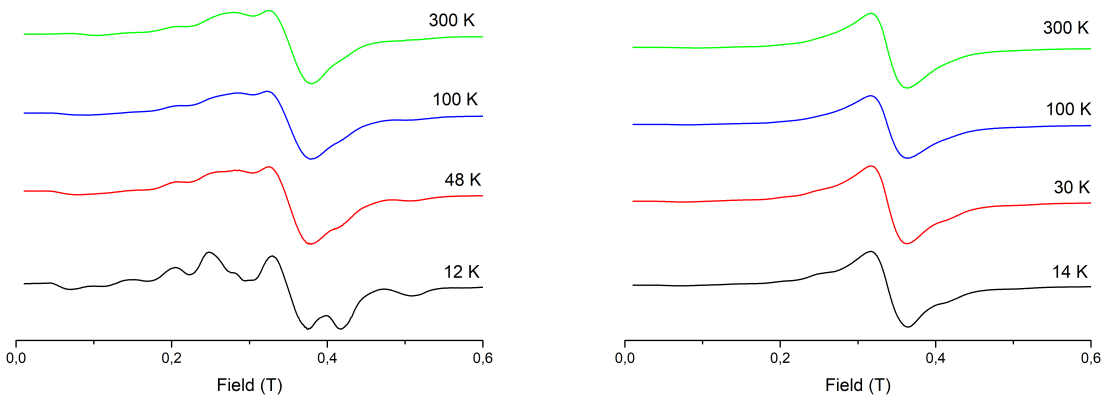

(a) (b)

Figure 35: (a)X-band EPR spectra of $[\{Mn(bpy)(AntCO_2)\}_2(\mu\text{-}(AntCO_2)_2(\mu\text{-}OH_2)]$ at various temperatures. (b)X-band EPR spectra of $[Mn(bpy)_2(AntCO_2)_2]_n$ at various temperatures.

The signal of monodimensional Mn^{II} systems is difficult to interpret. Two main factors enter in competition on their signal: dipolar interactions and isotropic exchange.[185,186] On one hand, the dipolar interaction in 1D-systems leads to a broadening of the signal. In addition, due to a large number of spins contributing to the system, multiple transitions can appear, contributing to widen the signal.[185,186] On the other hand, in the presence of isotropic exchange, the numerous interactions lead to many different energetic levels more spins interact. The fact that this multiplets are degenerated, or not, depends on the anisotropy of the system (ZFS).[185,186] If the contribution of the dipolar interactions dominates the isotropic exchange, a broad signal is observed. If the exchange dominates the dipolar interactions another effect can occur, called *exchange narrowing*, where the signals are more defined and narrow, comparable to individual spins in a magnetic lattice. Usually, this effect is more limited for 1D-system than 2D or 3D, due to the weak contribution of the interchain coupling. In addition, 1D-systems are not exempt of more usual broadening effects, such as hyperfine coupling and crystal-field effects for Mn^{II}.[185,186]
Our compounds present quite a large peak-to-peak signal (470 G) that does not broaden when temperature is decreased. This is indicative of a weak antiferromagnetic behaviour.

The complexity of the signal of $[Mn_2^{II}]$ is typical of antiferromagnetic (AF) systems. AF species have a ground state of $S = 0$ and should not give any signal at low temperature. Nevertheless, their small J values allow electrons to populate the lowest excited states $S = 1$ and $S = 2$ from 4 K.
Simulations of the EPR spectrum at 12 K of $[Mn_2^{II}]$ are carried out with the software PHI,[184]

using a fixed J value, determined from the magnetic susceptibility, measurement. We tried to refine the ZFS parameters (D_{Mn} and E_{Mn}). The value of D_{Mn} parameter has to stay close to what was found with the susceptibility measurement, in absolute value, but it is now possible to find its sign. In addition the parameter E_{Mn} is introduced.
EPR spectra are very sensitive to distortions, and we observe from the crystallographic data that the environment of the Mn^{II} is a compressed octahedron with distortion axes at 90 ° one from the other. As we consider that the magnetic axes correspond approximately to structural axes, we introduce an Euler angle β of 90 ° between the two Mn ions. Finally a last simulation is run with the best parameters. The result of the simulation is displayed in **Figure 36**.

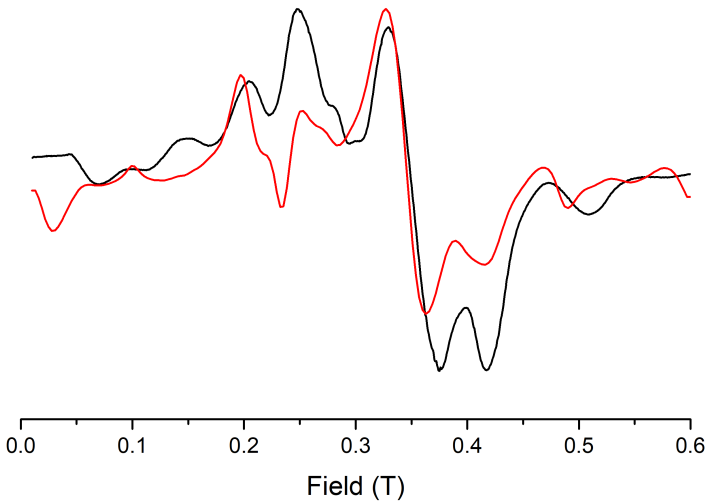

Figure 36: X-band EPR spectra of $[Mn_2^{II}]$ measured at 12 K and its best simulation. $g = 2.0$, $J = -4.8$ cm^{-1}, $D_{\mathrm{Mn}} = 0.28$ cm^{-1} and $E_{\mathrm{Mn}} = -0.03$ cm^{-1}.

Parameters found for the simulation of the EPR spectrum of the $[Mn_2^{II}]$ compound are $g = 2.0$ with an exchange parameter between the two Mn^{II} ions of $J = -4.8$ cm^{-1} and ZFS parameters $D_{\mathrm{Mn}} = 0.28$ cm^{-1} and $E_{\mathrm{Mn}} = -0.03$ cm^{-1} ($H = -JS_1S_2$). These values match figures found in the litterature for a similar octahedral geometry.[167] In addition, the J determined is close to the values found for dinuclear Mn^{II} compounds with the same type of triple bridges (see **Table 12** for more details).

It is possible to better understand the transitions that occur when the external magnetic field becomes more intense by drawing the plot of Zeeman energy levels. According to Boltzmann distribution, the population of the lowest energy levels, $S = 0$, 1 and 2, at 4 K is respectively, 55.2%, 42.6% and 2.2% for our system.
When the external field is applied to the dinuclear compound, the axial anisotropy of the crystal field of each ion (D_{Mn}) imposes two different behaviours along the axis y, and the molecular plane xz. There is a rotation of the symmetry break at the molecular level because the Mn atoms are tilted relatively to the molecular plane. It causes the observation of the axial anisotropy effect on the molecular axis y (rather than z as it would have been without

the introduction of the 90 ° angle). Hence, two different Zeeman plots, representing these two contributions (equatorial for xz and axial for y) can be drawn. For each of the permitted energy transition, contribution along the xz plane is, thus, twice as more important than the ones along the y axis.
In the range of intensity of the field studied (0 to 0.6 T) no transitions are observed between different S levels (because of the energy of the external field), so all energy transitions come from the contribution of M_S states of the same S level. Zeeman transitions of for $S = 1$ and $S = 2$ are represented **Figure 37**.

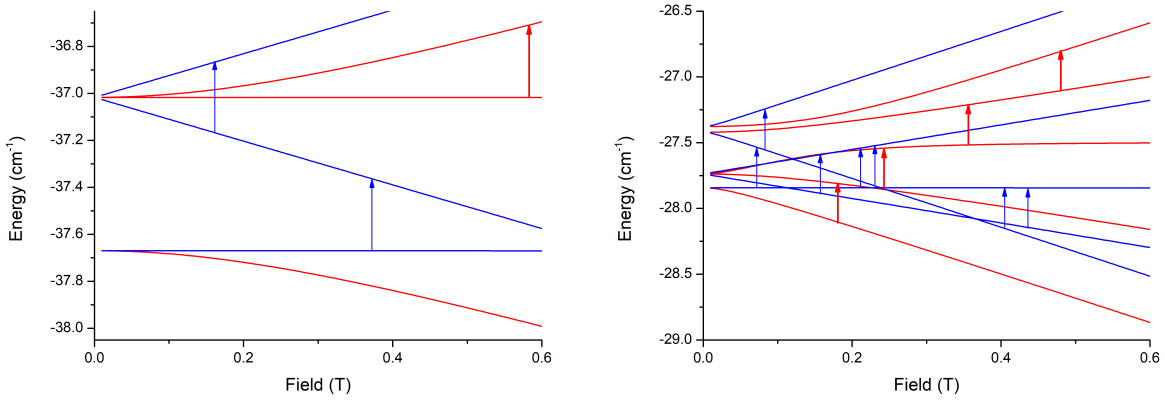

(a) (b)

Figure 37: Zeeman transitions for (a) $S = 1$ and (b) $S = 2$. For both diagrams blue lines represent the contribution along z axis and red lines in the xz plane. Hence, the difference of thickness between xz red arrow transitions, which contribute twice more to the signal that the y blue arrow contribution.

Once all these characterisation made, it is possible to compare our compounds with similar ones. **Table 12** sums up the values found for the magnetic coupling of complexes with one aqua and two carboxylate bridges. It is noticeable that the J value found for our complex is the closest to the value measured for the most similar compounds, the ones with N_2O_4 environment and coordinated to only one water molecule.
In particular, a very similar complex of $[\{Mn(AntCO_2)(phen)\}_2(\mu\text{-}AntCO_2)_2(\mu\text{-}H_2O)]$ formula[187] only differs from having phenantroline ligands instead of the bipyridines of our $[Mn_2^{II}]$ compound. This complex has almost the same distance between its Mn centres (3.58 Å versus 3.63 Å for ours) and a very close J value (-4.9 cm^{-1} versus -4.8 cm^{-1}). The Mn-O_w-Mn angle is 105.7 °, which is slightly smaller than the one measured for $[Mn_2^{II}]$ (106.9 °).
While no coupling is found for reduced natural TTC (in the Mn^{II} form) measurements, a signal can be recorded from phosphate-modified catalase (TTC(Ph)).[170] It is found to be stronger than all artificial mimics, but the introduction of a phosphate group in the vicinity of the catalytic center probably modifies strongly the interactions between the metal centres (as the apparition of the signal itself suggests it). The Mn$\cdots$Mn distance given for TTC(Ph) corresponds to the study of by Khangulov *et al.* It is a correspondence between D value of the $S = 2$ state, found with the EPR spectra of kin compounds and their crystallographic Mn$\cdots$Mn distance and does not correspond to an actual measurement.[170]

There is no easy relation that appears between the coupling referenced and either Mn$\cdots$Mn

ditance or Mn-O_w-Mn angle. The type of coordination of the carboxylate is *syn-syn* for all compounds with the exception of $[\{Mn(4\text{-}Cl\phi CO_2)(phen)_2\}_2(\mu\text{-}4\text{-}Cl\phi CO_2)_2(\mu\text{-}H_2O)]$ that has two *syn-anti* carboxylate ligands. Therefore, the influence of the coordination mode of the carboxylate on J cannot be questioned with these data. Even the nature of the carboxylate plays an unclear role. For instance, compounds with acetate ligands are found high in this J serie (-5.90 cm^{-1})[187] as well as low (-3.30 cm^{-1}).[177] The most important factor is probably the distortion of the geometry of the Mn ions environment caused by the ligands field, as suggested by Khangulov *et al.* study.[170] Unfortunately, suitable EPR data is scarce[14,170] and insufficient to explore this hypothesis.

Table 12: Environment of Mn ions, distance between the centres, angle of the aqua bridge and magnetic coupling constant (with $H = -JS_1S_2$ Hamiltonian) of TTC phosphate derivative and $Mn^{II}2$ complexes with one aqua and two carboxylates bridges.[170,176]

Compound	Mn environment	Mn-Ow-Mn (°)	Mn···Mn (Å)	J (cm^{-1})	reference
TTC(Ph)	NO_5		3.59±0.03	-11.2±0.1	[170]
$[Mn_2(F_5C_3O_2)_4(H_2O)_3L^I_2)(im)_4(AcO_2)_2]$	O_6	114.6±0.3	$3.739\pm2\times10^{-3}$	-3.30	[177]
$[Mn_2(H_2O)(piv)_4(Me_2bpy)_2]$	N_2O_4	110.2±0.1	$3.5950\pm9\times10^{-4}$	-5.46	[178]
$[Mn_2(H_2O)(AcO_2)_4(tmeda)_2]$	N_2O_4	110.0±0.2	$3.621\pm2\times10^{-3}$	-5.90	[178]
$[Mn_2(butca)(H_2O)_5]$	O_6	108.8±0.1	$3.6140\pm8\times10^{-4}$	-3.6	[188]
$[Mn_2(H_2O)(im)_4(AcO_2)_2]$	N_2O_4	114.2±0.2	3.777 ± 10^{-3}	-2.52	[176]
$[Mn_2(4\text{-}Cl\phi CO_2)_4(H_2O)(phen)_4]$	N_2O_4	101.94	3.484	-3.6	[14]
$[Mn_2(AntCO_2)_4(phen)_2(H_2O)]$	N_2O_4	105.7	3.584	-4.92	[187]
$[Mn_2(H_2O)(tolf\text{-}O,O')_2(tolf\text{-}O)_2(py)_4]$	N_2O_4	110.40	3.709	-2.6	[189]
$[Mn_2(bpy)_2(AntCO_2)_4H_2O]$	N_2O_4	106.93±0.01	$3.627\pm5\times10^{-4}$	-4.8	present work

$AntCO_2^-$: 9-anthracene carboxylate, bpy: 2,2'-bipyridine, butca: 1,2,3,4-butanetetracarboxylate, im: imidazole, L^I: 2-ethyl-4,4,5,5-tetramethyl-3-oxo-4,5-dihydro, piv: pivalate, tmeda: N,N,N',N'-tetramethylenediamine, tolf: tolfenamic acid, Ph: phosphate, phen: phenantroline, py: pyridine.

Concerning the $[Mn^{II}]_n$ compound, few compounds of the same type have been characterised. **Table 13** sums up the coupling constants of the referenced compounds. The weak antiferromagnetism displayed by $[Mn^{II}]_n$ (J = -1.3 cm^{-1}) falls in the average of other 1D Mn coordination polymers. Unfortunately, due to the lack of crystallographic data for our compound, it is impossible to extend the discussion on the influence of the coordination modes of the carboxylate.

Table 13: Magnetic coupling constants (J) of 1D Mn coordination polymers with two carboxylate bridges ($H = -\sum_{i=1}^{N}\sum_{j=1}^{N} J_{ij}S_iS_j$).

Compound	J (cm^{-1})	reference
$[Mn(3\text{-}ClC_6H_4CO_2)_2(phen)]_n$	-1.8	[14]
$[Mn(bpy)(3\text{-}Cl\phi CO_2)_2]_n$	-1.7	[186]
$[Mn(bpy)(4\text{-}Cl\phi CO_2)_2]_n$	-0.7	[186]
$[Mn(ClCH_2CO_2)_2(phen)]_n$	-0.9	[190]
$[Mn(FeC_6H_4CO_2)_2(phen)]_n$	-6.5	[191]
$[Mn(AntCO_2)_2(bpy)]_n$	-1.3	this work

ϕ: phenyl, $AntCO_2^-$: 9-anthracene carboxylate, bpy: 2,2'-bipyridine, phen: 1,10-phenantroline.

As far as we know there is no other compound that has been reported to form in similar conditions both dinuclear and chain compounds. However, Gomez *et al.*[14] report the

formation of a similar chain in the same mixture than their trinuclear Mn^{II} compound, as a byproduct that appears after it. In addition, Fontanet *et al.*[192] induce the formation of dinuclear Mn^{II} compounds ($[Mn_2(1\text{-R-2-}CO_2\text{-}1,2\text{-}closo\text{-}C_2B_{10}H_{10})_4(bpy)_2]$, R = H or CH_3) by employing a stoichiometric amount of 2,2'-bipyridine on the already formed 1D coordination polymer. It is a method inspired from restriction enzymes cleavage on DNA. Both works suggest that a larger proportion of bipyridine could lead to the exclusive formation of the dinuclear $[Mn_2^{II}]$. This assumption is strengthened by the work of Liu *et al.*[187] on their $[\{Mn(AntCO_2)(phen)\}_2(\mu\text{-}AntCO_2)_2(\mu\text{-}H_2O)]$ compound, where anthracenecarboxylate and bipyridine are employed in (1:1) ratio and lead to a (2:1) stoichiometry on the complex.

I.2.2 Mn^{III} compounds

In this section the synthesis and characterisation of a Mn^{III} compound is reported. In order to obtain a fluorescent compound the chosen ligands are the same than the ones used with the Mn^{II} compounds : 9-anthracene carboxylate and 2,2'-bipyridine.

The synthesis is a simple and direct reaction of comproportionation between the Mn^{II} of perchlorate or nitrate salts and the Mn^{VII} of permanganate. To begin with, anthracene carboxylic acid and Mn^{II} salts ($Mn(ClO_4)_2$ or $Mn(NO_3)_2$) are dissolved in acetonitrile. Tetrabutylammonium permanganate and 2,2'-bipyridine are then simultaneously added to the mix. The solution immediately turns black, but we wait a few minutes, to make sure that the reaction is completed, before filtering it. At this point, the yield is usually quite low ($y \simeq 7\%$) because all the compound did not precipitate. It is possible to wait for a longer time to reach a better yield. At first, the proportion used (1.6 MnX_2, 0.4 MnO_4^-, 2 bpy and 2 $antCO_2H$) were designed to match dinuclear stoichiometry (with a compound of formula $[Mn_2O(bpy)_2(AntCO_2)_2]X_n$) but elemental analysis (see next paragraph) quickly showed that the tetranuclear compound ($[MnO_2(bpy)_2(AntCO_2)_6X_2]$)) is preferentially formed. As a consequence, the relation between the reagent was changed to match the new nuclearity of the complex (1.6 MnX_2, 0.4 MnO_4^-, 1 bpy and 3 $AntCO_2H$).
The obtained compound is very insoluble in a wide range of solvents, as a result recrystallisation attempts of the first precipitate remained unsuccessful. However, the techniques mentioned in section I.1.3 can be used on the solution once the first precipitate is removed.
Small crystals of poor quality can be obtained by slow evaporation. These crystals take the form of urchin-like agglomerates of needles and have the same IR spectra than the solid previously obtained from the same solution.

Small amounts of the Mn_4^{III} compound are obtained over time, however, after more than a week the solution loses its black-brown colouration and becomes translucent yellow. At this point, by leaving the solution evaporating slowly, anthraquinone starts to crystallise and forms yellow needles (**Figure 38**). Interestingly, if the solution is left to crystallise for a longer time, red crystals start to form and these are viable for XRD resolution. They appear to be the 10-oxo-9,10-dihydroanthracene-9-yl anthracene-9-carboxylate a compound that, as far as we know has never been reported (details on this compound figure in the **Annexes** section). We tried to obtained this compound directly by oxydation of 9-anthracene carboxylic acid, with tetrabutylammonium permanganate in acetonitrile, but the attempt remained unsuccessful.

From the data available, it is difficult to know if the reaction between the quinone and the carboxylate is assisted by the Mn^{III} complex or not. However, considering the total bleaching of the solution, it seems that the Mn^{III} complex plays also some role in this step. All the stages of the evolution of the solution are gathered in the **Figure 38**.

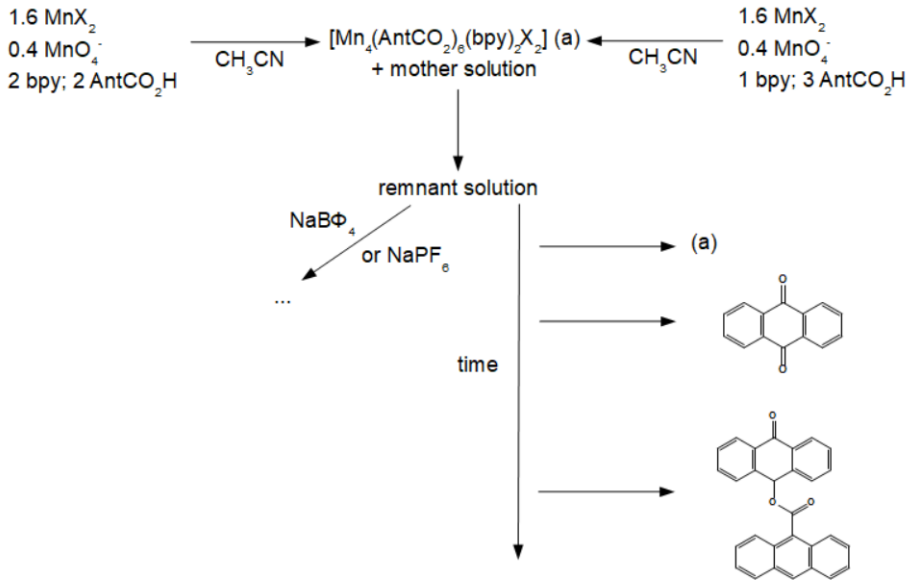

Figure 38: Preparation of $[Mn_4^{III}]$ complex and evolution of the solution with time. The arrow with $NaB\phi_4$ and $NaPF_6$ represent the recrystallisation attempts with bulky salts, which remain unsuccessfull. X: ClO_4^- or NO_3^-

The following graph (**Figure 39**) presents IR spectra of the Mn^{III} compounds ($[Mn_4O_2(AntCO_2)_6(bpy)_2X_2]$) obtained from the synthesis with $Mn(ClO_4)_2$ and $Mn(NO_3)_2$.

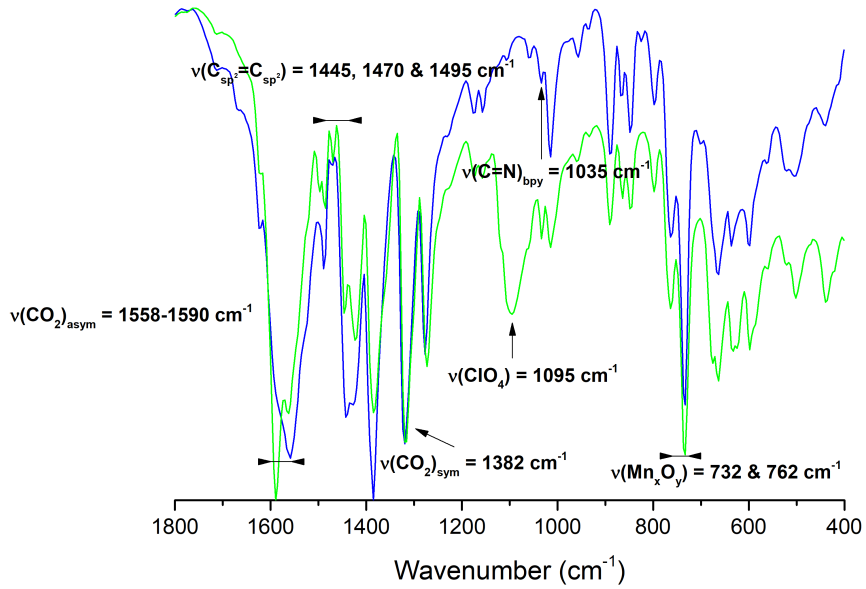

Figure 39: IR spectra of $[Mn_4O_2(AntCO_2)_6(bpy)_2X_2]$ compounds. The spectrum of the solid prepared with $Mn(NO_3)_2$ is blue, the one prepared with $Mn(ClO_4)_2$ is green.

Both spectra display similar IR bands: the $\Delta(\nu(CO_2)_{asym} - \nu(CO_2)_{sym})$ is around 200 cm^{-1} for both compounds, which is consistent with coordinated carboxylates.[12] The two bands at 732 and 762 cm^{-1} indicate the presence Mn-O group vibrations, possibly due to the coordination of $AntCO_2^-$ or the Mn_3O group from the butterfly. The vibration of the C_{sp^2} of the ligands also appears between 1445 and 1495 cm^{-1}. Finally, the solid synthesized with $Mn(ClO_4)_2$ clearly displays the wide band of the ClO_4^- group. Unfortunately NO_3^- bands cannot be discerned for sure because they should appear at 1380 cm^{-1}, where one of the intense $\nu(CO_2)_{sym}$ band of the carboxylate already is.
From now on, the analysis results presented come from solids prepared with $Mn(ClO_4)_2$, as it was decided to use primarily this salt for the Mn^{III} complex synthesis. We choose it because it is more soluble than the nitrate salt, which seemed more useful in order to crystallise the Mn^{III} compound. It will be simply referred as $[Mn_4^{III}]$.

Table 14 presents the results of the elemental analysis carried out on Mn^{III} solids prepared from $Mn(ClO_4)_2$ salt.
Table 14: Comparison between experimental mass percentages of light atoms and theoretical ones for $[Mn_4O_2(AntCO_2)_6(bpy)_2(ClO_4)_2]$.

	Experimental weight %	Theoretical weight %	Error %
N	2.8	2.7	3.7
C	65.4	63.2	3.5
H	3.6	3.4	5.9

The closest composition match found with these proportions of elements is a tetranuclear compound: $[Mn_4O_2(AntCO_2)_6(bpy)_2(ClO_4)_2]$. The error is inferior to 6% for each individual element, which gives us a good confidence for this composition. This means that this $[Mn^{III}]$ complex has a butterfly structure with two oxo-bridges (**Figure 40**). This assumption is reinforced by magnetic measurements (see later in this part).

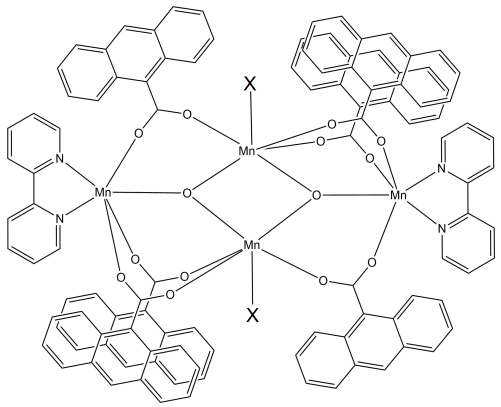

Figure 40: Assumption of the structure of the $[Mn^{III}]$ complex prepared from $Mn(ClO_4)_2$. The ligand X is ClO_4^-

The TGA (**Figure 41** and **Table 15)** can be interpreted the same way than for $[Mn^{II}]_n$, with the distinctive mass loss of the carboxylate between 239 and 429 °C and the bipyridine between 429 and 633 °C. We can see that bpy weight seems under estimated with our formula. Indeed, its decomposition starts a slightly before what was observed for $[Mn^{II}]_n$. Therefore, it is possible that the carboxylate did not decompose completely when the bipyridine starts to

decompose. This seems confirmed by the carboxylate mass loss, which is lower than expected. The first mass loss, below 239 °C is most likely coming from volatile chlorinated compounds. For this analysis, HCl was considered to be the main species, as it is the closest match in terms of mass loss.

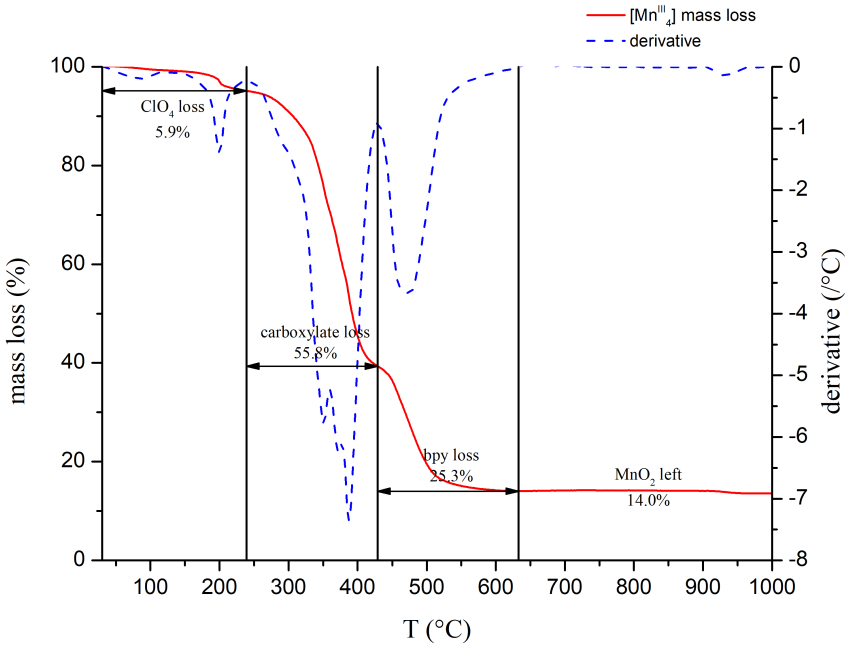

Figure 41: Thermogravimetric analysis of $[Mn_4O_2(AntCO_2)_6(bpy)_2(ClO_4)_2]$.

Table 15: Comparison between experimental and theoritical mass loss for each ligand group and final mass of Mn oxyde.

Group	Quantity	T	Experimental weight %	Theoretical weight %	Error %
HCl (ClO_4^-)	2	30-239	5.9	7.0	15.7
$AntCO_2^-$	6	239-429	55.8	63.5	12.1
bpy	2	429-633	25.3	14.9	69.8
MnO_2	4	$\geq$ 1000	14.0	19.1	31.9

Figure 42 displays the magnetic behaviour of the $[Mn_4^{III}]$ compound along with the best simulation obtained to describe it. First, the χT value reaches 8.5 cm^{-1} at room temperature, which is significantly inferior to the value of 12.0 cm^{-1} ($S = 2$) that would be expected for four uncoupled Mn^{III} ions. It is actually a very common feature of Mn_4^{III} butterfly compounds and shows that even at 300 K a strong antiferromagnetic coupling is present.[193–199] This behaviour is confirmed by the general shape of the curve, which decreases as the temperature drops. χT value is 3.9 cm^{-1} at 2K, which is normal for a tetranuclear compound. Indeed, due to the complex's geometry pure antiferromagnetic interactions between the four Mn atoms is not possible and some spin frustration must be present.

In order to quantify the antiferromagnetic coupling and the effect of the anisotropy (ZFS), it is necessary to fit the experimental data. It is done, once again, thanks to the PHI program.[184]
To begin with, we must find the antiferromagnetic coupling constants. The following Hamil-

tonian, which considers the interactions between all Mn ions is used:

$$H = -J_1(S_1S_2) - J_2(S_1S_3 + S_2S_4) - J_3(S_2S_3 + S_1S_4) - J_4(S_3S_4) \tag{21}$$

For the attribution of the spin of atoms and magnetic coupling constants, see **Figure 43**.

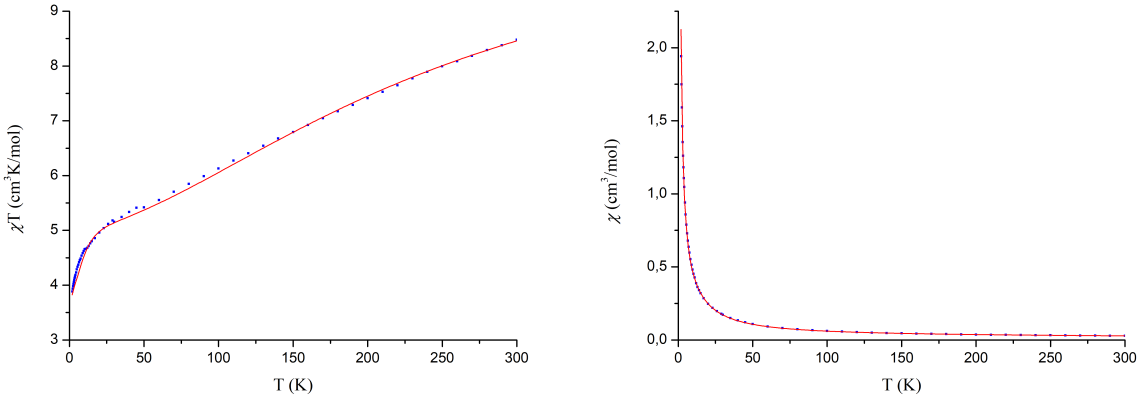

(a) (b)

Figure 42: (a) molar magnetic susceptibility times temperature of $[Mn_4^{III}]$ plotted versus temperature. (b) molar magnetic susceptibility of $[Mn_4^{III}]$ plotted versus temperature. Blue squares : experimental points ; red line : best simulation.

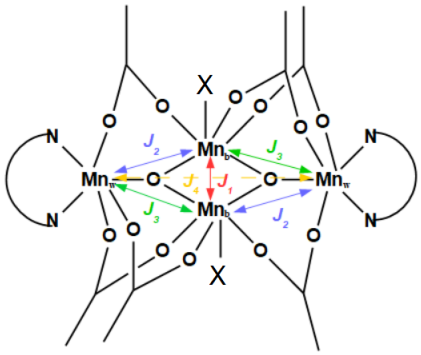

Figure 43: Schematic representation of the Mn···Mn interaction pathways used for the fit of $[Mn_4^{III}]$ susceptibility. 9-anthracene carboxylate and 2,2'-bipyridine are represented in simplified versions. X ligand is ClO_4^-. Mn_c = Mn_1, Mn_2; Mn_w = Mn_3, Mn_4. $J_{bb} = J_1$; J_{bw} is the average of J_2 and J_3.

Considering the distance between the two Mn_w, J_4 is neglected in our fits. For all the other butterfly Mn_4^{III} compounds reported from the literature[193–200] the same assumption has been considered. Indeed, the typical distance between the two external ions ($\simeq$ 6 Å) is to large to be significantly different from intermolecular interaction.
In most of the studies dealing with butterfly Mn^{III} compounds[193–195, 197–199] the J_2 and J_3 interactions are considered equivalent. However, for the fits run for our compound, introducing only two magnetic exchange pathways was not sufficient and we had to make a distinction between J_2 and J_3. Note that PHI only takes into account the disposition of the four Mn^{III} ions in the space and the applied external magnetic field. As a consequence, in our model, J_2 and J_3 are interchangeable. The best fit finds a strong antiferromagnetic interaction between

the two Mn^{III} ions than are linked through two oxo-bridges: J_1 = -41.0 cm^{-1}. Two more moderate antiferromagnetic interactions are found between the Mn^{III} ions that are linked through one oxo-bridge and one or two carboxylate bridges: J_2 = -11.2 cm^{-1} and J_3 = -8.6 cm^{-1}.

As discussed above, this anisotropic system necessitates the introduction of ZFS parameters. They split the degenerated M_S states for each S level in the absence of magnetic field. For the distorted octahedral geometry hereby considered, low negative values of D_{Mn} are expected[154–157] (see **Table 16**). As D_{Mn} is oriented along z axis, the relative orientation of the Jahn-Teller axes of Mn^{III} ions (β) is important to consider. Especially on the Mn^{III} ions coordinated to the bpy which are likely to be distorted. They perceive this field almost orthogonally and it has a strong impact on the ZFS at low temperatures.
Thus, several simulation were run including this rotation angle. As the exact structure, which could be provided by XRD, is not known, it is impossible to give an exact angle, but it is evaluated between 90° and 80° from similar complexes described in the literature. For smaller angle values, χT quickly drops to values lower than measured, which means that the effect of the ZFS is not strong enough to enable the population of the first excited level.
Once the β angle determined, the value of D_{Mn} can be evaluated. It is found to be approximately 2.5 which is consistent with Jahn-Teller distortion of the octahedral geometry.[154–157] E_{Mn} distortion is found to have little impact on the simulation and was finally not considered.

In order to have more information on the population of the low energy states at low temperature, measurements were made for various fields intensity. **Figure 44** displays the molar magnetisation of the sample versus field divided by the temperature. These measurements provide a better estimation of the ZFS parameters. For these measurements, fits are run on PHI with a set value for J_1 (41.0 cm^{-1}) and the other parameters (J_2, J_3, D_{Mn} and E_{Mn}) are left free. Very similar values than those established for χT measurements are found for J_2 and J_3 (respectively -10.6 and -8.4 cm^{-1}). The value of the axial deformation parameter is risen up to D_{Mn} = -3.7 cm^{-1}. $R_M = 8.4 \times 10^{-4}$ with these parameters.[ii]

Table 16 displays the parameters found in the literature for butterfly Mn_4^{III} compounds. These works usually model the butterflies complexes with only two J values, J_{bb} and J_{wb} that represent the interaction between the ions of the core of the butterfly (J_1 for us) and the interaction between the ions of the core and the wing (J_2 and J_3 in our case), respectively. But, despite this small difference, the value found for the magnetic coupling, g value and axial anisotropy are well in the range of these compounds and strengthen the butterfly geometry assumption. For all compounds the interaction between the Mn ions of the "body" is much stronger than the interaction between the "body" and the "wings" of the compound. This is due to the stronger coupling provided by the double oxo bridge bounding the two core ions. In addition, the D_{Mn} values are often found more important than the ones of Mn^{II} ions, evidencing the presence of the Jahn-Teller effect for Mn^{III} ions.

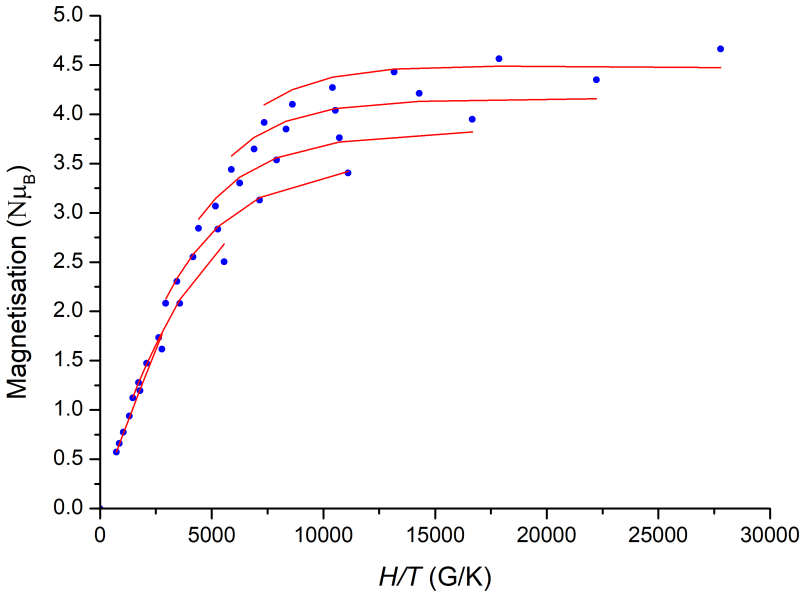

Figure 44: Molar magnetisation versus external magnetic field divided by temperature of [Mn_4^{III}]. The blue dots are experimental points, the red line is the simulation with the following parameters J_1 = -41.0 cm^{-1}, J_2 = -10.6 cm^{-1}, J_3 = -8.4 cm^{-1}, D_{Mn} = -3.7 cm^{-1} and β = 85 °.

Very recently Escriche and colleagues published a study[200] where they discuss more precisely how to relate the different coupling values to the fundamental spin state of the Mn^{III} tetranuclear compounds. It appears from their work, that the J_3/J_2 is the main criteria and make the distinction between $1 \geq J_3/J_2 \geq 0.7$ with $S_T = 3$ and $0.6 \leq J_3/J_2$ with $S_T = 0$ and intermediates values presenting mixed states. For our compound $J_3/J_2 = 0.8$, which means that it has a $S_T = 3$ ground state. It is however impossible to assign a precise combination of individual spin states for Mn ion. The fundamental $S_T = 3$ being a mix of the (3,1,4), (3,1,2) and (3,0,3) eigenstates (with (S_T, S_b, S_w) respectively the total spin of the system, the spin of the "body" ions and the spin of the "wings" ions).

Table 16: Magnetic coupling constants (J), gyromagnetic factor (g) and axial anysotropy (D_{Mn}) of butterfly Mn_4^{III} compounds ($H = \sum_i \sum_j -2JS_iS_j$).

Compound	J_1/J_{bb} (cm^{-1})	J_2 (cm^{-1})	J_3 (cm^{-1})	J_{wb} (cm^{-1})	g	D_{Mn} (cm^{-1})	reference
$[Mn_4O_2(O_2CH_3)_7(bipy)_2]^+$	-47.0			-15.6			[193]
$[Mn_4O_2(O_2C_2H_3)_7(pic)_2]^-$	-49.2			-10.6	1.96	3.7	[194]
$[Mn_4O_2(O_2C_2\phi)_6(dpm)_2]$	-55.0			-0.8		-1.87	[195]
	-77.4	1.6	-1.6	0	1.94	-3.8	[196]
$[Mn_4O_2(O_2C_2H_3)_4(O_3PC_6H_11)_2(phen)_2]$	-65.2			-17.8	2.13	-1.4	[197]
$[Mn_4O_2(O_2C\phi)_4(O_3PC_6H_11)_2(bpy)_2]$	-63.8			-16.2	2.22	-1.5	[197]
$[Mn_4O_2(CH_3PO_3)_2(O_2C_2H_3)_4(bpy)_2]$	-61.02			-15.24	2.18	-0.6084	[198]
$[Mn_4O_2(n\text{-}BuPO_3)_2(O_2C_2H_3)_4(bpy)_2]$	-54.52			-10.42	2.04	-0.58062	[198]
$[Mn_4O_2(O_2CTh)_9EtOH]^-$	-28.4			-9.2	1.99		[199]
$[Mn_4O_2(O_2C\phi)_9H_2O]^-$	-29.0			-9.7			[199]
$[Mn_4O_2(O_2C\phi\text{-}p\text{-}CH_3)_9H_2O]^-$	-28.4			-9.4			[199]
$[Mn_4O_2(O_2C\phi\text{-}3,5\text{-}CH_3)_9]^-$	-31.0			-9.8			[199]
$[Mn_4O_2(4\text{-}CH_3O\phi CO_2)_7(phen)_2]^+$	-45.5	-15.1	-4.4	-9.8	2.01	-3.5	[200]
$[Mn_4O_2(4\text{-}^t Bu\phi CO_2)_6(phen)_2]^{2+}$	-43.0	-14.7	-8.2	-11.4	2.01	-3.6	[200]
$[Mn_4O_2(AntCO_2)_6(bpy)_2(ClO_4)_2]$	-41.0	-10.6	-8.4	-9.5	2.1	-3.7	present work

For compounds that use the J_1, J_2, J_3 notation, J_{wb} is the average value of J_2 and J_3. *Bu: butyl, dpm: dipivaloymethane, pic: picolinate, Th: thiophene.*

Conclusion

In this chapter we presented the synthesis of three Mn compounds with anthracene carboxylate and bipyridine as ligands (see **Figure 45**). On one hand, a 1D coordination Mn^{II} polymer, for which we propose the $[Mn(bpy)(AntCO_2)_2]_n$ formula, and a dinuclear Mn^{II} complex of formula $[\{Mn(bpy)(AntCO_2)\}_2(\mu\text{-}(AntCO_2)_2(\mu\text{-}OH_2)]$, identified with XRD. IR and EPR analysis shows that the equilibrium of this reaction can lead to one or the other compound. This difficulty can be overcome with a micro-wave assisted synthesis to yield $[Mn_2^{II}]$ single crystals or recrystallisation of the chain compound to the same end.
The study of the magnetic properties of the $[Mn_2^{II}]$ complex shows that it presents moderate antiferromagnetism and a weak axial distortion, evidenced in the crystal structure with some compression of the octahedra (J = -4.8 cm^{-1}, D_{Mn} = 0.28 cm^{-1}). The $[Mn^{II}]_n$ compound presents a weak antiferromagnetic behaviour (J = -1.2 cm^{-1}), which is not surprising for a chain type compound.

On the other hand Mn^{III} complexes where synthesised with anthracene carboxylic acid, bipyridine and NBu_4MnO_4 and $Mn(NO_3)_2$ or $Mn(ClO_4)_2$ salts. The comproportionation reaction always leads to a tetranuclear compound. These compounds are very insoluble and hard to crystallise properly so direct XRD resolution could not be performed. We propose for them the following formula $[Mn_4(bpy)_2(AntCO_2)_6X_2]$, with $X = NO_3^-$ or ClO_4^-. The study was focused on the compound prepared with $Mn(ClO_4)_2$, with a combination of techniques: elemental analysis, TGA and the study of magnetic susceptibility.
They strongly suggest that the Mn^{III} adopts a tetranuclear "butterfly" geometry where Mn^{III} ions have a distorted octahedral environment (D_{Mn} = -3.7 cm^{-1}). It is found that a strong antiferromagnetic interaction takes place between the Mn^{III} ions bonded through two oxo-bonds ($J_1 = -41.0$ cm^{-1}) and that more moderate antiferromagnetic interactions exist between the four Mn^{III} linked through one oxo-bond and one, or two, carboxylate bridges ($J_2 = -10.6$

cm^{-1} and $J_3 = -8.4$ cm^{-1}), according to the butterfly model.

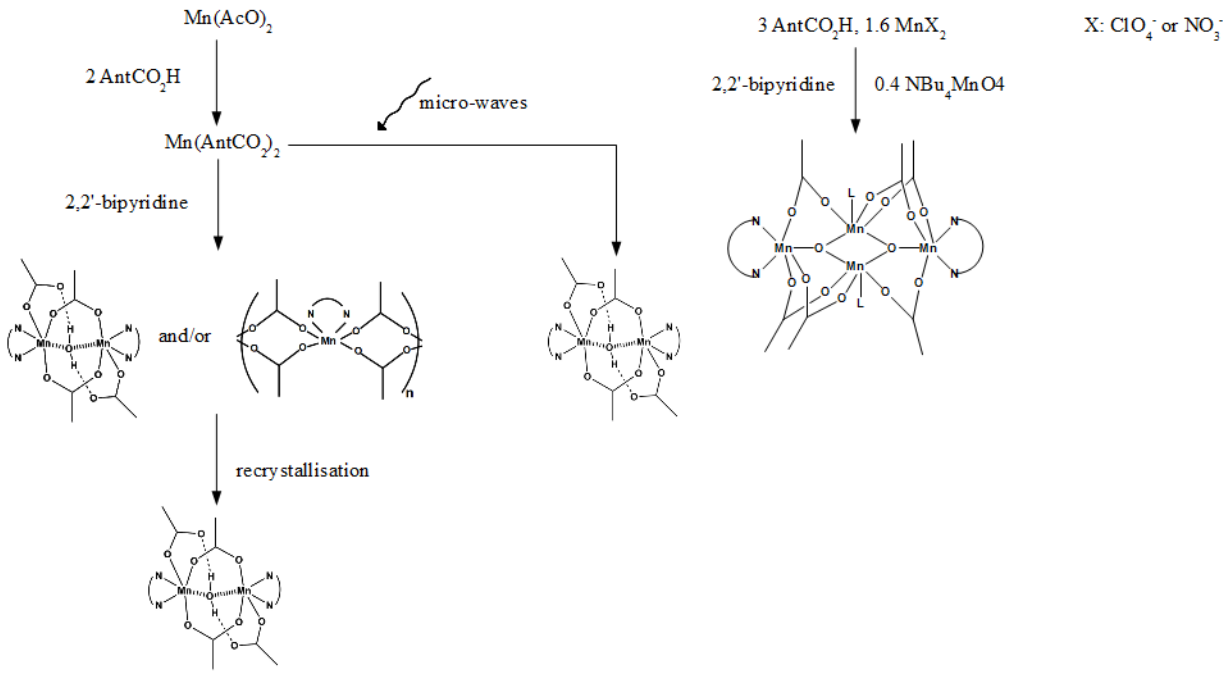

Figure 45: Diagrams displaying the obtention of the complexes mentionned in this paragraph.

I.3 Experimental section

If not precised that the manipulation is performed with a micro-wave apparatus, it is done under arobic conditions. Organic reagents were used as received. NBu_4MnO_4 is prepared as described in literature.[201]

The micro-wave apparatus employed is a Monowave 300 from Anton Paar.

I.3.1 Mn^{II} compounds

Manganese carboxylate

Synthesis of manganese carboxylate ($Mn(AntCO_2)_2$) from manganese carbonate. $MnCO_3$ (2.25 mmol, 0.57 g) and 9-anthracencarboxylic acid (4.50 mmol, 1.0 g) are mixed together in water (50 mL) and stirred for 48h at 60°C. Periodically a few milliters of water are added to keep the volume constant. The final brown solution is filtered and a brown precipitate of manganese carboxylate is obtained.
Yield: 89%. IR (cm^{-1}): 3387 (s), 3348 (s), 3086 (w), 3051 (w), 2924 (w), 2854 (w), 2353 (w), 2337 (w), 1670 (w), 1647 (w), 1624 (w), 1605 (w), 1554 (s), 1535 (s), 1520 (m), 1485 (w), 1443 (s), 1385 (s), 1315 (s), 1277 (m), 1176 (w), 1157 (w), 1014 (w), 1003 (w), 953 (w), 895 (m), 876 (m), 845 (m), 825 (w), 798 (m), 756 (m), 729 (s), 690 (w), 667 (w), 670 (m), 598 (w), 579 (w), 555 (w), 521 (m), 474 (w), 447 (w), 413 (m).

Synthesis of manganese carboxylate ($Mn(AntCO_2)_2$) from manganese acetate. Manganese acetate ($Mn(CH_3COO)_2.4H_2O$) (1.0 mmol, 0.246 g) is mixed in technical ethanol (50 mL) with 9-anthracencarboxylic acid (2.0 mmol, 0.444 g) at room temperature. A white precipitate instantaneously forms. The solution is left to stir 10 min and is then filtered. The resulting white solid is then washed with ether.
Yield: 84%. IR (cm^{-1}): 3587 (s), 3413 (bd), 3084 (w), 3049 (m), 3007 (w), 2941 (w), 2858 (w), 2360 (w), 2341 (w), 1942 (w), 1624 (m), 1576 (s), 1558 (s), 1487 (m), 1444 (s), 1392 (s), 1321 (s), 1279 (m), 1228 (w), 1176 (w), 1155 (w), 1144 (w), 1103 (w), 1047 (w), 1014 (m), 956 (w), 937 (w), 885 (m), 866 (m), 845 (m), 794 (w), 760 (m), 733 (s), 667 (m), 660 (m), 600 (m), 559 (m), 523 (m), 455 (w), 444 (w), 422 (m).

Mn^{II} compounds

Dinuclear compound ($[\{Mn(bpy)(AntCO_2)\}_2(\mu\text{-}(AntCO_2)_2(\mu\text{-}OH_2)]$) or chain ($[Mn(bpy)(AntCO_2)_2]_n$) from manganese carboxylate. Manganese anthracenecarboxylate ($Mn(C_{15}H_9O_2)_2$) (1.0 mmol, 50.0 mg) is mixed with 2,2'-bipyridine (1.0 mmol, 160 mg) in acetonitrile (40 mL) at room temperature. The yellow solution of anthracene carboxylate quickly forms a white precipitate with the addition of bipyridine. The suspension is left to stir for 10 min and filtered. The obtained white precipitate is then washed with ether.
Yield : 47%. IR (cm^{-1}): 3440 (bd), 3078 (w), 3045 (w), 3003 (w), 2966 (w), 2926 (w), 2872 (w), 2852 (w), 1593 (s), 1566 (s), 1489 (m), 1473 (m), 1441 (s), 1394 (s), 1319 (s),

1279 (m), 1246 (w), 1227 (w), 1173 (w), 1155 (m), 1115 (w), 1103 (w), 1061 (w), 1016 (m), 958 (w), 887 (m), 866 (m), 847 (m), 796 (w), 760 (m), 735 (s), 665 (m), 652 (m), 638 (m), 629 (w), 600 (w), 559 (m), 525 (w), 415 (m).

If the chain is obtained from the synthesis above (see EPR), it can be dissolved and crystallised to obtain the dinuclear compound ([{Mn(bpy)($AntCO_2$)}$_2$(μ-($AntCO_2$)$_2$(μ-OH_2)]). The chain is dissolved (0.15 g/L) in acetonitrile in presence of water (100:1 CH_3CN/H_2O mix) for a few days. Yellow polyhedric crystals are obtained.
IR (cm^{-1}): 3444 (bd), 3085 (w), 3043 (w), 2967 (w), 2924 (w), 2855 (w), 1601 (s), 1539 (m), 1486 (w), 1475 (w), 1439 (s), 1394 (s), 1322 (s), 1280 (m), 1244 (w), 1228 (w), 1172 (w), 1155 (w), 1098 (w), 1085 (w), 1052 (w), 1042 (w), 1017 (m), 950 (w), 937 (w), 890 (w), 881 (m), 860 (w), 843 (w), 769 (w), 766 (m), 748 (m), 732 (s), 665 (m), 648 (m), 637 (m), 627 (w), 600 (w), 558 (m), 525 (w), 457 (w), 418 (m).

Dinuclear compound ([{Mn(bpy)($AntCO_2$)}$_2$(μ-($AntCO_2$)$_2$(μ-OH_2)]) from manganese carboxylate, microwave-assisted Manganese carboxylate (Mn($C_{15}H_9O_2$)$_2$) (1.0 mmol, 50.0 mg) is mixed with 2,2'-bipyridine (1.0 mmol, 160 mg) in ethanol (20 mL) at ambient. The solution is heated up to 85°C in 12 min thanks to a micro-wave apparatus, held at 85°C for 2 mn then cooled with compressed air to 65°C then 30°C. After few days dark yellow crystals form.
IR (cm^{-1}) : 3444 (bd), 3082 (w), 3053 (w), 2926 (w), 2852 (w), 1942 (w), 1603 (s), 1566 (s), 1489 (w), 1473 (w), 1439 (s), 1394 (m), 1321 (s), 1279 (m), 1246 (w), 1173 (w), 1155 (w), 1101 (w), 1061 (w), 1043 (w), 1016 (m), 889 (w), 881 (w), 860 (w), 845 (w), 796 (w), 766 (m), 735 (s), 665 (m), 652 (w), 638 (w), 600 (w), 559 (w), 526 (w), 459 (w), 420 (w), 411 (w).

I.3.2 Mn^{III} compounds

Tetranuclear compound with perchlorate [Mn_4(bpy)$_2$($AntCO_2$)$_6$(ClO_4)$_2$] 9-anthracencarboxylic acid (2.89 mmol, 0.44g) is added to a solution containing Mn(ClO_4)$_2$, 4H_2O (1.32 mmol, 0.325 g) in 100 mL of acetonitrile.
On one hand NBu_4MnO_4 (0.32 mmol, 0.12 g) is dissolved in 10 mL of acetonitrile and filtered. On the other hand 2,2-bpyridine (0.83 mmol, 0.13 g) is dissolved in 10 mL of acetonitrile. Both solutions are slowly added to the first one, which immediately turns dark brown. The solution is then stirred for 10 min. It is subsequently filtered and washed with acetonitrile and a black solid is obtained.
Yield : 7%. $C_{110}H_{70}Mn_4N_4O_{18}$,2($ClO_4$). Weight%: C, 65.4; N, 2.8; H, 3.6. IR (cm^{-1}): 3444 (br), 3113 (w), 3082 (w), 3047 (m), 2970 (w), 2924 (w), 2858 (w), 2334 (w), 2029 (w), 1944 (w), 1818 (w), 1624 (w), 1589 (s), 1562 (s), 1497 (s), 1485 (m), 1470 (w), 1446 (m), 1423 (m), 1385 (s), 1319 (s), 1273 (m), 1176 (w), 1157 (w), 1095 (m), 1034 (w), 1014 (w), 960 (w), 933 (w), 891 (m), 864 (w), 848 (w), 798 (w), 764 (m), 733 (s), 675 (m), 663 (m), 633 (m), 598 (m), 559 (w), 521 (w), 501 (m), 440 (m).

Tetranuclear compound with nitrate [$Mn_4(bpy)_2(AntCO_2)_6(NO_3)_2$] 9-anthracencarboxylic acid (2.89 mmol, 0.44g) and $Mn(NO_3)_2$, $4H_2O$ (1.32 mmol, 0.325 g) are mixed together in a solution of CH_3CN (50 mL) warmed at 35°C.
On one hand NBu_4MnO_4 (0.32 mmol, 0.12 g) is dissolved in 10 mL of acetonitrile and filtered. On the other hand 2,2'-bipyridine (0.83 mmol, 0.13 g) is dissolved in 10 mL of acetonitrile. Both solutions are slowly added to the first one, which immediately turns dark brown. The solution is then stirred for 10 min. It is subsequently filtered and washed with acetonitrile and a black solid is obtained.
Yield: 6%. $C_{110}H_{70}Mn_4N_4O_{18}$,2($NO_3$). IR ($cm^{-1}$): 3406 (bd), 3117 (w), 3082 (w), 3051 (m), 2426 (w), 2334 (w), 1944 (w), 1809 (w), 1713 (w), 1624 (w), 1558 (s), 1489 (m), 1470 (w), 1439 (s), 1427 (s), 1385 (s), 1319 (s), 1277 (s), 1230 (w), 1176 (w), 1157 (w), 1107 (w), 1061 (w), 1034 (w), 1014 (m), 957 (w), 937 (w), 891 (m), 868 (w), 849 (m), 825 (w), 798 (w), 764 (m), 733 (s), 702 (w), 663 (m), 636 (m), 598 (w), 563 (w), 521 (m), 505 (m), 440 (w).

I.3.3 Characterisations

Elemental analysis (C, H, N) were carried out at the Centres Científics i Tecnológics de la Universitat de Barcelona (CCiTUB).

Infrared spectra were recorded on KBr pellets with a Thermo Nicolet Avatar 330 FTIR spectrometer.

Thermogravimetric analysis was undertaken with a NETZSCH STA 409 PC Luxx apparatus under air with a increase of temperature of 10 °C/min.

Magnetic susceptibility measurements were performed at the Unitat de Mesures Magnètiques of the Universitat de Barcelona by the Dr. Núria Clos with a magnetometer Quantum Design MPMS XL5 SQUID (Superconducting Quantum Interference Device).

EPR measurements were performed at the Unitat de Mesures Magnètiques of the Universitat de Barcelona by the Dr. Núria Clos with a Bruker ELEXSYS E500 spectrometer with a frequency of 9.4 GHz (X band).

The XRD measurements and resolution were performed by Mercè Font-Bardia at the Unitat de Difracció de RX. Centres Científics i Tecnològics de la Universitat de Barcelona (CCiTUB). See the **Annexes** section for more informations.

Part II

Catalase bio-mimetic materials

This chapter reports the synthesis of the porous nanoparticles used as support for the Mn-catalase mimics and describes the insertion of the compounds inside the materials. First, we need to introduce the techniques that are employed in this chapter for the characterisation of the materials.

II.1 Introductory remarks

II.1.1 ^{29}Si nuclear magnetic resonance (^{29}Si NMR)

The nuclear magnetic resonance (NMR) spectroscopy of ^{29}Si can provide information on the morphology of the silica phases. The relaxing time of the nuclear spin of ^{29}Si is indeed different according the type of atoms that the silicon is bound to. A nomenclature has been established in order to classify the possible environments of silicon in materials (**Figure 46**). Silicon linked to one, two, three or four oxygen atoms are labelled respectively M, D, T, Q. When Si atoms are linked to other Si through the oxygen bound, it is also indicated in this nomenclature. For instance Q^3 indicates that the Si is linked to four oxygens and that three of these are linked to another Si. This is particularly useful to quantify the condensation rate of a material.

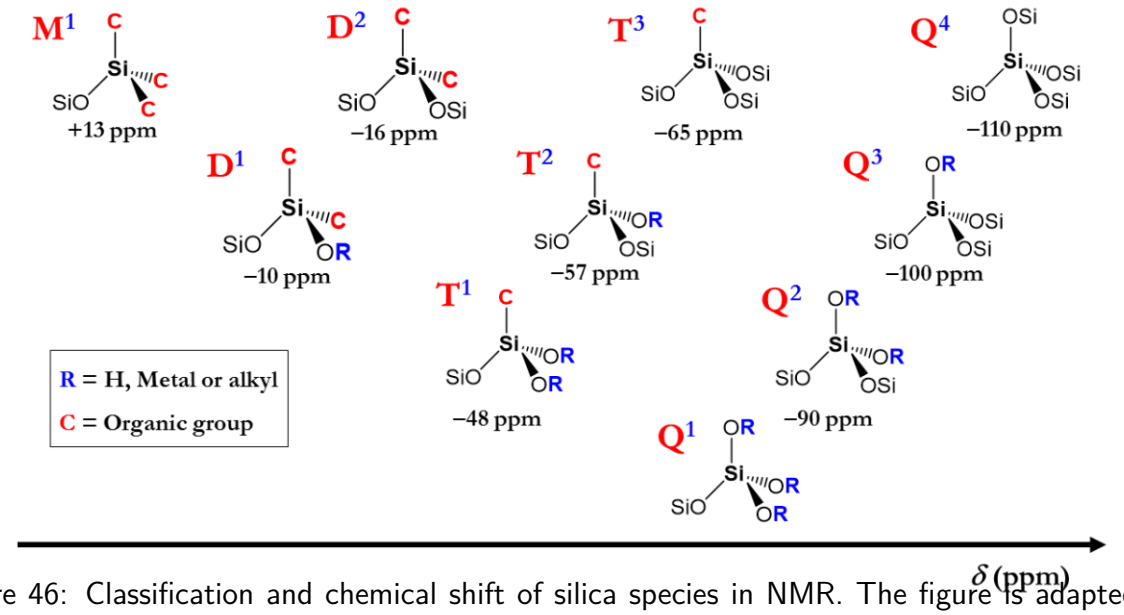

Figure 46: Classification and chemical shift of silica species in NMR. The figure is adapted from the PhD thesis of L.Fang.[202]

With ^{29}Si HPDEC (High Power Decoupled), it is possible to deconvolute the NMR signal to attribute an area to each Si type. In practice, no Q^1 is detected because the probability for a silicate to possess three unreacted silanol groups is very low. For instance, the average $Q^2/Q^3/Q^4$ of a 2D-hexagonal LUS material (MCM-41 type) is 5/45/55 (**Figure 47**).

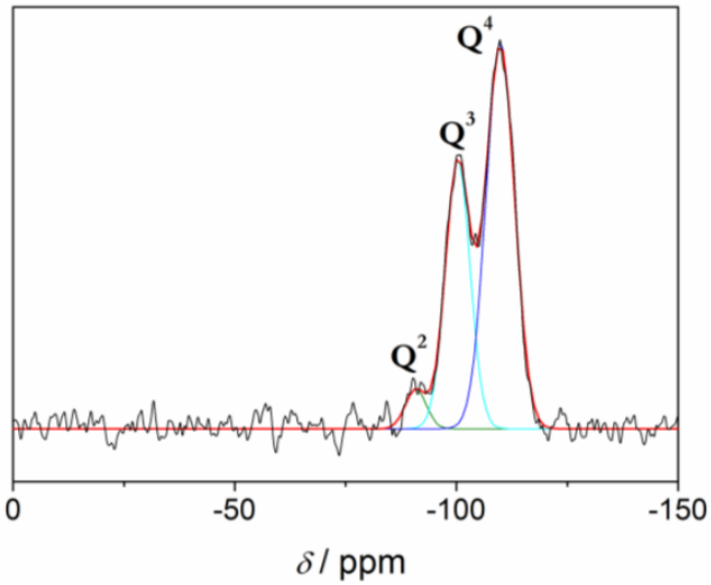

Figure 47: ^{29}Si HPDEC NMR spectrum of LUS silica. Cumulative peak (red line) and deconvolution of Q^4 (blue line), Q^3 (cyan line) and Q^4 (green line). Figure adapted from the PhD thesis of L. Escriche-Tur.[203]

II.1.2 Raman spectroscopy

The Raman spectroscopy techniques relies on inelastic interactions between the photons of an incident beam and the molecular electronic cloud of the sample.
The vast majority of light is normally dissipated by elastic interactions, what is called Rayleigh scattering. But a tiny amount of photons, 1 in every 10^6-10^8 is submitted to inelastic interactions. It is caused by a change of the electronic levels of the molecule due to electric dipole-electric dipole polarisability interactions with the beam. These interactions modify the energy levels of the molecule. They can cause the electron to transition from its ground state to a higher energy level through a virtual energy state. The photon emitted when the electron de-excites from the virtual level to the new energy level is then of lower energy than the one caused by a normal (elastic) transition. It is called a Stokes shift.
On the other hand the modification of the rovibronic level can cause the electron to transition from a higher energy level to its ground state, again through a virtual energy level. In that case, the emitted photon is of higher energy and it is an anti-Stokes shift. The principle of Raman scattering is illustrated **Figure 48**.

As the Raman transition originates from the molecular vibrations that cause the change of polarisability of the electronic cloud, symmetric vibration modes contribute more because they involve the largest distortions. So, the position of the Raman peak is linked to the vibration mode of a chemical group. However, more structural information can be deduced from the Raman spectra. The peak is shifted due to the environment of the vibrating group as the neighbouring dipoles affect the polarisability of the vibration. In addition, the width of a peak is indicative of the crystallinity of the sample. The thinner the peak, the more similar is the environment of the same functions, the more crystalline the sample is.

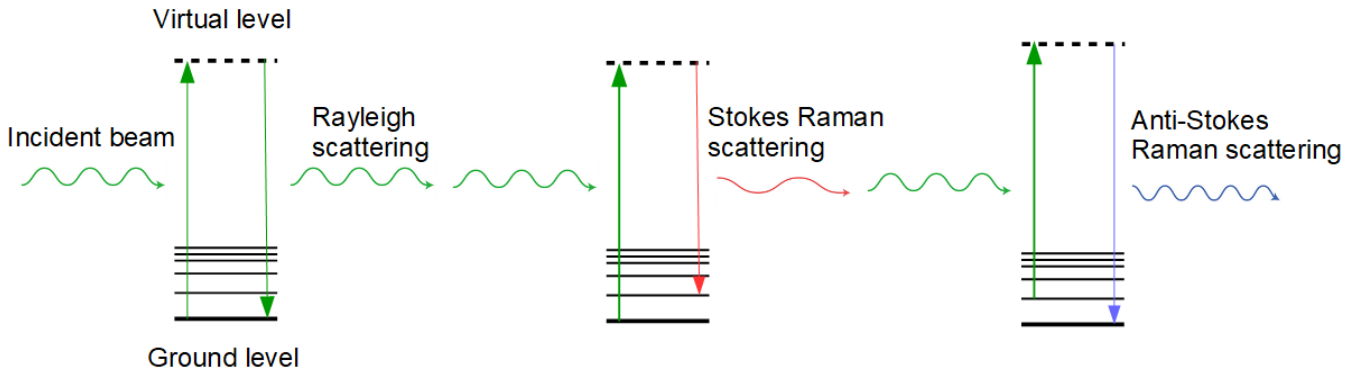

Figure 48: Principle of Raman scattering.

II.1.3 Nitrogen sorbtion isotherms

N_2-sorption isotherms is a technique that relies on the addition of small quantities of liquid nitrogen at 77 K to a sample of material. The N_2-sorption device measures the adsorbed volume of nitrogen (V_a) versus the relative pressure in the sample cell (p/p_0). In order to perform an accurate measurement of the porosity, the sample must be as dry and clean as possible and thus is subject to pre-treatment under vacuum and heat to remove as much solvent or adsorbed humidity as possible (see details in the following sections).

The IUPAC nomenclature states six types of sorption isotherms.[204] In our materials, the recorded isotherms generally correspond to type IV which are characteristic of organised porous materials where the adsorbed N_2 layers form one after the other rather than randomly mixed together.[204,205] **Figure 49** represents a typical type IV isotherm. Usually, five regions are observable : i) a steep slope at low pressure, which corresponds to N_2 filling the micropores; ii) a second more moderate increase, with $p/p_0 \leq 0.3$ attributed to N_2 layers progressively filling the mesopores : the BET adsorption; iii) another steep rise matching capillary condensation, usually around $p/p_0 \simeq 0.35$; iv) it is followed by a plateau with a low slope between $0.4 \leq p/p_0 \leq 0.9$ as the external surface of the particles is covered by a N_2 layer; v) finally a last increase around $p/p_0 = 1.0$ for interparticular or large macropores filling.

It has to be noted that, as most of our particles display a dendritic pore network, the average size of each type of porosity is less well defined than for classical MCM-41 silica or other pore shapes like strawberry or wormhole types.[107] This usually results in a less steep slope for capillary condensation as it occurs gradually in all the porous network.

In order to recover as most information as possible from these measurements, a series of data manipulations are performed, namelly, Brunauer-Emmet-Teller (BET) method, t-plot (thickness) and Barret-Joyner-Halenda (BJH) method, their principles are presented in the following paragraph. Curves obtained from these manipulations are shown in **Figures 50, 51** and **52**.

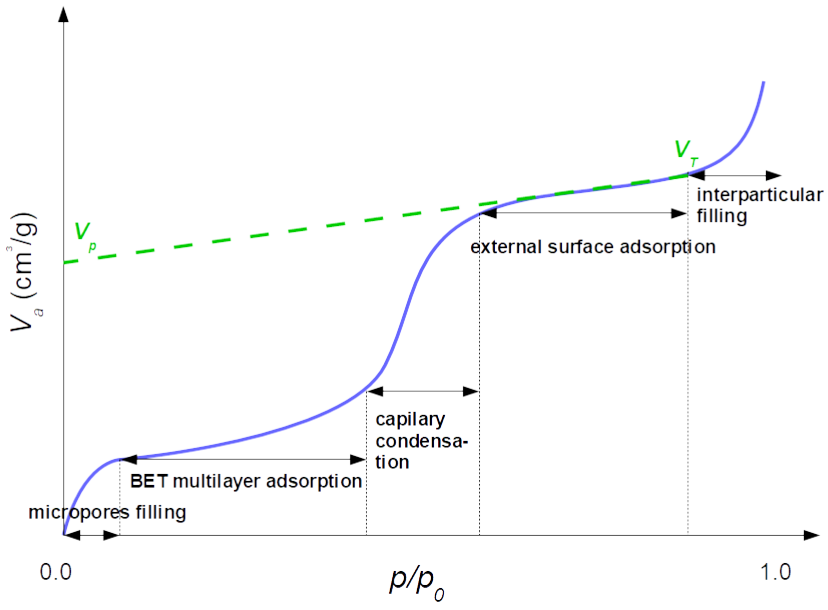

Figure 49: Exemple of a type IV N_2 sorption isotherm.

Brunauer-Emmet-Teller (BET)

The BET method states, according to the Langmuir multilayer adsorption mechanism on which it is based, that gas molecules, by randomly encountering the adsorption sites, progressively form a monolayer followed by a multilayer organisation.[206] BET method is based on five assumptions :

- Adsorption only occurs on well defined sites on the material surface, one per molecule.
- The only molecular interaction considered is adsorption between molecules from two different layers.
- The top layer of molecules is in thermodynamic equilibrium with the gas phase, which implies that adsorption and desorption occur at the same rate.
- The desorption is a kinetically-limited process.
- At the saturation pressure the molecule layers number tend to infinity. The material is then considered to be surrounded by a liquid phase.

The BET equation that is resulting from these assumptions is :

$$\frac{1}{V_a\left(\frac{p}{p_0}\right)-1} = \frac{C-1}{V_m C}\left(\frac{p}{p_0}\right) + \frac{1}{V_m C} \tag{22}$$

where V_m is the volume of a monolayer of gas and C the BET constant (related to energies of adsorption and liquefaction of the gas). Thus, from a linear fit of the BET-plot, C and $a_{S,BET}$ can be deduced (see **Figure 50**) :

$$C = 1 + \frac{a}{I} \tag{23}$$

where a and I are, respectively, the slope and the intercept value of the linear fit.

$$a_{S,BET} = \frac{V_m N s}{V_{M,gas} m_{sample}} \tag{24}$$

where N is the Avogadro number, s, the adsorption cross section of the adsorbing species, $V_{M,gas}$, the molar volume of the adsorbed gas and m_{sample}, the mass of the sample.

C value reported later in this part as C_{BET} is a measure of the affinity of the adsorbed gas for the material. The higher it is, the stronger is the affinity between the gas and the sample. This calculus does not, however, make a distinction between different types of porosity, inner and exterior volume. V_a, V_t and $a_{S,BET}$ are average values, hence the use of the t-plot calculation.

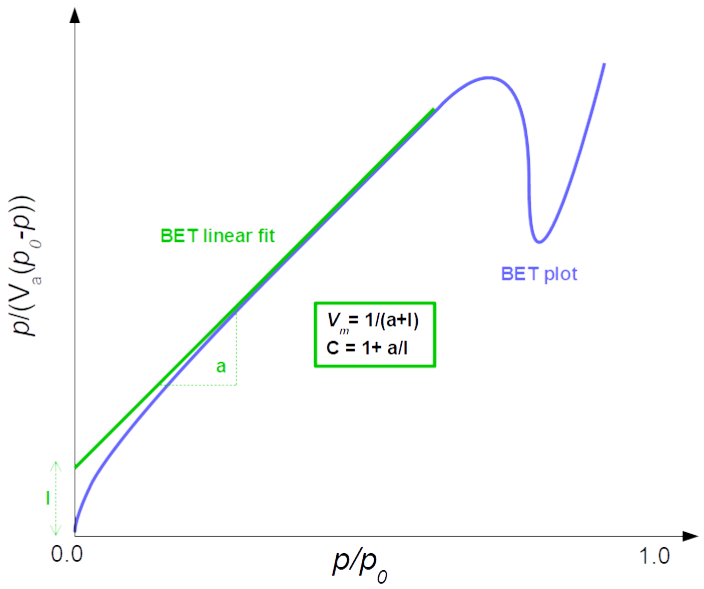

Figure 50: Exemple of a BET curve and its linear fit.

t-plot

The t-plot represents the adsorbed volume (V_a) versus the thickness of a gas layer.[207,208] The statistical thickness of a sample, t_s is given by the following equation :

$$t_s = 0.354 \frac{V_a}{V_m} \tag{25}$$

The value of 0.354 comes directly from the assumption that N_2 molecules adsorbed on the sample's surface form a close packed hexagonal network, and has to be adapted for other gases.

The t value is derivated from sorption isotherms of reference samples with a close C value and its general form is:

$$t = a \left(\frac{1}{ln\left(\frac{p}{p_0}\right)} \right)^{1/b} \tag{26}$$

Where a is a factor of the packing value ($a = 5 \times 0.354$ for N_2) and b depends of the nature of the sample.

The deviations between the experimental curve and the theoretical one give informations on the behaviour of the sample at various pressures. According to this, the deviation between the linear fit and the curve for $t \leq 0.5$ nm gives the internal surface (a_{int}) and the volume of the micropores (V_{micro}). Whereas the external surface(a_{ext}) and the volume of the mesopores (V_{meso}) are found for $t \geq 1$ nm.

Typically, for the materials presented in this work, which are synthesised from a Stöber-like process,[62] the microporosity is not well-defined. It usually comes from the mark left by the silica oligomers when condensating around the positively charged ammonium head of the surfactant. It corresponds, therefore, more to rough spots left by the specific cation chosen for the synthesis.

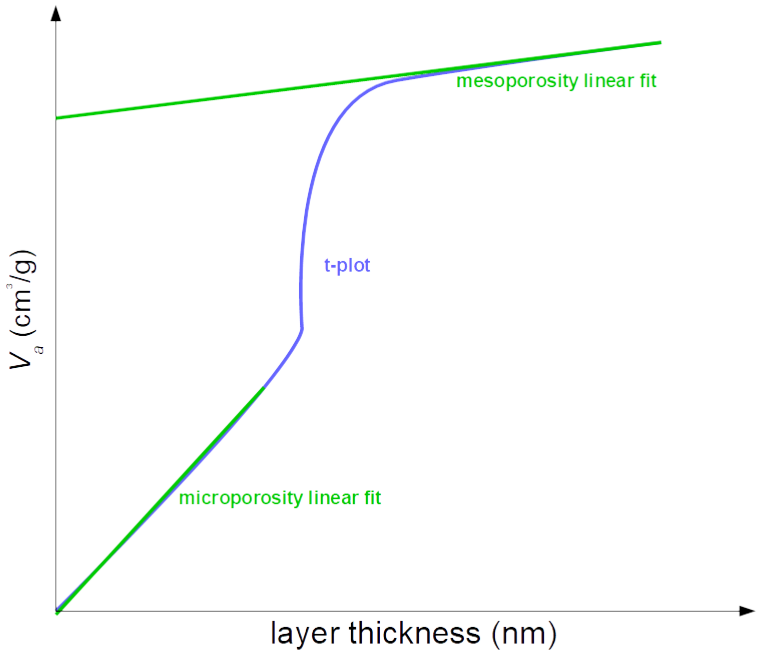

Figure 51: Exemple of a t-plot and its linear fits.

Barret-Joyner-Halenda (BJH)

In most mesoporous materials, the shape, pressure range and hysteresis type of the sorption isotherms around the capillary condensation step give a lot of information on the porosity type of the sample.[209,210] A narrow range of pressure indicates an homogeneous network with a well defined pore size. On the other hand, a flatter slope is characteristic of a wider distribution of diameters, which can be found in materials with open channels or dendritic networks.
When both adsorption and desorption curves are ploted on the same graph an hysteresis loop might be observed, depending on the material. The IUPAC classifies them in four categories that are related to various origins.[204] The hysterisis loop may be caused in materials with a very narrow and well defined pore size to the instability of nitrogen meniscus.[211] In less uniform materials it can be due to the defects provided by the interconnectivity between chambers or channels. Finally in materials with more flexibility, the hysteresis might originate from variations of the structure due to the pressure.

The BJH method is based on the step by step analysis of the hysteresis loop during capillary condensation.[205,212] As such it is designed, and the most accurate, for type IV isotherms.
This method is based on the following assumptions :

- The porous texture is supposed to be rigid and made of independent and well defined mesopores.
- The mesopore wall where the multimolecular adsorption takes place, is considered a plane surface.
- The Kelvin law, which describes liquid-vapor interface equilibrium, is supposed to be adapted to the cavity.
- The condensation takes place when the mesopores are already covered with a multilayer molecular film.
- The adsorbant material is supposed to be perfectly wet (contact angle of adsorbed gas is zero).

These assumptions alone, should make us wary about the results of this method for most of the materials studied in this work. Firstly, most of the particles are based on a stellar pore network, which are, by construction, interconnected. Secondly, the polyphenol that constitutes the organic part of the hybrid nanoparticles is a flexible material. As a consequence, in some of the following BJH calculus, some pore radius have not managed to be properly evaluated. A rule of thumb employed to evaluate the meaningfulness of the method is to compare the cumulative surface calculated with BJH, a_c, and the BET surface, $a_{S,BET}$, and see if their ratio is inferior to 10%.

For the BJH method, the desorption branch is often the one commented, as the transition between gaseous N_2 and condensed N_2 is easier to spot. At the relative pressure for which the saturation plateau is observed all the mesopores are considered to be filled. For points between this equilibrium pressure, the difference between the p_{n-1} and p_n points is coming from the evaporation of the condensed N_2 inside the pores and the reduction of the thickness

of the multimolecular layer. The obtained curve, is the derivative of the porous volume towards the average radius of the pores radius (dV_p/dr_p) versus the pores size (r_p) commonly represented in logarithmic scale.
The average pore size is attributed to the radius value of the maximum of the distribution, $\frac{dV_p}{dr_p}_{\max}$, and the minimum and the maximum pore size to the values obtained at $\left(\frac{dV_p}{dr_p}_{\max}\right)/2$.

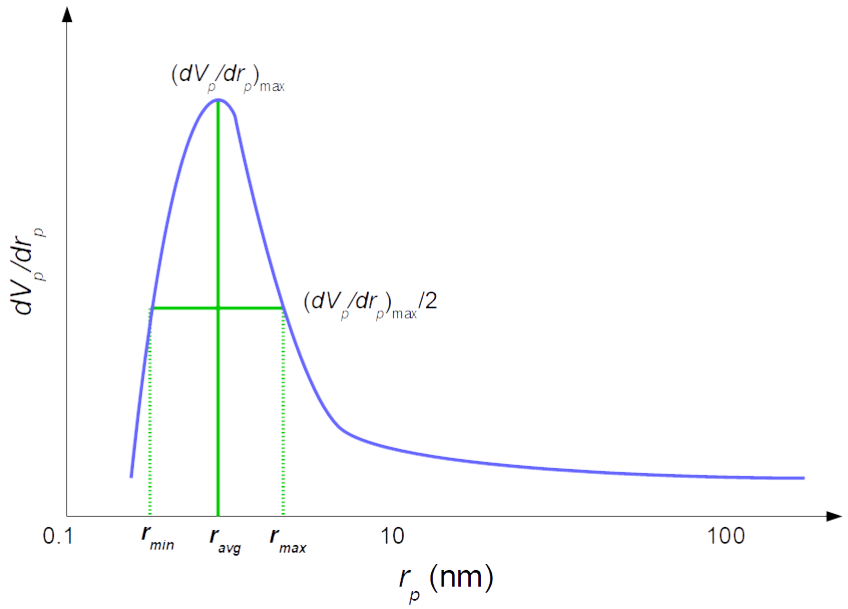

Figure 52: Exemple of a BJH plot.

Other methods can be employed to describe pore size, such as the Broekhoff and De Boer (BdB) and Horvàth-Kawazoe (HK) methods but they are even less adapted to our materials. Moreover, the BJH method is the most common and can be used for comparisons with other works.

II.1.4 Electronic Microscopy

Scanning Electron Microscopy (SEM)

Scanning Electron Microscopy is the most common and accessible type of electronic microscopy. As for other electronic microscopies it relies on a beam of electron focused with a series of magnetic lenses (magnets). The electron beam then interacts with the studied sample and different types of electrons are collected with detectors, and enables a reconstructed image of the sample.[213]
As the free path time of the electron is rather limited in air, electronic microscopy requires a moderate to high vacuum inside the apparatus (10^{-6} to 10^{-10} Pa) to allow a maximum of electrons to hit the sample and provide an accurate image. The energy of the beam can be tuned and might allow the electrons to penetrate the sample thickness for a few nanometres. As such, it is always important to keep in mind that the observed image is a reconstructed

one, which combines the features of the surface of the sample as well as a thin layer of its interior.

A variety of signals can be observed with a SEM provided the presence of adapted detectors. They are usually, secondary electrons (SE), back-scattered electron (BS), Auger electrons (AE), X-rays and light cathodoluminescence (CL). These emissions are coming from a series of elastic or inelastic interactions between the electron beam and the sample. For this study, the main detector used is for SE. Secondary electrons are electrons produced by the ionization of the sample and are emitted from a close range of the sample surface. As such they can provide an image with a good resolution (up to 0.5 nm for high resolution SEM).

The preparation of the samples is very simple. The nanoparticles are dispersed in water or ethanol through sonication at differenct concentrations regarding the aim of the observation (single particle, layers or aggregates). A drop of this suspension (approximately 20 μL is then sat down on a support, a copper sticky band or a silicium wafer and left to evaporate in a clean environment.

Transmission Electron Microscopy (TEM)

The second electron microscopy technique employed in this work is the Transmission Electron Microscopy (TEM). TEM relies on the same principles than SEM but uses a different position for the electron source and electrons themselves are usually of higher energy.
The TEM would be the equivalent of traditional optical transmission microscopes, with the light source placed below the sample and the detector, above, on the other side (but it is usually the opposite for TEM as the detector is not the eye of the operator). The detector collects the light transmitted through the sample which enables to observe the sample in transparency and have information on its composition, given the different absorption of different areas. The principle is the same with TEM except than the source is an electron beam and their energy can be adapted to lower wavelength in order to have a better resolution than visible light. Again the image obtained is a reconstructed one, gathered with the electron that were able to pass through the sample. In order for the electrons to be transmitted, the sample preparation generally requires special grids, with less than 100 nm thickness, as support. The best high-resolution TEM with suitable aberration-correction mechanism and high energy electrons (200 keV) can reach nowadays up to 50 pm resolution.[214] Though most of the ones used for routine imaging have roughly 0.5 nm resolution. **Figure 53** presents the scheme of the different microscopes mentionned in these two paragraphs.

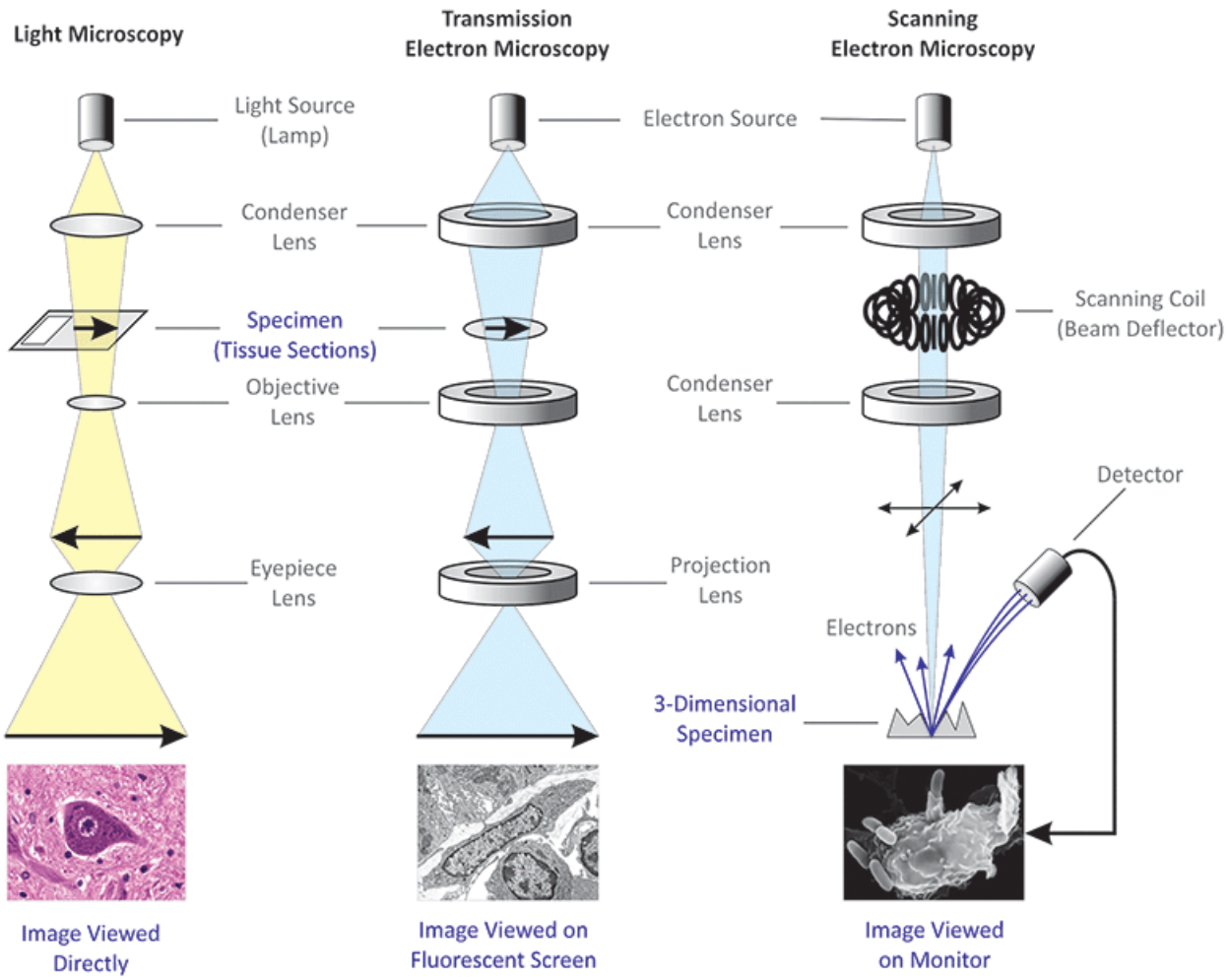

Figure 53: Light and electron microscope types. Image taken from microbiologyinfo.com website.[215]

Energy-dispersive X-ray Spectroscopy (EDS)

With an electron source of tunable energy and high precision detectors, the electron microscope can be equipped to fill another task: spectroscopical mapping of the sample. This technique called energy-dispersive X-ray spectroscopy (EDS) relies on the detection of the X-rays emitted during the interaction of the incident electron and the atoms of the studied material. An electron of the inner shell is expelled by the energy of the incident electron and the subsequent rearrangement of the electronic layers causes an X-ray emission.
The interest of the method is that the X-rays emitted by different atoms have quantified energy linked to the discrete levels of its electronic layers and, as such, provide information on its chemical composition. The X-ray range corresponds to high energy electrons belonging to the inner electronic layers of the atoms, as a consequence, this technique is very sensitive to the electronic density of the targeted atoms. That is why, for instance, that in the following section, the precision on the amount of Mn inserted inside the particles is more important than for N, even if they are present in comparable quantities.

II.1.5 Atomic Force Microscopy (AFM)

Atomic Force Microscopy (AFM) is another imaging method employed to overcome the visible light resolution frontier. An AFM is made of a cantilever ended by a sharp tip, the thickness of the latter directly dictates the resolution of the image, so its peak is usually a few nanometers or less. This cantilever is bound to an oscillator and capped with a small mirror. When the AFM is running the tip oscillates, probing the surface of the sample as it scans it (**Figure 54**); a wide variety of oscillation modes can be used depending on the sample type and the information desired. A laser beam is focused on the mirror on the top of the cantilever and the deviation angle of the reflected beam is measured by a detector. The AFM image is then reconstructed from the oscillation of this beam.
The AFM is a relatively simple technique, it only requires sharp and clean tips and good optics but no vacuum system or complex sample preparation as it is sometimes required for electronic microscopy, and it is very versatile. By choosing an adapted cantilever (Young modulus and length) and tip (length, sharpness and hardness) , it is possible to perform imaging on wide variety of sample types and media from classic organic or inorganic materials to biological samples *in-vivo* or liquid ones.
Traditionally, two main information are studied, the topological aspect of the surface and its mechanical properties. They are extracted from phase-contrast imaging and linked to the mechanical response of the tip when it enters in contact with the sample. This mechanical properties mapping was our focus when we performed AFM on the hybrid silica-resol nanoparticles, as one of the phases is hard (the silica) and the other soft (the resol polymer). But these studies are only the most common ones, specific AFM can be designed to map other properties of the sample: the magnetic answer (with a magnetic tip), the thermal conductivity (with a heated tip) or the chemical functions (by recording the oscillation of the atomic bonds, similar to IR spectroscopy).

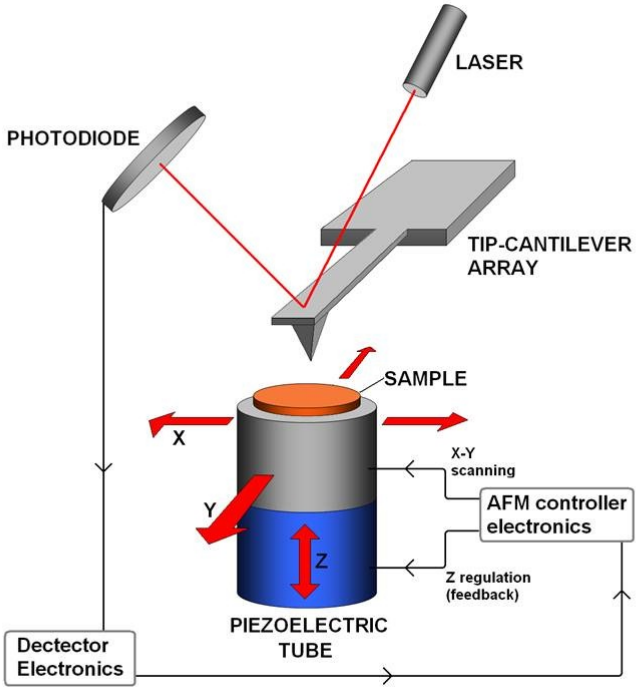

Figure 54: Atomic Force Microscope scheme

II.2 Hybrid Mesoporous Nanoparticles

II.2.1 Synthesis of mesoporous nanoparticles : resol-SiO_2, C-SiO_2 and SiO_2 nanoparticles

The strategy employed here is to use the triphasic syntaxic approach developed by K. Zhang and coworkers[144] to create hybrid silica-resorcinol nanoparticles. The point of this method is that by employing a one-pot synthesis, the obtained material can be further thermally treated to yield different NPs types with similar porosity. As such it is an interesting method to compare the behaviour of the inserted [Mn] compounds within different materials.
The syntaxic approach relies on complex interactions between three phases, namely, the silica anionic tetrahedra (I^-), the positively charged micelles (S^+) and the anionic polyphenolates (O^-). In order to obtain an homogeneous dendritic system for the two hard phases, mastering the kinetics of the reaction is a priority. The two main factors that influence the condensation rate of the materials are their concentration and the pH of the suspension.

In classic basic conditions, around pH = 10, the condensation rate of the polyphenol is inferior to the one of the silica and leads to non-porous resol spheres coated with a silica shell.[144] At neutral pH, the opposite happens and the two phases condense in separate aggregates. However, when the conditions are carefully tuned, around pH = 8, both condensation reactions happen at the same rate, leading to a cooperative growth system, the syntaxy. In these conditions, both silica tetrahedrons and polyphenolic anions are adsorbed on the surface of the micelles and develop their network at the same time. During these nucleation and growth steps, the two phases have to interact constantly with each other, thus leading to two porous phases which are the negative of each other.[144] **Figure 55** sums up the principles of this synthesis.

The various types of mesoporous nanoparticles, resol-SiO_2 (RSMNPs), C-SiO_2 (CSMNPs) and SiO_2 (SMNPs), were synthesized according to the method reported by Zhang and coworkers in *Chem Eur. J.* 2018.[144] Cetyltrimethylammonium bromide (CTAB) is the micellar templating agent, triethanolamine (TEA) is used to adjust the pH in ideal weakly basic conditions and is responsible for the porosity type[107] , here qualified as "stellate". Tetraethoxysilane (TEOS) is the silica source and resorcinol (1,3-dihydroxybenzene) and formaldehyde (methanal) are the two precursors of the resol (also called resorcinol-formaldehyde resin) network. Ethanol is used, in addition to water, as a co-solvent for kinetical and thermodynamical purposes. It slows down the polymerisation speed of the resin, which is crucial for the syntaxy to happen, and alters the superficial tension of the micelles in order to control the NPs diameter.[139]

After this, the obtained hybrid resol-silica nanoparticles can be thermically treated to obtain pure mesoporous silica nanoparticles or hybrid carbon-silica nanoparticles. SMNPs require a calcination in air at 550 °C to remove the organic part. Whereas CSMNPs are carbonized under N_2 atmosphere at 900 °C in order to decompose the organic part in carbon without degradation in CO_2.

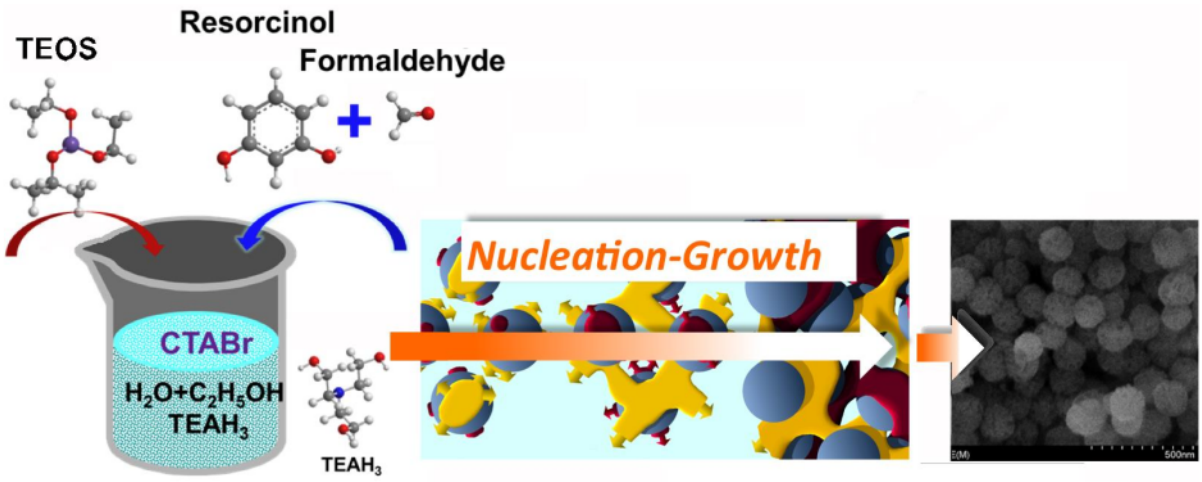

(a)

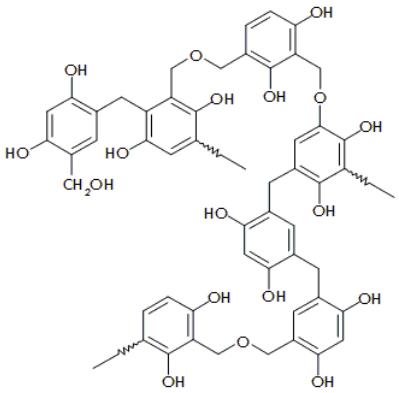

(b)

Figure 55: (a) Schematic representation of the synthesis of RSMNPs. (b) Strucutre of resorcinol-formaldehyde resin *i. e.* resol.

Attempts to modify the RSMNPs synthesis

These hybrid resol-silica nanoparticles present, however, colloidal stability issue. Their synthesis requires high concentrations of precursor in the media which makes it very productive and adapted in terms of scale up potential. But this important concentration of particles invariably leads to their aggregation and precipitation.
It is possible to achieve more stable suspensions by dispersing the particles in aqueous solution and to submit them to a strong sonication (tens of minutes length with a high intensity). However, our first approach consisted to achieve direct colloidal stability by working with a more dilute suspension from the beginning and to use soft methods to remove the surfactant without provoking the aggregation.
Given that size and morphology of the particles is strongly dependant on concentration and pH factors, a simple dilution of the precursors does not lead to a more diluted solution of similar particles but to entirely different particles with a wider range of diameter and, most likely, a different morphology.

To overcome this problem, a different synthesis type was considered. It is an adaptation of Zhang's work on the hybrid nanoparticle presented earlier with the contribution of Yamamoto and coworkers in *Chem. Mater.* 2014 on mesoporous silica nanoparticles synthesis.[216] They present a synthesis that is highly reproducible, forms mesoporous nanoparticles of tunable diameter (from 40 to 160 nm) and insures colloidal stability.[216]
The principle of the modified synthesis is exactly the same than the one of Zhang *et al.* except than the amounts of precursor were decreased and the amount of surfactant increased. The colour of the suspension indicated the successful condensation of resorcinol, with the rise of the distinctive terracotta colour of resol, while it showed both translucency due to the lower concentration of particles and Tyndall effect. The result is a suspension of 70 nm diameter homogeneously dispersed spheres, which was measured with dynamic light scattering (DLS) and electronic microscopy (SEM and TEM) (**Figure 56**). As, at this point, the concentration of surfactant is important, the suspension can maintain colloidal stability for months.

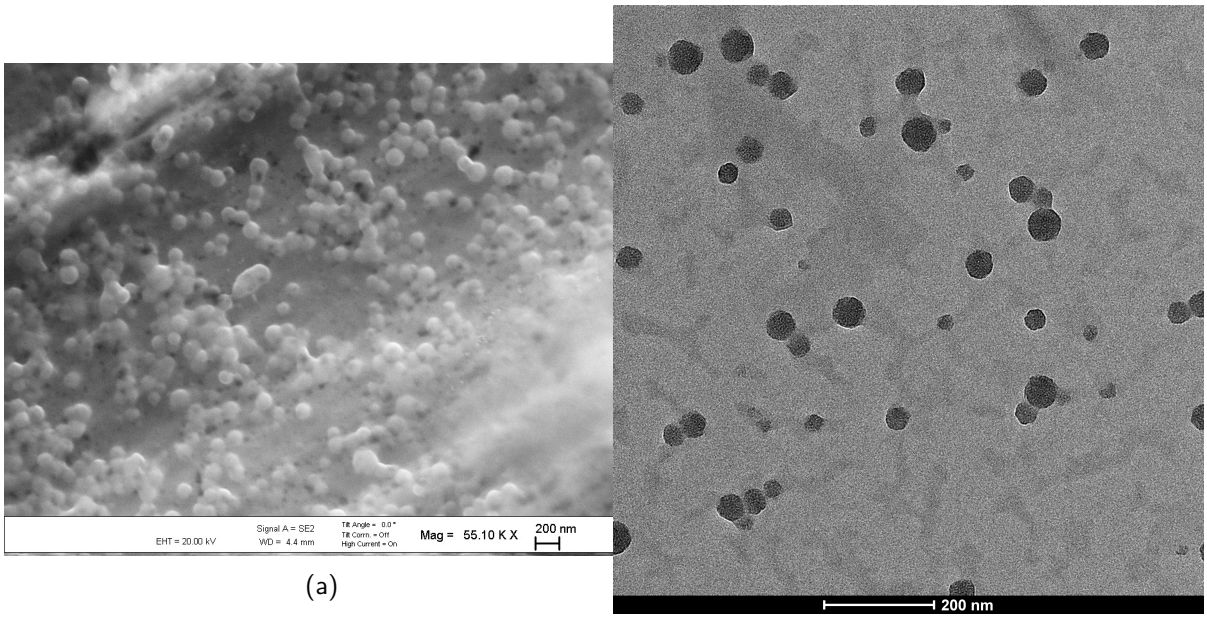

(a) (b)

Figure 56: (a) SEM picture of the RSMNPs from modified synthesis before surfactant removal. (b) TEM picture of the same particles.

In order to exploit this result, it is needed to extract the surfactant without provoking the aggregation of the nanoparticles. This forbids traditionnal treatments like simple powder wash. Unfortunately, despite some work on mesoporous resol material and even the synthesis of nanoparticles containing this material,[139] colloidal stability of such systems was, as far as we know, never considered. They are indeed usually employed as capacitor material, which requires its deposition.
At first, an attempt was considered with the use of double-ion resins to exchange the surfactant, as Yamamoto and colleagues mention its use in their work on silica NPs.[216] Regrettably, the resin specified (the Amberlite MB-1 from Dow) is not produced any more. We tried to achieve the same result with two resins (one anionic and one cationic) instead of the double-ion one but these attempts remained unsuccessful.

The alternative (that is actually also used by Yamamoto) is the use of more traditional dialysis systems. Multiple dialysis conditions were tested, with different exchange solvents and pH but invariably lead to the same result: the aggregation of the hybrid nanoparticles into flakes. SEM of these aggregates gave no significant result to understand the phenomenon, only showing nanospheres stacks. However, the use of AFM on dilute dispersed samples had more interesting results. The reconstructed images (from force-curve mode) enable to see the mechanical answer of the material. They exhibit contrast between the hard silica phase and the soft resin. These images show that the polymer form filament balls around silica particles. The resin filaments entanglement leads to the formation of irreversible aggregates (**Figure 57**).

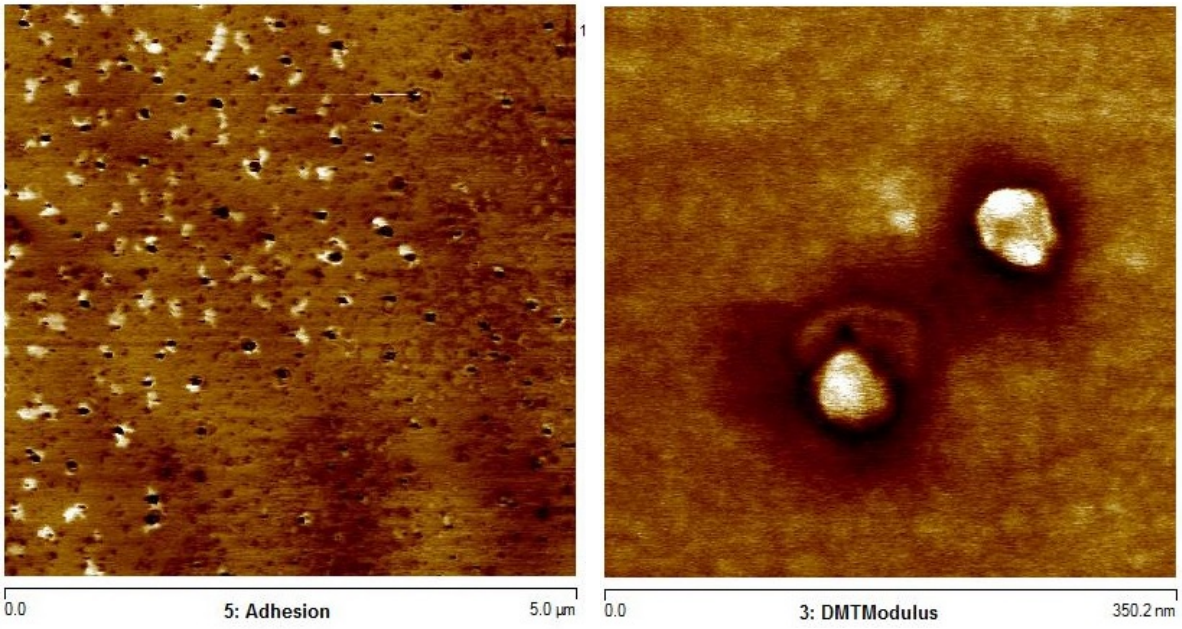

(a) (b)

Figure 57: AFM picture of the RSMNPs from modified synthesis after surfactant removal. (a) adhesion imaging mode and (b) Derjaguin-Muller-Toporov (DMT) imaging mode corresponding to Young modulus response. The two images contrast are the reverse of each other.

The amount of AFM images collected is insufficient to make some statistics on this structure. But the silica core appears roughly the size of the original particles measured with DLS, prior to the dialysis. Which would mean that the resin loses its structure and is dragged out of the particles at the same time than the surfactant, during the dialysis. This might be due to a partial condensation of the resorcinol. Indeed, the observation of porosity on Zhang's nanoparticles can only be made in specific conditions: after acidic powder washing and overnight drying of this acid solvent. This acidic treatment is originally designed to protonate phenols and silanols in order to disrupt their interaction with CTA^- and facilitate its extraction. However, as condensation conditions of the resorcinol are similar to silica and actually catalysed in acidic media, this step could be decisive for the strengthening of the resol branched network. In addition, unpublished tests have been run by Zhang's team in order to remove the silica by HF etching, after the end of the NPs synthesis and it leads to a loss of porosity in the material. These tests mean that silica has a significant role to play on

the structure of its sister phase. Thus, resol is still, after formation, susceptible to mechanical stress and the surfactant extraction method seems decisive to maintain the mesorporous structure.
Given, the time restrictions of this project, it was decided to come back to Zhang's original nanoparticle design and to count on methods like sonication or freeze-drying to ensure the nanoparticles redispersion in solution.

II.2.2 Characterisation of the materials

Infrared spectra of the different materials synthesised after Zhang's and coworker method[144] are shown in **Figure 58**. In all particles types the bands characteristic of silica are clearly visible.
Firstly, two bands that can be attributed to stretching modes : the wide intense band between 1240 and 1040 cm^{-1} of Si-O-Si and a moderate band at 970 cm^{-1} for silanols. Secondly, two less intense bands at 800 cm^{-1} and 465 cm^{-1} which are respectively bending and rocking modes of Si-O-Si bonds. Between 1620 and 1640 cm^{-1} the bending mode of molecular H_2O shows that water quickly adsorbs in the particle's cavity even in dried material.
In hybrid resole-silica NPs, a series of more structured bands appears in the 1345-1550 cm^{-1} range. They match aromatic sp^2 C=C bonds vibrations and the C-O stretching mode of the polyphenolic network. Also, not represented in this graph, but in the 2930-2855 cm^{-1} area, two small bands representative of the C_{sp^2}-H and C_{sp^3}-H stretching modes are characteristic of the CTA^+ surfactant. It shows that even after several acid washings a small part of the templating agent remains inside the material.
Finally, in carbon-silica NPs, the bands of the resol polymer are replaced by a wider and less intense band between 1500 and 1670 cm^{-1} due to the stretching mode of sp^2 C=C bonds. Water contribution to the spectrum (bands at 3500 and 1800 cm^{-1}) is much smaller.

The Raman spectroscopy of CSMNPs was also performed (**Figure 59**). It shows the three characteristic bands of graphitised materials. The G band at 1600 cm^{-1} corresponds to the in-plane vibrations of graphene, the stretching of C_{sp^2}=C_{sp^2} bonds. The D band at 1330 cm^{-1} is attributed to structural defects in the graphene layers that disrupt the normal stretching mode. In our case in can be attributed to the presence graphite-oxyde due to the non-total decomposition of the resol base material. Finally the G' (or $2D$) band at 2800 cm^{-1} results from a two-phonon resonance phenomenon that occurs between the graphene sheets. The graphitisation rate of our material can be evaluated by comparing the intensity ratio between D and G bands to the one of pure graphite material. We find that $\frac{I_D}{I_G} = 0.85$ compared to 0.16 for pure graphite.[217,218] This value is well in the range of other graphite oxide materials.[217,218]

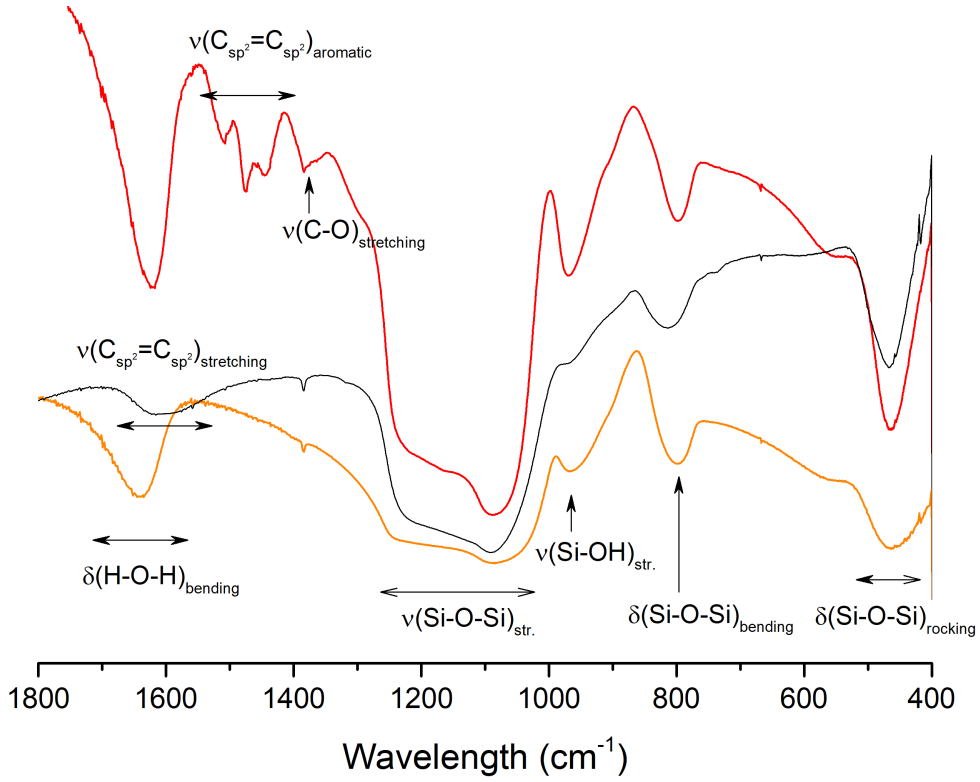

Figure 58: Infrared spectra of mesoporous silica nanoparticles (SMNPs) (orange line), mesoporous resole-silica nanoparticles (RSMNPs) (red line) and mesoporous carbon-silica nanoparticles (CSMNPs) (black line).

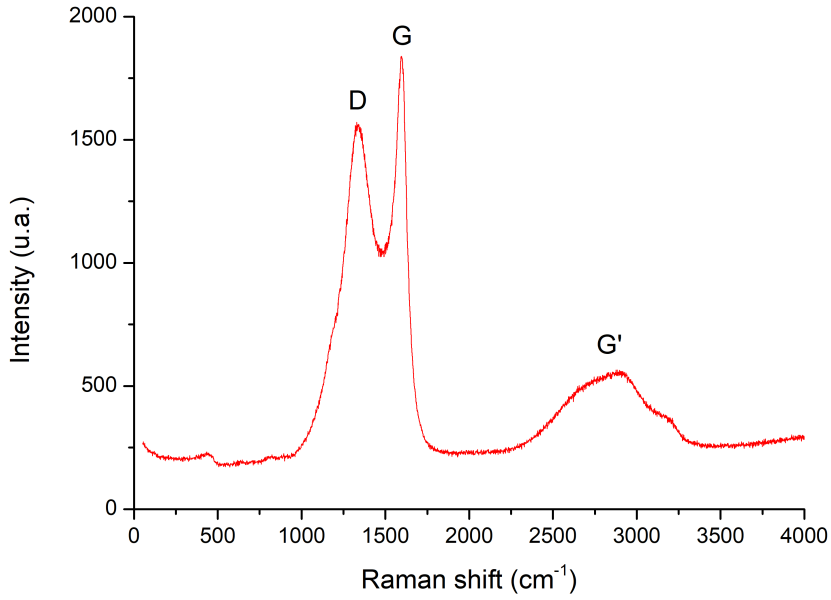

Figure 59: Raman spectrum of CSMNPs.Excitation wavelength: $\lambda = 532$ nm.

The ^{29}Si NMR spectra shows (Figure **??**) that the initial material prepared (RSMNPs) presents a large amount of Q^3 and Q^4 silica (respectively at -100 and -110 ppm) along with a small quantity of Q^2 silica (-90 ppm). A fit with multiple gaussian curves (see section **II.1.1**) of the HPDEC NMR spectrum of RSMNPs gives us a 10.7/60.9/28.4 ratio for $Q^2/Q^3/Q^4$. It shows that the silica phase is not fully condensed after the initial synthesis. When the particles are submitted to thermal treatments to yield SMNPs and CSMNPs we can see that the Q^3 peak contribution to the signal is greatly diminished and that only the Q^4 peak is clearly visible. This is due to the condensation of surface silanols to SiO_2 that occurs at high temperature. Unfortunately we lack exploitable HPDEC spectra to quantify $Q^2/Q^3/Q^4$ on thermically treated NPs in order to compare them with RSMNPs.

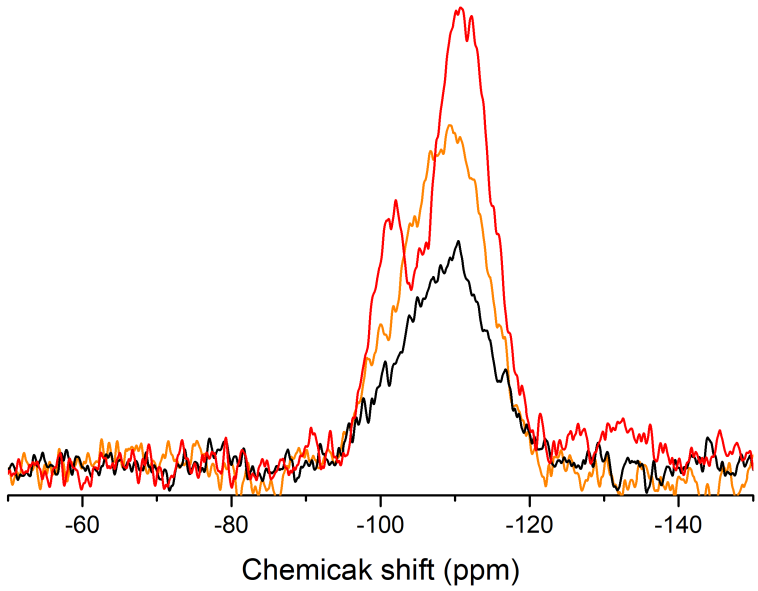

Figure 60: ^{29}Si NMR spectra of RSMNPs (red), SMNPs (orange) and CSMNPs (black).

^{13}C NMR was also performed, both on RSMNPs and CSMNPs. The attribution of the band peaks was made after Werstler's analysis[219] and Zhang's interpretation.[144] The spectra closely match the ones presented by Zhang and coworkers. The peak at 152, 131 and 104 ppm are attributed to phenolic carbons **a**, **b** in meta, and **c** respectively (see **Figure 61**). **a** et **c** are equivalent on the formula of the monomer and contribute to the same signal after decoupling. However, the spectrum of the polymer in RSMNPs (red line) cannot be the same. If one of the OH is involved in a C-C coupling in the polymer, as it should occur, **a** and **c** are different like in the dimer represented on the right. The massif of peaks in the region 10 to 30 ppm are alkyl -**C**H_2-. The peaks at 54 and 66 ppm are assigned to aromatic -**C**H_2OH and **C**H_2-CH_2OH respectively. The peak at 120 ppm is attributed to the aromatic carbon in ortho position bearing the CH_2 introduced during condensation. **c'** and **d'**are not equivalent in the polymer but the signal is not resolved.
The spectrum of CSMNPs is not very different from RSMNPs, which suggests that the structure of the polymer is not greatly modified by thermal treatment under N_2 atmosphere. The -**C**H_2- signal left on the calcined CSMNPs is at 12-13 ppm and corresponds to the bridge between the aryl groups on the rigth of **c'** on the dimer. The disappearance of the peak at

66 ppm is due to the degradation of Si-OEt during the calcination and reveals that no Si-C peak is present at 64 ppm, showing that the silica and carbon phase share no bonds.

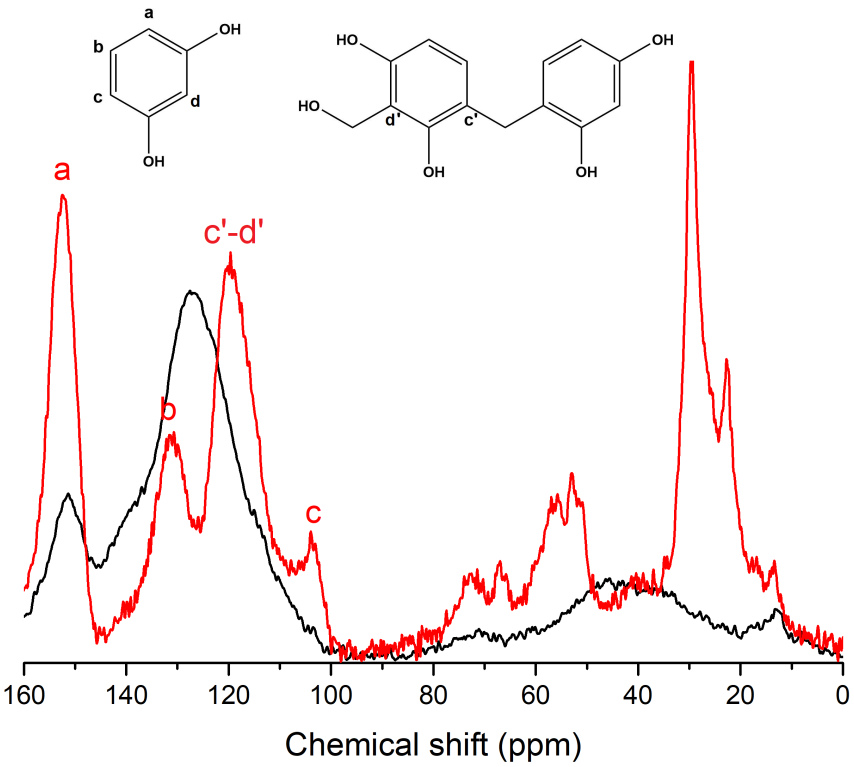

Figure 61: ^{13}C NMR spectra of RSMNPs (red) and CSMNPs (black), with matching carbon attributions.

TGA analysis is a simple and useful tool to observe the composition of the material (**Figure 62**). The first part of all TGA spectra of materials contains a first mass loss below 180 °C, it is simply attributed to solvent or humidity adsorbed inside the material. Its contribution is minor, generally inferior to 3%, but shows that even for materials treated at high temperatures, some water is quickly readsorbed after the end of the process.
For hybrid resol-silica and carbon-silica an important mass loss occurs respectively between 250 and 650 °C and 500 and 750 °C and is attributed to carbonaceous species. Interestingly, the slope of the degradation of carbon is steeper and occurs at higher temperatures for carbon-silica NPs. The increased stability is relevant considering the structure change from organic to inorganic carbon with different degradation mechanisms **Figures 62(a) and 62(c)**.

On the TGA curve of hybrid resol-silica nanoparticles, it is also possible to make out a change of the slope around 430 °C thanks to the derivative. This change can be attributed to inhomogeneities in the organic material and likely comes from a difference between the degradation of the resol and the degradation of the remaining CTA^+, it is however difficult to assign clear areas to specific organic species.
Finally, on the curve of the silica network a regular mass loss can be observed between 180 and 1000 °C completed by a steeper one around 500 °C **Figure 62(b)**. The mass loss around 500 °C comes from residual organic species that remained after the thermal treatment. The more regular mass loss all along the curve is due to condensation of the silica as with temperature,

the surface silanols tends to reform into more thermodynamically stable silica tetrahedron, thus releasing water molecules. This phenomenon can occur for a wide range of temperature, depending if the original silanol is linked to one, two or three oxygens before forming the tetrahedron.

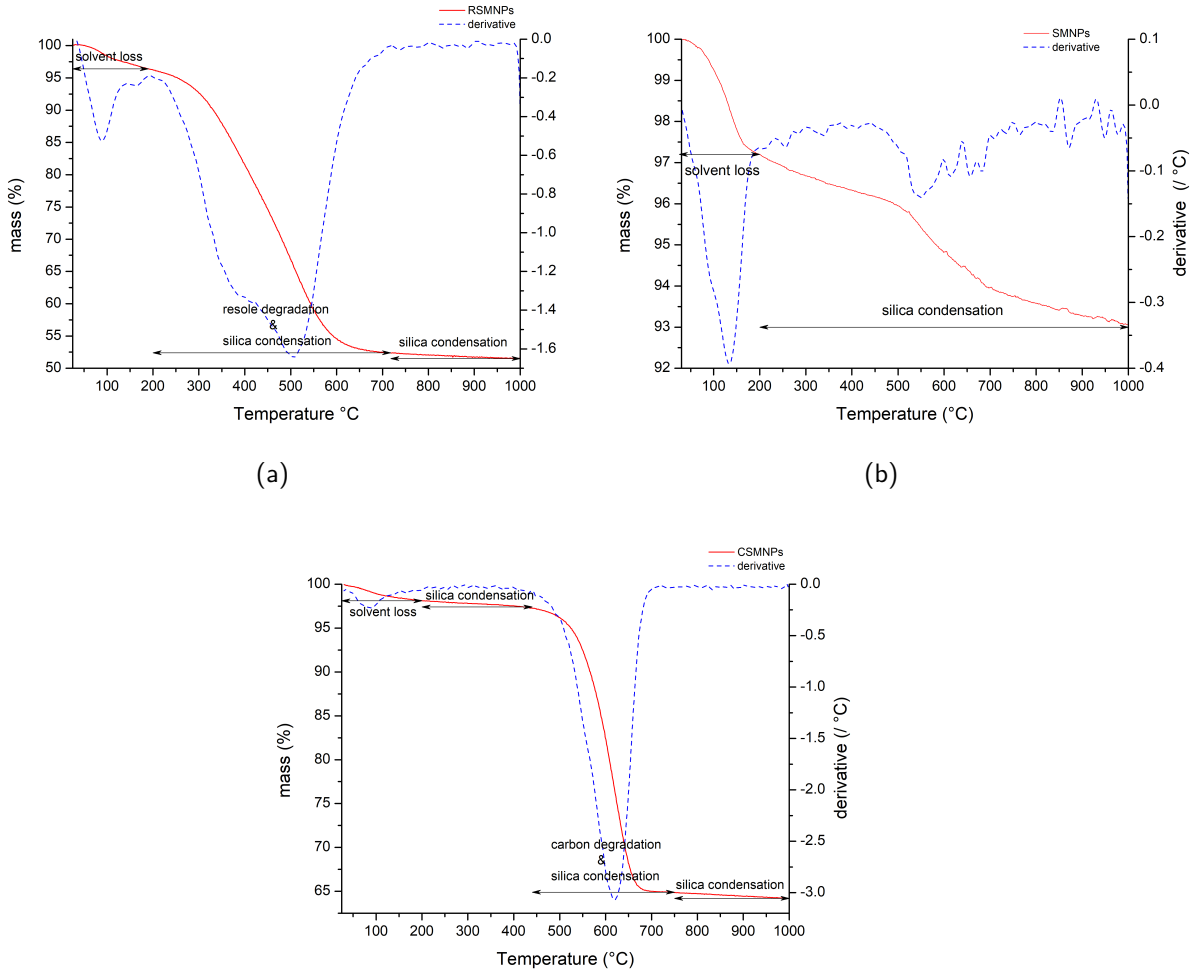

Figure 62: (a) (on the upper left) TGA of hybrid resol-silica mesoporous nanoparticles (RSMNPs) (plain line) and its derivative (dashed line). It evidences a mass ratio of 43% silica and 55% resorcinol. (b) (on the upper right) TGA of silica mesoporous nanoparticles (SMNPs) (plain line) and its derivative (dashed line). (c) (in the lower middle) TGA of hybrid carbon-silica mesoporous nanoparticles (CSMNPs) (plain line) and its derivative (dashed line). It shows a mass ratio of 64% silica and 33% carbon.

II.2.3 Evaluation of the particle's size

Scanning Electron Microscopy (SEM) provides images of all three types of nanoparticles (**Figure 63**) with a good resolution with the secondary electron detector. For all the NPs types, the pictures show well-defined spheric nanoparticles with a diameter of approximately 150 nm with a low dispersion in terms of size and shape.

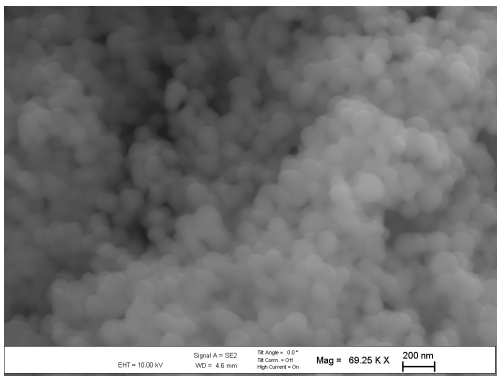

(a)

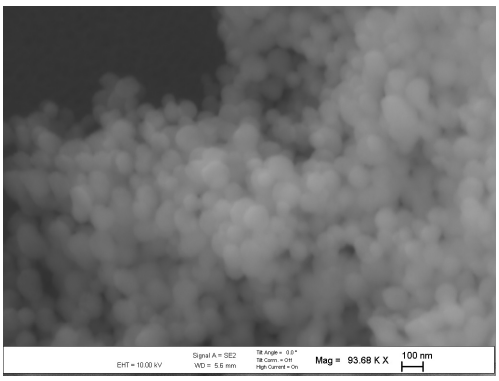

(b)

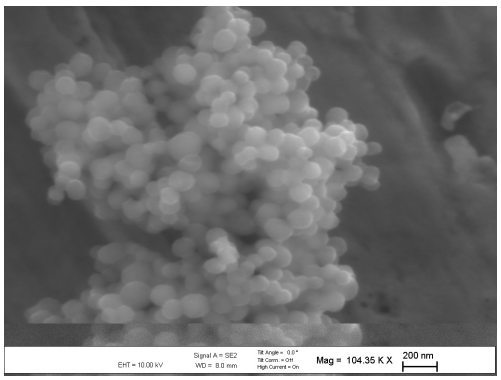

(c)

Figure 63: (a) (on the upper left) SEM image of hybrid resol-silica mesoporous nanoparticles (RSMNPs). (b) (on the upper right) Silica mesoporous nanoparticles (SMNPs). (c) (in the lower middle) Hybrid carbon-silica mesoporous nanoparticles (CSMNPs).

II.2.4 Characterisation of the porosity

In order to be able to compare the empty material with the ones impregnated with Mn compounds that are studied in the next paragraphs, an additional treatment is applied to the particles for them to have been submitted to the same number of washing and drying cycles. To this end a subsequent washing step in an acetonitrile bath is performed (1.00 g of material for 200 mL of solvent for one day), followed by another drying step at 80 °C overnight. Yet, the materials treated with these additional steps do not show a significant change in terms of porosity (or any other characterisation).

Pre-treatment of the samples is necessary to desorb a maximum of water due to air humidity and remaining solvent (CH_3CN) in order to have a measurement as accurate as possible. It consists of a first drying step at ambient temperature and moderate vacuum (a few dozen of minutes) followed by a second longer step (a few hours) under high vacuum and heating. Pure

silica samples are heated up to 130 °C whereas samples containing polymer or other sensitive compounds are kept at 80 °C. TGA shows that the mass loss associated to this pre-treatment is 1 to 3%.
The pressure measurement gives the adsorption-desorption isotherm: adsorbed N_2 volume V_a (cm^3/g) versus pressure relative to ambient, p/p_0, at 77 K. Methods mentioned in II.1.3 enable then to calculate BET, t and BJH -plots, which give tag numbers for the porosity characterisation.

Table 17: Porosity data from N_2-sorption isotherms for extracted hybrid silica-resol nanoparticles (RSMNPs), calcined silica nanoparticles (SMNPs) and carbonised carbon-silica nanoparticles (CSMNPs): BET: Total pore volume (V_t), BET area ($a_{\mathrm{S,BET}}$) and C coefficient (C_{BET}); t-plot: internal (a_{int}) and external (a_{ext}) pore area and microporous (V_{meso}) and mesoporous (V_{meso}) volume; microporous ratio (V_{micro}/V_t).

	Sample		
	RSMNPs	SMNPs	CSMNPs
	BET		
V_t (cm^3/g) [a]	0.55	1.33	0.48
$a_{\mathrm{S,BET}}$ (m^2/g) [b]	404	689	313
C_{BET}	102	100	900
	t-plot		
a_{int} (m^2/g) [c]	367	654	206
a_{ext} (m^2/g) [d]	39	114	39
V_{micro} (cm^3/g) [c]	8.7×10^{-3}	7.3×10^{-3}	4.7×10^{-2}
V_{meso} (cm^3/g) [d]	0.27	0.65	0.19
V_{meso}/V_t	0.49	0.49	0.39
	BJH		
D_{BJH} (nm) [e]	2.5	2.5	2.4
D_{min} (nm) [f]	1.4	1.5	1.4
D_{max} (nm) [g]	4.2	7.1	4.8

From BET plot (a) for $p/p_0 = 0.99$; (b) $0.05 \geq p/p_0 \geq 0.16$. Calculated from t-plot (c) for $t \leq 0.5$; (d) for $t \geq 1.0$. From BJH plot, with $D_i = 2r_i$ (e) for $\frac{dV_p}{dr_p}_{\max}$; (f) for $\frac{dV_p}{dr_p}_{\max} - \left(\frac{dV_p}{dr_p}_{\max}\right)/2$; (g) for $\frac{dV_p}{dr_p}_{\max} + \left(\frac{dV_p}{dr_p}_{\max}\right)/2$.

The overall porosity of SMNPs is higher than the one of RSMNPs and CSMNPs, which is consistent with the thermal treatment that burned the organic part away and thus, left wider cavities.
It is important to compare these values (**Table 17**) with the ones obtained in the original paper[144] herein reported in **Table 18**. We can see that these values, especially for the raw material are very close and therefore reproduce well the synthesis.
An interesting point to notice is while the pure silica and hybrid resol-silica material have a C_{BET} value in the usual range for silica material ($C_{\mathrm{BET}} \sim 100$) this value is much higher for the hybrid carbon-silica material ($C_{\mathrm{BET}} = 900$). In siliceous materials it is interpreted as the interaction between polar silanol and apolar N_2 inducing a dipolar moment between the molecules. A similar effect is likely to appear with the phenol group of the resol phase which is seems confirmed by its C_{BET} value (102). But the graphitised surface of the hybrid

carbon-silica appears to stabilise free $\dot{\mathrm{C}}$ radicals.[220–222] According to the C_{BET} value (900) they seem to contribute to a stronger interaction with N_2 molecules, strongly increasing its affinity for the material.

Table 18: Total pore volume (V_t) and BET area ($a_{\mathrm{S,BET}}$) of extracted hybrid resol-silica nanoparticles (PS-MSNS-1), calcined silica nanoparticles (S-MSNS-1) and carbonised carbon-silica nanoparticles (CS-MSNS-1) reported by Zhang *et al.*[144]

	Sample		
	PS-MSNS-1	S-MSNS-1	CS-MSNS-1
	BET		
V_t (cm^3/g)	0.57	1.65	0.37
$a_{\mathrm{S,BET}}$ (m^2/g)	495	577	321

All three (RSMNPs, SMNPs and CSMNPs) sorption isotherms can be assigned in the IUPAC classification to type IV.[204] They display a slow increase of the adsorbed volume under 0.42 p/p_0 followed by a constant stage where capillary condensation happens, which is characteristic of materials presenting a mesoporosity. As the capillary condensation is not reversible, an hysteresis occurs in the desorption branch.
RSMNPs and CSMNPs display a type II hysteresis, which is observed in materials where different types of mesopores are in communication. This is consistant with the entangled sisters dendritic porosity of these hybrid nanoparticles.[144] They have a mesoporous stellate network of silica in interconnection with a slightly bigger (and probably more deformable) network of resol or graphitised carbon cavities.
On the other hand, SMNPs hysteresis is closer to type IV, characteristic of a different type of linked porosity. This again, supports the stellate morphology of the silica phase, as the channel do not present a regular diameter but rather a gradually increasing one.

In this section we presented the synthesis of three nanoparticles types: RSMNPs, SMNPs and CSMNPs. Some efforts were made to adapt the synthesis of Zhang and coworkers in more diluted conditions. Unfortunately the conditions of the synthesis, which have to be precisely respected to obtain syntaxy, did not allow it. We had to carry on with the initial synthesis and evidenced that the particles we prepared correspond to the morphology described by Zhang's team. Now that the porosity of the different particle types is established it is possible to jump to the next step: the insertion of the Mn compounds inside the different NPs types.

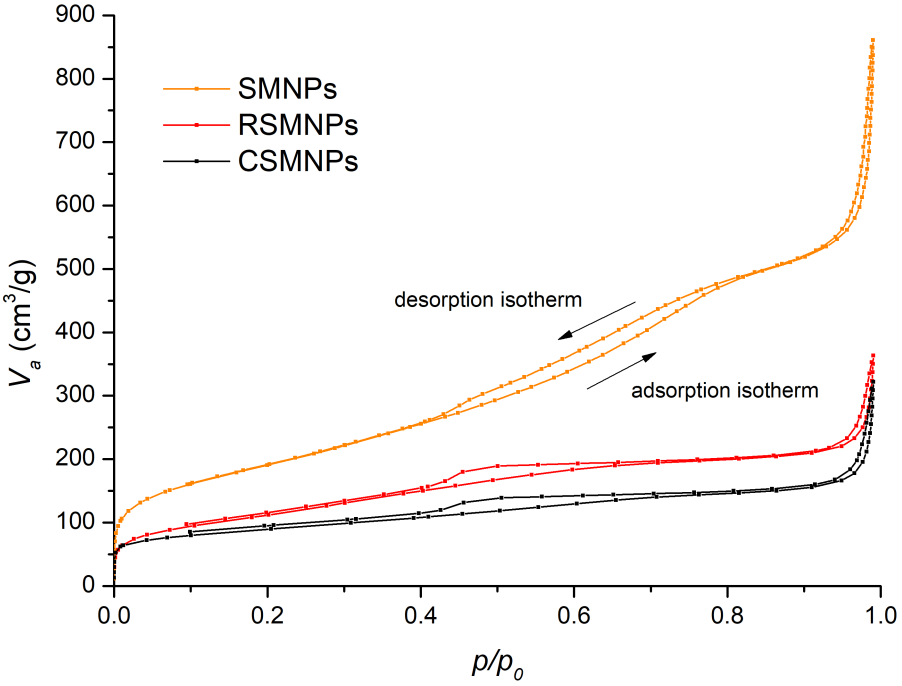

Figure 64: N_2-sorption isotherms at 77 K of extracted hybrid resol-silica nanoparticles (RSMNPs), calcined silica nanoparticles (SMNPs) and carbonised carbon-silica nanoparticles (CSMNPs).

II.3 Catalase bio-mimetic materials

For each material, three different quantities of compounds were loaded inside the particles : 1.0, 2.9 and 4.8% in mass of $[Mn(bpy)(AnthCO_2)_2]_n$ ($[Mn^{II}]_n$) and $[Mn_4O_2(AnthCO_2)_6(bipy)_2(ClO_4)_2]$ ($[Mn_4^{III}]$) compounds. $[Mn^{II}]_n$ is supposed to break in $[Mn_2^{II}]$ in presence of water, which is the case during loading as mesoporous nanoparticles tend to absorb humidity. Once inserted inside the nanoparticles, the compounds will be referred in the following as $[Mn^{II}]$ and $[Mn^{III}]$ respectively, as their nuclearity has to be discussed.

II.3.1 Synthesis & characterisation of $[Mn^{III}]$@resol-SiO_2 mesoporous nanoparticles

$[Mn^{III}]$@resol-SiO_2 mesoporous nanoparticles are synthesised by impregnation of the desired amount of $[Mn_4^{III}]$ compound (10, 30 and 50 mg for materials loaded with 1.0, 2.9 and 4.8% $[Mn_4^{III}]$ respectively) inside 1.00 g of RSMNPs in acetonitrile.

Due to the relatively low load of complex inside the NPs, the infrared spectrum of $[Mn^{III}]$@RSMNPs (**Figure 65**) does not show many differences with the raw material. However, the weak bands found at 738 cm^{-1} and 765 cm^{-1} denote the presence of the compound inside the particles (see previous chapter). The 765 cm^{-1} band is attributed to aromatic δ(CH) of the anthracenecarboxylate ligand. The 738 cm^{-1} is assigned to ν(MnO) but it is

not possible to make a distinction between Ant**CO_2-Mn** or Mn-O of bridging oxygens.

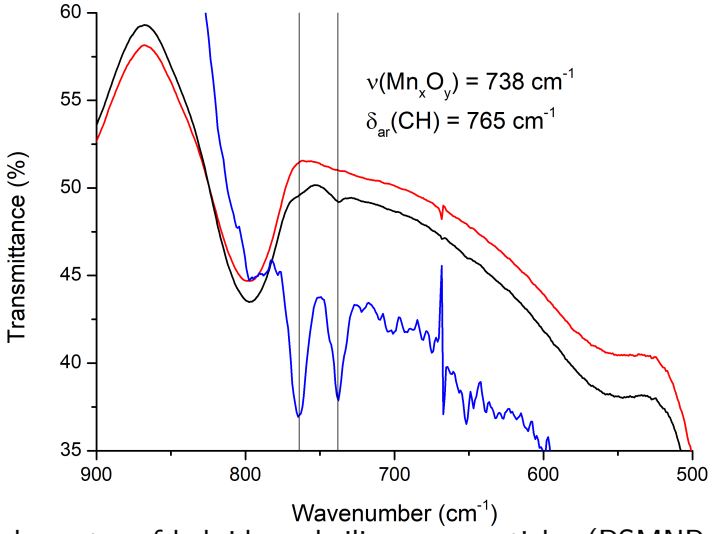

Figure 65: Infrared spectra of hybrid resol-silica nanoparticles (RSMNPs) (red line), [Mn^{III}]-loaded particles ([Mn^{III}]@RSMNPs) (black line) and difference between the two spectra (blue line).

With TGA, it is difficult to give an accurate estimation of the mass loss due to the [Mn^{III}] for [Mn^{III}]@RSMNPs. This difficulty comes, again, from the low amount of complex inside the material. When measured separately, the [Mn_4^{III}] compounds is decomposed between 180 °C and 540 °C (see **I.2.2**) leaving residual MnO_2. On the other hand, as seen in **II.2.2**, the organic polymer is degraded between 250 °C and 700 °C.
However, when the manganese compound is inserted inside the hybrid resol-silica nanoparticles, it clearly appears that the organic part is decomposed faster (**Figure 66**). It is a problem as the pure RSMNPs samples cannot be used as a reference to quantify the quantity of [Mn_4^{III}] inserted as they do not follow the same degradation profile.
Using the derivative mode, we observe that the last inflexion of the curves occurs at 506 °C for the empty RSMNPs, at 489 °C for the ones loaded with 10 mg of [Mn_4^{III}], at 455 °C for 30 mg and at 436 °C for 50 mg. This is attributed to the amount of manganese oxydes generated by the calcination. They are indeed oxidative species and they catalyse the degradation of the material. As a consequence, the more complex is inside the particles, the more oxydes are generated, and the faster the material is degraded.

Elemental analyses of the [Mn^{III}]@RSMNPs samples give the results reported in **Table 19**. First line is the amount of complex used for the insertion, and second line the corresponding quantity of Mn atoms. Third line displays the amount of Mn measured with elemental analysis. The fourth line evaluate the yield of insertion of Mn and, finally, the last line is the particle's load of manganese complex [Mn^{III}] deduced from the Mn amount. Other elements were measured, but we decided to take Mn as reference because it is the only element that comes for sure from our complex and not from other sources. It cannot however ascertain that the complex structure is intact (and it appears not to be the case, see **III.2.2**). The results are in accordance with TGA observations and moreover, show a quasi-total insertion ratio.

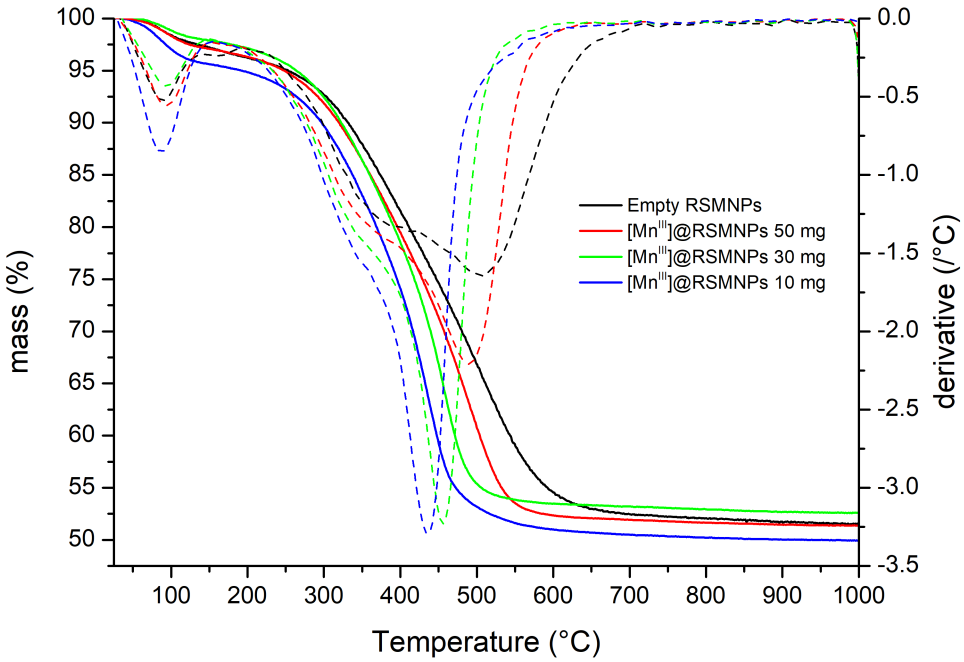

Figure 66: TGA curves of empty RSMNPs nanoparticles and the ones loaded with 10, 30 and 50 mg of [Mn^{III}] per gram of material. Plain line represents mass (%) per temperature (°C), dashed line its derivative.

Table 19: Results from elemental analyses for [Mn^{III}]@RSMNPs

Mass of [Mn_4^{III}] dissolved (mg)	50	30	10
Corresponding Mn quantity (mol)	4.6×10^{-6}	1.6×10^{-6}	1.8×10^{-7}
Mn quantity measured in the material (mol)	4.3×10^{-6}	1.5×10^{-6}	1.8×10^{-7}
Ratio of Mn inserted	0.96	0.93	1.0
[Mn^{III}] in the material (wt%) [a]	4.6	2.7	1.0

(a) Calculated relatively to the Mn amount measured.

Figure 67 displays TEM images of [Mn^{III}]@RSMNPs (4.6 wt%). From these pictures we can clearly see the porosity of the particles with pores below 10 nm. It appears also that the porous particles seem to be coated with a thin layer of polymer. It is confirmed by the degradation of the material when submitted to the focused electron beamed used for EDS. The resol network is damaged while the silica part is more resistant. The fact that the beam can pierce through the layer confirms that it is mainly polymers. The apparition of this thin layer is not surprising as the same synthesis performed at higher pH yields core-shell resol@SiO_2 particles.[144]

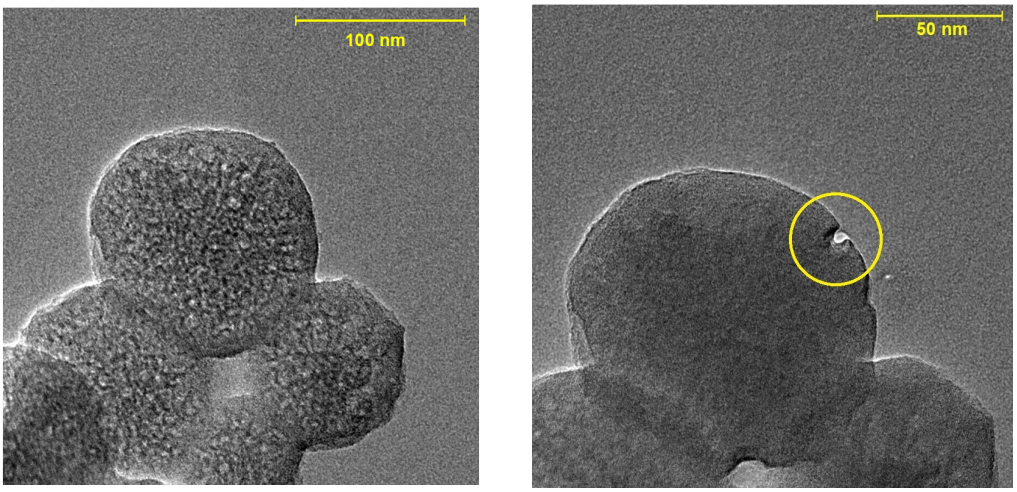

(a) (b)

Figure 67: (a) TEM image of [Mn^{III}]@RSMNPs. (b) TEM image of [Mn^{III}]@RSMNPs after EDS analysis, the cropped part is due to the electron beam action.

EDS on the particles was performed for four elements: N, O, Si and Mn. C was ruled out because of its natural abundance in our environment. Contrary to elemental analysis which gives a mass ratio between the weight of the element and the total sample weight, EDS detects the X-rays emitted with different energies. Hence, the abundance of an element is described relatively to the other element measured, by comparing the intensity of an emission ray to the intensity of other element's rays.

Figure 68 present a typical EDS spectra obtained for [Mn^{III}]@RSMNPs (4.6 wt%). If copper appears on the EDS spectra in large amount, it is due to the copper grid where the particles are dispersed when samples are prepared for microscopy. It shows why the EDS measurement are relative, as some elements have to be excluded by assumption. **Table 20** compares the measures from different points taken on three individual particles to the average value obtained in elemental analysis.

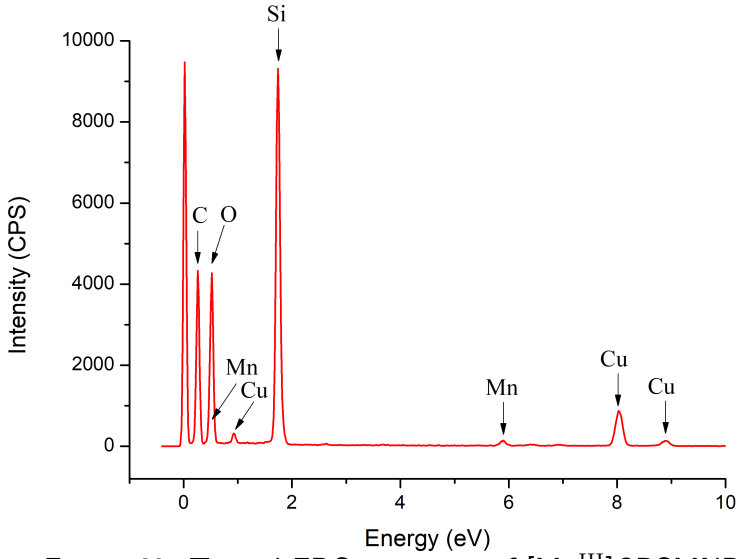

Figure 68: Typical EDS spectrum of [Mn^{III}]@RSMNPs.

Table 20: Mass ratio of the considered elements between each others for [Mn^{III}]@RSMNPs (4.6 wt%). First line is the conversion of the elemental analysis from absolute to relative %. Second line is the averaged contribution of the elements for all measure points of the sample. Third line shows the average value obtained for points taken on the edge of the particles. The last line are the average values measured for points at the center of the particle.

	element mass ratio (%)				molar ratio (%)
Sample	N	O	Si	Mn	Mn/Si
elemental analysis	0.6	61.6	37.0	0.8	1.1
EDS average	2.6	43.5	52.9	1.0	1.0
EDS NP edge	8.6	38.3	51.3	1.8	1.8
EDS NP center	0	44.8	54.5	0.6	0.6

It is possible to see on **Table 20** that the nitrogeninwith the elemental analysis. However the amount of nitrogen detected is greatly dependent on the position where the spectra is recorded. As nitrogen can originate from the complex ligands as well as from some remaining surfactant ammonium heads or acetonitrile solvent, it is hard to comment this difference.

The amount of oxygen is clearly higher for the particles measured than for the bulk material. On the other hand, the silicon quantity is much lower than the sample's average. This shows an imbalance in the resol/silica ratio compared to average values. Nevertheless, EDS reflects the composition of the individual particles, so it means that the ratio between resol and silica has some variations from a particle to another. It is could also simply be due to a different amount of water adsorbed inside the particles when elemental analysis and EDS were recorded.
Finally, the quantity of manganese recorded is close to the average value. More interestingly, the amount of Mn seems to be more important at the particle's periphery than inside. This would mean that the complex do not fill homogeneously the particle's pore. More complex stay close to the particle surface than penetrate deep inside.

N_2 sorption isotherms also enable to evaluate the insertion of the [Mn_4^{III}] compound inside the RSMNPs. **Figure 69** and **Table 21** show the results of N_2 sorption isotherms. The values have been corrected with results of the elemental analysis to pass from results per gram of total material (including the complex) to results per gram of RSMNPs support (without the complex) which allows a direct comparison between samples loaded with different amount of [Mn^{III}]. This study shows that BET and t-plot figures evolve accordingly to the filling of the pores of the particles as the [Mn^{III}] ratio increases. The size of the pores, measured with BJH, is the same for all the NPs and is comprised between 1.4 and 3.7 nm. The average 2.5 nm is the same as for the empty RSMNPs but a bit less spread in size with a $D_{\max}$ of 3.7 nm compared to 4.2 for empty RSMNPs. Nevertheless, due to the stellate morphology of the particles, BJH measurement underestimates the size of the pore (see paragraph II.1.3). As a consequence D_{BJH} is more a useful tool to verify that all nanoparticles retain the same pore distribution than an accurate measurement.
Interestingly, all the [Mn^{III}]@NPs show a V_t and $a_{\mathrm{S,BET}}$ higher to extracted RSMNPs. Considering the mechanical properties of resorcinol-formaldehyde resin, which is very flexible and has and tendency to inflate with the solvent, the insertion of [Mn^{III}] may contribute to change the NPs pore morphology. Either by pushing the flexible resol walls or by draging the polymer in the periphery or outside the silica network.

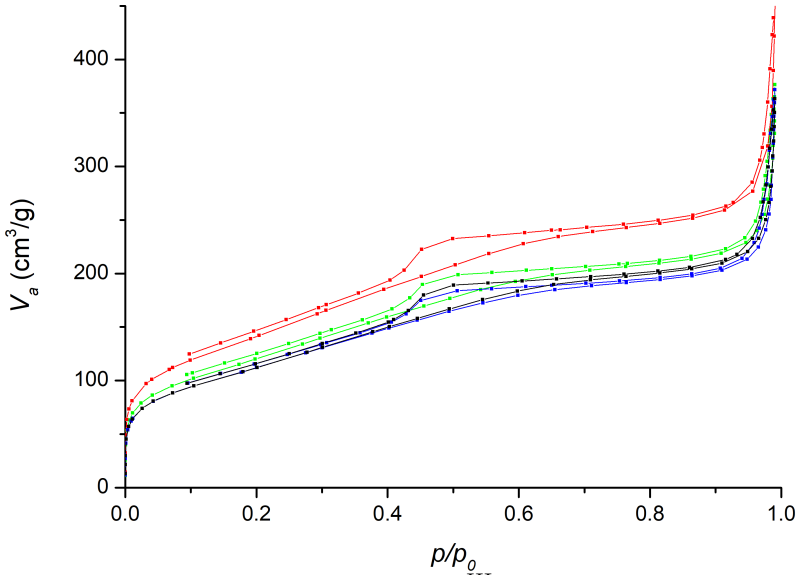

Figure 69: N_2-sorption isotherms at 77 K of [Mn^{III}]@RSMNPs loaded with 50 (blue line), 30 (green line) and 10 (red line) mg [Mn_4^{III}] for 1.00 g of RSMNPs. Black line is the blank with empty RSMNPs.

Table 21: Porosity data from N_2-sorption isotherms for [Mn^{III}]@RSMNPs: BET : Total pore volume (V_t), BET area ($a_{S,BET}$) and C coefficient (C_{BET}); t-plot : internal (a_{int}) and external (a_{ext}) pore area and microporous (V_{meso}) and mesoporous (V_{meso}) volume; microporous ratio (V_{micro}/V_t) of hybrid silica-resol nanoparticles. The head-column number for each sample is [Mn^{III}] load deduced from material Mn elemental analysis.

	Samples			
	0%	1.0%	2.7%	4.6%
	BET			
V_t (cm^3/g) [a]	0.55	0.67	0.57	0.55
$a_{S,BET}$ (m^2/g) [b]	404	505	422	386
C_{BET}	102	103	102	95
	t-plot			
a_{int} (m^2/g) [c]	367	474	376	346
a_{ext} (m^2/g) [d]	39	50	39	37
V_{micro} (cm^3/g) [c]	8.7×10^{-3}	6.4×10^{-3}	1.2×10^{-2}	9.7×10^{-3}
V_{meso} (cm^3/g) [d]	0.27	0.33	0.28	0.25
V_{meso}/V_t	0.49	0.49	0.48	0.44
	BJH			
D_{BJH} (nm) [e]	2.5	2.5	2.5	2.5
D_{min} (nm) [f]	1.4	1.4	1.4	1.4
D_{max} (nm) [g]	4.2	3.7	3.7	3.7

From BET plot (a) for $p/p_0 = 0.99$; (b) $0.05 \geq p/p_0 \geq 0.16$. Calculated from t-plot (c) for $t \leq 0.5$; (d) for $t \geq 1.0$. From BJH plot, with $D_i = 2r_i$ (e) for $\frac{dV_p}{dr_p}_{max}$; (f) for $\frac{dV_p}{dr_p}_{max} - \left(\frac{dV_p}{dr_p}_{max}\right)/2$; (g) for $\frac{dV_p}{dr_p}_{max} + \left(\frac{dV_p}{dr_p}_{max}\right)/2$.

II.3.2 Synthesis & characterisation of [Mn^{III}]@SiO_2 nanoparticles

[Mn^{III}]@SiO_2 are synthesised by impregnation of the desired amount of [Mn^{III}] compound (10, 30 and 50 mg for materials loaded with 1.0, 2.9 and 4.8% [Mn^{III}_4] respectively) inside 1.00 g of SMNPs in acetonitrile.

The infrared spectrum of the material after insertion of [Mn^{III}] (**Figure 70**) is similar to the raw material, the two weak bands at 765 and 738 cm^{-1} can be observed and are attributed respectively to aromatic CH deformation modes of the anthracenecarboxylate ligand and to MnO group as discussed in the previous section.

For [Mn^{III}]@SMNPs, the amount of [Mn^{III}] incorporated inside the particles can be roughly evaluated compared to the other hybrid NPs types. Indeed, pure silica nanoparticles have a more limited mass loss in the 180-540 °C range (the range of degradation of the [Mn^{III}] compound), compared to RSMNPs and CSMNPs. Instead of having important amounts of polymer or carbon degraded for these temperatures, SMNPs mass loss should exclusively be due to silica condensation. However, due to the uncertainty spreading in the measurement[iii]

[iii] $I = \sqrt{\sum_i \left(\frac{\Delta_{m_i}}{m_i}\right)^2}$ Where I is the total uncertainty of the measurement, m the value of the individual

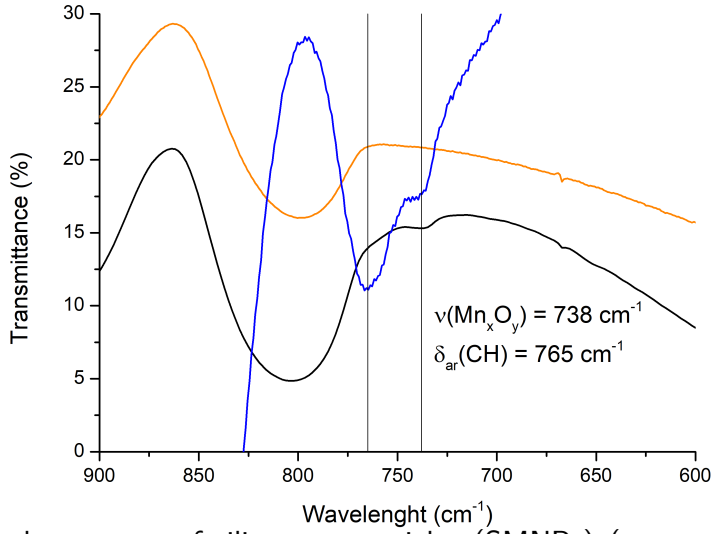

Figure 70: Infrared spectrum of silica nanoparticles (SMNPs) (orange line), [Mn^{III}]-loaded particles [Mn^{III}]@SMNPs (black line) and difference between the two spectra (blue line).

quantities calculated can only give an order of magnitude that can be compared later to the other methods.

To evaluate the amount of compound inside the particles through TGA, the mass loss curve of the sample is compared to the one of a blank of pure SMNPs prepared in the same conditions.
The mass loss due to the ligand is estimated by subtracting the mass loss of the blank to the mass loss of the sample between 180 °C and 540 °C. It is then converted to the equivalent mass loss for the compound. In our case, the ligands represent 86.7% of the total mass of the cationic complex so the estimated compound mass is Δ_m(ligands)/0.867 for the ligands contribution (**Table 22**).

Table 22: Estimation of the amount of [Mn^{III}] inside the SMNPs in weight % with TGA.

Sample (aimed wt%)	Δ_m(ligands) (%)[iv]	Corresponding [Mn^{III}] wt%
1.0% [Mn^{III}]	0.75±0.16	0.87±0.19
2.9% [Mn^{III}]	1.32±0.33	1.53±0.38
4.8% [Mn^{III}]	1.27±0.06	1.47±0.07

The calculated values of (**Table 22**) are within the order of magnitude aimed for the insertion, but even with the large estimated uncertainty, the mass loss due to the ligand is somewhat below the expected value for the two most concentrated samples. This is confirmed later in this part with the elemental analysis and indicates a partial decoordination of the ligands when the compounds are inserted inside the SMNPs.

[Mn^{III}]@SMNPs powder elemental analysis results are displayed in **Table 23**. They show an amount of Mn close to what was aimed for the compound insertion (from 80 % to 90

measurement and Δ_m the uncertainty on each single measurement.

[iv] $\Delta_m(\text{ligands}) = [m_{\text{sample}}(540°\text{C}) - m_{\text{sample}}(180°\text{C})] - [m_{\text{blank}}(540°\text{C}) - m_{\text{blank}}(180°\text{C})]$

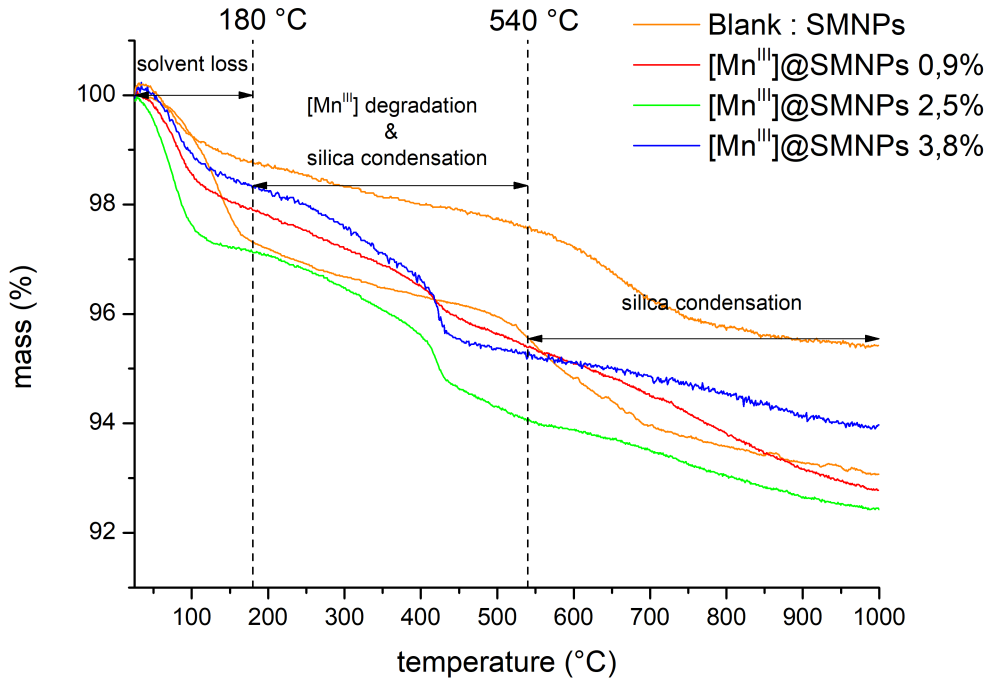

Figure 71: Thermogravimetric analysis of silica mesoporous nanoparticles (SMNPs) and particles loaded with 0.9%, 2.5% and 3.8% [Mn^{III}] in mass, respectively. These values are given after elemental analysis of the Mn and correspond respectively to samples with an aimed amount of 1.0%, 2.9% and 4.8% [Mn^{III}] per gram of material (vide infra).

% of the aimed value). However, the amount of carbon is lower than expected. The pure complex shows a C/Mn ratio of 27.5, according to previous elemental analysis. However, for the analysed samples of [Mn^{III}] inserted inside the particles this ratio never rises above 22.9 and even decreases with the amount of compound inserted. This shows that there is a maximum amount of complex that can be inserted intact inside the silica particles. It is in accordance with TGA, which shows, for the samples with an aimed load of 2.9 and 4.8 wt%, that even with the maximum value allowed with our uncertainty, the mass of ligand measured is inferior to the expectations for the [Mn^{III}] load determined with the Mn mass. So apparently, a portion of the complex breaks and probably loses some ligands when it enters the particles.
This behaviour also matches the geometry of the dendritic channels, which offer a wide entrance at the surface of the particles, progressively shrinking when moving to the inside. If the first complex binds on the surface or at the entrance of the channel, where they have more space to do so (which seems to be the case according to TEM), it leaves the narrower channels of the porous network to the other ones, where they likely have to decoordinate in order to penetrate.

Figure 72 displays TEM images of [Mn^{III}]@SMNPs. The stellate structure of the particles is clearly visible as well as the pores when zooming in. A statistic carried on picture **72(c)** shows that pores distribution is wide, ranging from 4.4 to 11.0 nm, with an average of 7.0 nm and a standard deviation of 1.68. This value is above D_{BJH} presented **Table 25** and close

Table 23: Results from elemental analysis for [Mn^{III}]@SMNPs

Mass of [Mn_4^{III}] dissolved (mg)	50	30	10
Corresponding Mn quantity (mol)	4.6×10^{-6}	1.6×10^{-6}	1.8×10^{-7}
Corresponding C quantity (mol)	1.3×10^{-4}	4.5×10^{-5}	5.0×10^{-6}
Mn quantity measured in the material (mol)	3.6×10^{-6}	1.4×10^{-6}	1.6×10^{-7}
Ratio of Mn inserted	0.80	0.87	0.90
[Mn^{III}] in the material (wt%) [a]	3.8	2.5	0.9
C quantity measured in the material (mol)	6.2×10^{-5}	2.6×10^{-5}	3.8×10^{-6}
Ratio of C inserted	0.50	0.58	0.75
[Mn^{III}] in the material (wt%) [b]	2.4	1.7	0.7
C/Mn molar ratio	17.2	18.5	22.9

(a) Calculated relatively to the Mn amount measured. (b) Calculated relatively to the C amount measured.

to the 7.1 nm of D_{max}. Again, BJH method underestimates the size of the pores. Furthermore, our statistics is only local, measurements are taken on a single particle and take only in account the diameter of the pores in surface, which is anyway poorly defined for stellar NPs.

EDS has also been performed on those NPs but only with two points. Therefore, it was not possible to do statistics. Nevertheless, **Table 24** shows that the measured composition closely matches the elemental analysis.

Table 24: Mass ratio of the considered elements between each others for [Mn^{III}]@SMNPs (3.8 wt%). First line is the conversion of the elemental analysis from absolute to relative %. Second line is the averaged contribution of the elements for all measure points of the sample.

	element mass ratio (%)				molar mass ratio (%)
Sample	N	O	Si	Mn	Mn/Si
elemental analysis	0.5	53.2	46.0	0.31	0.34
EDS average	0	55.2	44.4	0.31	0.36

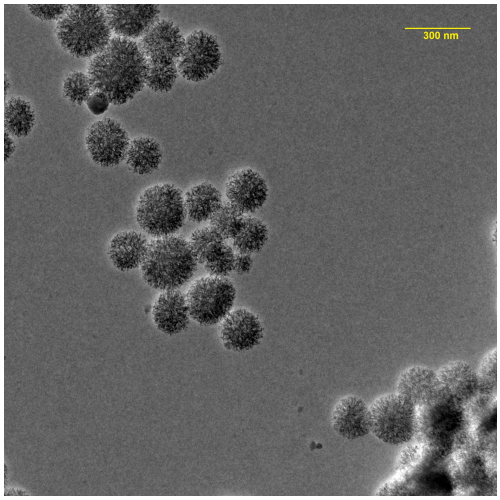

(a)

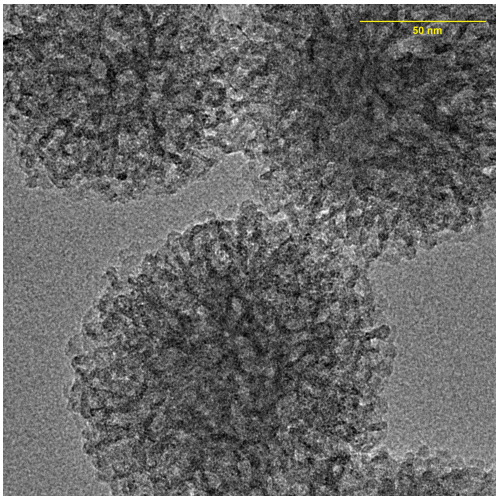

(b)

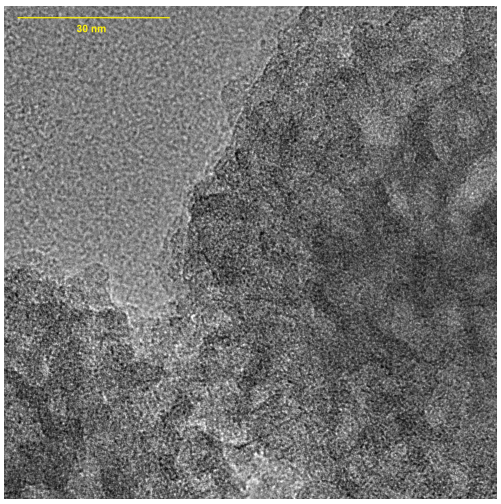

(c)

Figure 72: TEM images of [Mn^{III}]@SMNPs.

.

Finally, N_2 sorption isotherms can also measure the insertion of [Mn^{III}] compound inside the SMNPs. **Figure 73** and **Table 25** sum up the results of these measurements. Again, figures have been corrected with results of the elemental analysis to reflect more accurately the characteristics per gram of support instead of full material.

N_2-sorption isotherms are a lot clearer for [Mn^{III}]@SMNPs compared to [Mn^{III}]@RSMNPs, showing that the pores are, at least partially, filled with [Mn^{III}] compounds **Figure 73**. It is confirmed with values extracted from BET and t-plot **Table 17** : the space available in [Mn^{III}]@SMNPs is smaller than for SMNPs. The pore average diameter and dispersion are almost identical among loaded and empty SMNPs. It is not very surprising : the empty SMNPs have a high pore volume, which is only partially filled upon the incorporation of [Mn^{III}]. With 38 mg of compounds, V_t decreases by 6.8% and $a_{\mathrm{S,BET}}$ by 31% which is apparently not enough to increase significantly the average pore diameter and pore dispersion (especially D_{min}).

These figures also strengthen the idea that in hybrid resol-silica particles, modification of the characteristics of the cavities comes from the polymer phase and not from the more rigid silica phase.
Finally, these values when compared to **Table 17** clearly show a drop in V_t, $a_{\mathrm{S,BET}}$ and a_{int} when the first amount of [Mn^{III}] is added (10 mg). Then, with larger amounts (30 and 50 mg), the loss in pore volume and disponible area is much less important. $a_{\mathrm{S,BET}}$ decreases by 25% with 10 mg of [Mn^{III}] but only by 31% with an amount of compound four times higher. This further supports the idea that the initial loading takes place on the surface and entrance of the pores network, partially sealing the channels and that further complexes added have trouble penetrating the particles and probably partially break to do so.

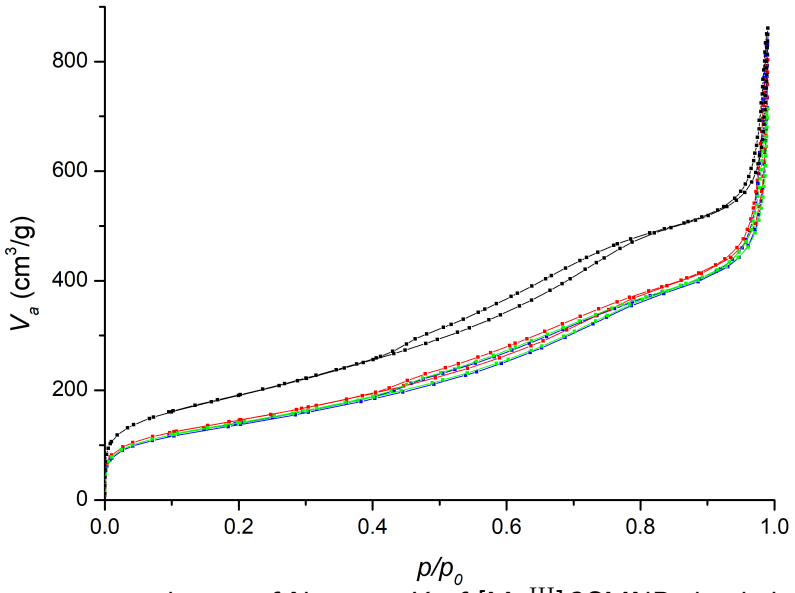

Figure 73: N_2-sorption isotherms of N_2 at 77 K of [Mn^{III}]@SMNPs loaded with 50 (blue), 30 (green) and 10 mg (red) [Mn_4^{III}] for 1.00 g of SMNPs. The isotherm of the blank with empty SMNPs is depicted in black.

Table 25: Porosity data from N_2-sorption isotherms for [Mn^{III}]@SMNPs: BET : Total pore volume (V_t), BET area ($a_{S,BET}$) and C coefficient (C_{BET}); t-plot : internal (a_{int}) and external (a_{ext}) pore area and microporous (V_{meso}) and mesoporous (V_{meso}) volume; microporous ratio (V_{micro}/V_t) of hybrid silica-resol nanoparticles. The head-column number for each sample is [Mn^{III}] load deduced from material Mn elemental analysis.

	Samples			
	0%	0.9%	2.5%	3.8%
	BET			
V_t (cm^3/g) [a]	1.33	1.22	1.07	1.24
$a_{S,BET}$ (m^2/g) [b]	689	520	494	477
C_{BET}	100	107	103	100
	t-plot			
a_{int} (m^2/g) [c]	654	504	471	462
a_{ext} (m^2/g) [d]	114	134	118	121
V_{micro} (cm^3/g) [c]	7.3×10^{-3}	2.0×10^{-3}	4.0×10^{-3}	7.3×10^{-4}
V_{meso} (cm^3/g) [d]	0.65	0.47	0.46	0.45
V_{meso}/V_t	0.49	0.38	0.42	0.35
	BJH			
D_{BJH} (nm) [e]	2.5	2.7	2.7	2.7
D_{min} (nm) [f]	1.5	1.5	1.5	1.5
D_{max} (nm) [g]	7.1	7.1	7.1	7.1

From BET plot (a) for $p/p_0 = 0.99$; (b) $0.05 \geq p/p_0 \geq 0.16$. Calculated from t-plot (c) for $t \leq 0.5$; (d) for $t \geq 1.0$. From BJH plot, with $D_i = 2r_i$ (e) for $\frac{dV_p}{dr_p}_{max}$; (f) for $\frac{dV_p}{dr_p}_{max} - \left(\frac{dV_p}{dr_p}_{max}\right)/2$; (g) for $\frac{dV_p}{dr_p}_{max} + \left(\frac{dV_p}{dr_p}_{max}\right)/2$.

II.3.3 Synthesis & characterisation of [Mn^{III}]@carbon-SiO_2 nanoparticles

[Mn^{III}]@carbon-SiO_2 are synthesised by impregnation of the desired amount of [Mn_4^{III}] compound (10, 30 and 50 mg for compounds loaded with 1.0, 2.9 and 4.8% [Mn_4^{III}] respectively) inside 1.00 g of carbon-silica mesoporous nanoparticles (CSMNPs) in acetonitrile.

Infrared spectrum of the material after insertion of [Mn^{III}] (**Figure 74**) does not show many differences with the raw material. As for the previous NPs, two weak bands at 761 and 734 cm^{-1} can be observed and are attributed respectively to aromatic C-H deformation modes of the anthracenecarboxylate ligand and to Mn-O vibrations.

The spectra of [Mn^{III}]@CSMNPs was also recorded with UV Resonant Raman Spectroscopy (UVRRS). This technique, allows to reduce the contribution of the D band of graphite by exciting the material with a higher energy (UV) beam.[223] It allows to detect less intense signals, in our case the ones coming from the ligands of the Mn compound incorporated inside the nanoparticles. With UVRRS (**Figure 75**), three new bands are detected (1020, 1250 and 1390 cm^{-1}) and the G band appears larger (1580-1600 cm^{-1}) than with the visible excitation. The weak band at 1020 cm^{-1} can be attributed to deformations of

aromatic rings[224,225] (δ(ring)), which gives us little information considering that both the ligands and the support present aromatic rings. The 1250 cm^{-1} is however more interesting and corresponds to a combination mode of aromatic deformation (δ(ring)) and CH deformation[224,225] (δ(CH)). It suggests the presence of the ligands, as the support is normally fully saturated. But as defects are present in the graphite, it is no sufficient proof. The 1390 cm^{-1} can be attributed to symmetrical stretching of the carboxylate[226] ($\nu_s(CO_2^-)$) and indicates the presence of the anthracenecarboxylate. Finally, the widening of the 1600 cm^{-1} can be due to multiple vibration modes like C=N or C_2O deformations,[224] which can be attributed to the bipyridine or the presence of graphite oxyde. All in all, the informations provided by UVRRS show the presence of organic aromatic rings and carboxylate functions, strongly suggesting the presence of the ligands inside the CSMNPs.

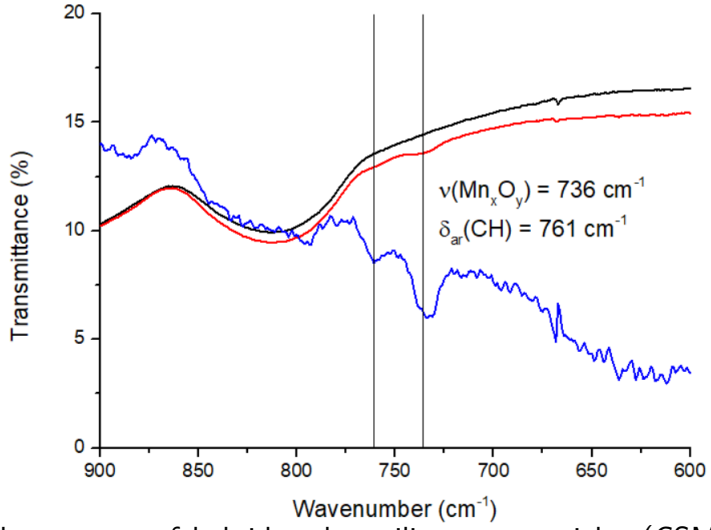

Figure 74: Infrared spectrum of hybrid carbon-silica nanoparticles (CSMNPs) (black line), [Mn^{III}]-loaded particles ([Mn^{III}]@CSMNPs) (red line) and the difference between the two spectra (blue line).

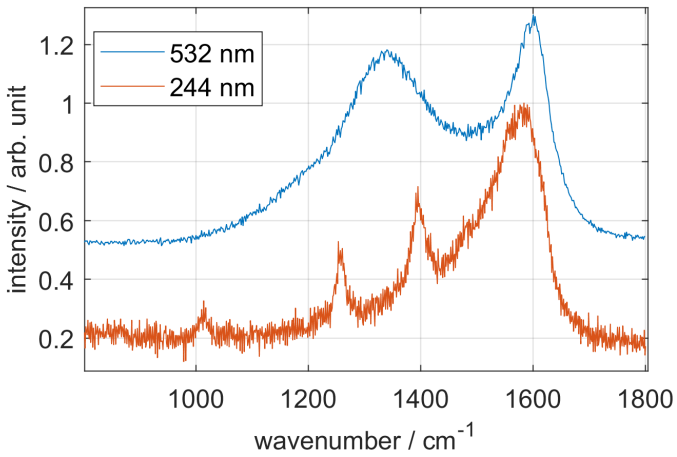

Figure 75: Visible (blue line) and UV (red line) Raman spectra of [Mn^{III}]@CSMNPs.

As for RSMNPs, it is difficult to give an accurate estimation of the mass loss due to the [Mn^{III}] for CSMNPs. Again, when alone, the carbon phase is degraded between 440 °C and 720 °C.

However, when the manganese compound is inserted inside the hybrid resol-silica nanoparticles, the carbon phase is decomposed faster. With these particles, the last inflexion of the curve occurs at 620 °C for the empty CSMNPs, 588 °C for the ones loaded with 10 mg of [Mn^{III}], 566 °C for 30 mg and 531 °C for 50 mg (**Figure 76**). As for RSMNPs, it is likely attributed to the oxidative effect of the generation of manganese oxides during the degradation of the material. The more compound is incorporated in the particle, the more oxides are generated, the lower the degradation temperature is observed.

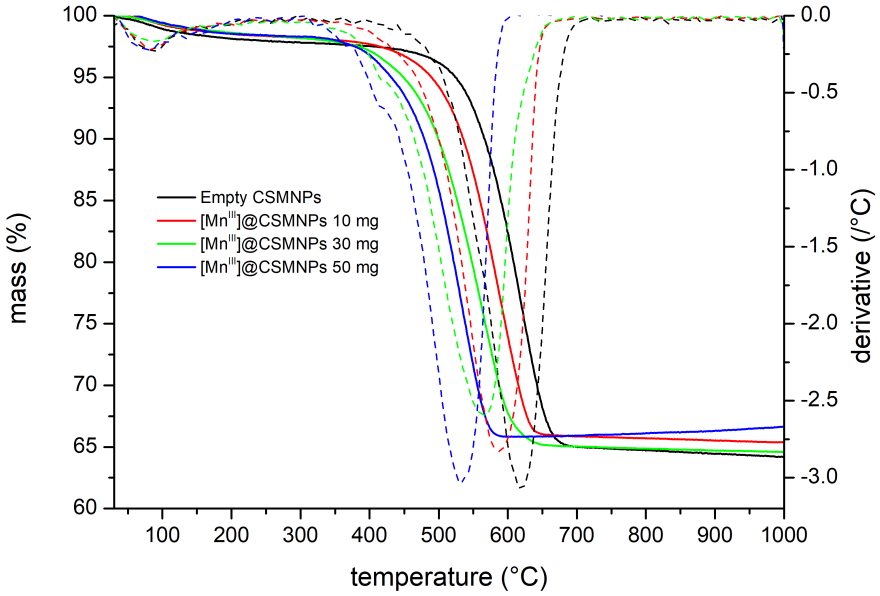

Figure 76: TGA curves of empty CSMNPs nanoparticles and the ones loaded with 10, 30 and 50 mg of [Mn_4^{III}] per gram of material. Plain line represents mass (%) per temperature (°C), dashed line its derivative.

Elemental analysis of the [Mn^{III}]@CSMNPs powder gives the results reported in **Table 26**. The insertion is efficient for the 4.8% and 1.0% samples (88% and 90% respectively). However the sample with 2.9% show a rather low insertion rate of 43%.

Table 26: Results from elemental analysis for [Mn^{III}]@CSMNPs

Mass of [Mn_4^{III}] dissolved (mg)	50	30	10
Corresponding Mn quantity (mol)	4.6×10^{-6}	1.6×10^{-6}	1.8×10^{-7}
Mn quantity measured in the material (mol)	4.0×10^{-6}	7.1×10^{-7}	1.6×10^{-7}
Ratio of Mn inserted	0.88	0.43	0.90
[Mn^{III}] in the material (wt%) [a]	4.2	1.2	0.9

(a) Calculated relatively to the Mn amount measured.

TEM images of [Mn^{III}]@CSMNPs are presented **Figure 77**. These pictures show that CSMNPs have are very similar in size and shape to RSMNPs.

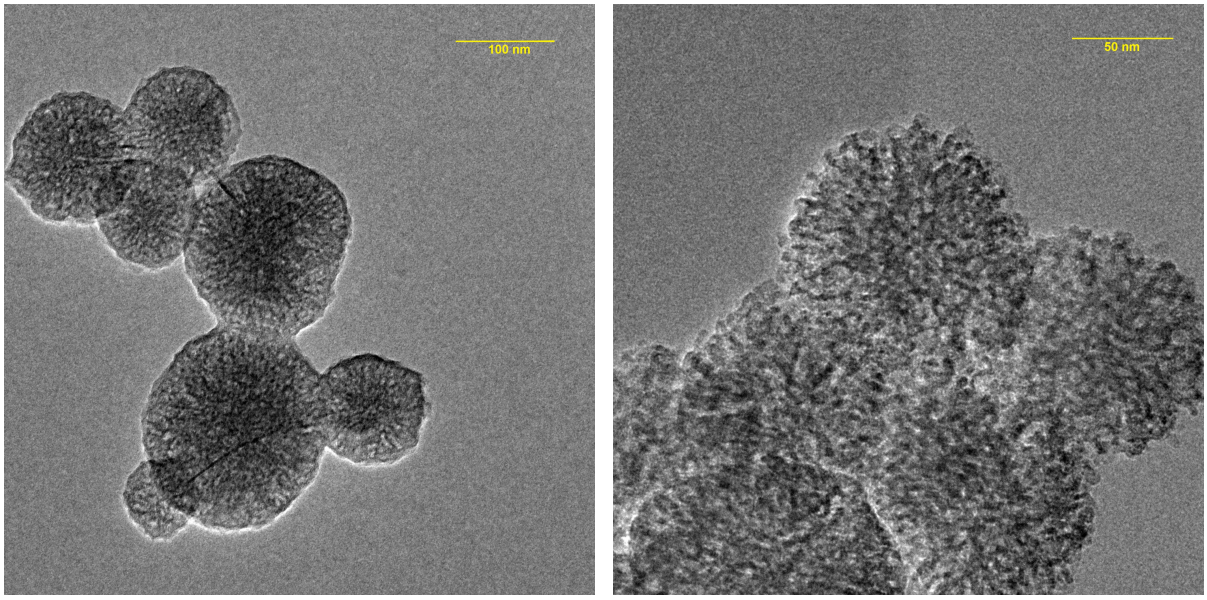

(a) (b)

Figure 77: TEM images of [Mn^{III}]@CSMNPs.

.

EDS analysis of [Mn^{III}]@CSMNPs is reported **Table 27**. The amount of Si and O is close to the average value measured with elemental analysis. However, the amount of Mn is much lower than what is expected, ,which suggests an inhomogeneous distribution of the complex between the particles. Nevertheless, the ratio of Mn recorded at the particles edge (0.38) is more important than in the center (0.18), which suggests once again that the penetration of [Mn^{III}] is not total and that the complex prefers to bind on the particle's surface or the the edge of the channels.

Table 27: Mass ratio of the considered elements between each others for [Mn^{III}]@CSMNPs (4.2 wt$\%$). First line is the conversion of the elemental analysis from absolute to relative $\%$. Second line is the averaged contribution of the elements for all measure points of the sample. Third line shows the average value obtained for points taken on the edge of the particles. The last line are the average values measured for points at the center of the particle.

	element mass ratio ($\%$)				molar mass ratio ($\%$)
Sample	N	O	Si	Mn	Si/Mn
elemental analysis	0.7	53.2	45.5	0.6	0.7
EDS average	0.0	51.5	48.3	0.3	0.3
EDS NP edge	0.0	46.7	52.9	0.4	0.4
EDS NP center	0.0	56.3	43.6	0.2	0.2

N_2 sorption isotherms also show the insertion of [Mn^{III}] compound inside the CSMNPs. **Figure 78** and **Table 28** gather the results of these measurements. Figures are corrected with results of the elemental analysis to reflect more accurately the characteristics per gram

of support instead of full material.

The porous volume V_t of carbon-silica mesoporous NPs and loaded CSMNPs, is clearly in accordance to the progressive filling of the porosity with [Mn^{III}] compounds. The C value also drastically evolves with the insertion of the complexes, starting at 900 and quickly dropping to 468 to finish at 291 for the most loaded sample. This shows either that the presence of [Mn^{III}] has a strong impact on N_2 affinity with the materials or that its insertion changes the inner configuration of the particle. The decrease of V_{meso} to 11% for the sample loaded with 50 mg and the slight increase of the maximum diameter from 4.8 nm for empty particles to 5.4 nm for 1.2% and 4.2% loaded ones suggests a change in the porosity.

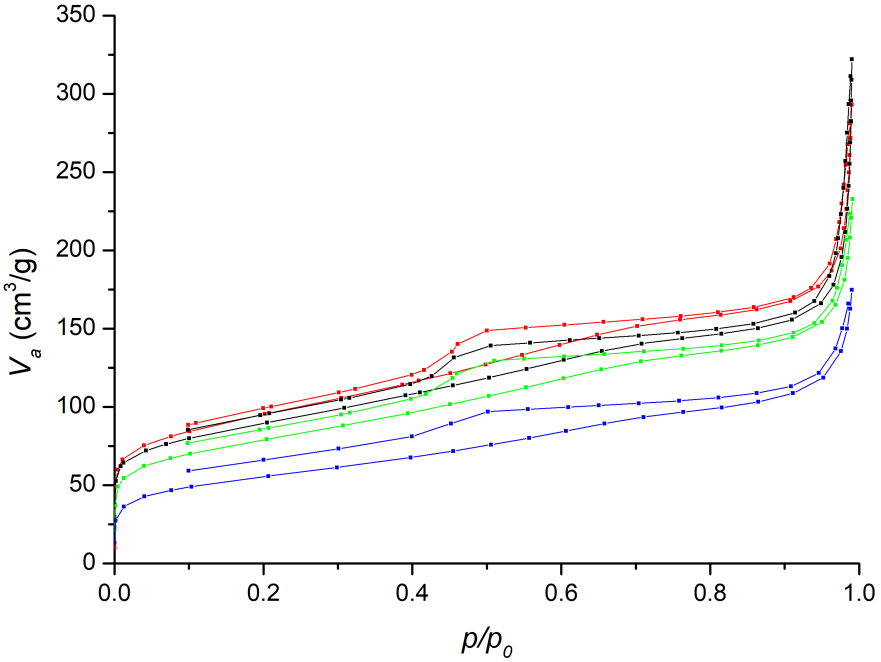

Figure 78: N_2-sorption isotherms of N_2 at 77 K of [Mn^{III}]@CSMNPs loaded with 50 (blue), 30 (green) and 10 mg (red) [Mn^{III}] for 1.00 g of CSMNPs. The black points and line is the blank with empty CSMNPs.

Table 28: Porosity data from N_2-sorption isotherms for [Mn^{III}]@CSMNPs: BET : Total pore volume (V_t), BET area ($a_{S,BET}$) and C coefficient (C_{BET}); t-plot : internal (a_{int}) and external (a_{ext}) pore area and microporous (V_{meso}) and mesoporous (V_{meso}) volume; microporous ratio (V_{micro}/V_t) of hybrid carbon-resol nanoparticles. The head-column number for each sample is [Mn^{III}] load deduced from material Mn elemental analysis.

	Samples			
	0%	0.9%	1.2%	4.2%
	BET			
V_t (cm^3/g) [a]	0.48	0.45	0.34	0.26
$a_{S,BET}$ (m^2/g) [b]	313	332	274	187
C_{BET}	900	468	434	284
	t-plot			
a_{int} (m^2/g) [c]	206	228	196	158
a_{ext} (m^2/g) [d]	39	38	35	35
V_{micro} (cm^3/g) [c]	4.7×10^{-2}	4.4×10^{-2}	3.4×10^{-2}	1.3×10^{-2}
V_{meso} (cm^3/g) [d]	0.19	0.21	0.17	0.11
V_{meso}/V_t	0.39	0.46	0.50	0.42
	BJH			
D_{BJH} (nm) [e]	2.4	2.4	2.7	2.4
D_{min} (nm) [f]	1.4	-	-	-
D_{max} (nm) [g]	4.8	4.8	5.4	5.4

From BET plot (a) for $p/p_0 = 0.99$; (b) $0.05 \geq p/p_0 \geq 0.16$. Calculated from t-plot (c) for $t \leq 0.5$; (d) for $t \geq 1.0$. From BJH plot, with $D_i = 2r_i$ (e) for $\frac{dV_p}{dr_p}_{max}$; (f) for $\frac{dV_p}{dr_p}_{max} - \left(\frac{dV_p}{dr_p}_{max}\right)/2$; (g) for $\frac{dV_p}{dr_p}_{max} + \left(\frac{dV_p}{dr_p}_{max}\right)/2$.

II.3.4 Synthesis & characterisation of [Mn^{II}]@resol-SiO_2 mesoporous nanoparticles

[Mn^{II}]@resol-SiO_2 mesoporous nanoparticles are synthesised by impregnation of the desired amount of $[Mn^{II}]_n$ compound (10, 30 and 50 mg for compounds loaded with 1.0, 2.9 and 4.8% $[Mn^{II}]_n$ respectively) inside 1.00 g of RSMNPs in acetonitrile.

The infrared spectrum of the material after insertion of [Mn^{II}] (**Figure 79**) shows two very weak bands at 765 and 719 cm^{-1}. The 719 cm^{-1} band is a bit more red shifted than the Mn-O vibrations measured on the IR of the $[Mn^{II}]_n$ compound. It is possible that the Mn atoms of the broken chain coordinate to the oxygens of the silanols or phenols present inside the material. The 765 cm^{-1} is attributed to δ_{ar}(CH) from the anthracenecarboxylate ligand.

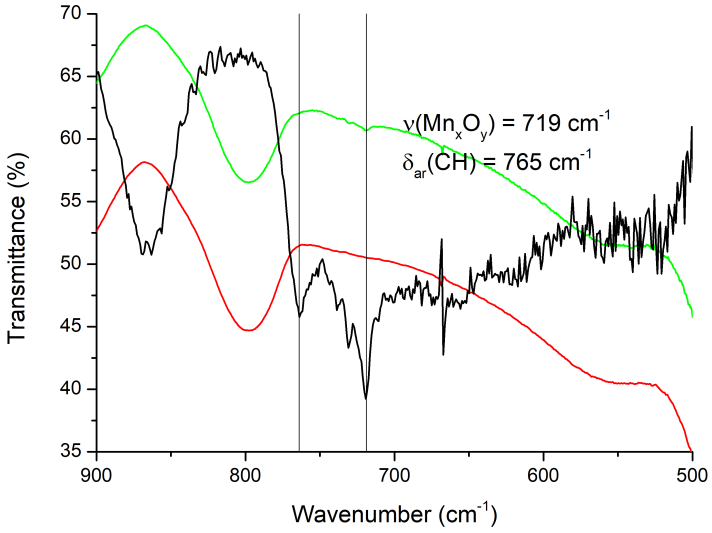

Figure 79: Infrared spectrum of hybrid resol-silica nanoparticles (RSMNPs) (red line), [Mn^{II}]-loaded particles ([Mn^{II}]@RSMNPs) (green line) and the difference between the two spectra (black line).

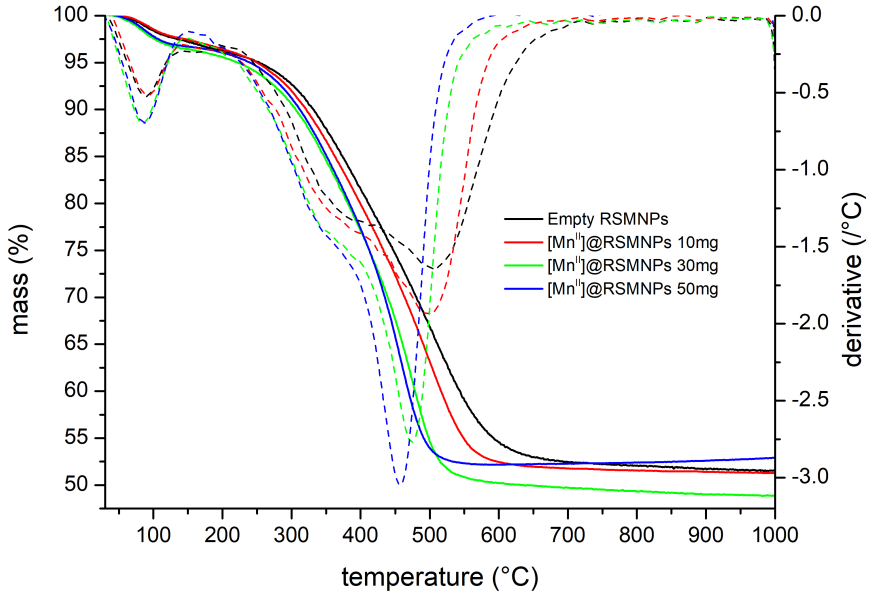

Figure 80: TGA curves of empty RSMNPs nanoparticles and the ones loaded with 10, 30 and 50 mg of $[Mn^{II}]_n$ per gram of material. Plain line represents mass (%) per temperature (°C), dashed line its derivative.

When measured separately, the $[Mn^{II}]_n$ compounds is decomposed between 280 °C and 550 °C (see **I.2.1**) leaving residual MnO_2 at 1000 °C. On the other hand, the organic polymer is degraded between 250 °C and 700 °C.
As seen previously, when the manganese compound is inserted inside the hybrid resol-silica nanoparticles, the carbon phase is decomposed faster. With the empty particles, the last in-

flexion of the TG curve occurs at 506 °C. For loaded ones, it is observed at 497 °C for 10 mg of $[Mn^{II}]_n$, 473 °C for 30 mg and 457 for 50 mg (**Figure 80**). As for $[Mn^{III}]$, it is attributed to the fact that the complex molecules trigger the instability of the organic network when it starts to be degraded.

$[Mn^{II}]$@RSMNPs powder elemental analysis results are displayed in **Table 29** which shows a poor insertion ratio.

Table 29: Results of elemental analysis for $[Mn^{II}]$@RSMNPs

Mass of $[Mn^{II}]_n$ dissolved (mg)	50	30	10
Corresponding Mn quantity (mol)	3.6×10^{-6}	1.3×10^{-6}	1.4×10^{-7}
Mn quantity measured in the material (mol)	2.2×10^{-6}	9.3×10^{-7}	9.1×10^{-8}
Ratio of Mn inserted	0.61	0.72	0.63
$[Mn^{II}]$ in the material (wt%) [a]	2.9	2.0	0.6

(a) Calculated relatively to the Mn amount measured.

N_2 sorption isotherms can also measure the incorporation of $[Mn^{II}]$ compound inside the RSMNPs. **Figure 81** and **Table 30** sum up the results of these measurements. Again, figures have been corrected with results of the elemental analysis to reflect more accurately the characteristics per gram of support instead of full material.

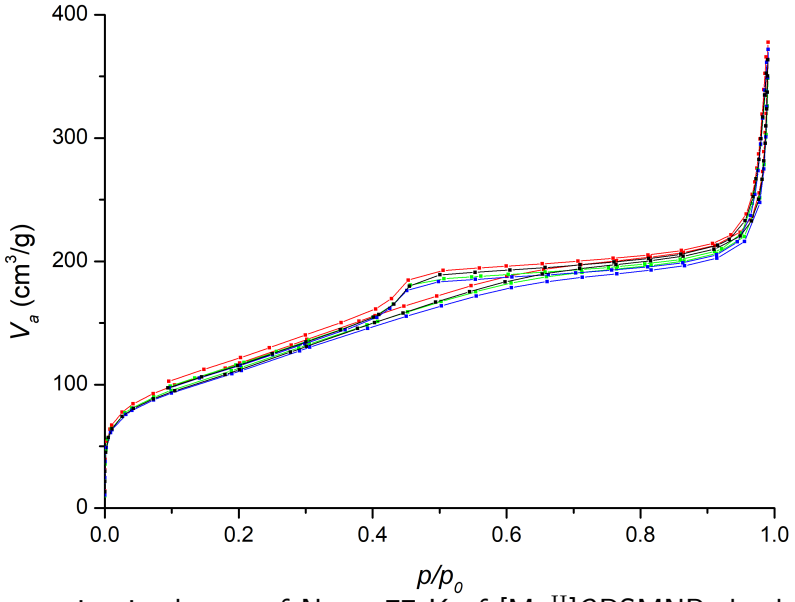

Figure 81: N_2-sorption isotherms of N_2 at 77 K of $[Mn^{II}]$@RSMNPs loaded with 50 (blue), 30 (green) and 10 mg (red) $[Mn^{II}]_n$ for 1.00 g of RSMNPs. Black point and line is the blank with empty RSMNPs.

These graphs and figures did not allow us to quantify the insertion of $[Mn^{II}]$. This might, again, come from the flexible nature of the polyphenol with the ability to adapt, to a certain point, to N_2 pressure. The only series of figures that can be commented is the C value of the BET isotherms. It goes from 102 for the empty material and 0.6% $[Mn^{II}]$@RSMNPs down to 98 for 2.9% $[Mn^{II}]$@RSMNPs, following the usual decrease of the C value with the amount

Mn compound inserted (see **Tables 21, 25 and 28**).

Table 30: Porosity data from N_2-sorption isotherms for [Mn^{II}]@RSMNPs: BET : Total pore volume (V_t), BET area ($a_{S,BET}$) and C coefficient (C_{BET}); t-plot : internal (a_{int}) and external (a_{ext}) pore area and microporous (V_{meso}) and mesoporous (V_{meso}) volume; microporous ratio (V_{micro}/V_t) of hybrid carbon-resol nanoparticles. The head-column number for each sample is [Mn^{II}] load deduced from material Mn elemental analysis.

	Samples			
	0%	0.6%	2.0%	2.9%
	BET			
V_t (cm^3/g) [a]	0.55	0.57	0.52	0.54
$a_{S,BET}$ (m^2/g) [b]	404	420	401	388
C_{BET}	102	103	102	98
	t-plot			
a_{int} (m^2/g) [c]	367	378	383	363
a_{ext} (m^2/g) [d]	39	39	41	38
V_{micro} (cm^3/g) [c]	8.7×10^{-3}	1.1×10^{-2}	3.1×10^{-3}	4.7×10^{-3}
V_{meso} (cm^3/g) [d]	0.27	0.27	0.26	0.25
V_{meso}/V_t	0.49	0.48	0.48	0.46
	BJH			
D_{BJH} (nm) [e]	2.5	2.5	2.5	2.4
D_{min} (nm) [f]	1.4	1.4	1.4	1.4
D_{max} (nm) [g]	4.2	4.2	7.1	3.7

From BET plot (a) for $p/p_0 = 0.99$; (b) $0.05 \geq p/p_0 \geq 0.16$. Calculated from t-plot (c) for $t \leq 0.5$; (d) for $t \geq 1.0$. From BJH plot, with $D_i = 2r_i$ (e) for $\frac{dV_p}{dr_p}_{max}$; (f) for $\frac{dV_p}{dr_p}_{max} - \left(\frac{dV_p}{dr_p}_{max}\right)/2$; (g) for $\frac{dV_p}{dr_p}_{max} + \left(\frac{dV_p}{dr_p}_{max}\right)/2$.

II.3.5 Synthesis & characterisation of [Mn^{II}]@SiO_2 nanoparticles

[Mn^{II}]@SiO_2 are synthesised by impregnation of the desired amount of [Mn^{II}]$_n$ compound (10, 30 and 50 mg for materials loaded with 1.0, 2.9 and 4.8% [Mn^{II}]$_n$ respectively) inside 1.00 g of SMNPs in acetonitrile.

The infrared spectrum of the material after insertion of [Mn^{II}] (**Figure 82**) is similar to the raw material, but a two weak bands at 765 and 738 cm^{-1} can be observed. They are attributed respectively to aromatic C-H deformation modes of the anthracenecarboxylate ligand and to MnO group as discussed previously.

As with [Mn^{III}]@SMNPs, a broad evaluation of the amount of ligands degraded during TGA can be made for [Mn^{II}]@SMNPs (**Figure 83**). The calculus performed in II.3.2 can be repeated but this time considering the degradation range of the ligands Δ_m(ligands) between 280 °C and 550 °C and their contribution to 89.9% of the compound mass according to the structure of the [Mn^{II}_2] compound. It is believed that the chain breaks into smaller dinuclear units when it is redissolved in acetonitrile (after the discussion of the first chapter). However, if the chain unit is considered, the result is sensibly the same as the only difference between

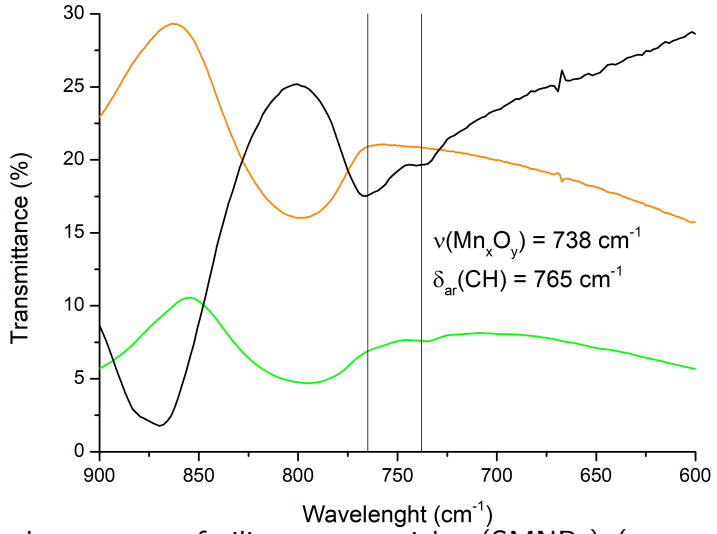

Figure 82: Infrared spectrum of silica nanoparticles (SMNPs) (orange line), [Mn^{II}]-loaded particles [Mn^{II}]@SMNPs (green line) and the difference between the two-spectra (black line).

the two m(Mn)/m(ligands) ratio is half a water molecule on the ligand side.

Table 31: Estimation of the amount of [Mn^{II}] inside the SMNPs in weight % with TGA.

Sample (aimed wt%)	Δ_m(ligands) (%)[v]	Corresponding [Mn^{II}] wt%
1.0% [Mn^{II}]	-0.1±1.6	-0.1±1.7
2.9% [Mn^{II}]	0.81±0.28	0.89±0.31
4.8% [Mn^{II}]	1.62±0.51	1.80±0.56

Table 31 is consistent with the increase of [Mn^{II}] quantity inside the nanoparticles when more compound is added in the dispersion. However, the amount of organic material is below what would be expected for intact complexes and suggests again at least a partial decoordination of the ligands while the metallic core penetrates inside the porous network.

[Mn^{II}]@SMNPs powder elemental analysis results are displayed in **Table 32**. The C/Mn molar ratio is to be compared to 40.0 for [Mn_2^{II}] compound. These figures show a good insertion rate for Mn and apparently a mistake on the amount of compound used for the 10 mg sample. Again, the rate of insertion is less important for the ligands than for the Mn. Though it is interesting to compare these rates with the ones of [Mn^{III}]@SMNPs. For the later the insertion rate of the ligand are respectively of 50% and 58% for the 50 and 30 mg samples. Here it is of 60% and 85% for the 50 and 30 mg samples of [Mn^{II}]@SMNPs. Which shows that less ligands are lost for the [Mn^{II}] compound than for [Mn^{III}]. It is consistent with the fact that chain fragmentation in dinuclear units for [Mn^{II}] preserves the ligand/Mn ions stoichiometry. Whereas, as discussed later in section **III.2.2**, [Mn_4^{III}] also seems to break into dinuclear units inside the particles. But they probably do not keep the same stoichiometry, and carboxylate ligands are likely to detach.

[v] $\Delta_m(\text{ligands}) = [m_{\text{sample}}(550°\text{C}) - m_{\text{sample}}(280°\text{C})] - [m_{\text{blank}}(550°\text{C}) - m_{\text{blank}}(280°\text{C})]$

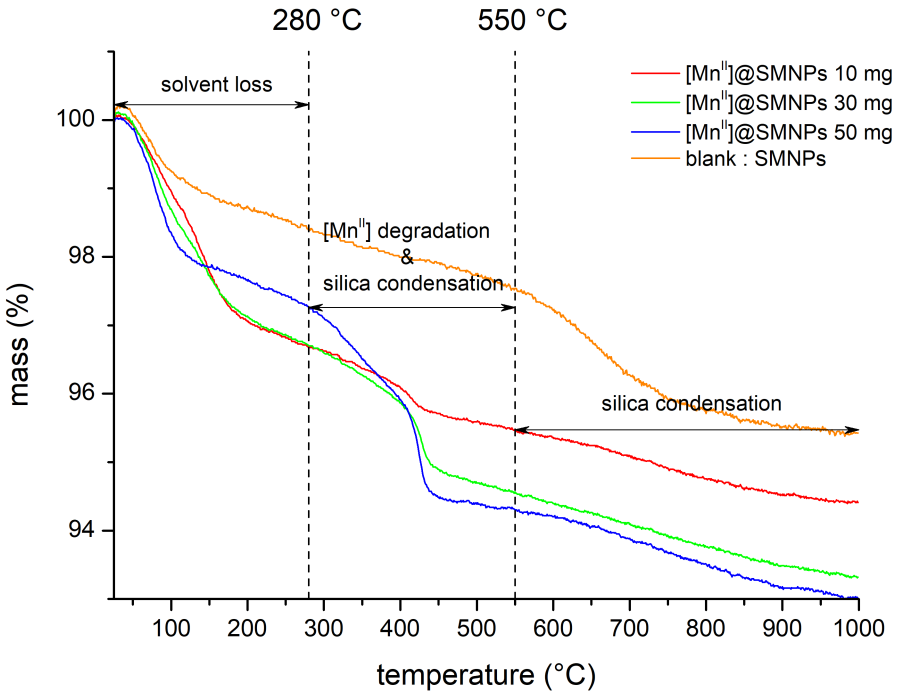

Figure 83: TGA curves of empty SMNPs nanoparticles and the ones loaded with 10, 30 and 50 mg of $[Mn^{II}]_n$ per gram of material.

Table 32: Results from elemental analysis for $[Mn^{II}]$@SMNPs

Mass of $[Mn^{II}]_n$ dissolved (mg)	50	30	10
Corresponding Mn quantity (mol)	3.6×10^{-6}	1.3×10^{-6}	1.4×10^{-7}
Corresponding C quantity (mol)	1.4×10^{-4}	5.2×10^{-5}	5.8×10^{-6}
Mn quantity measured in the material (mol)	2.9×10^{-6}	1.3×10^{-6}	1.8×10^{-7}
Ratio of Mn inserted	0.81	1.0	1.3
$[Mn^{II}]$ in the material (wt%) [a]	3.9	2.9	1.2
C quantity measured in the material (mol)	8.7×10^{-5}	4.4×10^{-5}	1.1×10^{-5}
Ratio of C inserted	0.60	0.85	1.9
$[Mn^{II}]$ in the material (wt%) [b]	3.9	2.9	1.8
C/Mn molar ratio	29.7	33.6	60.4

(a) Calculated relatively to the Mn amount measured. (b) Calculated relatively to the C amount measured.

N_2 sorption isotherms are used to evaluate the efficiency of the insertion of $[Mn^{II}]$ compound inside the SMNPs. **Figure 84** and **Table 33** sum up the results of these measurements. Again, figures have been corrected with results of the elemental analysis to reflect more accurately the characteristics per gram of support instead of full material.

V_t does not significantly vary with the insertion the different quantities of $[Mn^{II}]$ inside the nanoparticles.
However, $a_{S,BET}$, a_{int}, a_{ext} clearly show a decreasing trend in the surface area. The loss of 7 to 33% of the internal area compared to SMNPs and the diminution of the external area of

up to 5% show that the compounds are located inside the particle's cavities. This area loss is higher when the amount of compound inserted increases, compared to [Mn^{III}]@SMNPs. It shows a better insertion of [Mn^{II}] molecules, which progressively fill the pores, whereas [Mn^{III}] seems to impede them quicker.
On the other hand, the characteristic diameters measured do not change significantly, indicating that the pore structure stays the same.

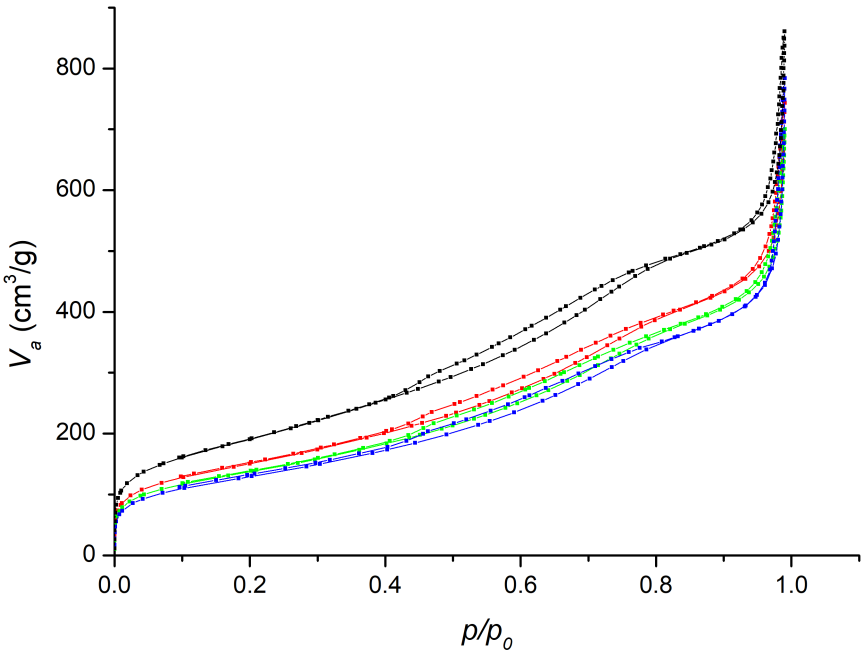

Figure 84: N_2-sorption isotherms of N_2 at 77 K of [Mn^{II}]@SMNPs loaded with 50 (blue), 30 (green) and 10 mg (red) $[Mn^{II}]_n$ for 1.00 g of SMNPs. Black line and points are the isotherms of the blank with empty SMNPs.

Table 33: Porosity data from N_2-sorption isotherms for [Mn^{II}]@SMNPs: BET : Total pore volume (V_t), BET area ($a_{S,BET}$) and C coefficient (C_{BET}); t-plot : internal (a_{int}) and external (a_{ext}) pore area and microporous (V_{meso}) and mesoporous (V_{meso}) volume; microporous ratio (V_{micro}/V_t) of silica nanoparticles. The head-column number for each sample is the [Mn^{II}] load deduced from material Mn elemental analysis.

	Samples			
	0%	1.2%	2.9%	3.9%
	BET			
V_t (cm^3/g) [a]	1.33	1.37	1.05	1.15
$a_{S,BET}$ (m^2/g) [b]	689	652	482	449
C_{BET}	100	131	107	100
	t-plot			
a_{int} (m^2/g) [c]	654	611	453	439
a_{ext} (m^2/g) [d]	114	156	118	107
V_{micro} (cm^3/g) [c]	7.3×10^{-3}	9.3×10^{-3}	6.9×10^{-3}	-
V_{meso} (cm^3/g) [d]	0.65	0.60	0.45	0.44
V_{meso}/V_t	0.49	0.52	0.42	0.37
	BJH			
D_{BJH} (nm) [e]	2.5	2.7	2.7	2.7
D_{min} (nm) [f]	1.5	1.5	1.5	1.5
D_{max} (nm) [g]	7.1	7.1	8.1	8.1

From BET plot (a) for $p/p_0 = 0.99$; (b) $0.05 \geq p/p_0 \geq 0.16$. Calculated from t-plot (c) for $t \leq 0.5$; (d) for $t \geq 1.0$. From BJH plot, with $D_i = 2r_i$ (e) for $\frac{dV_p}{dr_p}_{max}$; (f) for $\frac{dV_p}{dr_p}_{max} - \left(\frac{dV_p}{dr_p}_{max}\right)/2$; (g) for $\frac{dV_p}{dr_p}_{max} + \left(\frac{dV_p}{dr_p}_{max}\right)/2$.

II.3.6 Synthesis & characterisation of [Mn^{II}]@carbon-SiO_2 nanoparticles

[Mn^{II}]@carbon-SiO_2 are synthesised by impregnation of the desired amount of [Mn^{II}]$_n$ compound (10, 30 and 50 mg for compounds loaded with 1.0, 2.9 and 4.8% [Mn^{II}]$_n$ respectively) inside 1.00 g of CSMNPs in acetonitrile.

The infrared spectrum of the material after insertion of [Mn^{II}] (**Figure 85**) is similar to the raw material. The two bands at 761 and 736 cm^{-1} are very weak. They are assigned respectively to aromatic CH deformation modes of the anthracenecarboxylate ligand and to MnO vibrations.

The thermogravimetric analysis (**Figure 86**) is once again not precise enough to give direct reliable results on the amount of [Mn^{II}] inserted inside the hybrid carbon-silica nanoparticles. However, the early degradation of the carbon phase can be correlated with the amount of compound added to the material. The last inflexion of the TGA curve, given by its derivative, is measured at 620 °C for the empty CSMNPs. Whereas it goes down to 608 °C for particles with 10 mg of [Mn^{II}]$_n$, 592 °C for 30 mg and finally 554 °C for 50 mg. These measurements account that increasing quantities of compounds have well been inserted inside the material.

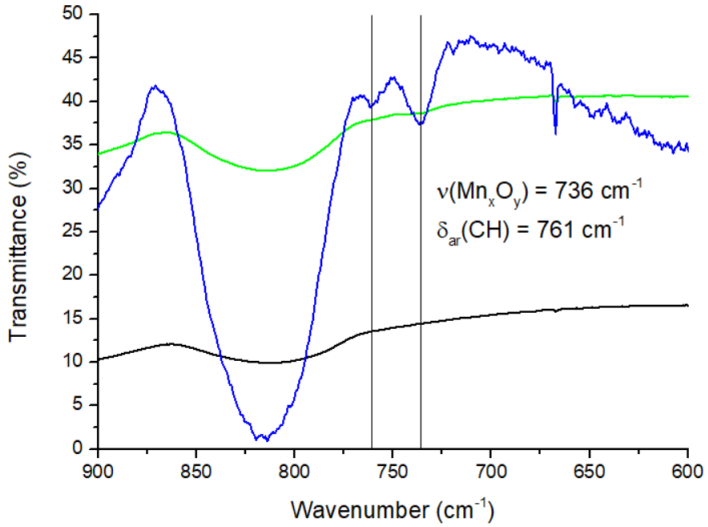

Figure 85: Infrared spectrum of silica nanoparticles (CSMNPs) (black line) and [Mn^{II}]-loaded particles [Mn^{II}]@CSMNPs (green line) and the difference between the two spectra (blue line).

[Mn^{II}]@CSMNPs powder Mn elemental analysis results are displayed in **Table 34**. They shows a good insertion ratio for particles loaded with 50 and 30 mg (respectively 88% and 92%) but a rather low one for the sample with 10 mg of [Mn^{II}]$_n$ compound (35%).

Table 34: Results from elemental analysis for [Mn^{II}]@CSMNPs

Mass of [Mn^{II}] dissolved (mg)	50	30	10
Corresponding Mn quantity (mol)	3.6×10^{-6}	1.3×10^{-6}	1.4×10^{-7}
Mn quantity measured in the material (mol)	3.5×10^{-6}	1.3×10^{-6}	5.5×10^{-8}
Mn ratio inserted	0.96	1.0	0.38
[Mn^{III}] in the material (wt%) [a]	4.6	2.9	0.4

(a) Calculated relatively to the Mn amount measured.

N_2 sorption isotherm (**Figure 87**) shows that the pores of the particles are progressively filled upon the increasing quantity of compound. This is further supported by the BET and t-plot analysis (**Table 35**), figures are once again corrected with the results of the elemental analysis to be closer to the values per gram of support. V_t and $a_{S,BET}$ show a progressive decrease of the available space from respectively 10% and 2% for 10 mg of [Mn^{II}] to 40% and 76% for 50 mg. Again the C_{BET} quickly drops (from 900 to 576) as soon as the Mn compounds are inserted. T-plots also show that a_{int} decreases fast (up to 70%) while a_{ext} stays stable which shows that [Mn^{II}] is going inside the particles, more likely in the mesoporosity as the V_{meso}/V_t ratio is also getting smaller with the increasing complex quantities. On the other hand, the pore's average and extremal diameter do no change significantly, indicating a stability of the walls and that a significant amount of space is still available inside the NPs.

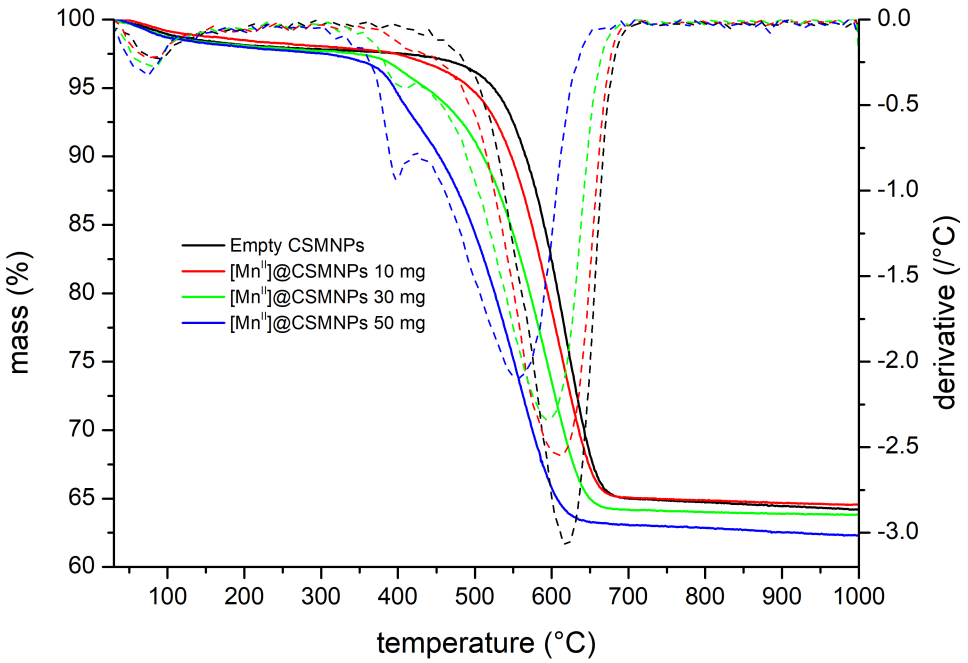

Figure 86: TGA curves of empty CSMNPs nanoparticles and the ones loaded with 10, 30 and 50 mg of $[Mn^{II}]_n$ per gram of material. Plain line represents mass (%) per temperature (°C), dashed line its derivative.

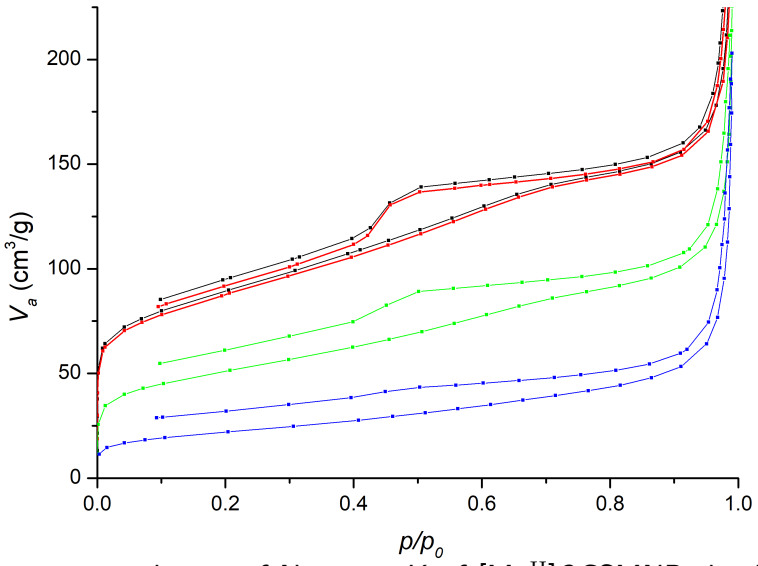

Figure 87: N_2-sorption isotherms of N_2 at 77 K of $[Mn^{II}]$@CSMNPs loaded with 50 (blue), 30 (green) and 10 mg (red) $[Mn^{II}]_n$ for 1.00 g of CSMNPs. Black line and points are the isotherms of the blank with empty CSMNPs.

Table 35: Porosity data from N_2-sorption isotherms for [Mn^{II}]@CSMNPs: BET : Total pore volume (V_t), BET area ($a_{S,BET}$) and C coefficient (C_{BET}); t-plot : internal (a_{int}) and external (a_{ext}) pore area and microporous (V_{meso}) and mesoporous (V_{meso}) volume; microporous ratio (V_{micro}/V_t) of hybrid carbon-silica nanoparticles. The head-column number for each sample is the [Mn^{II}] load deduced from material Mn elemental analysis.

	Samples			
	0%	0.4%	2.9%	4.6%
	BET			
V_t (cm^3/g) [a]	0.48	0.43	0.33	0.29
$a_{S,BET}$ (m^2/g) [b]	313	307	174	74
C_{BET}	900	576	330	197
	t-plot			
a_{int} (m^2/g) [c]	206	210	133	61
a_{ext} (m^2/g [d])	39	37	37	36
V_{micro} (cm^3/g) [c]	4.7×10^{-2}	4.3×10^{-2}	1.8×10^{-2}	5.6×10^{-3}
V_{meso} (cm^3/g) [d]	0.19	0.19	0.10	3.0×10^{-2}
V_{meso}/V_t	0.39	0.43	0.30	0.10
	BJH			
D_{BJH} (nm) [e]	2.4	2.4	2.4	2.4
D_{min} (nm) [f]	1.4	1.4	1.4	1.4
D_{max} (nm) [g]	4.8	4.8	5.4	5.4

From BET plot (a) for $p/p_0 = 0.99$; (b) $0.05 \geq p/p_0 \geq 0.16$. Calculated from t-plot (c) for $t \leq 0.5$; (d) for $t \geq 1.0$. From BJH plot, with $D_i = 2r_i$ (e) for $\frac{dV_p}{dr_p}_{max}$; (f) for $\frac{dV_p}{dr_p}_{max} - \left(\frac{dV_p}{dr_p}_{max}\right)/2$; (g) for $\frac{dV_p}{dr_p}_{max} + \left(\frac{dV_p}{dr_p}_{max}\right)/2$.

II.3.7 Conclusion on the synthesis of nanocarriers and [Mn^{II}] and [Mn^{III}] compounds insertion

In this part we have shown, thanks to many different types of analysis (IR, TGA, N_2-sorption isotherms and electronic microscopy), that we successfully synthesised three different types of mesoporous nanoparticles. The hybrid resol-silica ones serve as base material to prepare pure silica and hybrid carbon-silica nanoaprticles. All this particles are monodisperse in size (around 150 nm) an exhibit the same type of dendritic porosity (stellar-shaped particles), although they have various available porous volumes and different mechanical properties.

As suitable nanocarrier, these particles were used for the insertion of the manganese compounds presented in the previous part. The same techniques used to characterised the nanoparticles, along with elemental analysis have shown that for all particles and compounds types, increasing amounts of Mn compounds lead to increasingly loaded nanoparticles.
For most types of particles the insertion rate of Mn is good (72% to 96%). However, the study of pure silica nanoparticles suggests that only a small amount of complex can be incorporated intact inside the particles. [Mn_4^{III}] molecules, quickly impede the entrance of the porous network and have to break in order to penetrate deeper inside. Whereas the smaller [Mn^{II}] units can enter more easily and need less decoordination to fill the particles.
An interesting result has also been observed for hybrid resol-silica nanoparticles, whose structure seems sensitive to the stress imposed by the insertion of the [Mn^{III}] compounds. The more flexible resol pore-walls seem to be pushed by the molecule to enable their insertion inside the particle's channels. With these new hybrid materials prepared, let us now study their physical and chemical properties.

II.4 Experimental Section

II.4.1 Synthesis of the nanoparticles

The following three paragraphs present the nanoparticles synthesized according to the method reported by K. Zhang *et al.*[144]

Resol-silica mesoporous nanoparticles (RSMNPs)

Mesoporous silica-resol nanoparticles (RSMNPs) are synthesized by using a one-pot soft-templating method. Resorcinol (5.0 g, 4.5×10^{-2} mol) and CTAB (5.0 g, 1.4×10^{-2} mol.) are mixed together in an aqueous ethanol solution (EtOH 200 mL/water 500 mL) of TEA (10.6 g, 7.1×10^{-2} mol). The solution is then stirred (140 rpm) for 30 min at ambient, at this point pH $\approx$ 9.0.
A solution of formaldehyde is then added to the mixture (5.0 mL, 37 wt$\%$) followed by TEOS (25 mL, 1.1×10^{-1} mol) 2 min later (pH $=$ 9.1). This solution is first stirred 24 h at room temperature then heated up to 80 °C for another 24 h (Final pH $=$ 8.0).
The suspension of aggregated particles is then filtered and the solid washed a couple times with a solution of HCl in EtOH (2.0 mol/L) then with pure ethanol. The material is subsequently dried in an oven overnight at 80 °C and yields 16 g of product.
TGA analysis shows a ratio of 43$\%$ silica and 55$\%$ resorcinol (residual 2$\%$ is water absorbed within the porosity and resulting from high temperature silica condensation). IR (cm^{-1}): 3424 (bd), 2929 (w), 2855 (w), 1624 (s), 1506 (w), 1474 (w), 1448 (w), 1384 (w), 1152 (bd), 1085 (s), 969 (m), 799 (m), 556 (w), 462 (s).

Calcinated silica mesoporous nanoparticles (SMNPs)

Biphasic RSMNPs are calcinated in a tubular furnace under a small air flux. Temperature is increased at the rate of 3 °C/min up to 550 °C and maintained in these conditions for 6 h.
Residual mass (silica) is 46$\%$ of the initial sample. IR (cm^{-1}): 3445 (bd), 1645 (s), 1389 (w), 1152 (bd), 1088 (s), 968 (m), 800 (m), 565 (w), 464 (s).

Carbonised carbon-silica mesoporous nanoparticles (CSMNPs)

Biphasic RSMNPs are calcinated in a tubular furnace in inert conditions under a small N_2 flux. Temperature is increased at the rate of 3 °C/min up to 900 °C and maintained in these conditions for 3 h. Residual mass is 61$\%$ of the initial sample.
TGA analysis shows a ratio of 64$\%$ silica and 33$\%$ carbon. IR (cm^{-1}): 3449 (bd), 1608 (bd), 1384 (w), 1152 (bd), 1090 (s), 965 (w), 818 (m), 467 (s).

Modified synthesis of mesoporous silica-resol nanoparticles

The following synthesis is a modified version of the resol-silica mesoporous nanoparticles preparation reported by Zhang and coworkers,[144] inspired from the work of Yamamoto *at*

al.[216]

Resorcinol (3.1×10^{-2} g, 2.8×10^{-4} mol) and CTAB (0.66 g, 1.8×10^{-3} mol.) are mixed together in 100 mL of an aqueous solution of TEA (0.19 g, 1.3×10^{-3} mol). The solution is then stirred (140 rpm) for one hour at 80 °C.
A solution of formaldehyde is then added to the mix (49.9 μL, 37 wt%) followed by TEOS (1.56×10^{-4} L, 7.0×10^{-4} mol) 2 min later. This solution is first stirred one hour at 80 °C then maintained at 30 °C for 24 h.

The dialysis method used before the AFM pictures were taken is 4×6 hours in ethanol/acetic acid (2M) (1:2) followed by 4×6 hours in distilled water.

II.4.2 Synthesis of catalase bio-mietic materials

[Mn]@NPs materials are prepared by simple impregnation of the desired complex in NPs suspension.

Synthesis of [Mn^{III}]@resol-SiO_2 mesoporous nanoparticles

[Mn^{III}]@SiO_2-resol mesoporous nanoparticles are synthesised by impregnation of the desired amount of [Mn_4^{III}] compound (10, 30 and 50 mg for compounds loaded with 1.0, 2.9 and 4.8% [Mn_4^{III}] respectively) inside 1.00 g of RSMNPs in an acetonitrile (200 mL). The dispersion is left to stir at ambient temperature for 24 h before filtration of the solid. The powder is then dried overnight in an oven set at 80 °C.

Table 36: Elemental analysis for [Mn^{III}]@RSMNPs

Mass of [Mn_4^{III}] dissolved (mg)	C (wt%)	Mn (wt%)	Cl (wt%)	N (wt%)
10	27.16	0.10	0.04	0.31
30	26.86	0.28	0.05	0.35
50	27.16	0.48	0.04	0.37

Synthesis of [Mn^{III}]@SiO_2 nanoparticles

[Mn^{III}]@SiO_2 are synthesised by impregnation of the desired amount of [Mn_4^{III}] compound (10, 30 and 50 mg for compounds loaded with 1.0, 2.9 and 4.8% [Mn_4^{III}] respectively) inside 1.00 g of SMNPs in acetonitrile (200 mL). The dispersion is left to stir at ambient temperature for 24 h before filtration of the solid. The powder is then dried overnight in an oven set at 80 °C.

Table 37: Elemental analysis for [Mn^{III}]@SMNPs

Mass of [Mn_4^{III}] dissolved (mg)	C (wt%)	Mn (wt%)	Cl (wt%)	N (wt%)
10	0.45	0.09	0.01	0.26
30	1.05	0.26	0.01	0.33
50	1.50	0.40	0.01	0.34

Synthesis of [Mn^{III}]@carbon-SiO_2 nanoparticles

[Mn^{III}]@carbon-SiO_2 are synthesised by impregnation of the desired amount of [Mn_4^{III}] compound (10, 30 and 50 mg for compounds loaded with 1.0, 2.9 and 4.8% [Mn_4^{III}] respectively) inside 1.00 g of carbon-silica mesoporous nanoparticles (CSMNPs) in acetonitrile (200 mL). The dispersion is left to stir at ambient temperature for 24 h before filtration of the solid. The powder is then dried overnight in an oven set at 80 °C.

Table 38: Elemental analysis for [Mn^{III}]@CSMNPs

Mass of [Mn_4^{III}] dissolved (mg)	C (wt%)	Mn (wt%)	Cl (wt%)	N (wt%)
10	30.33	0.09	0.02	0.34
30	29.93	0.13	0.04	0.42
50	31.06	0.44	0.05	0.53

Synthesis of [Mn^{II}]@resol-SiO_2 mesoporous nanoparticles

[Mn^{II}]@SiO_2-resol mesoporous nanoparticles are synthesised by impregnation of the desired amount of [$Mn^{II}]_n$ compound (10, 30 and 50 mg for compounds loaded inside 1.0, 2.9 and 4.8% [$Mn^{II}]_n$ respectively) with 1.00 g of RSMNPs in acetonitrile (200 mL). The dispersion is left to stir at ambient temperature for 24 h before filtration of the solid. The powder is then dried overnight in an oven set at 80 °C.

Table 39: Elemental analysis for [Mn^{II}]@RSMNPs

Mass of [$Mn^{II}]_n$ dissolved (mg)	C (wt%)	Mn (wt%)	N (wt%)
10	27.21	0.05	0.32
30	26.66	0.17	0.30
50	27.08	0.24	0.39

Synthesis of [Mn^{II}]@SiO_2 nanoparticles

[Mn^{II}]@SiO_2 are synthesised by impregnation of the desired amount of [$Mn^{II}]_n$ compound (10, 30 and 50 mg for compounds loaded with 1.0, 2.9 and 4.8% [$Mn^{II}]_n$ respectively) inside 1.00 g of SMNPs in acetonitrile (200 mL). The dispersion is left to stir at ambient temperature for 24 h before filtration of the solid. The powder is then dried overnight in an oven set at 80 °C.

Table 40: Elemental analysis for [Mn^{II}]@SMNPs

Mass of [$Mn^{II}]_n$ dissolved (mg)	C (wt%)	Mn (wt%)	N (wt%)
10	1.32	0.10	0.19
30	1.76	0.24	0.26
50	2.08	0.32	0.29

Synthesis of [Mn^{II}]@carbon-SiO_2 nanoparticles

[Mn^{II}]@carbon-SiO_2 are synthesised by impregnation of the desired amount of [$Mn^{II}]_n$ compound (10, 30 and 50 mg for compounds loaded with 1.0, 2.9 and 4.8% [$Mn^{II}]_n$ respectively)

inside 1.00 g of CSMNPs in acetonitrile (200 mL). The dispersion is left to stir at ambient temperature for 24 h before filtration of the solid. The powder is then dried overnight in an oven set at 80 °C.

Table 41: Elemental analysis for [Mn^{II}]@CSMNPs

Mass of $[Mn^{II}]_n$ dissolved (mg)	C (wt%)	Mn (wt%)	N (wt%)
10	29.46	0.03	0.40
30	30.58	0.24	0.38
50	30.93	0.38	0.40

II.4.3 Characterisations

Elemental analysis were carried out by the institut des Sciences Analytiques (ISA) for C, H and N; and Crealins company in Villeurbanne (69) for Mn and Si (see the **Annexes** section for more details.)

Infrared spectra were recorded with a Jasco FT/IR-4200 equipped with an ATR pro ONE of the same brand, for the supports, and on KBr pellets with a Thermo Nicolet Avatar 330 FTIR spectrometer for [Mn]@NPs.

Thermogravimetric analysis was undertaken with a NETZSCH STA 409 PC Luxx apparatus under air with a increase of temperature of 10 °C/min.

Nitrogen sorption isotherms were recorded with a volumetric gas adsorption instrument BELSORP-max from MicrotracBEL. The measurement is preceded by a vacuum drying of at least 6 h at 130 °C for pure SMNPs and CSMNPs and at 80 °C for all the other samples. Measurement is made under N_2 at 77 K with an average initial pressure of 1.36 ($\pm$0.09)$\times 10^{-5}$ Pa.

Scanning Electron Microscopy was performed with a Zeiss SUPRA 55 VP microscope using secondary electron mode and a 5 keV tension.

TEM and EDS analysis were performed by Dr. Clémentine Fellah from the Laboratoire de Géologie, Terre, Planètes, Environnement (LGL-TPE) of the ENS de Lyon.
The samples were characterized by high resolution transmission electron microscopy with a JEOL 2010F TEM operating at 200 kV. The samples for TEM were sonicated in ethanol and deposited onto carbon coated copper grids.

The AFM is a JPK Nanowizard 4. Measurements were performed in peak-force mode.

Raman spectroscopy analysis was conducted by Dr. Gilles Montagnac from the Laboratoire de Géologie, Terre, Planètes, Environnement (LGL-TPE) of the ENS de Lyon.
Raman measurements were performed with 2 different wavelength, 244 nm and 532 nm. Multi-wavelength study is particularly informative for these graphitic materials because of dispersive behavior of some Raman modes. Unpolarized Raman spectra excited with 532 nm of a continuous wave (CW) solid-state laser, were recorded by a HoribaTM LabRam HR800

spectrometer with a magnification 100 objective. Laser power is a threat for these samples because they strongly absorb the light. Consequently, we paid a particular attention to avoid sample degradation by working with laser mean power under 100 μW. Typical collection time was 5 minutes for the first or the second order of each spectrum. Unpolarized UV Resonant Raman Spectroscopy (UVRRS) was excited with 244 nm and collected by a dedicated Horiba-aTM LabRam HR800 spectrometer with a magnification 40 objective. The laser source is a frequency doubled argon ion laser. Working with continuous mean power under 100 μW was not enough to preserve the sample. We had to spread the powder on the glass slide surface and rotated it with a motorized microscope turntable. By this way, the laser power is divided on a larger surface and the laser spot is always focused during the light collection (3 or 5 minutes).

^{29}Si and ^{13}C NMR measurement were done by Chantal Lorentz from the Institut de recherches sur la catalyse et l'environment de Lyon (IRCELYON).

Part III

Physical and chemical properties of [Mn]@NPs materials

In this chapter we present the magnetic and optical properties of the materials prepared and we report the preliminary H_2O_2 disproportionation catalytic tests. To begin with, the main new techniques used in that part are presented.

III.1 Introductory remarks

III.1.1 Notations

In this chapter, we assume that the Mn quantity measured with elemental analysis can be directly related to the load of each sample in Mn compound (even if it is debatable). The [Mn]^w@NPs notation is used with w the weight percentage of the compound, [Mn], loaded in the particle, NP.
The [Mn^{II}] and [Mn^{III}] notation, without nuclearity mentioned, is also used to describe, respectively, [$Mn^{II}]_n$ and [Mn_4^{III}] after their insertion inside the particles. It is necessary because we suspect that the original compounds break, at least partially, when inserted. And, despite our attempts, it is very difficult to characterise precisely these fragments.

III.1.2 Luminescence spectroscopy

As described earlier for IR spectroscopy, molecules can absorb electromagnatic radiations in a wide range of energies. For IR, it corresponds to the excitation of the vibration modes of molecular bonds, for visible and UV (200 to 800 nm) it is the excitation of valence electrons and with X-rays, it can go down to electrons on inner orbitals. The analysis of UV and visible absorption in itself, is a widely used technique that provides information on the electronic structure of molecules and has a wide range of applications, from the determination of a concentration, following Beer-Lambert law, to the study of metal-ligand complexation with Tanabe-Sugano diagrams.
When the molecules cease to be submitted to these external stimulation, they usually return quickly to their fundamental state by dissipating energy, be it with chocks (heat),vibrations or energy transfer to other molecules. But some molecules can also dissipate energy by radiating a photon of energy equal or lower than the excitation they were submitted to, this radiative transfer is called luminescence. The difference between the wavelength of excitation and the wavelength of the emitted radiation is the Stokes shift. If the transfer is quick (in the range of nanoseconds) and happens between singlet states it is fluorescence. If it is longer (milliseconds to hours) and requires rearrangement from triplet to singlet state it is phosphorescence. To describe the transitions between this different energy states and the emissions, a Perrin-Jablonsky diagram is the most common tool. **Figure 88** shows an example of a simple diagram for the luminescence of a molecule.

To study the luminescence of a species, two spectra are usually recorded with the spectrofluorimeter: emission and excitation spectra. The emission spectrum is the response of the species when submitted to the stimulation of a precise wavelength. The detector scans the desired range of the electromagnetic spectrum and records the light emitted at different wavelengths. The excitation spectrum is essentially the opposite, the detector is set to record the emission at a specific wavelength and the sample is excited with a wide range of radiations.

This latter technique is similar to the recording of an absorption spectrum, except than the light intensity measured is not transmitted through the sample but emitted by it (and thus requires a different detector set up).

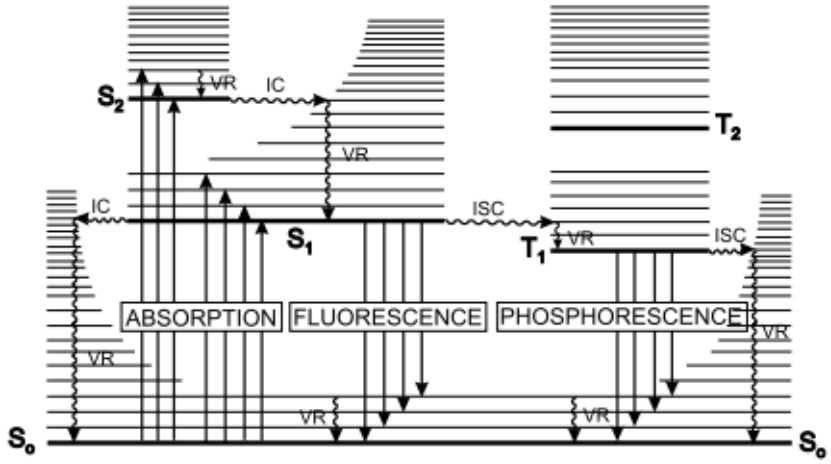

Figure 88: Perrin-Jablonsky diagram presenting the different luminescence types.

III.1.3 Gas volumetry

The gas volumetry set-up is designed to measure the amount of dioxygen generated by hydrogen peroxyde decomposition, according to the following reaction :

$$2H_2O_2 \rightarrow 2H_2O + O_2 \quad (27)$$

The efficiency of the catalyst can be linked to the volume of O_2 when compared to the amount of H_2O_2 used. **Figure 89** presents the arrangement employed to measure O_2 volume. A similar set-up was used is the literature for other compounds.[56,57,175,227,228]
The closed flask containing the solution or suspension to be tested is connected to a gas-burette filled with water or n-hexane and equilibrated at ambiant pressure with an opened reservoir. The H_2O_2 aqueous solution is injected with a syringe through the septum that caps the flask and does not necessitates the opening of the set-up. The flask containing the solution is immersed in water at ambient temperature in order to prevent any gas expansion due to the potential heat generated by H_2O_2 disproportionation.

The overpressure caused by O_2 production moves the liquid in the burette, therefore providing the volume of oxygen generated by the reaction (V_{O_2}). This volume does not however correspond to standard pressure ($V^0_{O_2}$) and the system has to be calibrated to find the corrective volume factor ($\alpha = \frac{V^0_{O_2}}{V_{O_2}}$).
The calibration is made by the disproportionation of set amounts of H_2O_2 with $KMnO_4$. The $KMnO_4$ quantity used corresponds to three times the stoichiometry value in order to insure that the reaction is total. The correction factor is found to be $\alpha = 0.73$. Once $V^0_{O_2}$ is determined, the amount of oxygen produced (n_{O_2}) can be deduced using the ideal gas law.

Gas-volumetry experiments ultimate goal in this work, is to compare the activity of the synthesized [Mn] compounds and materials. The fundamental issue of these complex and the reason why a work is performed on [Mn]@NPs materials is that the bio-mimetic catalase compounds prepared are inactive in water. An important parameter of the discussion is the effect of pH on the molecule's catalytic activity. In order to do so in acetonitrile-water solutions the pH units must be converted from ${}^{s}_{w}$pH (pH measured by the electrode, calibrated in 100% water media) to ${}^{s}_{s}$pH ("real" pH in the acetonitrile-water (9:1 v/v) solution). All the experiment performed in acetonitrile media correspond to CH_3CN-H_2O (9:1 v/v). According to the work of L.G. Gagliardi *et al.*[229] the δ factor adjustment between both media is defined as:

$$ {}^{s}_{s}\mathrm{pH} = {}^{s}_{w}\mathrm{pH} - \delta \tag{28} $$

and for our proportions δ = -1.61 at 20 °C.

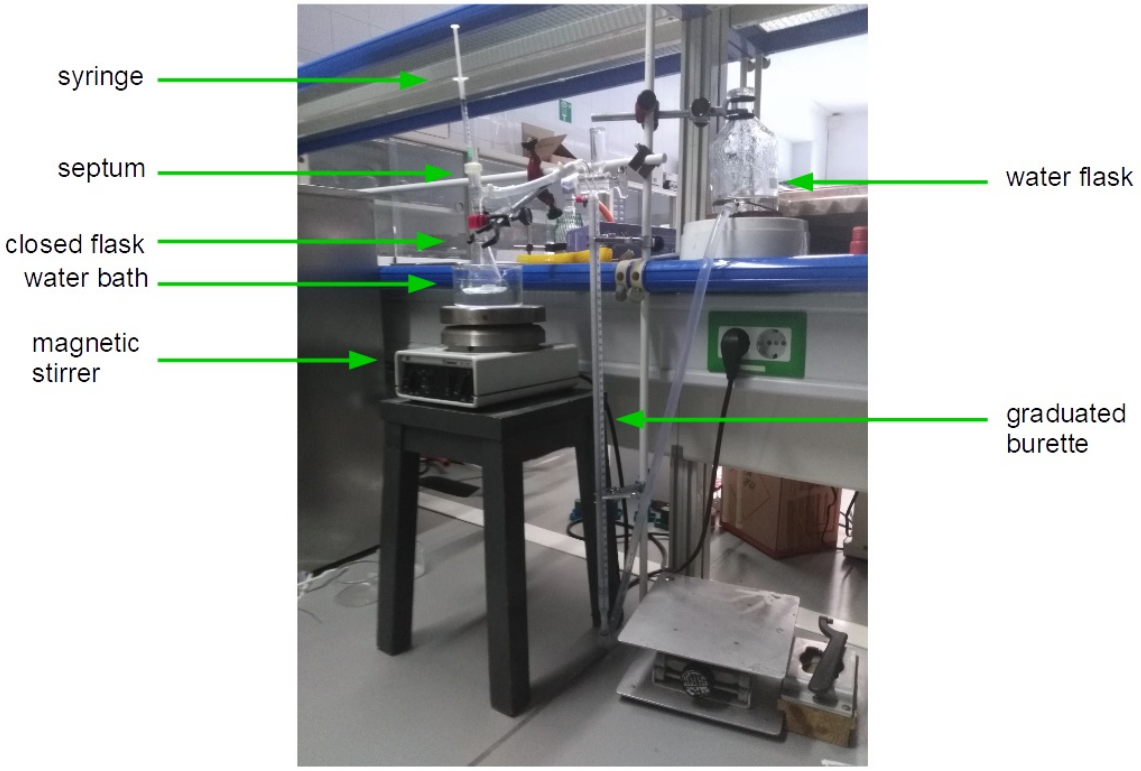

Figure 89: Experimental set-up used to measure the catalytic activity of [Mn] compounds and [Mn]@NPs materials.

III.2 Study of the magnetic properties of [Mn]@NPs materials

In order to understand better what happens to Mn compounds when they are inserted inside the mesoporous nanoparticles, the magnetic properties of the [Mn]@NPs materials was studied. The aim of this section is to detect the magnetic answer of the [Mn]@NPs materials and to deduce from it if the compounds inside are intact. And, if they are not, to try to understand what kind of fragment could be present. To avoid misinterpretation the magnetic behaviour of the support itself was also studied.

III.2.1 Study of the magnetic properties of NPs

SMNPs and CSMNPs have a significant answer to magnetic field, contrary to RSMNPs. As a consequence, it possible to assign these signals to the presence of paramagnetic defects inside the NPs matrix, induced by the thermal treatment (**Figure 90**). These impurities probably originate from carbon or carbon induced defects in the silica. Indeed, for the other [Mn]@silica materials from the literature,[56,90,179,230] the silica support (MCM-41) does not present such a magnetic answer. Actually, they were either prepared without thermal treatment[56,90,179] or with largely smaller amount of organic material during calcination.[230]

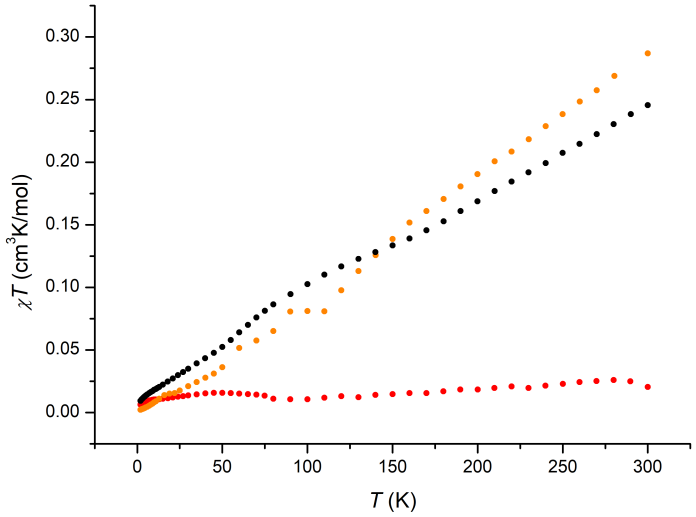

Figure 90: Molar magnetic susceptibility times temperature plotted versus temperature for RSMNPs support (red circles), SMNPs support (orange circles) and CSMNPs support (black circles).

The presence of such impurities is further supported by the detection of carbon radicals in the CSMNPs material (**Figure 91**). The presence of these radicals has been documented for graphitised mesoporous systems[231] and nanoparticles.[220,232]

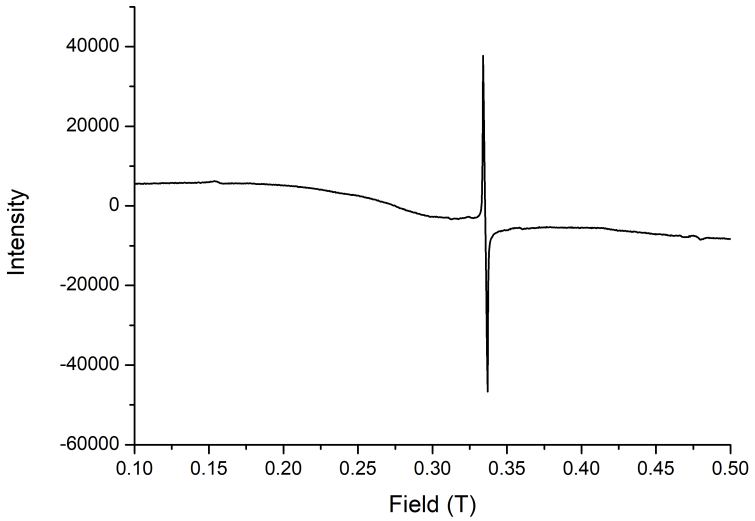

Figure 91: X-band EPR spectrum of CSMNPs powder at 12K.

III.2.2 Study of the magnetic properties of [Mn]@NPs materials

Unfortunately, the simple subtraction of the blank for SMNPs and CSMNPs leads to a strong distortion of the signal. Moreover their curves display shoulders characteristic of the presence of dioxygen impurities. It should also be noted that the amount of compound is quite small compared to the mass of the sample (between 2.9% and 4.6%), weakening the magnetic answer and making the signal more sensitive to the effect of the impurities. As a consequence these spectra cannot be exploited.
The signal of [Mn^{II}]@RSMNPs and [Mn^{III}]@RSMNPs is however clean enough to make observations and interpretations (**Figure 92**). As the magnetic answer of RSMNPs alone is negligible, the signal detected for [Mn]@RSMNPs can be attributed to the Mn entities loaded inside.

χT versus T curves of both [Mn^{II}]@RSMNPs and [Mn^{III}]@RSMNPs decrease as temperature fall but they do not reach zero for the lowest temperature.
To explain the shape of these χT graphs, several simulations were carried out. It is not possible to reproduce the graph considering only the ZFS of the Mn ions or only the magnetic interaction and both were necessary to obtain a good simulation. From the different simulations we can propose that:

- The magnetic data of the [Mn_4^{III}] system inside the RSMNP suggests that the tetranuclear entity is broken and a dinuclear entity seems to be formed.

- In both cases (Mn^{II} and Mn^{III}) a dinuclear entity is considered and a weak magnetic interaction is found between the Mn ions. Simulations found a J of -0.6 cm^{-1} for both [Mn^{II}]@RSMNPs and [Mn^{III}]@RSMNPs

- The graph for the [Mn^{III}]@RSMNPs system is simulated with usual values of ZFS of the Mn^{III} ions and a dinuclear unit. The introduction of a weak antiferromagnetic factor

(-0.6 cm^{-1}) along with D_{Mn} (-3 cm^{-1}) and orthogonal directions of the Jahn-Teller axes gives a good simulation of the evolution of the experimental data points.

- The simulation or [Mn^{II}]@RSMNPs do not reproduce well the behaviour of experimental data at low temperatures. It seems that the magnetic coupling constant is weak (J = -0.6 cm^{-1}) and the orthogonal distortion higher than expected for Mn^{II} ions (D_{Mn} = -1 cm^{-1}).

From these results we can expect that a dinuclear entity is present inside the NPs in all the cases.

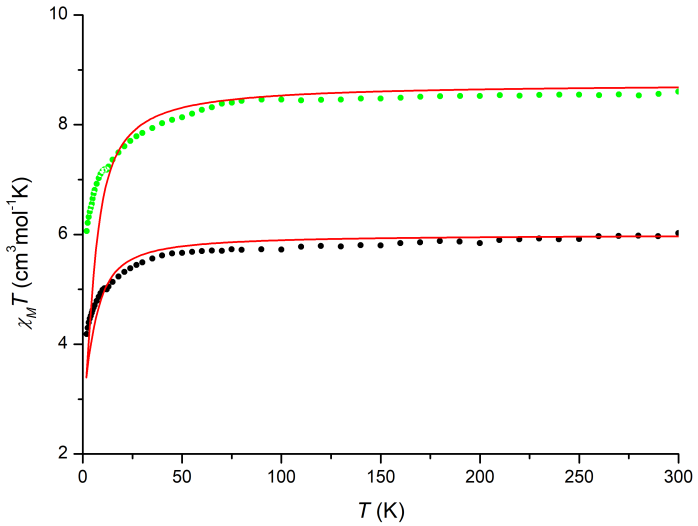

Figure 92: Molar magnetic sensibility times temperature plotted versus temperature for [Mn^{II}]@RSMNPs (green circles) and [Mn^{III}]@RSMNPs (black circles). The simulated curves for each material are represented in red.

The EPR spectra of the [Mn^{II}]@NPs at 77 K shows six bands of different intensities (**Figure 93**). This kind of spectrum is usually found in solution.[56,90,230] It is assigned to dinuclear Mn^{II} system with weak magnetic interactions and hyperfine coupling due to the $I_{Mn} = \frac{5}{2}$. The spectrum with the best resolution is found for the RSMNPs. The spectrum for SMNPs has a lower resolution for the six characteristic bands of the Mn^{II} ion, probably due to the presence of the impurities detected in the magnetic measurement of the support. The spectrum of the CSMNPs shows a sharp band characteristic of a radical (see above) together with the six smaller bands dues to the [Mn^{II}] complex.

Unfortunately, we are not able to simulate this kind of spectrum with the PHI software because it does not take into account hyperfine coupling. However, this kind of shape has been simulated in the past by other members of our group on the "easyspin" software[?] for dinuclear Mn^{II} systems with low magnetic interactions, ZFS and hyperfine coupling. As a consequence, it seems that every interpretation points toward dinuclear systems with weak coupling and hexacoordination of the Mn^{II} ions. However, it is not possible to conclude in some structural changes like ligand exchange or Mn$\cdots$Mn distance variation.

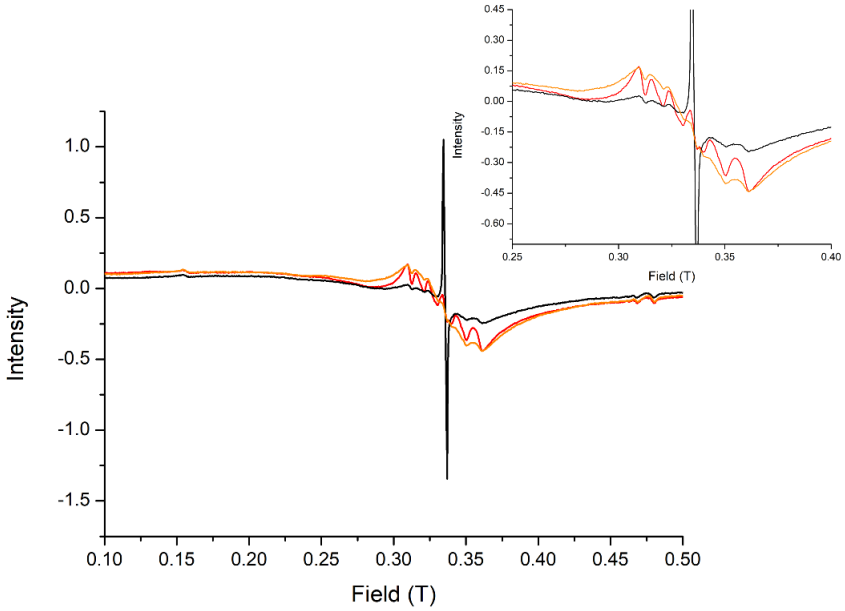

Figure 93: X-band EPR spectrum of [Mn^{II}]@RSMNPs (red line), [Mn^{II}]@SMNPs (orange line) and [Mn^{II}]@CSMNPs (black line) measured at 77 K.

III.3 Luminescence of [Mn] complexes

The aim of the use of luminescent ligand is that, first, as silica is a transparent media, successfully grafted Mn complexes with a luminescent ligand could provide the position of the nanovector through fluorescence microscopy. And second, that modification of the environment of the fluorophore (complexation, contact with the vector or the solvent) would quench, amplify or otherwise modify the luminescence of the carboxylate ligand, thus providing information on its behaviour in or outside the particles. 9-anthracene carboxylate was selected as anthracene is a well known and common luminescent molecule.
The anthracene molecule ($C_{14}H_{10}$) emission is measured in the 400-500 nm range and has been widely studied.[233] It has two sets of absorption bands, from 220 to 280 and 290 to 400 nm. They correspond to $\pi \rightarrow \pi^*$ transitions and have a distinctive vibronic structure due to transition moments oriented through different molecular axes.
The position of these bands, their quantum yield and lifetime are independent from solvent polarity.[234–237] However, this is not the case of 9-anthracene carboxylic acid, which displays sensitivity to the polarity of its environment.[238–240] Modification causes of the luminescence of the 9-anthracene carboxylic acid have been widely discussed and multiple explanations were proposed: acid-base equilibrium, solvent or concentration-dependent formation of dimers or higher order aggregates and structural reorganisation of the anthracene ring occurring in excited states.[237,241–248] Thus, the modification of 9-anthracene carboxylate ligand luminescence can provide informations on its coordination, concentration or pH of its environment.

The absorption and emission spectra of 9-anthracene carboxylic acid are displayed in **Figure 94**. In the absorption spectrum the band centred at 254 nm correspond to the $^1A \rightarrow {}^1B_b$ transition (in Platt notation) and bands at 384 nm, 365, 347 and 330 nm match the $A^1 \rightarrow L^1$ transition. As expected, the emission spectra mirrors the latter bands with the separation of the Stoke's shift. These bands, found at 390, 412, 438 and 464 nm correspond to the L^1

$\rightarrow A^1$ transition.[243,246] The apparition of a large and intense band at 470 nm can occur in case of a change in concentration of the solution, a modification of the solvent polarity or of its pH.
A discussion on the effect of these parameters has been presented in a recent paper of Rowe and colleagues.[246] By studying the effect of the positions of the carboxylic acid groups on anthracene carboxylic diacids they came to the conclusion that the structure of the emission is strongly affected by the contribution of the carboxylic acid groups to the excited state of the molecule. Effects that prevent their contribution (hindrance of the rotation angle, deprotonation or inductive effects) favour the contribution of anthracene ring atoms to the excited states, therefore structuring the emission. On the other hand, if the contribution of the carboxylic acid to the excited state is promoted (by factors opposite to the ones previously cited), the bands widen and lose their structure. Giving rise to a so-called exciton band. Moreover, effects that stabilise the energy of the main excited state (like the solvent polarity or the functionalisation of the ring) tend to favour a bathochromic shift (in the range of 20-30 nm for the studied examples).[246]

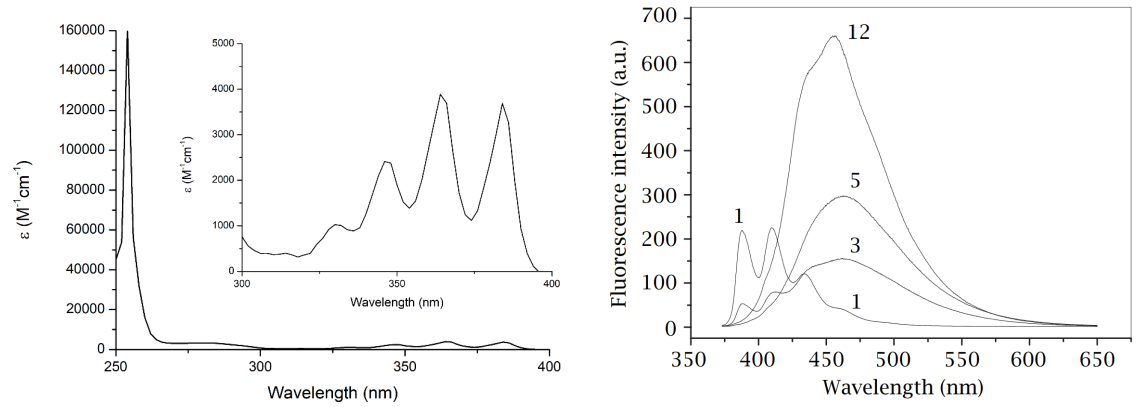

(a) (b)

Figure 94: (a) Absorption spectrum of 9-anthracene carboxylic acid in EtOH (6.2×10^{-5} mol/L). (b) Emission spectra at 363 nm of 9-anthracene carboxylic acid in different solvents (2.5×10^{-6} mol/L): 1: water, 3: ethanol, 5: acetonitrile, 12: cyclohexane. This figure comes from the *Int. J. Photoenergy* 2000 from M. S. A. Abdel-Mottaleb *et al.*[243]

$[Mn^{II}]_n$ and $[Mn_4^{III}]$ complexes exhibit a strong luminescence in ethanol solution as well. No matter the concentration, $[Mn^{II}]_n$ emission always has the same shape with distinctive anthracene-like vibronic bands at 390, 412, 438 and 462 nm (see **Figure 95**).

On the other hand $[Mn_4^{III}]$ emission is strongly concentration dependant. Its spectrum also displays vibronic bands at 390, 412 and 438 but presents a large band with a maximum between 460 and 468 nm whose intensity increases with concentration. **Figure 96** and **Figure 97** show the evolution of the shape of the spectrum with this parameter. It is interesting to notice that the maximum of this band is always below the 470 nm observed in ethanol for the free molecule which tends to dismiss the hypothesis of ligands decoordination in solution.[243]

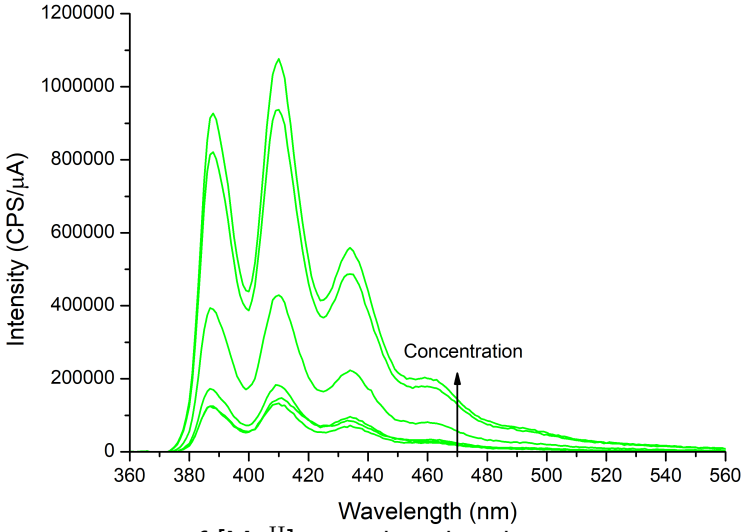

Figure 95: Emission spectra of $[Mn^{II}]_n$ in ethanol with increasing concentrations ($\sim 10^{-7}$ to 10^{-6} mol/L). Excitation wavelength: 362 nm.

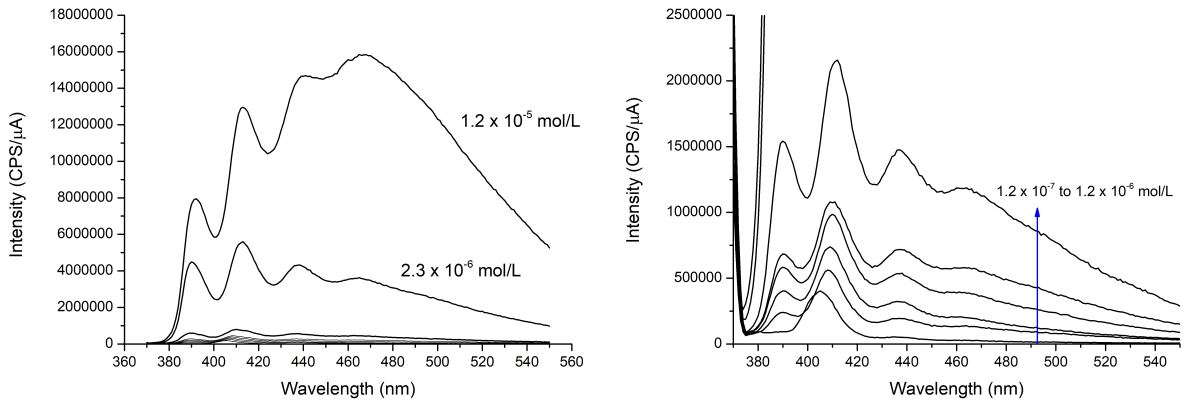

(a) (b)

Figure 96: Emission spectra of $[Mn_4^{III}]$ in ethanol with concentrations from 1.2×10^{-5} to 1.2×10^{-8} mol/L. Excitation wavelength: 362 nm. All spectra were recorded with two different spectrometers settings one adapted to the highest concentrations, the other to the lowest ones. The spectra displayed are the ones with the best resolution to saturation ratio, hence the change of unit scale.

In order to be able to discuss the apparition of the exciton band, a series of measurements of the emission of $[Mn_4^{III}]$ were performed a various concentrations in ethanol. The plot in **Figure 97** shows the evolution, for the $[Mn_4^{III}]$ compound, of the intensity ratio between the band at 412 nm, which is the most intense one below 6.4×10^{-6} mol/L, and the large band with its maximum between 460 and 468 nm, which becomes prevalent above this concentration. These values match the apparition of the large 470 nm exciton band for 9-anthracene carboxylic acid around 10^{-5} mol/L.[243] From the measurements, we tried to find a relation between the bands intensity and the $[Mn_4^{III}]$ concentration of the solution. We noticed a linear relationship between the intensity ratio of the two main bands and the decimal logarithm of concentration. The following equation is the result of the linear fit of these values:

$$\frac{I_{412\mathrm{nm}}}{I_{464\mathrm{nm}}} = \frac{\log(C)}{2} + 3.6 \tag{29}$$

where I_x is the intensity measured for a wavelength x and C the concentration of the solution. The R value is 0.98.[vi]

The apparition of the large 464 nm band in ethanol for the $[Mn_4^{III}]$ complex and not for the $[Mn^{II}]_n$ can also be related to the fact that the $[Mn_4^{III}]$ is much more insoluble than $[Mn^{II}]_n$ for the large range of solvents tested. It would be more likely for $[Mn_4^{III}]$ to form aggregates or oligomers in solution and explain, thus, the wide band emission.

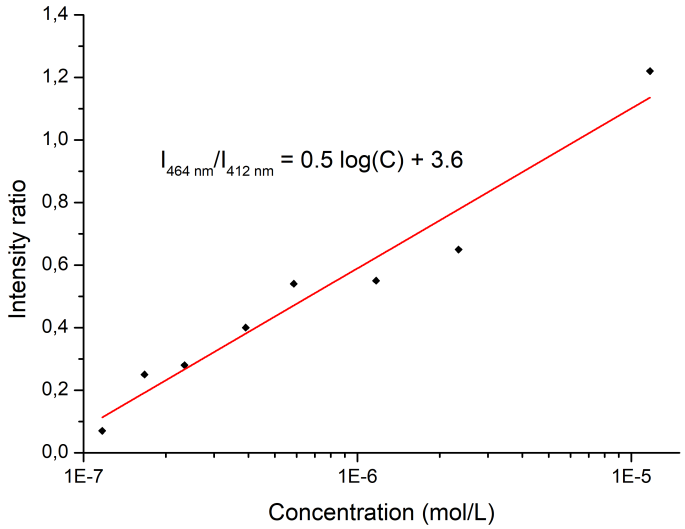

Figure 97: Ratio between the intensity measured at 464 nm and at 412 nm ploted versus the decimal logarithm of concentration for $[Mn_4^{III}]$.

When compared to pure 9-anthracene carboxylic acid, the emission of both complexes is less intense for a given concentration (**Figure 98**). This not very surprising given, the potential disruption provoked by electronic or magnetic interactions with neighbouring Mn ions. Again for a same concentration, the emission of $[Mn^{II}]_n$ complexes is less intense than for $[Mn_4^{III}]$. When the emission spectra is integrated, the ratio between the intensity of emission of both complexes is found to be 1.8 in favour of the $[Mn^{III}]$.

[vi] See ii page 66

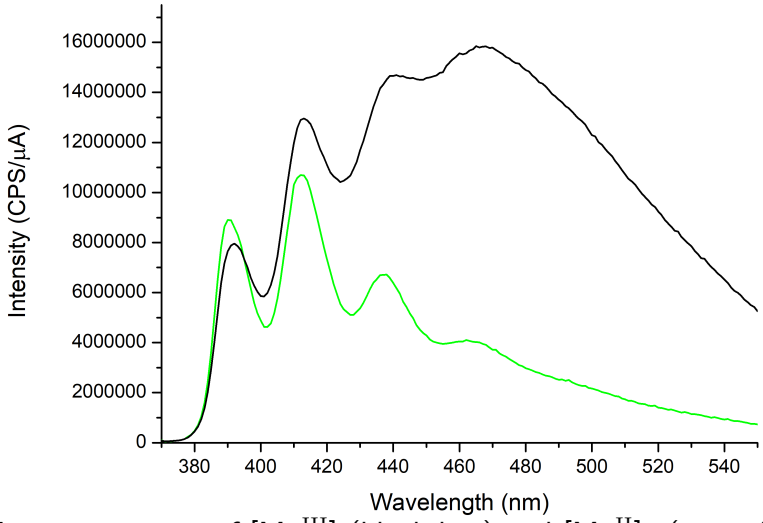

Figure 98: Emission spectra of $[Mn_4^{III}]$ (black line) and $[Mn^{II}]_n$ (green line) 1.2×10^{-5} mol/L in ethanol. Excitation wavelength: 362 nm.

III.4 Luminescence of [Mn]@NPs materials

After the insertion of the Mn complexes inside the particles, fluorescence is still detected but several questions arise. Is the emission of the complexes modified by its environment inside the molecule ? Are eventual modifications of the complexes structure detected through fluorescence spectroscopy ? Do the complexes leach out in the solution ? This section attempts to answer these interrogations.

III.4.1 Luminescence of NPs

First, it is needed to interpret the emission spectra of the nanoparticles in ethanol suspension (250 mg/L) and to see how they contribute to the luminescence of the whole hybrid material (**Figure 99**). The particles are excited at 362 nm which is our working wavelength for both Mn complexes. They all display the same 407 nm band that comes from the silica phase. This large band can be found in different siliceous materials, usually quartz crystals and silica aerogels. It is supposed to come from defects inside the silica structure and many defect-related mechanisms have been proposed (non-bridged oxygen hole centers, carbon impurities, nitrogen centred effects, charge transfer mechanisms or surface Si-OH states).[249,250] For silica nanoparticles, usually prepared in basic conditions, it is a lot rarer. Jakob and Schmedake in *Chem. Mater.* 2006 report this type of luminescence, for nanoparticles modified with (3-aminopropyl)triethoxysilane (APTES).[250] They link this phenomenon with the amount of carbon introduced with APTES inside their particles, and hence to the carbon impurities generated during calcination. In a later article they show that an emission transfer with lanthanides ions is possible and reduces the fluorescence of their material.[251] However, they do not observe any luminescence before thermal treatment of their particles contrary to our case.

In the emission spectrum of SMNPs, the band maximum is followed by a large shoulder with a maximum around 435 nm (**Figure 99**). For the other NPs types, this shoulder is a lot narrower and without a secondary maximum, more akin to an asymetric deformation of the main 407 nm band.
Finally, for RSMNPs another band is recorded around 475 nm and attributed to the luminescence of the resol polymer.[252–254] This band disappears for CSMNPs, which is a good indicator that the polymer is degraded to amorphous carbon.

Multiple interpretations can be given for the reduced intensity of RSMNPs and CSMNPs compared to SMNPs. The silica phase may transfer some energy to the organic phase, and it would quench the emission process. It is also possible to consider that, if other materials require a thermal treatment for luminescence to be observed, the effect of the defects present in our materials would be reinforced with the calcination process. This, however, would not explain why CSMNPs emit as much as RSMNPs. The intensity change could also be due to different interaction of the materials with the solvent molecules. Hybrid mesoporous nanoparticle are more hydrophilic than the pure silica ones, and are thus expected to retain more solvent. However, given the multiple possible origins of this luminescence phenomenon and the limited data we collected about it, it is impossible to give a definitive answer.
In order to study the impact of the luminescence of the particles on the [Mn]@NPs material, **Figure 100** represents the emission of the particles of each type with the smallest load compared to the emission of the vectors alone.

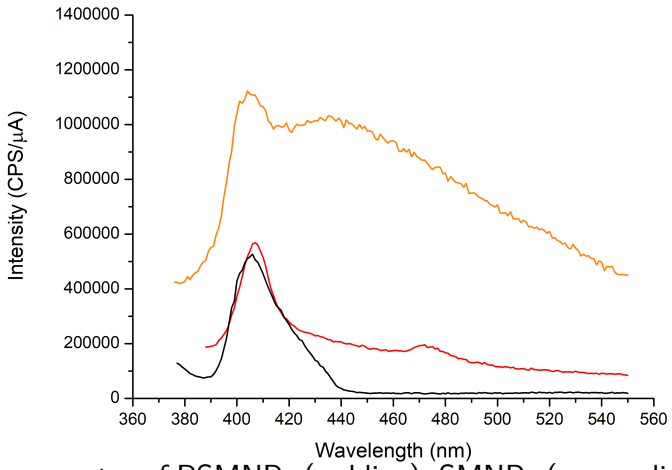

Figure 99: Emission spectra of RSMNPs (red line), SMNPs (orange line) and CSMNPs (black line) suspension in ethanol (250 mg/L) with a 362 nm excitation wavelength.

Interestingly, it seems that the emission of all particles types is largely quenched with only a small amount of both Mn complexes. And even the emission recorded for [Mn]@SMNPs and [Mn]@CSMNPs looks a lot more like the spectra of the complex than the spectra of the nano-vector material. Meaning that its contribution is greatly reduced overall. Moreover these graphs evidence that at least a minimal amount of complex stays inside or on the particles surface, enough to extinguish their emission. As a consequence of this discussion, in the following paragraph all the [Mn]@NPs emission spectra do not receive any blank subtraction as we consider that the luminescence of the NPs themselves is completely quenched.

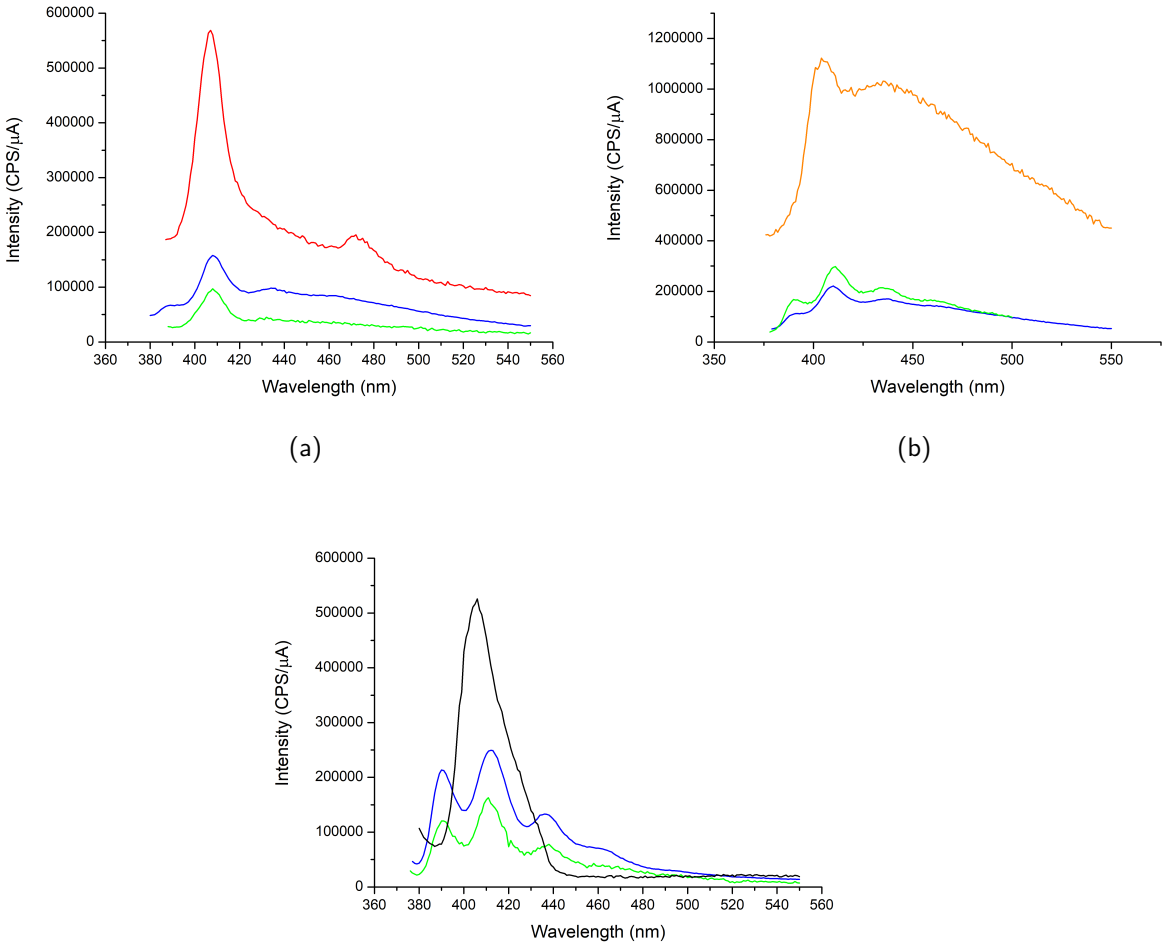

Figure 100: Emission spectra of [Mn]@NPs with the smallest Mn compound load for each NP type compared to the emission spectra of empty NPs. Suspensions correspond all to 250 mg/L of NPs in ethanol. Excitation wavelength: 362 nm. Concentrations refer to Mn compounds. (a) RSMNPs (red), $[Mn^{II}]^{0.6}$@RSMNPs (green) (1.1×10^{-7} mol/L), $[Mn^{III}]^{1.0}$@RSMNPs (1.1×10^{-7} mol/L) (blue) (b) SMNPs (orange), $[Mn^{II}]^{1.2}$@SMNPs (2.3×10^{-7} mol/L) (green), $[Mn^{III}]^{0.9}$@SMNPs (1.0×10^{-7} mol/L) (blue) and (c) CSMNPs (black), $[Mn^{II}]^{0.4}$@CSMNPs (6.7×10^{-8} mol/L) (green) and $[Mn^{III}]^{0.9}$@CSMNPs (1.0×10^{-7} mol/L) (blue).

III.4.2 Luminescence of [Mn^{II}]@NPs materials

To begin with the study of [Mn^{II}]@NPs, it is important to understand what exactly is observed with the spectrophotometer. Indeed, fluorescence is a very sensitive phenomenon, multiple effects can modify it (as mentioned earlier in this section) or extinguish it partially or completely, commonly referred as luminescence quenching.
The main way to achieve it in this study was the comparison between the material in suspension and the same solution stripped of the nanoparticles. For this, two methods were used. The first is the centrifugation of the suspension (4000 rpm, 10 min) in order to collect and study the supernatant without the particles. The second is the filtration of the suspension through 40 nm nylon filters to the same ends.
Emission spectra of these supernatants were recollected for the most important load of each [Mn^{II}]@NPs type with a concentration of 25 mg/L of particles in ethanol. Spectra are displayed in **Figure 101** and in **Figure 102**, showing the value of the integer for each curve (between 380 and 550 nm)

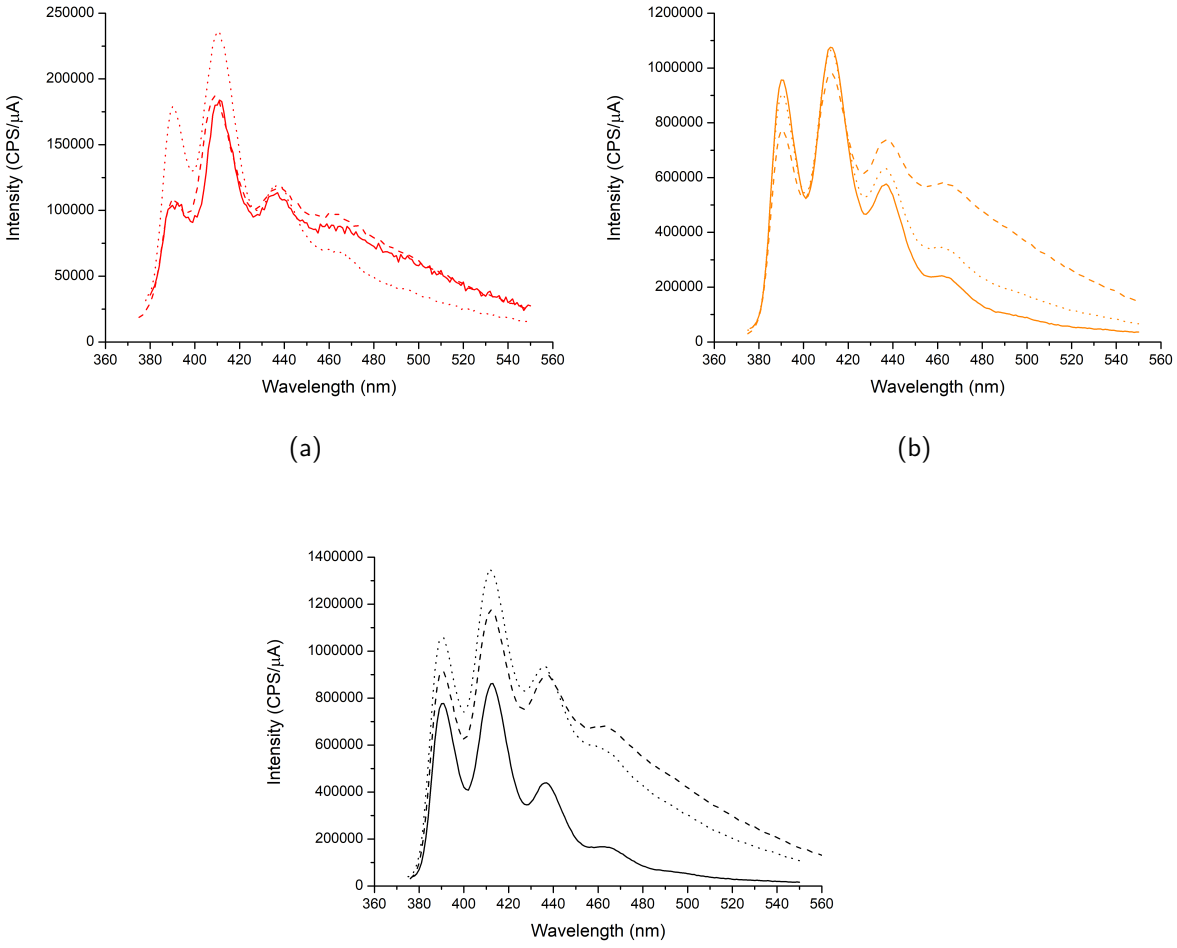

Figure 101: Emission spectra of [Mn^{II}]@NPs for each NP type (full line) compared to the emission spectra of the supernatant after centrifuagtion (dashed line) and the filtrate (dotted line).(a) [Mn^{II}]@RSMNPs, (b) [Mn^{II}]@SMNPs and (c) [Mn^{II}]@CSMNPs.

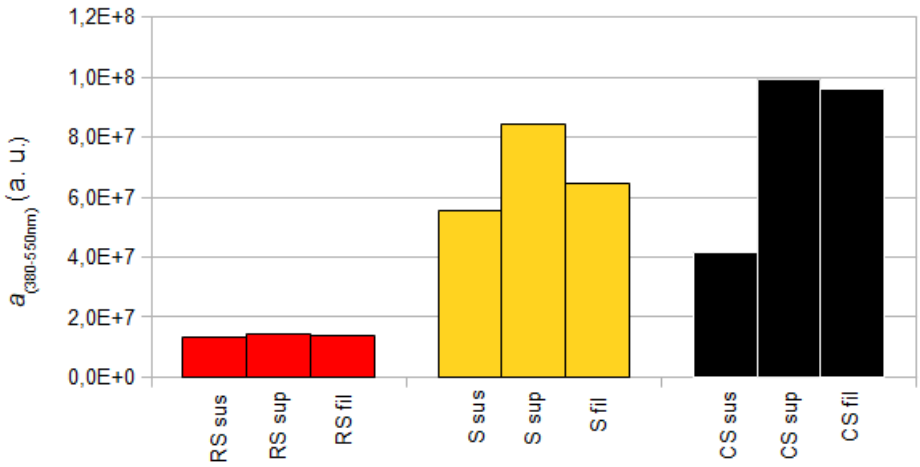

Figure 102: Value of the area below the emission curve between 380-550nm for $[Mn^{II}]^{2.9}$@RSMNPs (5.5×10^{-7} mol/L) (RS - red), $[Mn^{II}]^{3.9}$@SMNPs (7.3×10^{-7} mol/L) (S - yellow) and $[Mn^{II}]^{4.6}$@CSMNPs (8.7×10^{-7} mol/L) (CS - black). sus: suspension ; sup: supernatant ; fil: filtrate.

Graph **101(a)** shows that after the filtration, the intensity recorded is slightly superior to what is observed for $[Mn^{II}]$@RSMNPs in suspension (0.7%) but both are very low compared to the other materials. As a consequence it means that the luminescence of the compound is completely quenched inside the particles and that the emission observed in suspension is only coming from free $[Mn^{II}]$ compounds. As the intensity of this emission is particularly low, most compounds remain inside the particles. Considering the physical and chemical properties of the hybrid material it is not very surprising. As mentioned in section **II.3**, resol is an inflatable and flexible material, so it makes sense that it would be able to prevent $[Mn^{II}]$ from leaking by mechanically obstructing the channels. On the other hand, the resol structure, composed of polyphenol could provide a better link than SiO_2 or pure carbon thanks to π-stacking or other interactions with the aromatic rings of the complex. In previous studies in our laboratory, functionalisation of mesoporous silica with imidazoline or pyridin has been demonstrated to prevent dinuclear Mn^{III} compounds with pirydine or phenatroline ligands from leaking.[57,230] And the same properties that makes resol network a good $[Mn^{II}]$ trap are also likely to quench its emission. The more interaction the fluorophores have with their environment, the more likely they are to transfer their energy to it and possibly de-excitate in a non radiative way.
The emission of the supernatant after centrifugation is a bit more emissive (5.5%), this again suggests that the bulk of the emission is coming from free $[Mn_2^{II}]$ complexes released from the particle during the centrifugation. It makes sense that $[Mn^{II}]$ can be detached during a process which imposes stress on the particle rather than the filtration that is softer for the material.

For $[Mn^{II}]$@SMNPs and $[Mn^{II}]$@CSMNPs the observation is similar, however a significant increase in the intensity appears already with the filtration (17% and 130% respectively). Considering the nature of these materials, it makes sense that $[Mn^{II}]$ is more loosely bonded to it than for a resol-silica matrix. Unfortunately, it prevents us from assuming that $[Mn^{II}]$

is totally quenched inside the particle. Indeed, if the complex is only slightly luminescent but if massively released when subject to the filtration, the measured intensity will appear more intense due to the excess of released [Mn^{II}] instead of less intense due to the loss of contribution of the particles.

For SMNPs and CSMNPs, it could be argued that the treatments applied to the particles are responsible for the [Mn^{II}] release. That [Mn^{II}]@NPs are brightly emissive but that filtration and centrifugation empty the particles entirely. This argument can be dismissed because the overall emission is way less intense when it comes to [Mn^{II}]@NPs suspensions than their counterpart in ethanol solutions as shown by **Figure 103**. So [Mn^{II}] is, at least partially, quenched inside the NPs.
Even in the case where the compound would not be intact, as suggested in section **II.3**, if anthracene carboxylate ligands were to be released, the intensity of their emission should be more important than what is observed.

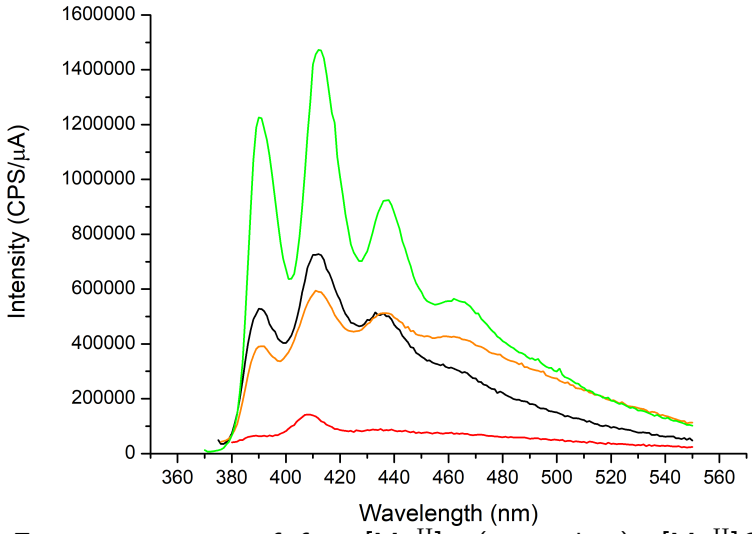

Figure 103: Emission spectra of free [$Mn^{II}]_n$ (green line), [Mn^{II}]@RSMNPs (red line), [Mn^{II}]@SMNPs (orange line and [Mn^{II}]@CSMNPs (black line). Concentration of [Mn^{II}] is 5.5×10^{-7} mol/L in ethanol for each solution/suspension. Excitation wavelength: 362 nm.

Table 42 sums up in a more quantitative way the difference between [Mn^{II}] emission free in solution, inside the particles and released with the two treatments. This table is only a guide line for SMNPs and CSMNPs, as it is hard to be sure that they totally quench [Mn^{II}] emission. However, assuming that the integral of the intensity is proportional to [Mn^{II}] concentration in solution, it gives a good approximation of the amount of complex released by RSMNPs in solution in different conditions, as [Mn^{II}] is, very likely, completely quenched in this type of NP.

Table 42: Evolution of the integrate of the emitted intensity measured for all NP types.

NP type	capture $\frac{a_{sol}-a_{sus}}{a_{sol}}$ (%)	centrifugation release $\frac{\lvert a_{sus}-a_{sup}\rvert}{a_{sus}}$ (%)	filtration release $\frac{\lvert a_{sus}-a_{fil}\rvert}{a_{sus}}$ (%)
[Mn^{II}]@RSMNPs	88	5.8	0.7
[Mn^{II}]@SMNPs	38	51	17
[Mn^{II}]@CSMNPs	46	138	130

a_{sol}: area below the the emission curve (380-550 nm) of free [Mn^{II}]$_n$ in ethanol suspension ; a_{sus}: area below the the emission curve of [Mn^{II}]@NPs in ethanol suspension ; a_{sup}: area below the the emission curve of the corresponding centrifugation supernatant ; a_{fil}: area below the the emission curve of the corresponding filtrate.

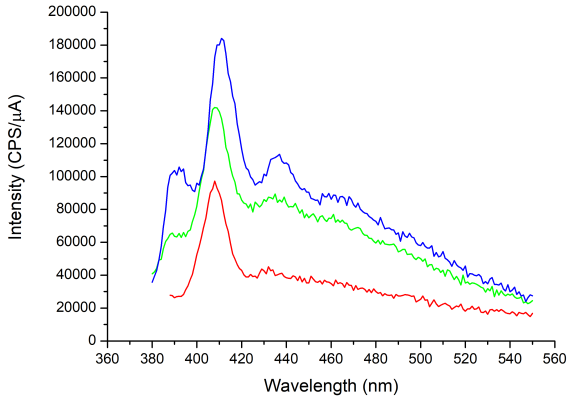

(a)

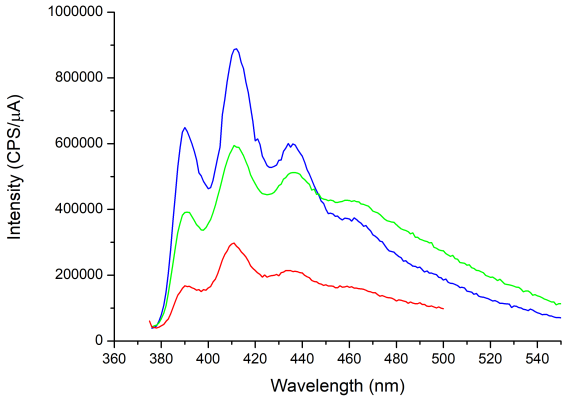

(b)

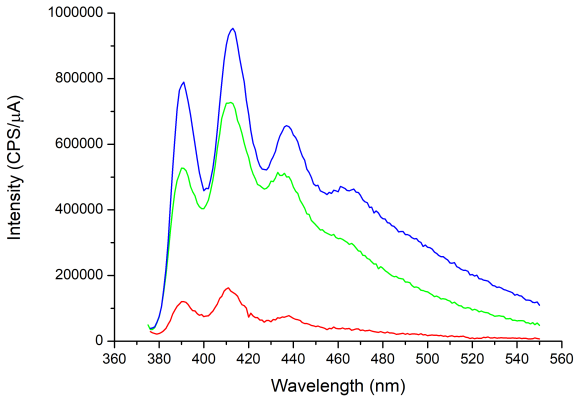

(c)

Figure 104: Emission spectra of [Mn^{II}]@NPs for each NP type. For each graph presented, the first value is the [Mn^{II}] load of the particle in wt%, the second the concentration of [Mn^{II}] is the suspension in mol/L. (a) (on the upper left) RSMNPs: 0.6 wt% ; 1.1×10^{-7} mol/L (red line) ; 2.0 wt% ; 3.9×10^{-7} mol/L (green line) ; 2.9 wt% ; 5.5×10^{-7} mol/L (blue line). (b) (on the upper right) SMNPs: 1.2 wt% ; 2.3×10^{-7} mol/L (red line) ; 2.9 wt% ; 5.5×10^{-7} mol/L (green line) ; 3.9 wt% ; 7.3×10^{-7} mol/L (blue line). (c) (in the lower middle) CSMNPs: 0.4 wt% ; 6.7×10^{-8} mol/L (red line) ; 2.9 wt% ; 5.5×10^{-7} mol/L (green line) ; 4.6 wt% ; 8.7×10^{-7} mol/L (blue line).

Figure 104 depicts the emission of various [Mn^{II}] loads for each NP type. It shows that the emission becomes more intense when the particle's load increases. That would mean that the quantity of [Mn^{II}] released is in relation with the NP load. The signal emitted by [Mn^{II}]@RSMNPs is however rather low for our detectors settings. At the lowest concentration (2.3×10^{-7} mol/L), the bands other than the one at 412 nm seem to disappear completely. But considering the signal to noise ratio it is hard to know if it is a real effect or if it is coming from the detector. We can nonetheless mention than a similar band disappearance can also be observed for a diluted solution of $[Mn^{II}]_n$ (1.2×10^{-7} mol/L) in ethanol, so, it is not an effect of the particles.

Figure 105 presents experimental fits of the integrated normalised emission intensity for each particle type in order to estimate if their is a simple relation between the particle load and the emission observed in suspension.
As the number of points is very limited, it is only a guide line, but the area described by the emission curve seems proportional to the amount of [Mn^{II}] loaded in the particle. This linear fit shows that for the particles that are believed to release [Mn^{II}] more easily, CSMNPs and SMNPs, the slope is steeper than for the best complex trap, RSMNPs (see **Figure 103**) which is not surprising.

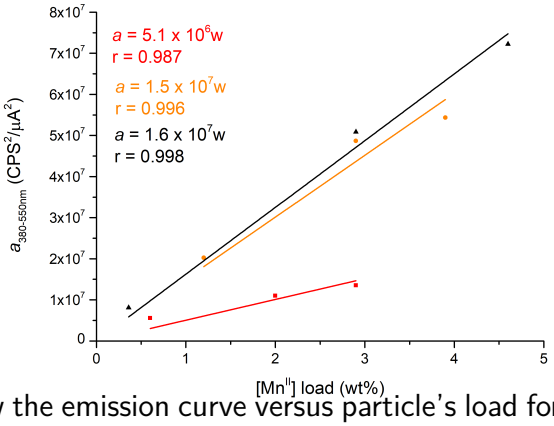

Figure 105: Area below the emission curve versus particle's load for [Mn^{II}] of [Mn^{II}]@RSMNPs (red squares), [Mn^{II}]@SMNPs (orange circles) and [Mn^{II}]@CSMNPs (black triangles) suspensions. Linear fits with their equations are plotted with matching colours.

The two points that are the furthest from the fit lines are the ones with the most deformed signal. For $[Mn^{II}]^{0.6}$@RSMNPs (1.1×10^{-7} mol/L) it simply comes from a lack of resolution of the detector. But for $[Mn^{II}]^{2.9}$@SMNPs (5.5×10^{-7} mol/L) it is a real modification of the emission intensity of the 462 nm band. Here, the intensity ratio between the 412 and 462 nm bands reaches 0.72, when it is usually around 0.20 for [Mn^{II}]. By examining the spectra recorded, it appears that this ratio can vary between 0.20 and 1.17 (**Figure 106(a)**). However, that kind of deformation never appears for free $[Mn^{II}]_n$ at such low concentrations, and even for free anthracenecarboxylic acid it should not appear below approximately 1.0×10^{-5} mol/L. Whereas the 1.17 ratio is recorded for a concentration of 5.5×10^{-7} mol/L maximum (because it comes from [Mn^{II}]@RSMNPs which is supposed to retain the particles, the "real" concentration in solution would be more around 7×10^{-8} mol/L).

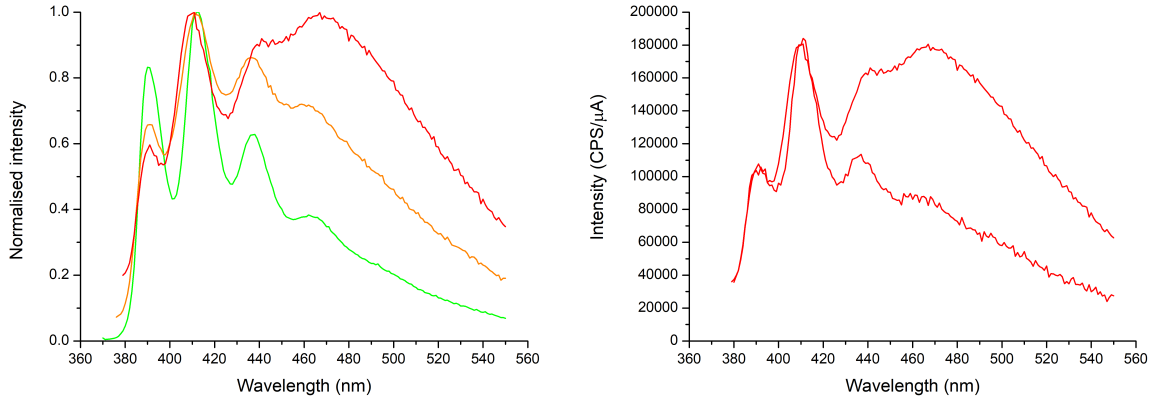

(a) (b)

Figure 106: (a) Normalised emission spectra of $[Mn^{II}]^{2.9}$@RSMNPs (5.5×10^{-7} mol/L) (red line), $[Mn^{II}]^{2.9}$@SMNPs (5.5×10^{-7} mol/L) (orange line) and free $[Mn^{II}]$ (5.5×10^{-7} mol/L) (green line) in ethanol. (b) Emission spectra of two $[Mn^{II}]^{2.9}$@RSMNPs (5.5×10^{-7} mol/L) suspensions in ethanol.

This behaviour is likely not coming from the particles as they are supposed to heavily quench our fluorophore's emission and this band can be quite intense (and again the most important deformation comes from RSMNPs, that are supposed to be best quenchers). By examining **Figure 103**, it looks that such deformation of the 462 nm band appears after our treatments on $[Mn^{II}]$@SMNPs and $[Mn^{II}]$@CSMNPs. This suggest that this modification of the signal comes from $[Mn^{II}]$ that leaked out of the particles. And, as this deformation is more present on supernatant spectra recorded after centrifugation, that is more brutal for the particles, it reinforces that hypothesis. Our interpretation is that some $[Mn^{II}]$ that are released from the particles are actually detached in clusters, maybe coming from preferential binding sites, rather than individually. The change in the signal would then come from local concentration of $[Mn^{II}]$ that are much higher than the average of the solution, giving rise to excimer emission, as observed for the highest concentration of $[Mn^{III}]$ or reported for anthracenecarboxylic acid.
This assumption is especially further reinforced by the difference between the two $[Mn^{II}]^{2.9}$@RSMNPs spectra of the same concentration (5.5×10^{-7} mol/L) (**Figure 106(b)**), whose main difference in preparation might come from the time passed in the ultrasonic bath while waiting for fluorescence measurement. Thus dispersing more, or less, the $[Mn^{II}]$ aggregates.

All in all, the fluorescence observed in $[Mn^{II}]$@NPs suspension is mainly coming from free $[Mn^{II}]$ released in solution. $[Mn^{II}]$ luminescence is, at least partially, quenched inside the particles. From the difference in intensity observed between free $[Mn^{II}]$ in ethanol and the spectra of $[Mn^{II}]$@NPs, a significant amount of the complex still seems to stay entrapped in the particles when they are redispersed in ethanol suspension.
RSMNPs appears to be the most suitable nanovectors, as they do not instantly release $[Mn^{II}]$ in solution and they seem to be more resistant to treatments like centrifugation or filtration. CSMNPs are second in terms of $[Mn^{II}]$ trapping, but are prone to leak a more important amount of complexes. Finally, SMNPs appear to be the worse at retaining the complex inside but seem to resist more than CSMNPs and less than RSMNPs when submitted to the above-

mentioned treatments. This is in agreement with former work from our team, that introduced some degree of functionalisation in order to avoid the release of other Mn compounds.[56,57,230] The quantity of complexes that leak out of the particles appears to be somewhat proportional to the particle's load, with a proportionality factor linked to the NP material type.
Finally, a deformation of the band at 462 nm is observed for different samples. It is attributed to an excimer luminescence due to [Mn^{II}] released from the nanoparticles forming local aggregates.

III.4.3 Luminescence of [Mn^{III}]@NPs materials

As for the previous paragraph, it is needed to compare the luminescence of the compounds in suspension and the emission spectra of the solution with the particles. The treatments are the same than for [Mn^{II}]@NPs : filtration through a 40 nm nylon filter and centrifugation 10 min at 4000 rpm.
Overall the emission spectra of [Mn^{III}]@NPs, is much more difficult to interpret for a main reason: [Mn_4^{III}] is much less soluble in ethanol than Mn^{II} compounds and forms excitons at much lower concentration, as seen in paragraph **III.3**. **Figure 107** presents the emission spectra of all three [Mn^{III}]@NPs materials as well as the emission spectra of the corresponding filtered solutions and the emission of supernatants after centrifugation. All these measurements were recorded with the most important loads of [Mn_4^{III}] and, as a minimum amount of compound appears to be sufficient to quench the luminescence of the support, for these samples the emission of the nanoparticle materials is considered to be quenched.

[Mn^{III}]@SMNPs and [Mn^{III}]@CSMNPs spectra (**Figures 107(b)** and **107(c)**) can essentially be interpreted like in the previous paragraph. The particles contribute to quench the luminescence of the complex. When the spectra of the filtrate or the supernatant is recorded, the intensity of the emission increases because some more [Mn^{III}] leak out in solution during the process. A change in the intensity ratio between the bands at 412 nm and 462 nm can be observed because the complexes extracted of the particles that contribute to enhance the emission are believed to stay in agglomerates that favour the apparition of exciton bands. The method used to collect the solution seems, however, to have less impact on the shape and intensity of the spectra, which means that [Mn^{III}] are probably more loosely bind to the particles than [Mn^{II}].

The interpretation is more delicate for [Mn^{III}]@RSMNPs. A large and intense band appears at 470 nm for the most concentrated samples ([Mn^{II}]$^{4.6}$@RSMNPs and [Mn^{II}]$^{2.7}$@RSMNPs) but not for the least-loaded one ([Mn^{II}]$^{1.0}$@RSMNPs) (**Figure 109(a)**). At the same time, it is observed in several supernatants (**Figure 107(a)** and **Figure 107(b)**). As the concentration of the suspension prepared is lower (5.5×10^{-7} mol/L) than the one where this phenomenon is observed for free [Mn_4^{III}] in ethanol solution (6.6×10^{-6} mol/L), our best interpretation is, so, to attribute it to the luminescence of [Mn^{III}] aggregates detached from particles, like in the previous paragraph. The fact that this deformation is more systematic and that we did not managed to mitigate it with different suspension's preparation is in accordance with the limited solubility of [Mn_4^{III}] in ethanol. This hypothesis is strengthened by looking at the clean shape of the signal of the [Mn^{III}]$^{4.6}$@RSMNPs filtrate, without a

large 470 nm band. If [Mn^{III}] forms large aggregates when released in solution they can be removed more efficiently with a filter rather than centrifugation if they retain colloidal stability.

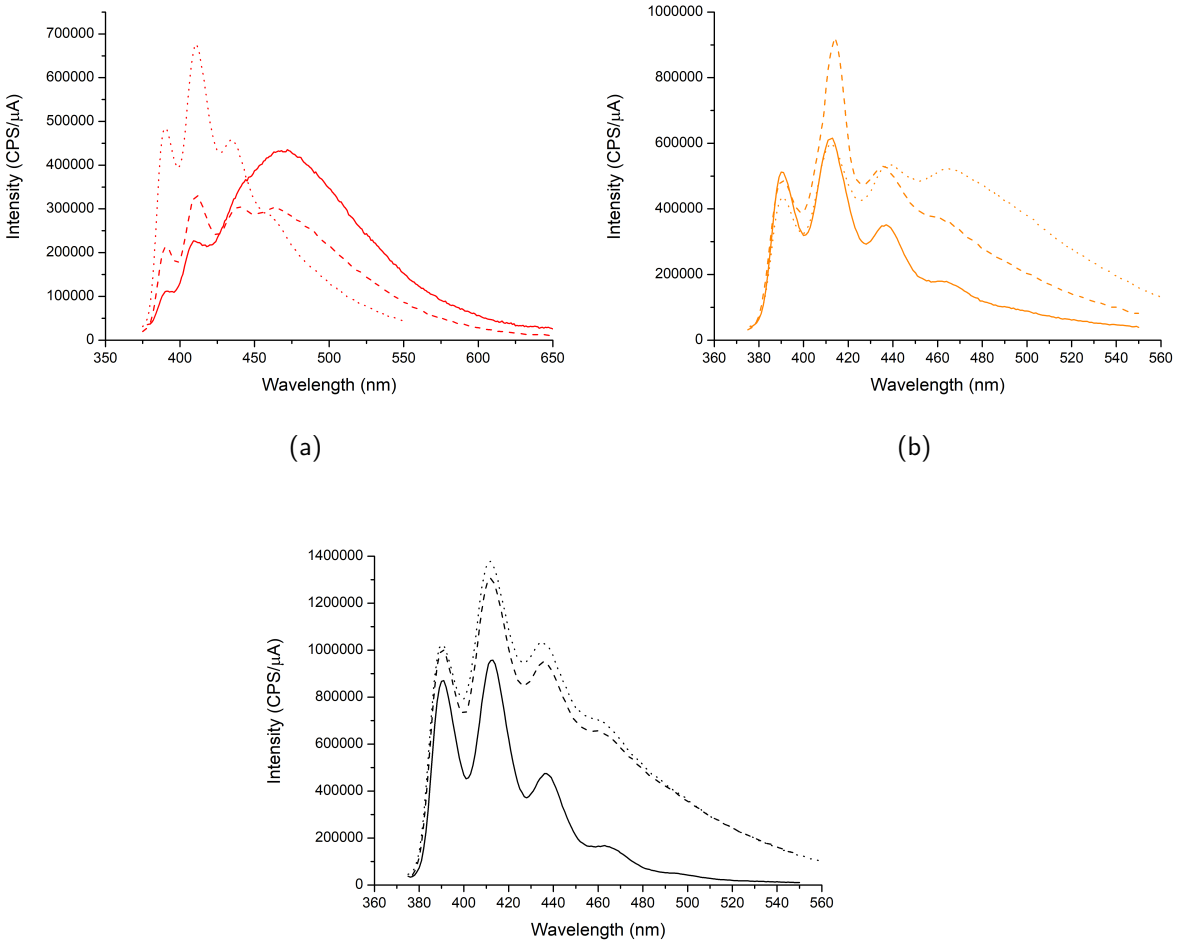

Figure 107: Emission spectra of [Mn^{III}]@NPs for each NP type (full line) compared to the emission spectra of the supernatant after centrifuagtion (dashed line) and the filtrate (dotted line). (a) $[Mn^{III}]^{4.6}$@RSMNPs (5.5×10^{-7} mol/L) (b) $[Mn^{III}]^{3.8}$@SMNPs (4.6×10^{-7} mol/L) and (c) $[Mn^{III}]^{4.2}$@CSMNPs (5.0×10^{-7} mol/L).

Because of this intense deformation of the signal, it is impossible to represent the loss of intensity more quantitatively for [Mn^{III}]@RSMNPs. However, from the general shape of the signal and its evolution with filtration and centrifugation treatments, it is possible to state that [Mn^{III}] seems a lot less strongly bonded to RSMNPs than [Mn^{II}]. Unfortunately, it cannot be stated for sure that the luminescence of [Mn^{III}] is completely quenched inside the particle as the signal of the suspension and its supernatant differs. Another evidence that shows that [Mn^{III}] is more prone to leak of RSMNPs than [Mn^{II}] is by comparing the total emission of the suspension to the signal of [Mn^{III}]@SMNPs and [Mn^{III}]@CSMNPs and to notice that it is much stronger than [Mn^{II}]@RSMNPs when compared to [Mn^{II}]@SMNPs and [Mn^{II}]@CSMNPs.

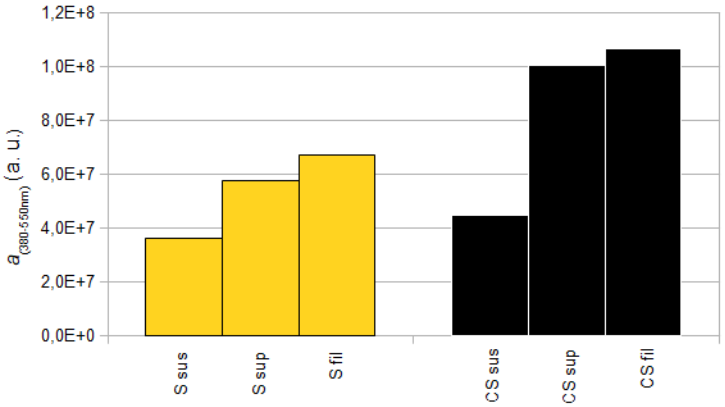

Figure 108: Value of the area below the emission curve between 380-550nm for [Mn^{III}]$^{4.6}$@SMNPs (4.6×10^{-7} mol/L) (S - yellow) and [Mn^{III}]$^{4.2}$@CSMNPs (5.1×10^{-7} mol/L) (CS - black). sus: suspension ; sup: supernatant ; fil: filtrate.

Figure 108 and **Table 43** present the evolution of the integrated emission curves of [Mn^{III}]@SMNPs and [Mn^{III}]@CSMNPs. We choose not to represent [Mn^{III}]@RSMNPs as the distortion of the 470 nm band is too important which would underestimate the leak in the calculation. With the same approach, as the signal is more deformed for supernatant and filtrate for [Mn^{III}]@SMNPs and [Mn^{III}]@CSMNPs, the leak is overestimated. Again these number have to be largely nuanced as it cannot be ascertained that [Mn^{III}] is completely quenched inside the nanoparticles, which again could overestimate the leak.

Table 43: Evolution of the integrate of the emitted intensity measured for all NP types.

NP type	capture $\frac{a_{sol}-a_{sus}}{a_{sol}}$ (%)	centrifugation release $\frac{\lvert a_{sus}-a_{sup}\rvert}{a_{sus}}$ (%)	filtration release $\frac{\lvert a_{sus}-a_{fil}\rvert}{a_{sus}}$ (%)
[Mn^{III}]@SMNPs	47	87	59
[Mn^{III}]@CSMNPs	40	139	125

a_{sol}: area below the the emission curve (380-550 nm) of free [Mn^{II}] in ethanol suspension ; a_{sus}: area below the the emission curve of [Mn^{II}]@NPs in ethanol suspension ; a_{sup}: area below the the emission curve of the corresponding centrifugation supernatant ; a_{fil}: area below the the emission curve of the corresponding filtrate.

Figure 109 displays the emission curves of [Mn^{III}]@NPs materials for the same NPs concentration in ethanol (250 mg/L) but different [Mn^{III}] loads. In the other hand, **Figure 110** shows the linear fits between the integration value of the emission curves and the particle's load. From these set of graphs we can see that the measured intensity is proportional to the particle's load. The only point that really stands out from this trend is [Mn^{III}]$^{1.2}$@CSMNPs (1.5×10^{-7} mol/L), whose load seems to have been underestimated with the elemental analysis (1.2 wt% versus a 2.9 wt% goal during the preparation). It has to be remembered that what the fluorimeter records, is mainly (but not totally) the emission of free fluorophores in solution. So these curves principally show that the release rate of the fluorophores is the same for any complex load.
Interestingly, we can see that in this case, the slope of [Mn^{III}]@RSMNPs does not stand out from the two other materials which would suggest than [Mn^{III}] is as loosely bind to RSMNPs

than to the other NPs types, contrary to [Mn^{II}] and in accordance to the leaking test. It has however to be nuanced as, [Mn^{III}]@RSMNPs, contrary to the two other nano-vectors, exhibit the strong excimer band at 470 nm which makes the direct comparison hazardous.

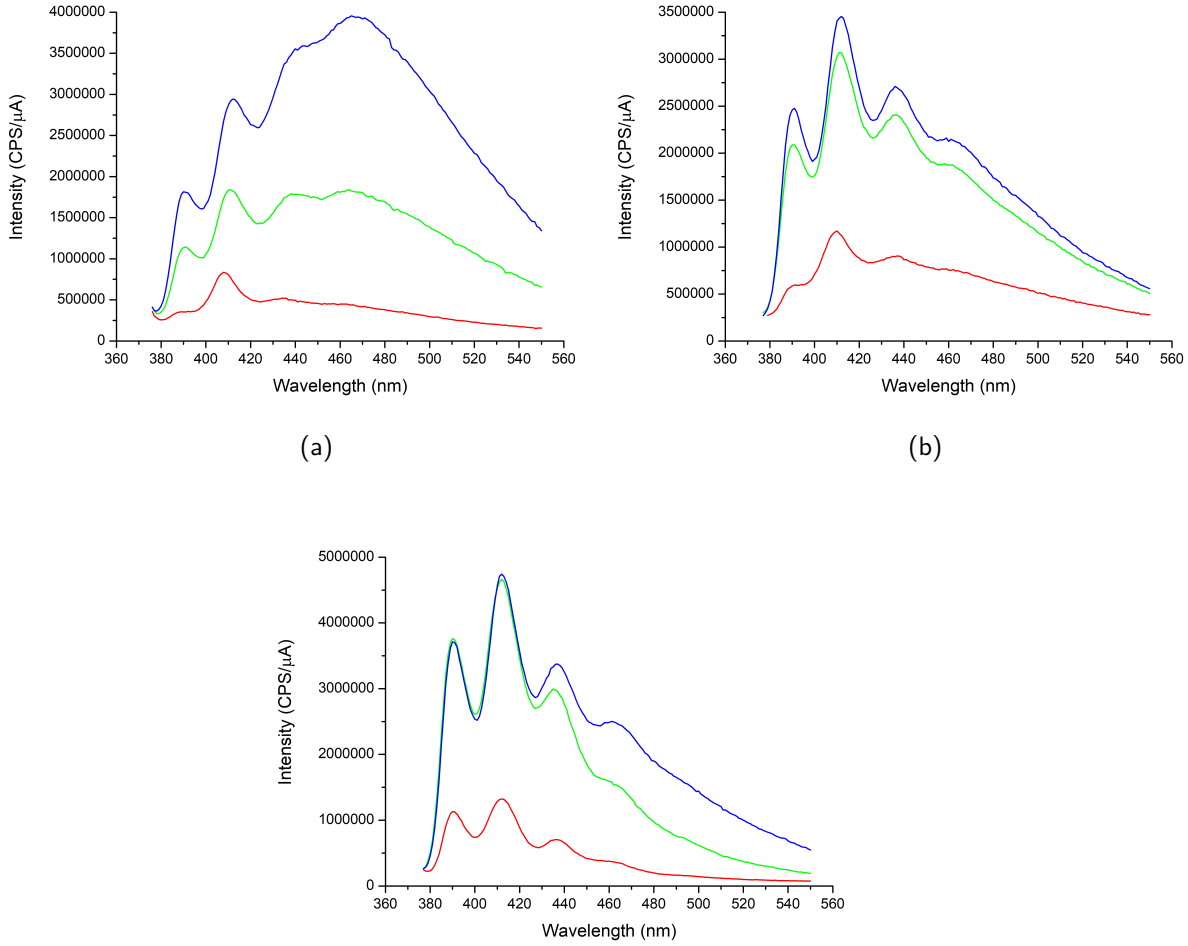

Figure 109: Emission spectra of [Mn^{III}]@NPs for each NP type. For each graph presented, the first value is the [Mn^{III}] load of the particle in wt%, the second the concentration of [Mn^{III}] is the suspension in mol/L. (a) (on the upper left) RSMNPs: 1.0 wt% ; 1.1×10^{-7} mol/L (red line) ; 2.7 wt% ; 3.2×10^{-7} mol/L (green line) ; 4.6 wt% ; 5.5×10^{-7} mol/L (blue line). (b) (on the upper right) SMNPs: 0.9 wt% ; 1.0×10^{-7} mol/L (red line) ; 2.5 wt% ; 2.9×10^{-7} mol/L (green line) ; 3.8 wt% ; 4.6×10^{-7} mol/L (blue line). (c) (in the lower middle) CSMNPs: 0.9 wt% ; 1.0×10^{-7} mol/L (red line) ; 1.2 wt% ; 1.5×10^{-7} mol/L (green line) ; 4.2 wt% ; 5.0×10^{-7} mol/L (blue line).

Figure 111 depicts the emission measured for suspensions of [Mn^{III}]@NPs and free [Mn^{III}] in ethanol for close concentrations. Even if the strict comparison between the area is impossible (due to the samples at our disposition) we can notice that the overall emission of the compounds is much closer in terms of intensity to the free [Mn^{III}_4] than what was observed for [Mn^{II}]$_n$ and [Mn^{II}]@NPs. It means, especially, that the majority of the compound is released in solution. And if we compare the intensity of free [Mn^{III}_4] in solution to the one of the

$[Mn^{III}]^{4.2}$@CSMNPs filtrate, it is even more intense. This is very likely caused by damaged complexes whose free carboxylate are more emissive than the coordinated ones.

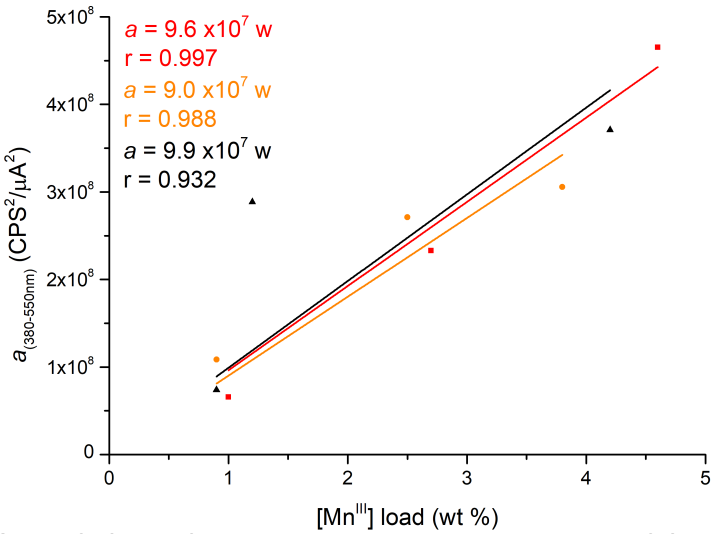

Figure 110: Area below the emission curve versus particle's load for $[Mn^{III}]$ of $[Mn^{III}]$@RSMNPs (red squares), $[Mn^{III}]$@SMNPs (orange circles) and $[Mn^{III}]$@CSMNPs (black triangles) suspensions. Linear fits with their equations are plotted with matching colours.

To sum up, the interpretation of the luminescent properties of $[Mn^{III}]$@NPs is more delicate for numerous reasons. $[Mn_4^{III}]$ compound is not very soluble in ethanol, quickly giving rise to exciton band emission that makes signal integration harder to compare and is even suspected to form agglomerates that could be carried away with particles during the purification processes.
Nevertheless, what can be interpreted from these measurements is that $[Mn^{III}]$ is, overall, not as strongly bonded to the particles than $[Mn^{II}]$ can be. In addition, it seems that $[Mn^{III}]$ signal is not totally quenched by the particle's environment. Which is in accordance with its chemicals properties toward the NP material. If the environment of the particle is less favourable to the complex stabilisation, it is also less likely to interact with its excited states and thus less prone to quench $[Mn^{III}]$ luminescence. Finally, the proportional relation between the particles' theoretical load and the luminescence observed in suspension, also suggest that a significant amount of compound is likely to be intact, as it should have been far more intense and less deformed if the carboxylate had broken free.

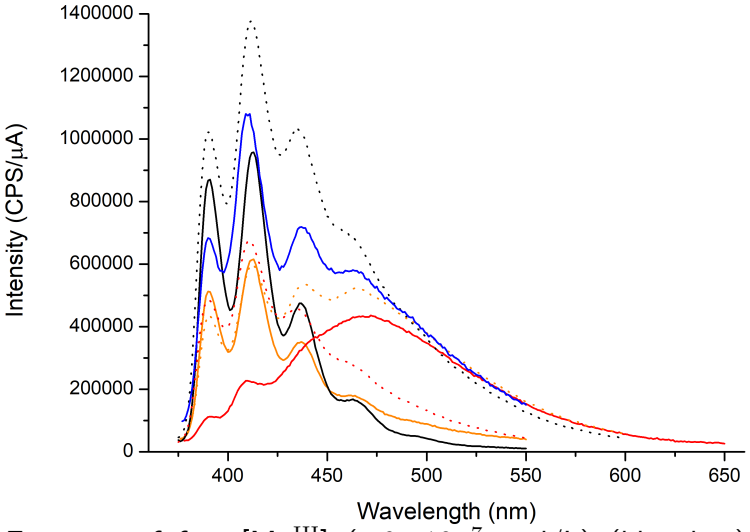

Figure 111: Emission of free $[Mn_4^{III}]$ (5.0×10^{-7} mol/L) (blue line), $[Mn^{III}]^{4.6}$@RSMNPs (5.5×10^{-7} mol/L) (red line), $[Mn^{III}]^{3.8}$@SMNPs (4.6×10^{-7} mol/L) (orange line) and $[Mn^{III}]^{4.2}$@CSMNPs (5.0×10^{-7} mol/L) (black line). Wavelength of excitation: 362 nm. The emission of corresponding filtrates is representated in dotted lines.

III.5 Catalytic activity

Preliminary catalytic tests on the disproportionation of H_2O_2 were run on $[Mn_4^{III}]$, $[Mn_2^{II}]$ and $[Mn^{II}]_n$ compounds in acetonitrile and $[Mn^{II}]$@RSMNPs in acetonitrile/water suspension.
The volume of O_2 produced by the reaction is followed versus time and converted in turnover number (TON). As we consider a two-step reaction with subsequent oxydation and reduction of H_2O_2, a TON is the evolution of the O_2 amount per quantity of Mn complex (both in mol.), it corresponds to the decomposition of two molecules of H_2O_2 (see equation **??**).

III.5.1 Catalytic activity of $[Mn_4^{III}]$

5 mL solutions of 8.0×10^{-4} mol/L of $[Mn^{III_4}]$ are prepared in acetonitrile and 0.6 mL of an aqueous solution of H_2O_2 (35 wt%) is injected. It represents a $\frac{n(H_2O_2)}{n([Mn_4^{III}])}$ ratio of 1.6. The amount of O_2 produced is then measured volumetrically.
The first observation to make is that the measurement cannot be repeated easily and the overall activity of the compound is quite low when compared to the catalase bio-mimetic compounds in the literature (**Figure 112**).[56,57,175,227] It ranges from 139 to 198 TON in one hour. The solubility of $[Mn_4^{III}]$ is very low. So, the behaviour of $[Mn_4^{III}]$ compound might be closer from a suspension than a solution, inducing surface related effect like for heterogenous catalysis and explaining why the efficiency vary. Also, for dinuclear Mn^{III} compounds,[56] the perchlorate counter-anions have been found to be labile and replaced in solution by solvent molecules or H_2O_2 which enables the disproportionation to be catalysed by the Mn core. As our compound is weakly soluble, the perchlorate are probably less labile, contributing to lower the activity of the compound.

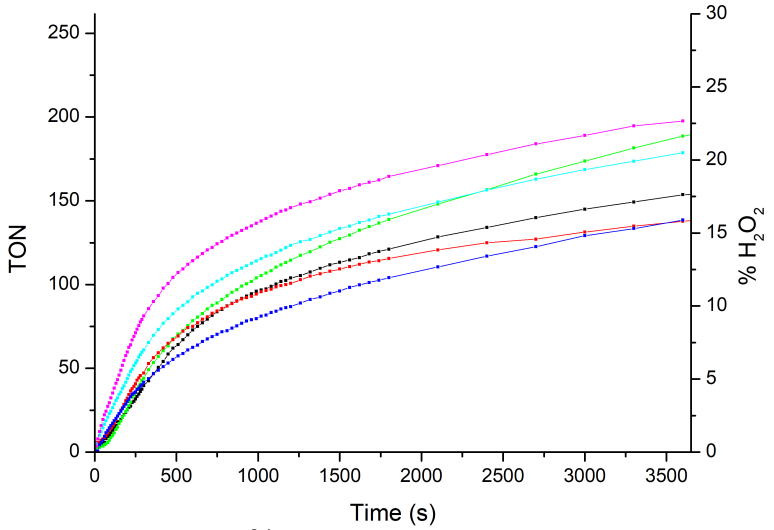

Figure 112: Turnover number and % of H_2O_2 disproportionnated, versus time, of several 8.0×10^{-4} mol/L $[Mn_4^{III}]$ solutions in acetonitrile/water. $n(H_2O_2)/n([Mn_4^{III}]) = 1.6$

To see if the $[Mn_4^{III}]$ compound is stable in the test's conditions and can be activated again by new substrate addition, several doses of H_2O_2 are added to the same sample successively. It appears that the catalytic activity is still observed for subsequent additions, but that its efficiency drops (**Figure 113**). In the first minutes of the reaction, the slope indicates the initial reaction rate. We can observe that it decreases after each H_2O_2 addition, suggesting some changes in the catalyst. In order to quantify the efficiency of the catalyst a fit is performed on the linear part of the curves. On **Figure 113**, the first slope is found to be 0.16 TON/s, but it quickly drops to 0.05 TON/s for the second addition and 0.01 TON/s for the third one, confirming that the complex is not likely to be very stable.

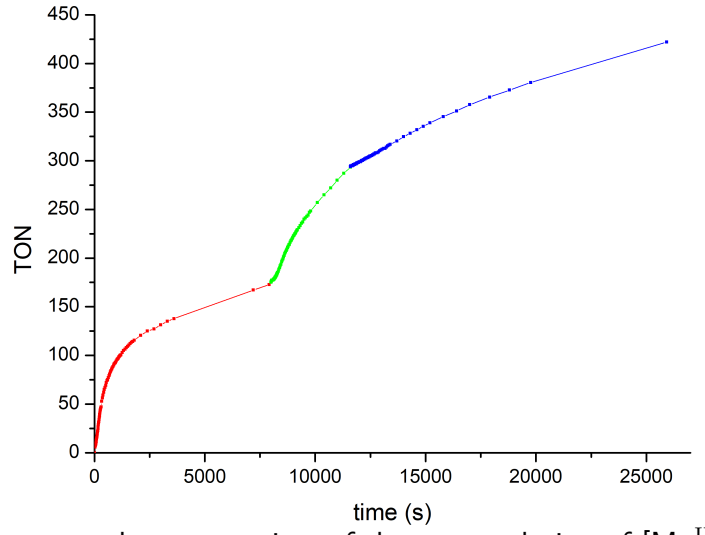

Figure 113: Turnover number versus time of the same solution of $[Mn_4^{III}]$ after one (in red), two (in green) and three (in blue) additions of H_2O_2 in acetonitrile/water.

III.5.2 Catalytic activity of $[Mn_2^{II}]$ and $[Mn^{II}]_n$

For both Mn^{II} compounds, it is necessary to think in terms of dinuclear units instead of amount of compound. First, the $[Mn^{II}]_n$ is supposed to break into dinuclear units in presence a water, which is the case for our tests. Second, taking this convention enables us to compare directly the TON of both compounds. Finally, it is probably more accurate from a mechanistic point of vue, as the mechanism of natural Mn-catalase seems to rely on a cooperative dinuclear process.
Both compounds are tested in the same conditions than $[Mn_4^{III}]$ ($\frac{n(H_2O_2)}{n([Mn_2^{II}])}$=1.6). The repeatability is better, likely because these compounds are much more soluble in acetonitrile than $[Mn_4^{III}]$. **Figure 114** displays the catalytic activity of both compounds. The TON/h of $[Mn^{II}]_n$ appears to be 2.2 times higher than $[Mn_2^{II}]$. To evaluate the kinetics of the reaction, the initial slopes of the curves are also measured. 0.7 TON/s is found for $[Mn^{II}]_n$ and 0.2 TON/s for $[Mn_2^{II}]$. It appears, so, that $[Mn^{II}]_n$ is more active than $[Mn_2^{II}]$, both in terms of efficiency and kinetics. It is difficult to give an explanation of this assessment. As, the water is introduced in the acetonitrile solution at the same time as H_2O_2, it might have to do with the chain breaking mechanism cooperating with the catalytic cycle. It could also be due to the availability of more neighbouring Mn ions, in the chain, to perform more easily the catalysis.

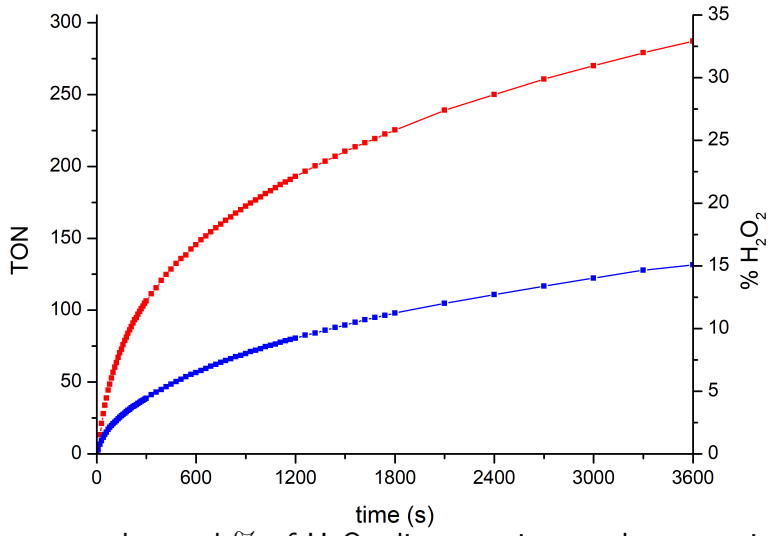

Figure 114: Turnover number and % of H_2O_2 disproportionnated, versus time, of 8.0×10^{-4} mol/L $[Mn_2^{II}]$ solution (blue line) and $[Mn^{II}]_n$ solution (red line) in acetonitrile/water. $n(H_2O_2)/n([Mn_2^{II}]) = 1.6$.

III.5.3 Catalytic activity of $[Mn^{II}]$@RSMNPs

As mentioned in section **III.4**, $[Mn^{II}]$@RSMNPs appears to be the best material to retain the complex. It seemed, so, to be the most suitable to test the activity towards H_2O_2.
Preliminary tests on the RSMNPs support show almost no activity both in acetonitrile and water. However, the nanoparticles bleach indicating a degradation of the polyphenol network by the H_2O_2.

For [Mn^{II}]@RSMNPs, tests were performed directly in water. As the resol was expected to be degraded with the reaction, [Mn^{II}]^{10}@RSMNPs that was set aside during the characterisation of the materials was used to perform these tests. The amount of intact complex is probably even lower than what was observed for samples with smaller loads but in order to make TON calculations, we estimate the concentration of [Mn^{II}] to 8.9×10^{-3} mol/L. ($\frac{n(H_2O_2)}{n([Mn_2^{II}])}$=0.14). Unfortunately, this high [Mn^{II}] concentration is due to an error during manipulations.

The first experiment made in water showed even less activity than what was observed for both free Mn^{II} compounds in acetonitrile. But the pH of the suspension was found to be pH = 5.0 whereas the pH of [Mn^{II}]$_n$ in acetonitrile is normally basic. This low pH in water is caused by the particles, and likely due to the presence of HCl that remained from the acidic extraction of the surfactant.
In order to adjust the pH toward more basic media, triethylamine was used. A test was run at pH = 7.5 and another at pH = 9.0 and they showed a much higher activity than what was observed previously, but still reaching a plateau before 100% decomposition of H_2O_2 (**Figure 115**).

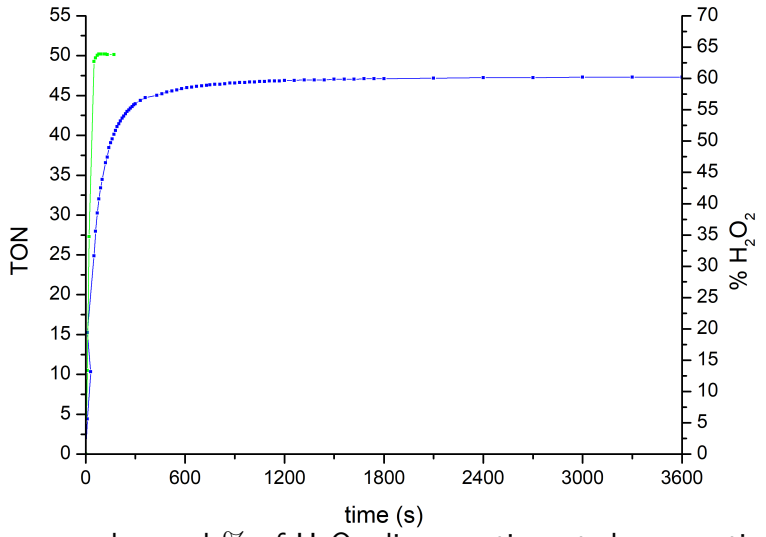

Figure 115: Turnover number and % of H_2O_2 disproportionnated, versus time, of 8.9×10^{-3} mol/L [Mn^{II}]^{10}@RSMNPs at pH = 7.5 (blue) and 9.0 (green) in water. $n(H_2O_2)/n([Mn_2^{II}])$ = 0.14.

The TON is much lower than for the 8.0×10^{-4} concentration of free [Mn^{II}]$_n$ in acetonitrile but it is not suprising considering that the concentration is eleven times more important. What is interesting to consider is the kinetics of the reaction. It is much faster than in acetonitrile for a comparatively lower pH, the slope measured in the linear area of the curve for [Mn^{II}]@RSMNPs is 0.4 TON/s for pH = 7.5 and 1.0 TON/s for pH = 9.0 in water. Whereas 0.6 TON/s is measured for [Mn^{II}]$_n$ alone at pH = 10.6 in acetonitrile. This increase might be due to the higher concentration of [Mn^{II}] compound or by the environment of the molecule inside the RSMNP particle.
Interestingly, both curves at pH = 7.5 and 9.0 reach a plateau, respectively at 61% and at 64%

of H_2O_2. It is very likely due to the competition between the catalytic disproportionation of H_2O_2 by [Mn^{II}] and the degradation of the resol network by H_2O_2 without producing O_2 (according to blank experiments). From the two-curves obtained we can deduce that the rate of degradation of the resol is slower than the catalytic disproportionation of H_2O_2. The faster this reaction is, the more O_2 is generated, hence, the more H_2O_2 is consumed. Further tests should be run to see if optimal conditions exists for [Mn^{II}]@RSMNPs in order to disproportionate all H_2O_2 without degrading the polymer network, hence allowing the recycling of the material.

III.6 Conclusions

First, the study of the magnetic properties of NPs supports shows than SMNPs and CSMNPs have a response towards magnetic field and that only RSMNPs are silent. This is probably due to carbon or carbon induced defects in the matrix during thermal treatment. EPR even shows that carbon radicals are present inside CSMNPs.
From the [Mn]@NPs materials, only [Mn^{II}]@RSMNPs and [Mn^{III}]@RSMNPs magnetic susceptibility could be properly studied. Both seem to contain dinuclear Mn entities with weak antiferromagnetic coupling and displaying strong distortions of their octahedral environment. The EPR spectra of [Mn^{II}]@NPs materials also points towards the presence of dinuclear units with weak magnetic coupling inside all NPs types.

On the other hand, the luminescent properties of this new [Mn]@NPs materials is complex to analyse but show promising perspectives. The synthesised nanoparticles themselves display luminescence and the interaction between the nanovector material and its load sounds interesting especially if it is possible to evidence some luminescence transfer between each other. The amount of fluorescence quenched seems to be linked to the stability of the Mn compounds inside the particles. It is thus possible to evaluate if the nanoparticles are suitable guests by studying the fluorescence of the compounds released in solution.
From this measurements, it appears that pure silica and hybrid carbon-silica are not the best host choice both for $[Mn^{II}]_n$ and $[Mn_4^{III}]$ compounds, even if a non-negligible amount seems to be retained inside. They need probably further organic functionalisation to avoid our compounds to leak out.
Encouragingly, the hybrid resol-silica nanoparticles appear to be very effective at entrapping $[Mn^{II}]_n$ compounds without further modification. Even when submitted to relatively violent treatment like centrifugation, the leaching is limited. As such, [Mn^{II}]@RSMNPs promise to be the material of choice to submit to catalytic activity tests.

Finally, with the catalytic tests run on free Mn compounds in solution, it appears that they are all active, with low to medium efficiency (140-280 TON/h) compared to other catalase mimics. $[Mn_4^{III}]$ has important solubility issues in acetonitrile and is not reusable for more than a few cycles. When TON is compared in terms of dinuclear Mn unit, $[Mn^{II}]_n$ appears to be the most efficient, followed by $[Mn_2^{II}]$ compound and finally $[Mn_4^{III}]$.
In addition, tests were run for [Mn^{II}]@RSMNPs in water and showed that if the TON is hardly comparable due to the [Mn^{II}] concentration difference, the kinetics of the reaction seems improved. It can be due to concentration, media or support effects and would need

further study. However, the existence of a competition between catalytic disproportionation and decomposition of the polyphenol is evidenced, opening the perspective of optimised pH and particle's load condition where the disproportionation would be dominating and hence preserve the support from degradation by H_2O_2.

III.7 Experimental section

III.7.1 Catalase activity

The catalytic tests of disproportionation of H_2O_2 into H_2O and O_2 are performed at 25 °C. The amount of oxygen produced is measured with a gas-volumetric burette (0.1 mL precision). 0.6 mL of an aqueous solution of 35 wt% of H_2O_2 is added through a syringe to closed flasks containing the solution to measure.

For $[Mn^{II}]_n$, $[Mn_2^{II}]$ and $[Mn_4^{III}]$ compounds, it is a 5 mL solution of 10^{-4} mol/L of compound in acetonitrile.

For $[Mn^{II}]^{10}$@RSMNPs, it is a suspension of 40 mg of material into 5 mL of water. The pH is adjusted with small amounts of triethylamine.

Blank experiments were performed on the RSMNPs support in the same conditions than the loaded particles (40 mg into 5 mL water solution) a showed no significant activity.

III.7.2 Characterisations

Magnetic susceptibility measurements were performed at the Unitat de Mesures Magnètiques of the Universitat de Barcelona by the Dr. Núria Clos with a magnetometer Quantum Design MPMS XL5 SQUID (Superconducting Quantum Interference Device).

EPR measurements were performed at the Unitat de Mesures Magnètiques of the Universitat de Barcelona by the Dr. Núria Clos with a Bruker ELEXSYS E500 spectrometer with a frequency of 9.4 GHz (X band).

Light absorption measurement were performed on a UV-visible spectrophotometer Cary 100scan from Varian.

Luminescence spectra were measured by using a Horiba Jobin Yvon SPEX Nanolog fluorescence spectrofluorimeter equipped with a three-slit double-grating excitation and emission monochromator with dispersions of 2.1 nm/mm (1200 grooves/mm). Steady-state luminescence was excited by unpolarized light from a 450 W xenon CW lamp and detected by a red-sensitive Hamamatsu R928 photomultiplier tube for solid-state measurements. Spectra were reference-corrected for both variation of the excitation source light intensity (lamp and grating) and the emission spectral response (detector and grating). The excitation wavelength used for all samples is 362 nm.

Part IV

Conclusion & prospects

In the first chapter we have shown that we successfully synthesised and characterised three new polynuclear Mn compounds with 2,2'-bipyridine and 9-anthracenecarboxylate ligands:

- A Mn^{II} 1D-coordination polymer of formula $[Mn(bpy)(AntCO_2)_2]_n$, which exhibits weak antiferromagnetic coupling (J = -1.2 cm^{-1}).

- A dinuclear Mn^{II} compound of formula $[\{Mn(bpy)(AntCO_2)\}_2(\mu\text{-}AntCO_2)_2(\mu\text{-}OH_2)]$ with moderate antiferromagnetic coupling (J = -4.8 cm^{-1}) and distorted octahedral geometry. It shows a low axial (D_{Mn} = 0.28 cm^{-1}) distorsion due to a compression of the octahedra and evidenced in the crystal structure.

An equilibrium exists between the two forms ($[Mn^{II}]_n$ and $[Mn_2^{II}]$) in acetonitrile solutions but the $[Mn^{II}]_n$ is likely to break in dinuclear units in the presence of a small amount of water.

- A Mn^{III} tetranuclear butterfly complex of formula $[Mn_4O_2(AntCO_2)_6(bpy)_2(ClO_4)_2]$ with strong antiferromagnetic coupling between the body Mn ions (J_1 = -41.0 cm^{-1}) and more moderate magnetic coupling between the body and wings Mn ions (J_2 = -10.6 cm^{-1} and J_3 = -8.4 cm^{-1}). The Mn^{III} ions exhibit a strong axial anisotropy (D_{Mn} = -3.7 cm^{-1}), probably caused by Jahn-Teller effect.

In addition, the synthesis of $[Mn_4^{III}]$ compounds yields crystals of an organic co-product, the 10-oxo-9.10-dihydroanthracene-9-yl anthracene-9-carboxylate, apparently characterised for the first time.

In the second chapter, we reproduced successfully the synthesis of a series of mesoporous nanoparticles based on hybrid resol-silica mesoporous nanoparticles (RSMNPs). Thermal treatments yields silica mesoporous nanoparticles (SMNPs) through calcination under air and carbon-silica mesoporous nanopartilces (CSMNPs) through carbonisation under N_2 atmosphere. All these nanoparticles have the same average diameter (150 nm) and present a stellar porosity but have different available volumes and mechanical properties.
This particles were used as support for the incorporation of $[Mn^{II}]_n$ and $[Mn_4^{III}]$ compounds. In most cases, the insertion of the Mn compounds proved to be efficient (72% to 96% incorporation ratio). However, it appears that the complexes probably break into smaller dinuclear units when they enter the particles. In particular, it seems that RSMNPs porosity is modified when the compounds are inserted. This is likely due to the flexibility of the resol polymer network.

Finally, in the third chapter, we studied the physical and chemical properties of the six new [Mn]@NPs materials.
The loaded materials, [Mn]@NPs, proved complex to analyse. The magnetic measurement confirms that both $[Mn^{II}]_n$ and $[Mn_4^{III}]$ are broken into smaller units, likely dinuclear, when incorporated inside the particles. These units display weak antiferromagnetic coupling and strong distortions of the octahedral environment of Mn ions.
The study of the luminescence of the Mn compounds shows that they are both strongly fluorescent in the 390-462 nm range with a structured emission characteristic of anthracene derivatives. The shape of the emission spectra of $[Mn_4^{III}]$ is dependent of its concentration in ethanol and can display a large exciton band in the 460-470 nm range.

It appears that all three types of nanoparticles supports are luminescent, with a large band at 407 nm. This band originates from the silica phase but its exact cause is difficult to ascertain. The incorporation of the manganese compounds inside the nanoparticles quenches, at least partially, the luminescence of both parts. The study of the fluorescence of the NPs suspensions and of supernatants shows that [Mn^{II}] compounds seem to be more retained inside the particles than [Mn^{III}]. However, all the materials types, at the notable exception of [Mn^{II}]@RSMNPs, proved to leak substantially. As a consequence, [Mn^{II}]@RSMNPs appears to be the best suited material for theragnostic applications.
Finally, some catalytic tests of H_2O_2 disproportionation were run for all three ($[Mn^{II}]_n$, $[Mn_2^{II}]$ and $[Mn_4^{III}]$) compounds in acetonitrile/water media and for [Mn^{II}]@RSMNPs in water. All Mn compounds show an activity, from weak to moderate. The most active compound, both in terms of efficiency and kinetics, is the $[Mn^{II}]_n$. [Mn^{II}]@RSMNPs appears to be active in water, though only the kinetics can be commented from our experiments. They show that the disproportion reaction rate is faster for [Mn^{II}]@RSMNPs in water than for $[Mn^{II}]_n$ in acetonitrile/water and that it is linked to the pH of the suspension. A competition between disproportionation of H_2O_2 by [Mn^{II}] and the oxydation of the resol by H_2O_2 is also observed.

The conclusions of this work seem to confirm that the long-term goal of the project, to use Mn catalase mimics based on polynuclear compounds and supported by mesoporous nanoparticles as antioxydative therapy, is achievable. From the discussions and questioning that arose during this study, multiple perspectives can be envisioned.
The NP support could be further functionalised with PEG or zwitterions to improve their colloidal stability and redispersion. Or, for SMNPs and CSMNPs, to include grafting functions like pyridine or imidazole groups, in order to bind more strongly the Mn complexes inside the materials.
More detailed modelling of the EPR spectra of [Mn^{II}]@NPs could help us to characterise better the fragmentation of the $[Mn^{II}]_n$ when incorporated inside the nanoparticles.
The study of the luminescent properties of the supports could be investigated in order to understand the cause of the luminescence of the silica phase. In addition, lifetime fluorescence could be used as a powerful tool to study the energy transfers that take place between the support and the Mn-compounds and possibly to discriminate several species and their location inside or outside the nano-vectors.
Catalytic tests could be optimised to find the best conditions of operation for the[Mn^{II}] @RSMNPs material and if it is possible to avoid degradation of the resol network. If they prove interesting, experiments in physiological conditions and on cell culture could be carried out.

Annexes

XRD data of [{Mn(bpy)(AntCO$_2$)}$_2$(μ-(AntCO$_2$)$_2$(μ-OH$_2$)]

A yellow prism-like specimen of $C_{82}H_{60}Mn_2N_4O_{10}$, approximate dimensions 0.172 mm $\times$ 0.173 mm $\times$ 0.321 mm, was used for the X-ray crystallographic analysis. The X-ray intensity data were measured on a D8 Venture system equipped with a multilayer monochromator and a Mo microfocus (λ = 0.71073 Å).

The frames were integrated with the Bruker SAINT software package using a narrow-frame algorithm. The integration of the data using a triclinic unit cell yielded a total of 368372 reflections to a maximum θ angle of 29.18° (0.73 Å resolution), of which 35730 were independent (average redundancy 10.310, completeness = 99.7%, R_{int} = 5.93%, R_{sig} = 2.82%) and 28306 (79.22%) were greater than 2σ(F^2). The final cell constants of a = 16.1410(7) Å, b = 17.5745(8) Å, c = 24.6954(9) Å, α = 108.768(2)°, β = 91.291(2)°, γ = 90.413(2)°, volume = 6630.4(5) Å^3, are based upon the refinement of the XYZ-centroids of 2818 reflections above 20 σ(I) with 3.502° < 2θ < 49.43°. Data were corrected for absorption effects using the multi-scan method (SADABS). The calculated minimum and maximum transmission coefficients (based on crystal size) are 0.7156 and 0.7458.

The structure was solved and refined using the Bruker SHELXTL Software Package,[255–257] using the space group P -1, with Z = 4 for the formula unit, $C_{82}H_{60}Mn_2N_4O_{10}$. The final anisotropic full-matrix least-squares refinement on F^2 with 1779 variables converged at R1 = 3.65%, for the observed data and wR2 = 9.17% for all data. The goodness-of-fit was 1.019. The largest peak in the final difference electron density synthesis was 1.193 e-/Å^3 and the largest hole was -0.379 e-/Å^3 with an RMS deviation of 0.062 e-/Å^3. On the basis of the final model, the calculated density was 1.374 g/cm^3 and F(000), 2840 e-.

Table 44: Crystal data and structure refinement for [{Mn(bpy)(AntCO$_2$)}$_2$(μ-(AntCO$_2$)$_2$(μ-OH$_2$)]

Empirical formula	$C_{82}H_{60}Mn_2N_4O_{10}$		
Formula weight	1371.22		
Temperature	100(2) K		
Wavelength	0.71073 Å		
Crystal system	Triclinic		
Space group	P-1		
Unit cell dimensions	a = 16.1410(7) Å	α = 108.768(2)°	
	b = 17.5745(8) Å	β = 91.291(2)°	
	c = 24.6954(9) Å	γ = 90.413(2)°	
Volume	6630.4(5)Å^3		
Z	4		
Density (calculated)	1.374 Mg/m^3		
Absorption coefficient	0.448 mm^{-1}		
F(000)	2840		
Crystal size	0.321 × 0.173 × 0.172 mm^3		
Theta range for data collection	2.178 to 29.178°		
Index ranges	-22≤h≤22	-24≤k≤24	-33≤l≤33
Reflections collected	368372		
Independent reflections	35730 [R(int) = 0.0593]		
Completeness to theta = 25.242°	99%		
Absorption correction	Semi-empirical from equivalents		
Max. and min. transmission	0.7458 and 0.7156		
Refinement method	Full-matrix least-squares on F^2		
Data / restraints / parameters	35730 / 14 / 1779		
Goodness-of-fit on F^2	1.019		
Final R indices [I>2sigma(I)]	R1 = 0.0365	wR2 = 0.0836	
R indices (all data)	R1 = 0.0539	wR2 = 0.0917	
Extinction coefficient	n/a		
Largest diff. peak and hole	1.193 and -0.379 e-.Å^3		

Analyses of 10-oxo-9.10-dihydroanthracene-9-yl anthracene-9-carboxylate

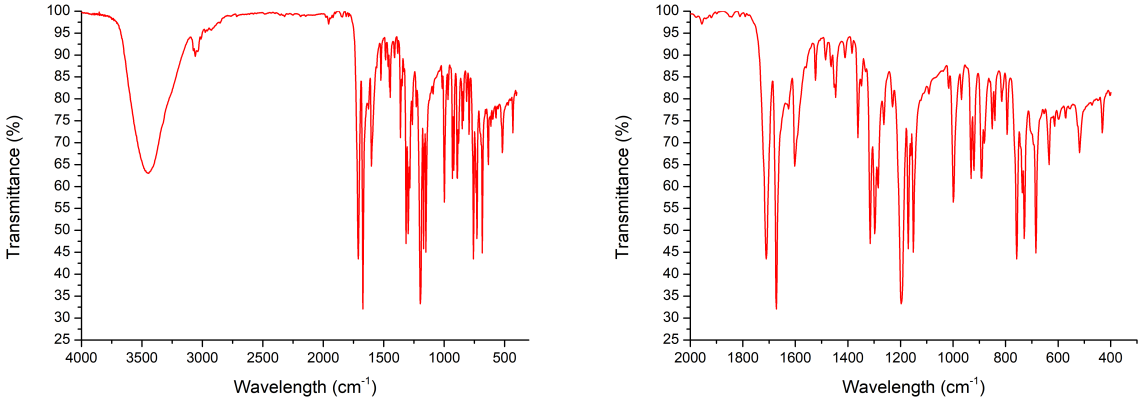

(a) (b)

Figure 116: IR spectra of 10-oxo-9.10-dihydroanthracene-9-yl anthracene-9-carboxylate (a) between 4000 and 300 cm^{-1} and (b) between 2000 and 300 cm^{-1}

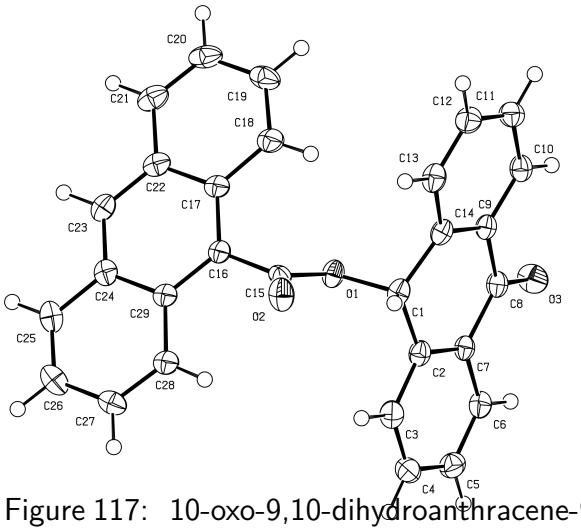

Figure 117: 10-oxo-9,10-dihydroanthracene-9-yl anthracene-9-carboxylate structure resolved from XRD.

Figure 118: Distances and angles of 10-oxo-9,10-dihydroanthracene-9-yl anthracene-9-carboxylate. values given inside the parenthesis are standard deviations.

atoms label	distance (Å)	atoms label	angle (°)
O_1-C_1	1.479(2)	C_1-O_1-C_{15}	118.88(15)
O_3-C_8	1.223(2)		
O_1-C_{15}	1.344(2)	O_1-C_{15}-O_2	124.00(2)
O_2-C_{15}	1.205(2)		
C_{15}-C_{16}	1.495(3)		

The total exposure time was 17.26 hours. The frames were integrated with the Bruker SAINT software package using a narrow-frame algorithm. The integration of the data using a triclinic unit cell yielded a total of 21680 reflections to a maximum θ angle of 24.74° (0.85 Å resolution), of which 3236 were independent (average redundancy 6.700, completeness = 94.7%, R_{int} = 4.10%, R_{sig} = 2.61%) and 2541 (78.52%) were greater than $2^{\sigma}(F^2)$. The final cell constants of a = 9.5385(7) Å, b = 10.2860(7) Å, c = 11.9881(8) Å, α = 67.471(2)°, β = 83.343(2)°, γ = 67.209(2)°, volume = 1000.88(12) $Å^3$, are based upon the refinement of the XYZ-centroids of 6052 reflections above 20 σ(I) with 4.727° < 2θ < 49.40°. Data were corrected for absorption effects using the multi-scan method (SADABS). The ratio of minimum to maximum apparent transmission was 0.912. The calculated minimum and maximum transmission coefficients (based on crystal size) are 0.6797 and 0.7451.

The structure was solved and refined using the Bruker SHELXTL Software Package,[255–257] using the space group P -1, with Z = 2 for the formula unit, $C_{29}H_{18}O_3$. The final anisotropic full-matrix least-squares refinement on F^2 with 289 variables converged at R1 = 4.40%, for the observed data and wR2 = 14.77% for all data. The goodness-of-fit was 1.162. The largest peak in the final difference electron density synthesis was 0.349 e-/Å^3 and the largest hole was -0.379 e-/Å^3 with an RMS deviation of 0.119 e-/Å^3. On the basis of the final model, the calculated density was 1.375 g/cm^3 and F(000), 432 e-.

Table 45: Crystal data and structure refinement for 10-oxo-9,10-dihydroanthracene-9-yl anthracene-9-carboxylate.

Empirical formula	$C_{29}H_{18}O_3$		
Formula weight	414.43		
Temperature	100(2) K		
Wavelength	0.71073 Å		
Crystal system	Triclinic		
Space group	P-1		
Unit cell dimensions	a = 9.5385(7) Å	α = 67.471(2)°	
	b = 10.2860(7) Å	β = 83.343(2)°	
	c = 11.9881(8) Å	γ = 67.209(2)°	
Volume	1000.88(12)Å^3		
Z	2		
Density (calculated)	1.375 Mg/m^3		
Absorption coefficient	0.088 mm^{-1}		
F(000)	432		
Crystal size	0.439 × x 0.181 × 0.136 mm^3		
Theta range for data collection	2.311 to 24.744°		
Index ranges	-11≤h≤10	-12≤k≤12	-14≤l≤14
Reflections collected	21680		
Independent reflections	3236 [R(int) = 0.0410]		
Completeness to theta = 25.242°	89.2%		
Absorption correction	Semi-empirical from equivalents		
Max. and min. transmission	0.7451 and 0.6797		
Refinement method	Full-matrix least-squares on F^2		
Data / restraints / parameters	3236 / 0 / 289		
Goodness-of-fit on F^2	1.162		
Final R indices [I>2sigma(I)]	R1 = 0.0440	wR2 = 0.1257	
R indices (all data)	R1 = 0.0651	wR2 = 0.1477	
Extinction coefficient	n/a		
Largest diff. peak and hole	0.349 and -0.379 e-.Å^3		

Sorption isotherms of modified mesoporous silica-resol nanoparticles

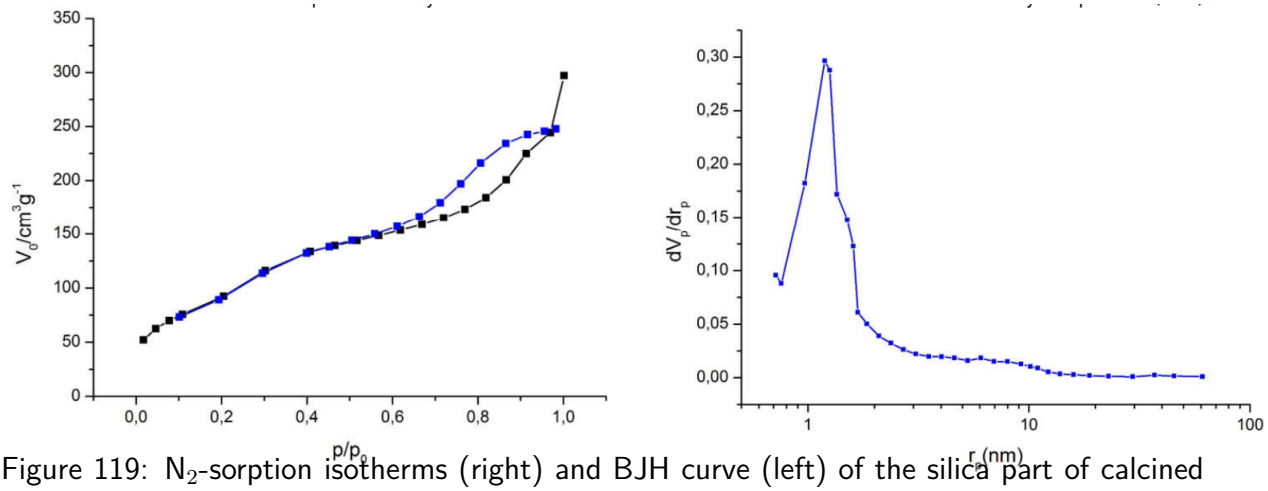

Figure 119: N_2-sorption isotherms (right) and BJH curve (left) of the silica part of calcined modified RSMNPs (modified SMNPs equivalent).

Table 46: BET: Total pore volume (V_t), BET area ($a_{\mathrm{S,BET}}$) and C coefficient (C_{BET}); t-plot: internal (a_{int}) and external (a_{ext}) pore area and microporous (V_{meso}) and mesoporous (V_{meso}) volume; microporous ratio (V_{micro}/V_t) of modified hybrid silica-resol nanoparticles after calcination (modified SMNPs equivalent).

	modified SMNPs
	BET
V_t (cm^3/g)	0.43
$a_{\mathrm{S,BET}}$ (m^2/g)	392
C_{BET}	60
	t-plot
a_{int} (m^2/g)	324
a_{ext} (m^2/g)	167
V_{micro} (cm^3/g)	5.7×10^{-3}
V_{meso} (cm^3/g)	0.12
V_{meso}/V_t	0.28
	BJH
D_{BJH} (nm)	2.4
D_{min} (nm)	1.6
D_{max} (nm)	15.8

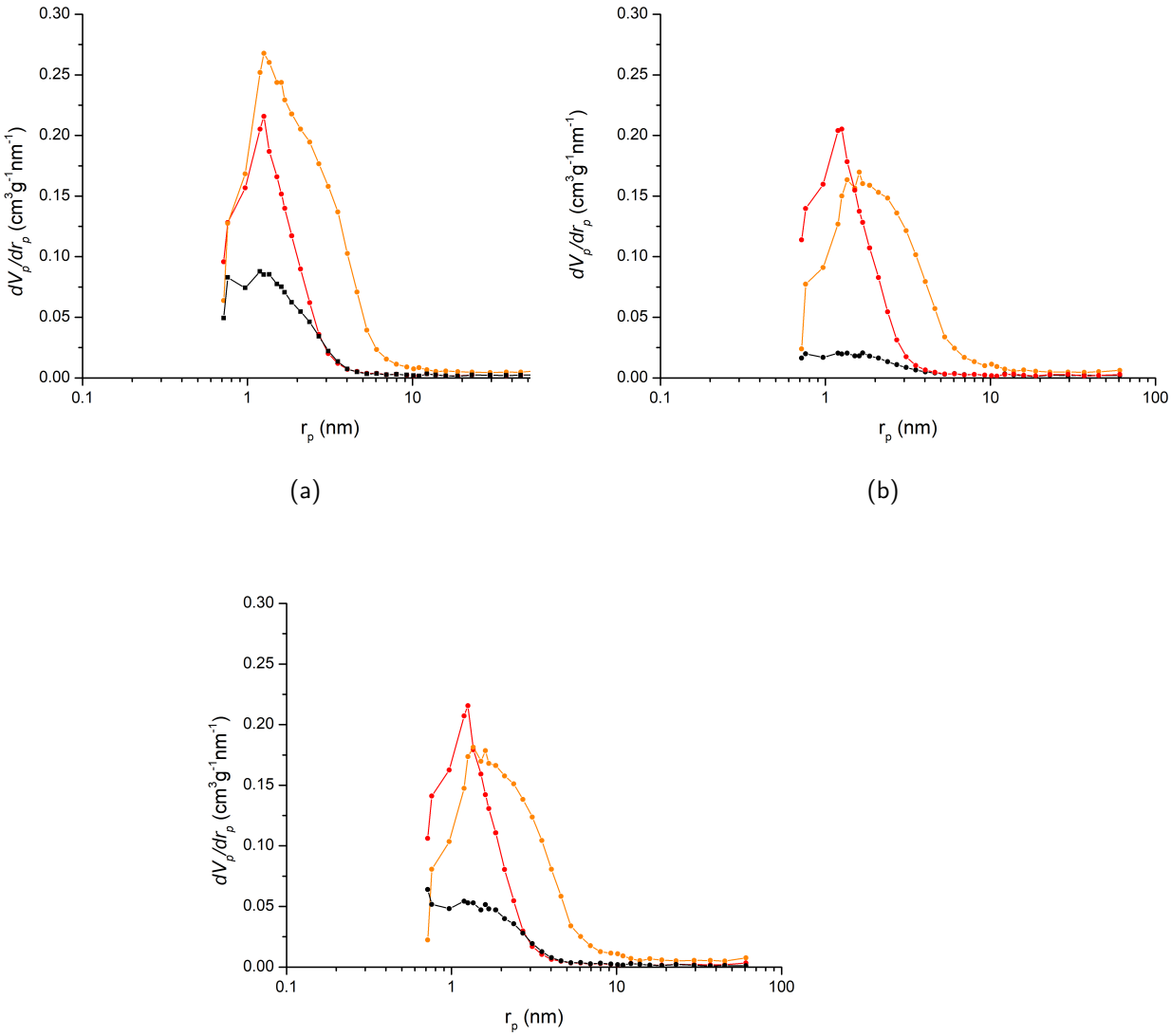

Figure 120: (a) (on the upper left) BJH plot of RSMNPs (red), SMNPs (orange) and CSMNPs (black). (b) (on the upper right) BJH plot of [Mn^{II}]@RSMNPs loaded with 50 mg (red), [Mn^{II}]@RSMNPs loaded with 50 mg (orange) and [Mn^{II}]@RSMNPs loaded with 50 mg (black). (c) (in the lower middle) BJH plot of [Mn^{III}]@RSMNPs loaded with 50 mg (red), [Mn^{III}]@RSMNPs loaded with 50 mg (orange) and [Mn^{III}]@RSMNPs loaded with 50 mg (black).

Details on the elemental analysis provided by the Institut des Sciences Analytiques

Total carbon and nitrogen analyses are determined using two homemade micro-analysers (Institut des Sciences Analytiques, Villeurbanne, France).

Carbon quantification: The sample sealed in silver capsule is dropped in a flow of oxygen. The combustion unit is held at 1050 °C followed by a post combustion furnace maintained at 850 °C containing copper oxide. The flash combustion allows the complete transformation of the carbon into carbon dioxide (CO_2) which is quantified using a non-dispersive infrared detector.

Nitrogen quantification: The sample sealed in silver cup is dropped in a flow of helium-oxygen in the combustion unit previously described where nitrogen is converted into nitrogen oxides. The flow of gases is conveyed through a tube filled with copper wires where nitrogen oxide is reduced in pure nitrogen and quantified on a Thermo Conductivity Detector (TCD).

Total chlorine quantification Total chlorine determination has been performed using an Automatic Quick Furnace AQF100 (Mitsubishi Chemical Analytech, Yamato, Japan) connected to an Ion Chromatography ICS 1100 (Thermo Fisher Scientific, Sunnyvale, CA, USA). From 2 to 5 mg of sample previously weighted in a ceramic sample boat are introduced in a hot furnace maintained at 1000 °C in a flow of a mix of oxygen-argon. Chlorine is extracted in the gas stream and trapped (Cl_2) in a hydrogen peroxide solution. An amount of 25 μl of this absorption solution is directly injected to the ion chromatic Integrion for analysis.

Bibliography

[1] FA Cotton and G Wilkinson. Advanced inorganic chemistry, 1972.

[2] Barry B Snider. Manganese (III)-based oxidative free-radical cyclizations. *Chemical Reviews*, 96(1):339–364, 1996.

[3] Masayuki Yagi and Masao Kaneko. Molecular catalysts for water oxidation. *Chemical Reviews*, 101(1):21–36, 2001.

[4] Andrew Murphy, Geraud Dubois, and TDP Stack. Efficient epoxidation of electron-deficient olefins with a cationic manganese complex. *Journal of the American Chemical Society*, 125(18):5250–5251, 2003.

[5] Andrew Murphy, Allyson Pace, and T Daniel P Stack. Ligand and pH influence on manganese-mediated peracetic acid epoxidation of terminal olefins. *Organic Letters*, 6(18):3119–3122, 2004.

[6] Andrew Murphy and T Daniel P Stack. Discovery and optimization of rapid manganese catalysts for the epoxidation of terminal olefins. *Journal of Molecular Catalysis A: Chemical*, 251(1-2):78–88, 2006.

[7] Isaac Garcia-Bosch, Anna Company, Xavier Fontrodona, Xavi Ribas, and Miquel Costas. Efficient and selective peracetic acid epoxidation catalyzed by a robust manganese catalyst. *Organic Letters*, 10(11):2095–2098, 2008.

[8] D Pijper, P Saisaha, JW de Boer, R Hoen, C Smit, A Meetsma, and R Hage. The unexpected role of pyridine-2-carboxylic acid in manganese based oxidation catalysis with pyridin-2-yl based ligands. *Dalton Trans*, 39:10375–10381, 2010.

[9] Anastasios J Tasiopoulos, Alina Vinslava, Wolfgang Wernsdorfer, Khalil A Abboud, and George Christou. Giant Single-Molecule Magnets: A $\{Mn_{84}\}$ Torus and Its Supramolecular Nanotubes. *Angewandte Chemie International Edition*, 43(16):2117–2121, 2004.

[10] R Winpenny. *Comprehensive Coordination Chemistry II*. Pergamon: Oxford, 2003.

[11] Vincent L Pecoraro. *Manganese redox enzymes*. VCH, 1992.

[12] GB Deacon and RJ Phillips. Relationships between the carbon-oxygen stretching frequencies of carboxylato complexes and the type of carboxylate coordination. *Coordination Chemistry Reviews*, 33(3):227–250, 1980.

[13] Stephen J Lippard and Jeremy Mark Berg. *Principles of bioinorganic chemistry*. University Science Books, 1994.

[14] Verónica Gómez and Montserrat Corbella. Versatility in the Coordination Modes of n-Chlorobenzoato Ligands: Synthesis, Structure and Magnetic Properties of Three Types of Polynuclear MnII Compounds. *European Journal of Inorganic Chemistry*, 2009(29-30):4471–4482, 2009.

[15] Neil A Law, M Tyler Caudle, and Vincent L Pecoraro. Manganese redox enzymes and model systems: properties, structures, and reactivity. In *Advances in Inorganic Chemistry*, volume 46, pages 305–440. Elsevier, 1998.

[16] G Charles Dismukes. Manganese enzymes with binuclear active sites. *Chemical Reviews*, 96(7):2909–2926, 1996.

[17] Satadal Paul, Frank Neese, and Dimitrios A Pantazis. Structural models of the biological oxygen-evolving complex: achievements, insights, and challenges for biomimicry. *Green Chemistry*, 19(10):2309–2325, 2017.

[18] James A Imlay. The molecular mechanisms and physiological consequences of oxidative stress: lessons from a model bacterium. *Nature Reviews Microbiology*, 11(7):443, 2013.

[19] Carl Nathan and Amy Cunningham-Bussel. Beyond oxidative stress: an immunologist's guide to reactive oxygen species. *Nature Reviews Immunology*, 13(5):349, 2013.

[20] Cheves Walling. Fenton's reagent revisited. *Accounts of Chemical Research*, 8(4):125–131, 1975.

[21] Vitor Costa and Pedro Moradas-Ferreira. Oxidative stress and signal transduction in saccharomyces cerevisiae: insights into ageing, apoptosis and diseases. *Molecular Aspects of Medicine*, 22(4-5):217–246, 2001.

[22] David S Warner, Huaxin Sheng, and Ines Batinić-Haberle. Oxidants, antioxidants and the ischemic brain. *Journal of Experimental Biology*, 207(18):3221–3231, 2004.

[23] Marian Valko, Dieter Leibfritz, Jan Moncol, Mark TD Cronin, Milan Mazur, and Joshua Telser. Free radicals and antioxidants in normal physiological functions and human disease. *The International Journal of Biochemistry & Cell Biology*, 39(1):44–84, 2007.

[24] Lawrence M Sayre, George Perry, and Mark A Smith. Oxidative stress and neurotoxicity. *Chemical Research in Toxicology*, 21(1):172–188, 2007.

[25] Jim Watson. Oxidants, antioxidants and the current incurability of metastatic cancers. *Open Biology*, 3(1):120144, 2013.

[26] Thales P Ribeiro, Fernanda L Fonseca, Mariana DC de Carvalho, Rodrigo MC Godinho, Fernando Pereira de Almeida, Tatiana Saint'Pierre, Nicolás A Rey, Christiane Fernandes, Adolfo Horn, and Marcos Pereira. Metal-based superoxide dismutase and catalase mimics reduce oxidative stress biomarkers and extend lifespan of saccharomyces cerevisiae. *Biochemical Journal*, 2016.

[27] Brian J Day. Catalytic antioxidants: a radical approach to new therapeutics. *Drug Discovery Today*, 9(13):557–566, 2004.

[28] Brian J Day. Antioxidants as potential therapeutics for lung fibrosis. *Antioxidants & Redox Signaling*, 10(2):355–370, 2008.

[29] Brian J Day. Catalase and glutathione peroxidase mimics. *Biochemical Pharmacology*, 77(3):285–296, 2009.

[30] Ines Batinić-Haberle, Júlio S Rebouças, and Ivan Spasojević. Superoxide dismutase mimics: chemistry, pharmacology, and therapeutic potential. *Antioxidants & Redox Signaling*, 13(6):877–918, 2010.

[31] Amparo Escribano, Mónica Amor, Sara Pastor, Silvia Castillo, Francisco Sanz, Pilar Codoñer-Franch, and Francisco Dasí. Decreased glutathione and low catalase activity contribute to oxidative stress in children with α-1 antitrypsin deficiency. *Thorax*, 70(1):82–83, 2015.

[32] Yossi Gilgun-Sherki, Eldad Melamed, and Daniel Offen. The role of oxidative stress in the pathogenesis of multiple sclerosis: the need for effective antioxidant therapy. *Journal of Neurology*, 251(3):261–268, 2004.

[33] Werner J Geldenhuys and Altaf S Darvesh. Pharmacotherapy of Alzheimer's disease: current and future trends, 2015.

[34] Monica Colamartino, Massimo Santoro, Guglielmo Duranti, Stefania Sabatini, Roberta Ceci, Antonella Testa, Luca Padua, and Renata Cozzi. Evaluation of levodopa and carbidopa antioxidant activity in normal human lymphocytes in vitro: implication for oxidative stress in parkinson's disease. *Neurotoxicity Research*, 27(2):106–117, 2015.

[35] Martin Karlík, Peter Valkovič, Viera Hančinová, Lucia Krížová, L'ubomíra Tóthová, and Peter Celec. Markers of oxidative stress in plasma and saliva in patients with multiple sclerosis. *Clinical Biochemistry*, 48(1-2):24–28, 2015.

[36] Omar A Jaffer, A Brent Carter, Philip N Sanders, Megan E Dibbern, Christopher J Winters, Shubha Murthy, Alan J Ryan, Adam G Rokita, Anand M Prasad, Joseph Zabner, et al. Mitochondrial-targeted antioxidant therapy decreases transforming growth factor-β–mediated collagen production in a murine asthma model. *American Journal of Respiratory Cell and Molecular Biology*, 52(1):106–115, 2015.

[37] Dennis P Nelson and Lutz A Kiesow. Enthalpy of decomposition of hydrogen peroxide by catalase at 25 C (with molar extinction coefficients of H_2O_2 solutions in the UV). *Analytical Biochemistry*, 49(2):474–478, 1972.

[38] Yasuhisa Kono and Irwin Fridovich. Isolation and characterization of the pseudocatalase of Lactobacillus plantarum. *Journal of Biological Chemistry*, 258(10):6015–6019, 1983.

[39] Wayne F Beyer Jr and Irwin Fridovich. Pseudocatalase from Lactobacillus plantarum: evidence for a homopentameric structure containing two atoms of manganese per subunit. *Biochemistry*, 24(23):6460–6467, 1985.

[40] Vladimir V Barynin, Mei M Whittaker, Svetlana V Antonyuk, Victor S Lamzin, Pauline M Harrison, Peter J Artymiuk, and James W Whittaker. Crystal structure of manganese catalase from Lactobacillus plantarum. *Structure*, 9(8):725–738, 2001.

[41] GS Allgood and JJ Perry. Characterization of a manganese-containing catalase from the obligate thermophile Thermoleophilum album. *Journal of Bacteriology*, 168(2):563–567, 1986.

[42] SV Antonyuk, VR Melik-Adamyan, AN Popov, VS Lamzin, PD Hempstead, PM Harrison, PJ Artymyuk, and VV Barynin. Three-dimensional structure of the enzyme dimanganese catalase from thermus thermophilus at 1 Å resolution. *Crystallography Reports*, 45(1):105–116, 2000.

[43] Subhash C Bihani, Dhiman Chakravarty, and Anand Ballal. KatB, a cyanobacterial Mn-catalase with unique active site configuration: implications for enzyme function. *Free Radical Biology and Medicine*, 93:118–129, 2016.

[44] James W Whittaker. Non-heme manganese catalase–the 'other' catalase. *Archives of Biochemistry and Biophysics*, 525(2):111–120, 2012.

[45] Sandra Signorella and Christelle Hureau. Bioinspired functional mimics of the manganese catalases. *Coordination Chemistry Reviews*, 256(11-12):1229–1245, 2012.

[46] Mei M Whittaker, Vladimir V Barynin, Takao Igarashi, and James W Whittaker. Outer sphere mutagenesis of Lactobacillus plantarum manganese catalase disrupts the cluster core: Mechanistic implications. *European Journal of Biochemistry*, 270(6):1102–1116, 2003.

[47] Mary Shank, Vladimir Barynin, and G Charles Dismukes. Protein coordination to manganese determines the high catalytic rate of dimanganese catalases. comparison to functional catalase mimics. *Biochemistry*, 33(51):15433–15436, 1994.

[48] Sandra Signorella, Claudia Palopoli, and Gabriela Ledesma. Rationally designed mimics of antioxidant manganoenzymes: Role of structural features in the quest for catalysts with catalase and superoxide dismutase activity. *Coordination Chemistry Reviews*, 365:75–102, 2018.

[49] Paramita Kar, Michael GB Drew, and Ashutosh Ghosh. Synthesis, structure and catalase activity of three new manganese (III) complexes with a N, N, O donor Schiff-base ligand. *Inorganica Chimica Acta*, 405:349–355, 2013.

[50] Yukinobu Noritake, Naoki Umezawa, Nobuki Kato, and Tsunehiko Higuchi. Manganese Salen Complexes with Acid–Base Catalytic Auxiliary: Functional Mimetics of Catalase. *Inorganic Chemistry*, 52(7):3653–3662, 2013.

[51] Riku Kubota, Shinya Imamura, Takahiko Shimizu, Shoichiro Asayama, and Hiroyoshi Kawakami. Synthesis of water-soluble dinuclear Mn-porphyrin with multiple antioxidative activities. *ACS Medicinal Chemistry Letters*, 5(6):639–643, 2014.

[52] Riku Kubota, Shoichiro Asayama, and Hiroyoshi Kawakami. A bioinspired polymer-bound Mn-porphyrin as an artificial active center of catalase. *Chemical Communications*, 50(100):15909–15912, 2014.

[53] Gabriela N Ledesma, Hélène Eury, Elodie Anxolabehere-Mallart, Christelle Hureau, and Sandra R Signorella. A new mononuclear manganese (III) complex of an unsymmetrical hexadentate N_3O_3 ligand exhibiting superoxide dismutase and catalase-like activity: synthesis, characterization, properties and kinetics studies. *Journal of Inorganic Biochemistry*, 146:69–76, 2015.

[54] Magdalena Procner, G Stochel, R van Eldik, et al. Spectroscopic and kinetic evidence for redox cycling, catalase and degradation activities of mn III (TPPS) in a basic aqueous peroxide medium. *Chemical Communications*, 52(30):5297–5300, 2016.

[55] Claudia Palopoli, Carine Duhayon, Jean-Pierre Tuchagues, and Sandra Signorella. Synthesis, characterization, and reactivity studies of a water-soluble bis (alkoxo)(carboxylato)-bridged diMn III complex modeling the active site in catalase. *Dalton Transactions*, 43(45):17145–17155, 2014.

[56] Luis Escriche-Tur, Montserrat Corbella, Mercè Font-Bardia, Isabel Castro, Laurent Bonneviot, and Belén Albela. Biomimetic Mn-catalases based on dimeric manganese complexes in mesoporous silica for potential antioxidant agent. *Inorganic Chemistry*, 54(21):10111–10125, 2015.

[57] Beltzane Garcia-Cirera, Montserrat Corbella, Laurent Bonneviot, and Belén Albela. Bioinspired manganese mesoporous silica hybrid material as a water compatible antioxidant. *Microporous and Mesoporous Materials*, 261:150–157, 2018.

[58] Gabriela N Ledesma, Elodie Anxolabéhère-Mallart, Laurent Sabater, Christelle Hureau, and Sandra R Signorella. Functional modeling of the MnCAT active site with a dimanganese (III) complex of an unsymmetrical polydentate N_3O_3 ligand. *Journal of inorganic biochemistry*, 186:10–16, 2018.

[59] Dusan Losic, James G Mitchell, and Nicolas H Voelcker. Diatomaceous lessons in nanotechnology and advanced materials. *Advanced Materials*, 21(29):2947–2958, 2009.

[60] KSA Butcher, JM Ferris, MR Phillips, M Wintrebert-Fouquet, JW Jong Wah, Nemanja Jovanovic, Wim Vyverman, and VA Chepurnov. A luminescence study of porous diatoms. *Materials Science and Engineering: C*, 25(5-8):658–663, 2005.

[61] Richard Wetherbee, Jan L Lind, Jo Burke, and Ralph S Quatrano. Minireview—the first kiss: establishment and control of initial adhesion by raphid diatoms. *Journal of Phycology*, 34(1):9–15, 1998.

[62] Werner Stöber, Arthur Fink, and Ernst Bohn. Controlled growth of monodisperse silica spheres in the micron size range. *Journal of Colloid and Interface Science*, 26(1):62–69, 1968.

[63] Edward JA Pope and JD Mackenzie. Sol-gel processing of silica: II. The role of the catalyst. *Journal of Non-Crystalline Solids*, 87(1-2):185–198, 1986.

[64] Michael W Daniels, Jan Sefcik, Lorraine F Francis, and Alon V McCormick. Reactions of a trifunctional silane coupling agent in the presence of colloidal silica sols in polar media. *Journal of Colloid and Interface Science*, 219(2):351–356, 1999.

[65] Stephen E Rankin, Jan Sefcik, and Alon V McCormick. Similarities in the hydrolysis pseudoequilibrium behavior of methyl-substituted ethoxysilanes. *Industrial & Engineering Chemistry Research*, 38(9):3191–3198, 1999.

[66] C Jeffrey Brinker and Roger A Assink. Spinnability of silica sols structural and rheological criteria. *Journal of Non-Crystalline Solids*, 111(1):48–54, 1989.

[67] Keithd Keefer. Structure and growth of silica condensation polymers. 1987.

[68] KD Keefer. The effect of hydrolysis conditions on the structure and growth of silicate polymers. *MRS Online Proceedings Library Archive*, 32, 1984.

[69] Cesar R Silva and Claudio Airoldi. Acid and base catalysts in the hybrid silica sol–gel process. *Journal of Colloid and Interface Science*, 195(2):381–387, 1997.

[70] Ernst Heinrich Philipp August Haeckel and Jochen Martens. *Kunstformen der Natur: hundert Illustrationstafeln mit beschreibendem Text: Allgemeine Erlüterung und systematische Übersicht*. Marix Verlag, 1904.

[71] Nadine Nassif and Jacques Livage. From diatoms to silica-based biohybrids. *Chemical Society Reviews*, 40(2):849–859, 2011.

[72] L De Stefano, P Maddalena, L Moretti, I Rea, I Rendina, E De Tommasi, V Mocella, and Mario De Stefano. Nano-biosilica from marine diatoms: A brand new material for photonic applications. *Superlattices and Microstructures*, 46(1-2):84–89, 2009.

[73] Helmut K Schmidt, Horst Scholze, and Alfred Kaiser. Principles of hydrolysis and condensation reaction of alkoxysilanes.-Part I: Basic investigations on hydrolysis, condensation and densification I. 1984.

[74] F Devreux, JP Boilot, F Chaput, and A Lecomte. Sol-gel condensation of rapidly hydrolyzed silicon alkoxides: A joint ^{29}Si NMR and small-angle X-ray scattering study. *Physical Review A*, 41(12):6901, 1990.

[75] Jae Young Choi, Chong Hee Kim, and Do Kyung Kim. Formation and characterization of monodisperse, spherical organo-silica powders from organo-alkoxysilane-water system. *Journal of the American Ceramic Society*, 81(5):1184–1188, 1998.

[76] Norihiro Nishiyama, Kozo Horie, and Tetsuo Asakura. Adsorption behavior of a silane coupling agent onto a colloidal silica surface studied by ^{29}Si NMR spectroscopy. *Journal of Colloid and Interface Science*, 129(1):113–119, 1989.

[77] Yoshiyuki Sugahara, Seigo Okada, Shuji Sato, Kazuyuki Kuroda, and Chuzo Kato. ^{29}Si-NMR study of hydrolysis and initial polycondensation processes of organoalkoxysilanes. ii. methyltriethoxysilane. *Journal of Non-Crystalline Solids*, 167(1-2):21–28, 1994.

[78] Dongyuan Zhao, Ying Wan, and Wuzong Zhou. *Ordered mesoporous materials*. John Wiley & Sons, 2012.

[79] CT Kresge, ME Leonowicz, W Jelal Roth, JC Vartuli, and JS Beck. Ordered mesoporous molecular sieves synthesized by a liquid-crystal template mechanism. *nature*, 359(6397):710, 1992.

[80] Alain Monnier, F Schuth, Q Huo, D Kumar, D Margolese, RS Maxwell, GD Stucky, M Krishnamurty, P Petroff, A Firouzi, et al. Cooperative formation of inorganic-organic interfaces in the synthesis of silicate mesostructures. *Science*, 261(5126):1299–1303, 1993.

[81] Dongyuan Zhao, Jianglin Feng, Qisheng Huo, Nicholas Melosh, Glenn H Fredrickson, Bradley F Chmelka, and Galen D Stucky. Triblock copolymer syntheses of mesoporous silica with periodic 50 to 300 angstrom pores. *Science*, 279(5350):548–552, 1998.

[82] Frank Hoffmann, Maximilian Cornelius, Jürgen Morell, and Michael Fröba. Silica-based mesoporous organic–inorganic hybrid materials. *Angewandte Chemie International Edition*, 45(20):3216–3251, 2006.

[83] Qisheng Huo, David I Margolese, Ulrike Ciesla, Pingyun Feng, Thurman E Gier, Peter Sieger, Rosa Leon, Pierre M Petroff, Ferdi Schüth, and Galen D Stucky. Generalized synthesis of periodic surfactant/inorganic composite materials. *Nature*, 368(6469):317, 1994.

[84] Ying Wan and Dongyuan Zhao. On the controllable soft-templating approach to mesoporous silicates. *Chemical Reviews*, 107(7):2821–2860, 2007.

[85] Jie Fan, Shannon W Boettcher, Chia-Kuang Tsung, Qihui Shi, Martin Schierhorn, and Galen D Stucky. Field-directed and confined molecular assembly of mesostructured materials: basic principles and new opportunities. *Chemistry of Materials*, 20(3):909–921, 2007.

[86] Belén Albela and Laurent Bonneviot. Surface molecular engineering in the confined space of templated porous silica. *New Journal of Chemistry*, 40(5):4115–4131, 2016.

[87] JS Beck, JC Vartuli, WJ Roth, ME Leonowicz, CT Kresge, KD Schmitt, CTW Chu, DH Olson, EW Sheppard, SB McCullen, et al. Synthesis and comparative reactivity and electronic structural features of $[MFe_3S_4]^{z+}$ cubane-type clusters (M= iron, cobalt, nickel). *Journal of the American Chemical Society*, 114:10843–54, 1992.

[88] P Reinert, B Garcia, C Morin, A Badiei, P Perriat, O Tillement, and L Bonneviot. Cationic templating with organic counterion for superstable mesoporous silica. In *Studies in Surface Science and Catalysis*, volume 146, pages 133–136. Elsevier, 2003.

[89] Kun Zhang, Hong-Li Chen, Belén Albela, Jin-Gang Jiang, Yi-Meng Wang, Ming-Yuan He, and Laurent Bonneviot. High-Temperature Synthesis and Formation Mechanism of Stable, Ordered MCM-41 Silicas by Using Surfactant Cetyltrimethylammonium Tosylate as Template. *European Journal of Inorganic Chemistry*, 2011(1):59–67, 2011.

[90] Jérémy Chaignon, Salah-Eddine Stiriba, Francisco Lloret, Consuelo Yuste, Guillaume Pilet, Laurent Bonneviot, Belén Albela, and Isabel Castro. Bioinspired manganese (II) complexes with a clickable ligand for immobilisation on a solid support. *Dalton Transactions*, 43(25):9704–9713, 2014.

[91] L Du, J Li, C Chen, and Y Liu. Nanocarrier: a potential tool for future antioxidant therapy. *Free Radical Research*, 48(9):1061–1069, 2014.

[92] Erika Witasp, Natalia Kupferschmidt, Linnéa Bengtsson, Kjell Hultenby, Christian Smedman, Staffan Paulie, Alfonso E Garcia-Bennett, and Bengt Fadeel. Efficient internalization of mesoporous silica particles of different sizes by primary human macrophages without impairment of macrophage clearance of apoptotic or antibody-opsonized target cells. *Toxicology and Applied Pharmacology*, 239(3):306–319, 2009.

[93] Swadeshmukul Santra, Peng Zhang, Kemin Wang, Rovelyn Tapec, and Weihong Tan. Conjugation of biomolecules with luminophore-doped silica nanoparticles for photostable biomarkers. *Analytical chemistry*, 73(20):4988–4993, 2001.

[94] Hooisweng Ow, Daniel R Larson, Mamta Srivastava, Barbara A Baird, Watt W Webb, and Ulrich Wiesner. Bright and stable core-shell fluorescent silica nanoparticles. *Nano Letters*, 5(1):113–117, 2005.

[95] Zaki G Estephan, Jad A Jaber, and Joseph B Schlenoff. Zwitterion-stabilized silica nanoparticles: toward nonstick nano. *Langmuir*, 26(22):16884–16889, 2010.

[96] Zaki G Estephan, Philip S Schlenoff, and Joseph B Schlenoff. Zwitteration as an alternative to PEGylation. *Langmuir*, 27(11):6794–6800, 2011.

[97] Fenglin Hu, Kaimin Chen, Hong Xu, and Hongchen Gu. Functional short-chain zwitterion coated silica nanoparticles with antifouling property in protein solutions. *Colloids and Surfaces B: Biointerfaces*, 126:251–256, 2015.

[98] Juan L Vivero-Escoto, Igor I Slowing, Brian G Trewyn, and Victor S-Y Lin. Mesoporous silica nanoparticles for intracellular controlled drug delivery. *Small*, 6(18):1952–1967, 2010.

[99] Maria Vallet-Regi, Francisco Balas, and Daniel Arcos. Mesoporous materials for drug delivery. *Angewandte Chemie International Edition*, 46(40):7548–7558, 2007.

[100] Elena Aznar, Mar Oroval, Lluís Pascual, Jose Ramón Murguía, Ramón Martínez-Máñez, and Félix Sancenón. Gated materials for on-command release of guest molecules. *Chemical Reviews*, 116(2):561–718, 2016.

[101] Yang Xia, Chen Qiu-Yun, and Song Jing-Bao. Tumor-imaging core-shell nano-models for catalase. *Chinese Journal of Inorganic Chemistry*, 28(1):164–170, 2012.

[102] Anca Lascu, Anca Palade, Gheorghe Fagadar-Cosma, Ionela Creanga, Catalin Ianasi, Iuliana Sebarchievici, Mihaela Birdeanu, and Eugenia Fagadar-Cosma. Mesoporous manganese–porphyrin–silica hybrid nanomaterial sensitive to H_2O_2 fluorescent detection. *Materials Research Bulletin*, 74:325–332, 2016.

[103] Jinghua Yu, Lei Ge, Shiquan Liu, Ping Dai, Shenguang Ge, and Wei Zheng. Facile and scalable synthesis of a novel rigid artificial superoxide dismutase based on modified hollow mesoporous silica microspheres. *Biosensors and Bioelectronics*, 26(5):1936–1941, 2011.

[104] Zita Csendes, Gábor Varga, Nóra Veronika Nagy, Éva Gabriella Bajnóczi, Mónika Sipiczki, Stefan Carlson, Sophie E Canton, Anikó Metzinger, Gábor Galbács, P Sipos, et al. Synthesis, structural characterisation, and catalytic activity of Mn (II)–protected amino acid complexes covalently immobilised on chloropropylated silica gel. *Catalysis Today*, 241:264–269, 2015.

[105] Man Yang, Wu Jiang, Zhiquan Pan, and Hong Zhou. Synthesis, characterization and SOD-like activity of histidine immobilized silica nanoparticles. *Journal of Inorganic and Organometallic Polymers and Materials*, 25(5):1289–1297, 2015.

[106] Evan MW Rumberger, Hyun S Ahn, Alexis T Bell, and T Don Tilley. Water oxidation catalysis via immobilization of the dimanganese complex $[Mn_2(\mu\text{-}O)_2Cl(\mu\text{-}O_2CCH_3)(bpy)_2(H_2O)](NO_3)_2$ onto silica. *Dalton Transactions*, 42(34):12238–12247, 2013.

[107] Kun Zhang, Lang-Lang Xu, Jin-Gang Jiang, Nathalie Calin, Koon-Fung Lam, San-Jun Zhang, Hai-Hong Wu, Guang-Dong Wu, Belén Albela, Laurent Bonneviot, et al. Facile large-scale synthesis of monodisperse mesoporous silica nanospheres with tunable pore structure. *Journal of the American Chemical Society*, 135(7):2427–2430, 2013.

[108] CE Fowler, D Khushalani, B Lebeau, and S Mann. Nanoscale materials with mesostructured interiors. *Advanced Materials*, 13(9):649–652, 2001.

[109] Chihiro Urata, Yuko Aoyama, Akihisa Tonegawa, Yusuke Yamauchi, and Kazuyuki Kuroda. Dialysis process for the removal of surfactants to form colloidal mesoporous silica nanoparticles. *Chemical Communications*, (34):5094–5096, 2009.

[110] Asep Bayu Dani Nandiyanto, Soon-Gil Kim, Ferry Iskandar, and Kikuo Okuyama. Synthesis of spherical mesoporous silica nanoparticles with nanometer-size controllable pores and outer diameters. *Microporous and Mesoporous Materials*, 120(3):447–453, 2009.

[111] Yu-Shen Lin, Nardine Abadeer, Katie R Hurley, and Christy L Haynes. Ultrastable, redispersible, small, and highly organomodified mesoporous silica nanotherapeutics. *Journal of the American Chemical Society*, 133(50):20444–20457, 2011.

[112] Dechao Niu, Zuojin Liu, Yongsheng Li, Xiaofeng Luo, Junyong Zhang, Jianping Gong, and Jianlin Shi. Monodispersed and Ordered Large-Pore Mesoporous Silica Nanospheres with Tunable Pore Structure for Magnetic Functionalization and Gene Delivery. *Advanced Materials*, 26(29):4947–4953, 2014.

[113] Jian-Feng Chen, Hao-Min Ding, Jie-Xin Wang, and Lei Shao. Preparation and characterization of porous hollow silica nanoparticles for drug delivery application. *Biomaterials*, 25(4):723–727, 2004.

[114] Jian Liu, Shi Zhang Qiao, Jun Song Chen, Xiong Wen David Lou, Xianran Xing, and Gao Qing Max Lu. Yolk/shell nanoparticles: new platforms for nanoreactors, drug delivery and lithium-ion batteries. *Chemical Communications*, 47(47):12578–12591, 2011.

[115] Dietmar Knopp, Dianping Tang, and Reinhard Niessner. Bioanalytical applications of biomolecule-functionalized nanometer-sized doped silica particles. *Analytica Chimica Acta*, 647(1):14–30, 2009.

[116] Xu Wu, Min Wu, and Julia Xiaojun Zhao. Recent development of silica nanoparticles as delivery vectors for cancer imaging and therapy. *Nanomedicine: Nanotechnology, Biology and Medicine*, 10(2):297–312, 2014.

[117] Enrico Rampazzo, Sara Bonacchi, Marco Montalti, Luca Prodi, and Nelsi Zaccheroni. Self-organizing core-shell nanostructures: spontaneous accumulation of dye in the core of doped silica nanoparticles. *Journal of the American Chemical Society*, 129(46):14251–14256, 2007.

[118] Qing Chang, Lihua Zhu, Chen Yu, and Heqing Tang. Synthesis and properties of magnetic and luminescent $Fe_3O_4/SiO_2/Dye/SiO_2$ nanoparticles. *Journal of Luminescence*, 128(12):1890–1895, 2008.

[119] Michihiro Nakamura, Masayuki Shono, and Kazunori Ishimura. Synthesis, characterization, and biological applications of multifluorescent silica nanoparticles. *Analytical Chemistry*, 79(17):6507–6514, 2007.

[120] Liane M Rossi, Lifang Shi, Frank H Quina, and Zeev Rosenzweig. Stöber synthesis of monodispersed luminescent silica nanoparticles for bioanalytical assays. *Langmuir*, 21(10):4277–4280, 2005.

[121] Indrajit Roy, Tymish Y Ohulchanskyy, Dhruba J Bharali, Haridas E Pudavar, Ruth A Mistretta, Navjot Kaur, and Paras N Prasad. Optical tracking of organically modified silica nanoparticles as DNA carriers: a nonviral, nanomedicine approach for gene delivery. *Proceedings of the National Academy of Sciences*, 102(2):279–284, 2005.

[122] Joseph F Bringley, Thomas L Penner, Ruizheng Wang, John F Harder, William J Harrison, and Laura Buonemani. Silica nanoparticles encapsulating near-infrared emissive cyanine dyes. *Journal of Colloid and Interface Science*, 320(1):132–139, 2008.

[123] Dongling Ma, Arnold J Kell, Sophie Tan, Zygmunt J Jakubek, and Benoit Simard. Photophysical properties of dye-doped silica nanoparticles bearing different types of dye- silica interactions. *The Journal of Physical Chemistry C*, 113(36):15974–15981, 2009.

[124] L Armelao, S Quici, F Barigelletti, G Accorsi, G Bottaro, M Cavazzini, and E Tondello. Design of luminescent lanthanide complexes: From molecules to highly efficient photo-emitting materials. *Coordination Chemistry Reviews*, 254(5-6):487–505, 2010.

[125] Catherine A Rice-evans, Nicholas J Miller, Paul G Bolwell, Peter M Bramley, and John B Pridham. The relative antioxidant activities of plant-derived polyphenolic flavonoids. *Free Radical Research*, 22(4):375–383, 1995.

[126] Catherine A Rice-Evans, Nicholas J Miller, and George Paganga. Structure-antioxidant activity relationships of flavonoids and phenolic acids. *Free Radical Biology and Medicine*, 20(7):933–956, 1996.

[127] S Chow and PR Steiner. Determination of resorcinol content in phenol-resorcinol-formaldehyde resins by infrared spectrometry. *Holzforschung-International Journal of the Biology, Chemistry, Physics and Technology of Wood*, 32(4):120–122, 1978.

[128] Moon G Kim, Larry W Amos, and Edwin E Barnes. Investigation of a resorcinol–formaldehyde resin by ^{13}C-NMR spectroscopy and intrinsic viscosity measurement. *Journal of Polymer Science Part A: Polymer Chemistry*, 31(7):1871–1877, 1993.

[129] E Scopelitis and A Pizzi. The chemistry and development of branched PRF wood adhesives of low resorcinol content. *Journal of Applied Polymer Science*, 47(2):351–360, 1993.

[130] In Yang, Syehee Ahn, In-gyu Choi, Ho-Yong Kim, and Seichang Oh. Adhesives formulated with chemically modified okara and phenol–resorcinol–formaldehyde for bonding fancy veneer onto high-density fiberboard. *Journal of Industrial and Engineering Chemistry*, 15(3):398–402, 2009.

[131] A Sauget, X Zhou, and A Pizzi. Tannin-resorcinol-formaldehyde resin and flax fiber bio-composites. *Journal of Renewable Materials*, 2(3):173–181, 2014.

[132] Jürgen Ennker, Ina Carolin Ennker, Doris Schoon, Heinz Adolf Schoon, Sven Dörge, Michael Meissler, Manfred Rimpler, and Roland Hetzer. The impact of gelatin-resorcinol glue on aortic tissue: a histomorphologic evaluation. *Journal of Vascular Surgery*, 20(1):34–43, 1994.

[133] Jacques R Seguin, Eric Picard, Jean-Marc Frapier, and Paul-Andre Chaptal. Aortic valve repair with fibrin glue for type A acute aortic dissection. *The Annals of Thoracic Surgery*, 58(2):304–307, 1994.

[134] Yin Fang, Dong Gu, Ying Zou, Zhangxiong Wu, Fuyou Li, Renchao Che, Yonghui Deng, Bo Tu, and Dongyuan Zhao. A low-concentration hydrothermal synthesis of biocompatible ordered mesoporous carbon nanospheres with tunable and uniform size. *Angewandte Chemie*, 122(43):8159–8163, 2010.

[135] Chengdu Liang, Zuojiang Li, and Sheng Dai. Mesoporous carbon materials: synthesis and modification. *Angewandte Chemie International Edition*, 47(20):3696–3717, 2008.

[136] An-Hui Lu, Wen-Cui Li, Guang-Ping Hao, Bernd Spliethoff, Hans-Josef Bongard, Bernd Bastian Schaack, and Ferdi Schüth. Easy synthesis of hollow polymer, carbon, and graphitized microspheres. *Angewandte Chemie International Edition*, 49(9):1615–1618, 2010.

[137] Jian Liu, Shi Zhang Qiao, Hao Liu, Jun Chen, Ajay Orpe, Dongyuan Zhao, and Gao Qing Lu. Extension of the Stöber method to the preparation of monodisperse resorcinol–formaldehyde resin polymer and carbon spheres. *Angewandte Chemie*, 123(26):6069–6073, 2011.

[138] Jörg Schuster, Guang He, Benjamin Mandlmeier, Taeeun Yim, Kyu Tae Lee, Thomas Bein, and Linda F Nazar. Spherical ordered mesoporous carbon nanoparticles with high porosity for lithium–sulfur batteries. *Angewandte Chemie International Edition*, 51(15):3591–3595, 2012.

[139] Jian Liu, Tianyu Yang, Da-Wei Wang, Gao Qing Max Lu, Dongyuan Zhao, and Shi Zhang Qiao. A facile soft-template synthesis of mesoporous polymeric and carbonaceous nanospheres. *Nature Communications*, 4:2798, 2013.

[140] Hongwei Zhang, Owen Noonan, Xiaodan Huang, Yannan Yang, Chun Xu, Liang Zhou, and Chengzhong Yu. Surfactant-free assembly of mesoporous carbon hollow spheres with large tunable pore sizes. *ACS Nano*, 10(4):4579–4586, 2016.

[141] Shimei Zou, Xingyan Xu, Youqi Zhu, and Chuanbao Cao. Microwave-assisted preparation of hollow porous carbon spheres and as anode of lithium-ion batteries. *Microporous and Mesoporous Materials*, 251:114–121, 2017.

[142] Taohong Li, Ming Cao, Jiankun Liang, Xiaoguang Xie, and Guanben Du. Mechanism of Base-Catalyzed Resorcinol-Formaldehyde and Phenol-Resorcinol-Formaldehyde Condensation Reactions: A Theoretical Study. *Polymers*, 9(9):426, 2017.

[143] Ruili Liu, Yifeng Shi, Ying Wan, Yan Meng, Fuqiang Zhang, Dong Gu, Zhenxia Chen, Bo Tu, and Dongyuan Zhao. Triconstituent co-assembly to ordered mesostructured polymer-silica and carbon-silica nanocomposites and large-pore mesoporous carbons with high surface areas. *Journal of the American Chemical Society*, 128(35):11652–11662, 2006.

[144] Kun Zhang, Tai-Qun Yang, Bing-Qian Shan, Peng-Cheng Liu, Bo Peng, Qing-Song Xue, En-Hui Yuan, Peng Wu, Belén Albela, and Laurent Bonneviot. Dendritic and Core–Shell–Corona Mesoporous Sister Nanospheres from Polymer–Surfactant–Silica Self-Entanglement. *Chemistry–A European Journal*, 24(2):478–486, 2018.

[145] Peter Müller. Practical suggestions for better crystal structures. *Crystallography Reviews*, 15(1):57–83, 2009.

[146] Baghbanzadeh Mostafa, Carbone Luigi, Cozzoli P. Davide, and Kappe C. Oliver. Microwave-Assisted Synthesis of Colloidal Inorganic Nanocrystals. *Angewandte Chemie International Edition*, 50(48):11312–11359.

[147] Victor K LaMer and Robert H Dinegar. Theory, production and mechanism of formation of monodispersed hydrosols. *Journal of the American Chemical Society*, 72(11):4847–4854, 1950.

[148] WZ Ostwald. Blocking of Ostwald ripening allowing long-term stabilization. *Physical Chemistry*, 37:385, 1901.

[149] Peter W Voorhees. The theory of Ostwald ripening. *Journal of Statistical Physics*, 38(1-2):231–252, 1985.

[150] Younan Xia, Yujie Xiong, Byungkwon Lim, and Sara E Skrabalak. Shape-controlled synthesis of metal nanocrystals: simple chemistry meets complex physics? *Angewandte Chemie International Edition*, 48(1):60–103, 2009.

[151] Joan Ribas Gispert. *Coordination chemistry*, volume 483. Wiley-VCH Weinheim, 2008.

[152] P. Jeffrey Hay, Jack C. Thibeault, and Roald Hoffmann. Orbital interactions in metal dimer complexes. *Journal of the American Chemical Society*, 97(17):4884–4899, 1975.

[153] Olivier Kahn. Molecular magnetism. *VCH Publishers, Inc.(USA), 1993,*, page 393, 1993.

[154] Roman Boča. Zero-field splitting in metal complexes. *Coordination Chemistry Reviews*, 248(9-10):757–815, 2004.

[155] Silvia Gomez-Coca, Eduard Cremades, Nuria Aliaga-Alcalde, and Eliseo Ruiz. Mononuclear single-molecule magnets: tailoring the magnetic anisotropy of first-row transition-metal complexes. *Journal of the American Chemical Society*, 135(18):7010–7018, 2013.

[156] Guillem Aromí, Joshua Telser, Andrew Ozarowski, Louis-Claude Brunel, Helen-Margaret Stoeckli-Evans, and J Krzystek. Synthesis, Crystal Structure, and High-Precision High-Frequency and-Field Electron Paramagnetic Resonance Investigation of a Manganese(III) Complex: $[Mn(dbm)_2(py)_2](ClO_4)$. *Inorganic Chemistry*, 44(2):187–196, 2005.

[157] Carole Duboc, Dmitry Ganyushin, Kantharuban Sivalingam, Marie-Noelle Collomb, and Frank Neese. Systematic theoretical study of the zero-field splitting in coordination complexes of Mn(III). density functional theory versus multireference wave function approaches. *The Journal of Physical Chemistry A*, 114(39):10750–10758, 2010.

[158] Roshun B. Birdy and Margaret Goodgame. Electron spin resonance study of manganese (II) ions in $M(N_2H_4)_2X_2$. *Inorganica Chimica Acta*, 50:183 – 187, 1981.

[159] Jordi Cirera, Eliseo Ruiz, Santiago Alvarez, Frank Neese, and Jens Kortus. How to build molecules with large magnetic anisotropy. *Chemistry–A European Journal*, 15(16):4078–4087, 2009.

[160] Claus JH Jacobsen, Erik Pedersen, Joergen Villadsen, and Hoegni Weihe. ESR characterization of *trans*-diacidatotetrakis (pyridine) vanadium and-manganese *trans*-$V^{II}(py)_4X_2$ and *trans*-$Mn^{II}(py)_4X_2$ (X= NCS, Cl, Br, I; py= pyridine). *Inorganic Chemistry*, 32(7):121–1221, 1993.

[161] W Bryan Lynch, R Samuel Boorse, and Jack H Freed. A 250-GHz ESR study of highly distorted manganese complexes. *Journal of the American Chemical Society*, 115(23):10909–10915, 1993.

[162] Richard M Wood, Debra M Stucker, Laura M Jones, W Bryan Lynch, Sushil K Misra, and Jack H Freed. An EPR study of some highly distorted tetrahedral manganese (II) complexes at high magnetic fields. *Inorganic Chemistry*, 38(23):5384–5388, 1999.

[163] David ML Goodgame, Hassane El Mkami, Graham M Smith, Jing P Zhao, and Eric JL McInnes. High-frequency EPR of octahedral Mn(II) compounds with large zero-field splittings. *Dalton Transactions*, (1):34–35, 2003.

[164] Claire Mantel, Carole Baffert, Isabel Romero, Alain Deronzier, Jacques Pécaut, Marie-Noëlle Collomb, and Carole Duboc. Structural characterization and electronic properties determination by high-field and high-frequency EPR of a series of five-coordinated Mn(II) complexes. *Inorganic Chemistry*, 43(20):6455–6463, 2004.

[165] Carole Duboc, Thida Phoeung, Samir Zein, Jacques Pécaut, Marie-Noëlle Collomb, and Frank Neese. Origin of the zero-field splitting in mononuclear octahedral dihalide mnii complexes: An investigation by multifrequency high-field electron paramagnetic resonance and density functional theory. *Inorganic Chemistry*, 46(12):4905–4916, 2007.

[166] Carole Duboc, Thida Phoeung, Damien Jouvenot, Allan G Blackman, Lisa F McClintock, Jacques Pécaut, Marie-Noëlle Collomb, and Alain Deronzier. High-field EPR investigation of a series of mononuclear Mn(II) complexes doped into Zn(II) hosts. *Polyhedron*, 26(18):5243–5249, 2007.

[167] Carole Duboc, Marie-Noëlle Collomb, Jacques Pécaut, Alain Deronzier, and Frank Neese. Definition of Magneto-Structural Correlations for the Mn^{II} Ion. *Chemistry–A European Journal*, 14(21):6498–6509, 2008.

[168] Jordi Rich, Carmen E Castillo, Isabel Romero, Montserrat Rodríguez, Carole Duboc, and Marie-Noëlle Collomb. Investigation of the Zero-Field Splitting in Six-and Seven-Coordinate Mononuclear Mn^{II} Complexes with N/O-Based Ligands by Combining EPR Spectroscopy and Quantum Chemistry. *European Journal of Inorganic Chemistry*, 2010(23):3658–3665, 2010.

[169] Gustav Berggren, Ping Huang, Lars Eriksson, and Magnus F Anderlund. Synthesis, Characterization and Reactivity Study of a New Penta-Coordinated Mn(II) Complex. *Applied Magnetic Resonance*, 36(1):9, 2009.

[170] SV Khangulov, PJ Pessiki, VV Barynin, DE Ash, and GC Dismukes. Determination of the metal ion separation and energies of the three lowest electronic states of dimanganese (II,II) complexes and enzymes: catalase and liver arginase. *Biochemistry*, 34(6):2015–2025, 1995.

[171] Robert A Coxall, Steven G Harris, David K Henderson, Simon Parsons, Peter A Tasker, and Richard EP Winpenny. Inter-ligand reactions: in situ formation of new polydentate ligands. *Journal of the Chemical Society, Dalton Transactions*, (14):2349–2356, 2000.

[172] Robert Sidney Cahn, Christopher Ingold, and Vladimir Prelog. Specification of molecular chirality. *Angewandte Chemie International Edition in English*, 5(4):385–415, 1966.

[173] Lin Cheng, Wei-Xiong Zhang, Bao-Hui Ye, Jian-Bin Lin, and Xiao-Ming Chen. Spin canting and topological ferrimagnetism in two manganese (II) coordination polymers generated by in situ solvothermal ligand reactions. *European Journal of Inorganic Chemistry*, 2007(18):2668–2676, 2007.

[174] Gema Fernández, Montserrat Corbella, Gabriel Aullón, Miguel A Maestro, and José Mahía. New Dinuclear Mn^{III} Compounds with 2-MeC_6H_4COO and 2-FC_6H_4COO Bridges–Effect of Terminal Monodentate Ligands (H_2O, ClO_4–and NO_3–) on the Magnetic Properties. *European Journal of Inorganic Chemistry*, 2007(9):1285–1296, 2007.

[175] Verónica Gómez and Montserrat Corbella. Catalase Activity of Dinuclear Mn^{III} Compounds with Chlorobenzoato Bridges. *European Journal of Inorganic Chemistry*, 2012(19):3147–3155, 2012.

[176] Laura Cañadillas-Delgado, Oscar Fabelo, Jorge Pasán, Fernando S Delgado, Francesc Lloret, Miguel Julve, and Catalina Ruiz-Pérez. Unusual (aqua) bis (μ-carboxylate) bridge in homometallic M(II) (M= Mn, Co and Ni) two-dimensional compounds based on the 1, 2, 3, 4-butanetetracarboxylic acid: Synthesis, structure, and magnetic properties. *Inorganic Chemistry*, 46(18):7458–7465, 2007.

[177] Andrea Caneschi, Fabrizio Ferraro, Dante Gatteschi, Maria Chiara Melandri, Paul Rey, and Roberta Sessoli. Synthesis, Structure and Magnetic Properties of a Dinuclear Manganese(II) Complex with One μ-Aqua and Two μ-Carboxylato Bridges. *Angewandte Chemie International Edition in English*, 28(10):1365–1367, 1989.

[178] Shi Bao Yu, Stephen J Lippard, Itzhak Shweky, and Avi Bino. Dinuclear manganese (II) complexes with water and carboxylate bridges. *Inorganic Chemistry*, 31(17):3502–3504, 1992.

[179] Beltzane Garcia i Cirera. *Compostos polinuclears de manganès mimètics d'enzims redox. Inserció en suports mesoestructurats. Estudi de les propietats magnètiques i catalítiques*. PhD thesis, 2016.

[180] Tuncer Hökelek, Hakan Dal, Baris Tercan, Ozgür Aybirdi, and Hacali Necefoglu. catena-Poly [[[diaquabis [4-(diethylamino) benzoato-κO] manganese (II)]-μ-aqua] dihydrate]. *Acta Crystallographica Section E: Structure Reports Online*, 65(7):m747–m748, 2009.

[181] ID t Brown and RD Shannon. Empirical bond-strength–bond-length curves for oxides. *Acta Crystallographica Section A: Crystal Physics, Diffraction, Theoretical and General Crystallography*, 29(3):266–282, 1973.

[182] ID t Brown and Kang Kun Wu. Empirical parameters for calculating cation–oxygen bond valences. *Acta Crystallographica Section B*, 32(7):1957–1959, 1976.

[183] Michael E Fisher. Magnetism in one-dimensional systems—the heisenberg model for infinite spin. *American Journal of Physics*, 32(5):343–346, 1964.

[184] Nicholas F Chilton, Russell P Anderson, Lincoln D Turner, Alessandro Soncini, and Keith S Murray. PHI: A powerful new program for the analysis of anisotropic monomeric and exchange-coupled polynuclear d-and f-block complexes. *Journal of Computational Chemistry*, 34(13):1164–1175, 2013.

[185] Alessandro Bencini and Dante Gatteschi. *EPR of exchange coupled systems*. Courier Corporation, 2012.

[186] Belen Albela, Montserrat Corbella, Joan Ribas, Isabel Castro, Jorunn Sletten, and Helen Stoeckli-Evans. Synthesis, structural characterization (X-ray and EXAFS), and magnetic properties of polynuclear manganese (II) complexes with chlorobenzoato bridges. *Inorganic Chemistry*, 37(4):788–798, 1998.

[187] Chun-Sen Liu, E Carolina Sañudo, Li-Fen Yan, Ze Chang, Jun-Jie Wang, and Tong-Liang Hu. Two manganese (II) complexes based on anthracene-9-carboxylate: Syntheses, crystal structures, and magnetic properties. *Transition Metal Chemistry*, 34(1):51–60, 2009.

[188] Bao-Hui Ye, Toby Mak, Ian D Williams, and Xiao-yuan Li. Novel dimanganese (II) complexes with (μ-H_2O)(μ-OAc)$_2$ bridges. models fordimanganese enzymes. *Chemical Communications*, (18):1813–1814, 1997.

[189] Marianthi Zampakou, Natalia Rizeq, Vassilis Tangoulis, Athanasios N Papadopoulos, Franc Perdih, Iztok Turel, and George Psomas. Manganese (II) complexes with the non-steroidal anti-inflammatory drug tolfenamic acid: Structure and biological perspectives. *Inorganic Chemistry*, 53(4):2040–2052, 2014.

[190] Gema Fernández, Montserrat Corbella, José Mahía, and Miguel A Maestro. Polynuclear Mn^{II} Complexes with Chloroacetate Bridge- Syntheses, Structure, and Magnetic Properties. *European Journal of Inorganic Chemistry*, 2002(9):2502–2510, 2002.

[191] Hongwei Hou, Linke Li, Yu Zhu, Yaoting Fan, and Yuqin Qiao. Novel one-dimensional polymers generated from p-ferrocenylbenzoate: Syntheses, structures, and magnetic properties. *Inorganic Chemistry*, 43(15):4767–4774, 2004.

[192] Mònica Fontanet, Montserrat Rodríguez, Xavier Fontrodona, Isabel Romero, Francesc Teixidor, Clara Viñas, Núria Aliaga-Alcalde, and Pavel Matějíček. Water-Soluble Manganese Inorganic Polymers: The Role of Carborane Clusters and Producing Large Structural Adjustments from Minor Molecular Changes. *Chemistry–A European Journal*, 20(43):13993–14003, 2014.

[193] John B Vincent, Cheryl Christmas, Hsiu Rong Chang, Qiaoying Li, Peter DW Boyd, John C Huffman, David N Hendrickson, and George Christou. Modeling the photosynthetic water oxidation center. Preparation and properties of tetranuclear manganese complexes containing $[Mn_4O_2]^{6+,7+,8+}$ cores, and the crystal structures of $Mn_4O_2(O_2CMe)_6(bipy)_2$ and $[Mn_4O_2(O_2CMe)_7(bipy)_2](ClO_4)$. *Journal of the American Chemical Society*, 111(6):2086–2097, 1989.

[194] Eduardo Libby, James K McCusker, Edward A Schmitt, Kirsten Folting, David N Hendrickson, and George Christou. Preparation and properties of models for the photosynthetic water oxidation center: spin frustration in the manganese $[Mn_4O_2(O_2CR)_7(pic)_2]$-anion. *Inorganic Chemistry*, 30(18):3486–3495, 1991.

[195] Cristina Cañada-Vilalta, John C Huffman, and George Christou. Preparation, crystal structure and chelate substitution reactions of $[Mn_4O_2(O_2CPh)_6(dpm)_2]$(dpm= the anion of dipivaloylmethane). *Polyhedron*, 20(15):1785–1793, 2001.

[196] R Basler, G Chaboussant, C Cañada-Vilalta, G Christou, H Mutka, S Janssen, F Altorfer, and H-U Güdel. Magnetic and inelastic neutron scattering studies of a frustrated tetranuclear Mn^{3+} butterfly-type cluster. *Polyhedron*, 22(14-17):2471–2479, 2003.

[197] Yun-Sheng Ma, Hong-Chang Yao, Wei-Jie Hua, Shu-Hua Li, Yi-Zhi Li, and Li-Min Zheng. Tetranuclear manganese (III) clusters containing both carboxylate and phosphonate bridging ligands. *Inorganica Chimica Acta*, 360(5):1645–1650, 2007.

[198] Mei Wang, Chengbing Ma, Daqiang Yuan, Mingqiang Hu, Changneng Chen, and Qiutian Liu. Synthesis and characterization of a family of tetranuclear manganese (III) phosphonate complexes. *New Journal of Chemistry*, 31(12):2103–2110, 2007.

[199] Reda FM Elshaarawy, Yanhua Lan, and Christoph Janiak. Oligonuclear homo-and mixed-valence manganese complexes based on thiophene-or aryl-carboxylate ligation: Synthesis, characterization and magnetic studies. *Inorganica Chimica Acta*, 401:85–94, 2013.

[200] Luis Escriche-Tur, Belén Albela, Mercè Font-Bardia, and Montserrat Corbella. Singlet ground states in compounds with a $[Mn_4^{III}O_2]^{8+}$ core due to broken degeneration. *New Journal of Chemistry*, 41(8):2934–2940, 2017.

[201] Tony Sala and Melvyn V. Sargent. Tetrabutylammonium permanganate: an efficient oxidant for organic substrates. *Journal of the Chemical Society, Chemical Communications*, pages 253–254, 1978.

[202] Lin Fang. *Surface Engineering of Mesoporous Silica for Ti-Based Epoxidation Catalysts*. PhD thesis, Ecole normale supérieure de lyon-ENS LYON, 2012.

[203] Luis Escriche Tur. *Polynuclear manganese compounds with carboxylate bridging ligands models of redox enzymes: insertion inside mesoporous supports: study of their magnetic and catalytic properties*. PhD thesis, 2016.

[204] K. S. W. Sing. Reporting physisorption data for gas/solid systems with special reference to the determination of surface area and porosity. *Pure Appl. Chem.*, 57(4):603–619, 1985.

[205] Françoise Rouquerol, Laurent Luciani, Philip Llewellyn, Renaud Denoyel, and Jean Rouquerol. Texture des matériaux pulvérulents ou poreux. *Techniques de l'ingénieur. Analyse et caractérisation*, 2(P1050):p1050–1, 2003.

[206] Stephen Brunauer, P. H. Emmett, and Edward Teller. Adsorption of Gases in Multimolecular Layers. *Journal of the American Chemical Society*, 60(2):309–319, 1938.

[207] CG Schull. The determination of pore size distribution from gas adsorption data. *Journal of the American Chemical Society*, 70(4):1405–1410, 1948.

[208] B.C. Lippens and J.H. de Boer. Studies on pore systems in catalysts: V. The t method. *Journal of Catalysis*, 4(3):319 – 323, 1965.

[209] KSW Sing, DH Everett, RAW Haul, L Moscou, RA Pierotti, J Rouquerol, and T Siemieniewska. Physical and biophysical chemistry division commission on colloid and surface chemistry including catalysis. *Pure Applied Chemistry*, 57(4):603–619, 1985.

[210] M Kruk, M Jaroniec, and A Sayari. Application of large pore MCM-41 molecular sieves to improve pore size analysis using nitrogen adsorption measurements. *Langmuir*, 13(23):6267–6273, 1997.

[211] Sidney John Gregg, Kenneth Stafford William Sing, and HW Salzberg. Adsorption surface area and porosity. *Journal of The Electrochemical Society*, 114(11):279C–279C, 1967.

[212] Geza Horvath and Kunitaro Kawazoe. Method for the calculation of effective pore size distribution in molecular sieve carbon. *Journal of Chemical Engineering of Japan*, 16(6):470–475, 1983.

[213] K C A Smith and C W Oatley. The scanning electron microscope and its fields of application. *British Journal of Applied Physics*, 6(11):391, 1955.

[214] Rolf Erni, Marta D Rossell, Christian Kisielowski, and Ulrich Dahmen. Atomic-resolution imaging with a sub-50-pm electron probe. *Physical Review Letters*, 102(9):096101, 2009.

[215] Differences between light microscope and electron microscope. https://microbiologyinfo.com/differences-between-light-microscope-and-electron-microscope/.

[216] Eisuke Yamamoto, Masaki Kitahara, Takuya Tsumura, and Kazuyuki Kuroda. Preparation of size-controlled monodisperse colloidal mesoporous silica nanoparticles and fabrication of colloidal crystals. *Chemistry of Materials*, 26(9):2927–2933, 2014.

[217] Lling-Lling Tan, Wee-Jun Ong, Siang-Piao Chai, and Abdul Rahman Mohamed. Reduced graphene oxide-TiO_2 nanocomposite as a promising visible-light-active photocatalyst for the conversion of carbon dioxide. *Nanoscale Research Letters*, 8(1):465, 2013.

[218] Sherif A El-Khodary, Gaber M El-Enany, Mohamed El-Okr, and Medhat Ibrahim. Preparation and characterization of microwave reduced graphite oxide for high-performance supercapacitors. *Electrochimica Acta*, 150:269–278, 2014.

[219] DD Werstler. Quantitative ^{13}C NMR characterization of aqueous formaldehyde resins: 2. resorcinol-formaldehyde resins. *Polymer*, 27(5):757–764, 1986.

[220] Stefan Lijewski, Magdalena Wencka, Stanislaw K Hoffmann, Mateusz Kempinski, Wojciech Kempinski, and Malgorzata Sliwinska-Bartkowiak. Electron spin relaxation and quantum localization in carbon nanoparticle: Electron spin echo studies. *Physical Review B*, 77(1):014304, 2008.

[221] S. Swarnalatha, P.K. Selvi, A. Ganesh Kumar, and G. Sekaran. Nanoemulsion drug delivery by ketene based polyester synthesized using electron rich carbon/silica composite surface. *Colloids and Surfaces B: Biointerfaces*, 65(2):292–299, 2008.

[222] M. Baikousi, C. Daikopoulos, Y. Georgiou, A. Bourlinos, R. Zbořil, Y. Deligiannakis, and M. A. Karakassides. Novel Ordered Mesoporous Carbon with Innate Functionalities and Superior Heavy Metal Uptake. *The Journal of Physical Chemistry C*, 117(33):16961–16971, 2013.

[223] Gilles Montagnac. *In situ UV resonant Raman spectroscopy at high temperature and at high pressure*. PhD thesis, 2012.

[224] Humberto C Garcia, Renata Diniz, Maria I Yoshida, and Luiz Fernando C de Oliveira. An intriguing hydrogen bond arrangement of polymeric 1D chains of 4, 4′-bipyridine coordinated to Co^{2+}, Ni^{2+}, Cu^{2+} and Zn^{2+} ions having barbiturate as counterions in a 3D network. *CrystEngComm*, 11(5):881–888, 2009.

[225] Tommaso Salzillo, Elisabetta Venuti, Cristina Femoni, Raffaele Guido Della Valle, Riccardo Tarroni, and Aldo Brillante. Crystal Structure of the 9-Anthracene–Carboxylic Acid Photochemical Dimer and Its Solvates by X-ray Diffraction and Raman Microscopy. *Crystal Growth & Design*, 17(6):3361–3370, 2017.

[226] A Michota and J Bukowska. Surface-enhanced raman scattering (SERS) of 4-mercaptobenzoic acid on silver and gold substrates. *Journal of Raman Spectroscopy*, 34(1):21–25, 2003.

[227] Montserrat Corbella, Gema Fernández, Patricia González, Miguel Maestro, Mercè Font-Bardia, and Helen Stoeckli-Evans. Dinuclear Mn^{III} Compounds $[\{Mn(bpy)(H_2O)\}_2(\mu\text{-}4\text{-}RC_6H_4COO)_2(\mu\text{-}O)](NO_3)_2$ (R= Me, F, CF_3, MeO, tBu): Effect of the R Group on the Magnetic Properties and the Catalase Activity. *European Journal of Inorganic Chemistry*, 2012(13):2203–2212, 2012.

[228] Gema Fernández, Montserrat Corbella, Montserrat Alfonso, Helen Stoeckli-Evans, and Isabel Castro. A comparative XAS and X-ray diffraction study of new binuclear Mn (III) complexes with catalase activity. Indirect effect of the counteranion on magnetic properties. *Inorganic Chemistry*, 43(21):6684–6698, 2004.

[229] Leonardo G Gagliardi, Cecilia B Castells, Clara Ràfols, Martí Rosés, and Elisabeth Bosch. δ Conversion Parameter between pH Scales (and) in Acetonitrile/Water Mixtures at Various Compositions and Temperatures. *Analytical Chemistry*, 79(8):3180–3187, 2007.

[230] Jérémy Chaignon, Marie Gourgues, Lhoussain Khrouz, Nicolás Moliner, Laurent Bonneviot, Fabienne Fache, Isabel Castro, and Belén Albela. A bioinspired heterogeneous catalyst based on the model of the manganese-dependent dioxygenase for selective oxidation using dioxygen. *RSC Advances*, 7(28):17336–17345, 2017.

[231] M Baikousi, C Daikopoulos, Y Georgiou, A Bourlinos, R Zboril, Y Deligiannakis, and MA Karakassides. Novel ordered mesoporous carbon with innate functionalities and superior heavy metal uptake. *The Journal of Physical Chemistry C*, 117(33):16961–16971, 2013.

[232] S Swarnalatha, PK Selvi, A Ganesh Kumar, and G Sekaran. Nanoemulsion drug delivery by ketene based polyester synthesized using electron rich carbon/silica composite surface. *Colloids and Surfaces B: Biointerfaces*, 65(2):292–299, 2008.

[233] Jerome W Sidman. Electronic and vibrational states of anthracene. *The Journal of Chemical Physics*, 25(1):115–121, 1956.

[234] Radu-Ionut Tigoianu, A Airinep, and Dana-Ortansa Dorohoi. Solvent influence on the electronic fluorescence spectra of anthracene. *Revista de Chimie*, 61(5):491–494, 2010.

[235] William R Ware and Bernard A Baldwin. Absorption intensity and fluorescence lifetimes of molecules. *The Journal of Chemical Physics*, 40(6):1703–1705, 1964.

[236] William R Dawson and Maurice W Windsor. Fluorescence yields of aromatic compounds. *The Journal of Physical Chemistry*, 72(9):3251–3260, 1968.

[237] Roger A Lampert, Leslie A Chewter, David Phillips, Desmond V O'Connor, Anthony J Roberts, and Stephen R Meech. Standards for nanosecond fluorescence decay time measurements. *Analytical Chemistry*, 55(1):68–73, 1983.

[238] NS Bazilevskaya and AS Cherkasov. Excited Dimers of Anthracene Derivatives. I. *Optics and Spectroscopy*, 18:30, 1965.

[239] TC Werner and David M Hercules. Fluorescence of 9-anthroic acid and its esters. Environmental effects on excited-state behavior. *The Journal of Physical Chemistry*, 73(6):2005–2011, 1969.

[240] Satoshi Suzuki, Tsuneo Fujii, Nobuyuki Yoshiike, Shigeru Komatsu, and Toshiko Iida. Absorption and fluorescence spectra of anthracenecarboxylic acids. I. 9-anthroic acid and formation of excimer. *Bulletin of the Chemical Society of Japan*, 51(9):2460–2466, 1978.

[241] V Swayambunathan and EC Lim. Electronic structure and spectra of 9-anthroic acid and its esters in supersonic free jets. *Journal of Physical Chemistry*, 91(25):6359–6364, 1987.

[242] N Ghoneim, D Scherrer, and P Suppan. Dual luminescence, structure and excimers of 9-anthracene carboxylic acid. *Journal of Luminescence*, 55(5-6):271–275, 1993.

[243] MSA Abdel-Mottaleb, HR Galal, AFM Dessouky, M El-Naggar, D Mekkawi, SS Ali, and GM Attya. Fluorescence and photostability studies of anthracene-9-carboxylic acid in different media. *International Journal of Photoenergy*, 2(1):47–53, 2000.

[244] Ichiro Momiji, Chihiro Yoza, and Kazunori Matsui. Fluorescence spectra of 9-anthracenecarboxylic acid in heterogeneous environments. *The Journal of Physical Chemistry B*, 104(7):1552–1555, 2000.

[245] William Rodríguez-Córdoba, Raquel Noria-Moreno, Pedro Navarro, and Jorge Peon. Ultrafast fluorescence study of the effect of carboxylic and carboxylate substituents on the excited state properties of anthracene. *Journal of Luminescence*, 145:697–707, 2014.

[246] Jennifer M Rowe, Jennifer M Hay, William A Maza, Robert C Chapleski, Erin Soderstrom, Diego Troya, and Amanda J Morris. Systematic investigation of the excited-state properties of anthracene-dicarboxylic acids. *Journal of Photochemistry and Photobiology A: Chemistry*, 337:207–215, 2017.

[247] Salsabil Abou-Hatab, Vincent A Spata, and Spiridoula Matsika. Substituent effects on the absorption and fluorescence properties of anthracene. *The Journal of Physical Chemistry A*, 121(6):1213–1222, 2017.

[248] Brian D Wagner, Amy E Arnold, Spencer Gallant, Carmen R Grinton, Julia K Locke, Natasha Mills, Carrie Snow, Timara B Uhlig, and Christen Vessey. The Polarity Sensitivity Factor (PSF) of some Fluorescent Probe Molecules Used for Studying Supramolecular Systems and other Heterogeneous Environments. *Canadian Journal of Chemistry*, (ja), 2018.

[249] Cuimiao Zhang and Jun Lin. Defect-related luminescent materials: synthesis, emission properties and applications. *Chemical Society Reviews*, 41(23):7938–7961, 2012.

[250] Adam M Jakob and Thomas A Schmedake. A novel approach to monodisperse, luminescent silica spheres. *Chemistry of Materials*, 18(14):3173–3175, 2006.

[251] Arman Zhanbotin, Ronald B Soriano, Anita K Ikonen, Turlybek N Nurakhmetov, and Thomas A Schmedake. Luminescent mesoporous colloidal silica: A nanoporous substrate for photosensitization of lanthanide ions. *Materials Letters*, 65(1):10–12, 2011.

[252] Shi-Rui Guo, Jun-Yan Gong, Peng Jiang, Mian Wu, Yang Lu, and Shu-Hong Yu. Biocompatible, luminescent silver@phenol formaldehyde resin core/shell nanospheres: large-scale synthesis and application for in vivo bioimaging. *Advanced Functional Materials*, 18(6):872–879, 2008.

[253] Ping Yang, Yang Zhao, Yang Lu, Qi-Zhi Xu, Xue-Wei Xu, Liang Dong, and Shu-Hong Yu. Phenol formaldehyde resin nanoparticles loaded with CdTe quantum dots: a fluorescence resonance energy transfer probe for optical visual detection of copper (II) ions. *ACS Nano*, 5(3):2147–2154, 2011.

[254] Ping Yang, Qi-Zhi Xu, Sheng-Yu Jin, Yang Zhao, Yang Lu, Xue-Wei Xu, and Shu-Hong Yu. Synthesis of Fe_3O_4@phenol formaldehyde resin core–shell nanospheres loaded with Au nanoparticles as magnetic FRET nanoprobes for detection of thiols in living cells. *Chemistry–A European Journal*, 18(4):1154–1160, 2012.

[255] George M Sheldrick. Crystal structure refinement with SHELXL. *Acta Crystallographica Section C: Structural Chemistry*, 71(1):3–8, 2015.

[256] George M Sheldrick. XT, Program for the Solution of Crystal Structures. Bruker AXS Inc. Software package.

[257] George M Sheldrick. SADABS Version 2008/1. Bruker AXS Inc.